GENE SILENCING AND EDITING STRATEGIES FOR NEURODEGENERATIVE DISEASES

EDITED BY: Clévio Nóbrega and Sandro Alves
PUBLISHED IN: Frontiers in Neuroscience and Frontiers in Molecular Neuroscience

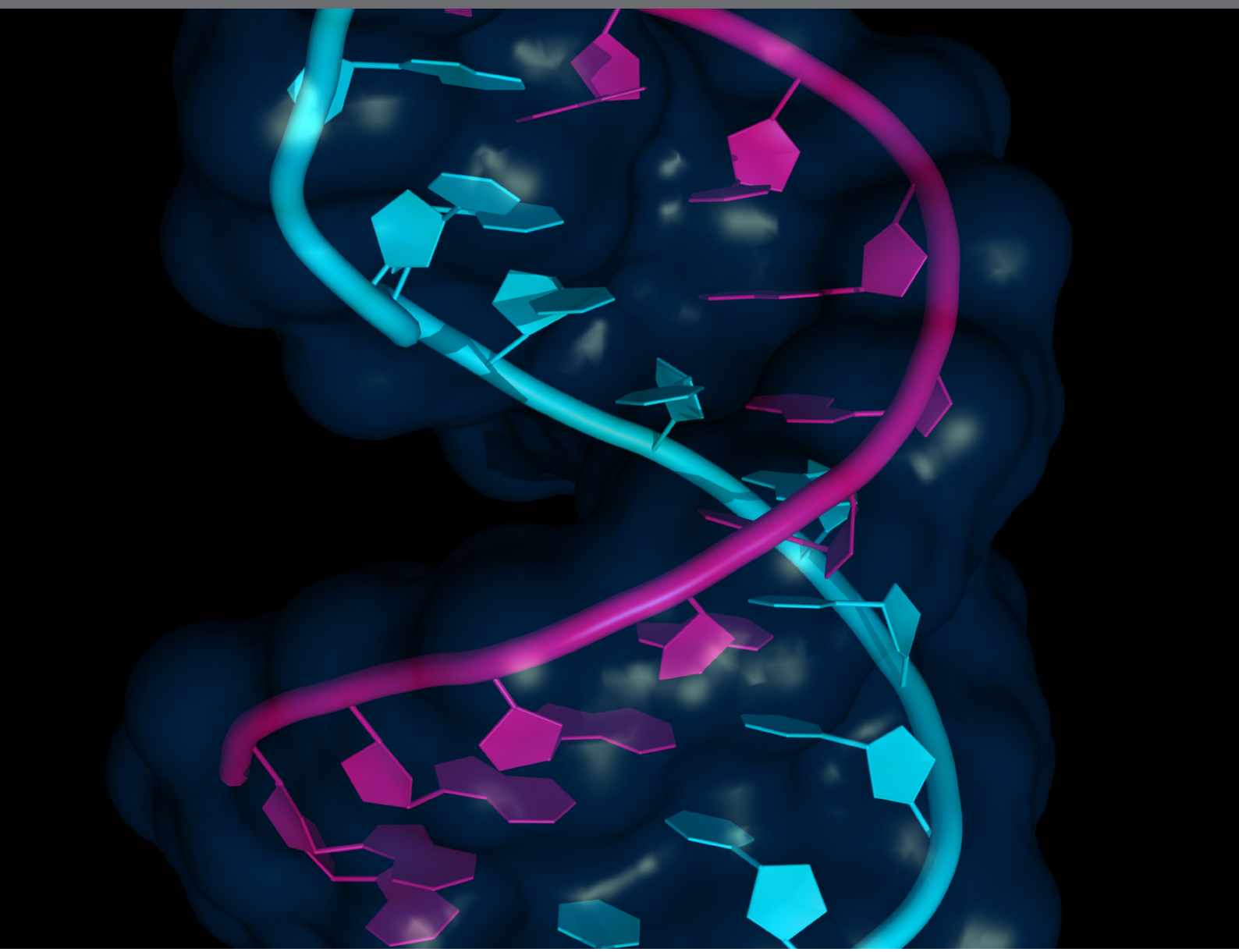

frontiers Research Topics

ISSN 1664-8714
ISBN 978-2-88945-551-5
DOI 10.3389/978-2-88945-551-5

About Frontiers

Frontiers is more than just an open-access publisher of scholarly articles: it is a pioneering approach to the world of academia, radically improving the way scholarly research is managed. The grand vision of Frontiers is a world where all people have an equal opportunity to seek, share and generate knowledge. Frontiers provides immediate and permanent online open access to all its publications, but this alone is not enough to realize our grand goals.

Frontiers Journal Series

The Frontiers Journal Series is a multi-tier and interdisciplinary set of open-access, online journals, promising a paradigm shift from the current review, selection and dissemination processes in academic publishing. All Frontiers journals are driven by researchers for researchers; therefore, they constitute a service to the scholarly community. At the same time, the Frontiers Journal Series operates on a revolutionary invention, the tiered publishing system, initially addressing specific communities of scholars, and gradually climbing up to broader public understanding, thus serving the interests of the lay society, too.

Dedication to Quality

Each Frontiers article is a landmark of the highest quality, thanks to genuinely collaborative interactions between authors and review editors, who include some of the world's best academicians. Research must be certified by peers before entering a stream of knowledge that may eventually reach the public - and shape society; therefore, Frontiers only applies the most rigorous and unbiased reviews.
Frontiers revolutionizes research publishing by freely delivering the most outstanding research, evaluated with no bias from both the academic and social point of view. By applying the most advanced information technologies, Frontiers is catapulting scholarly publishing into a new generation.

What are Frontiers Research Topics?

Frontiers Research Topics are very popular trademarks of the Frontiers Journals Series: they are collections of at least ten articles, all centered on a particular subject. With their unique mix of varied contributions from Original Research to Review Articles, Frontiers Research Topics unify the most influential researchers, the latest key findings and historical advances in a hot research area! Find out more on how to host your own Frontiers Research Topic or contribute to one as an author by contacting the Frontiers Editorial Office: researchtopics@frontiersin.org

GENE SILENCING AND EDITING STRATEGIES FOR NEURODEGENERATIVE DISEASES

Topic Editors:
Clévio Nóbrega, University of Algarve, Portugal
Sandro Alves, Brainvectis Therapeutics, France

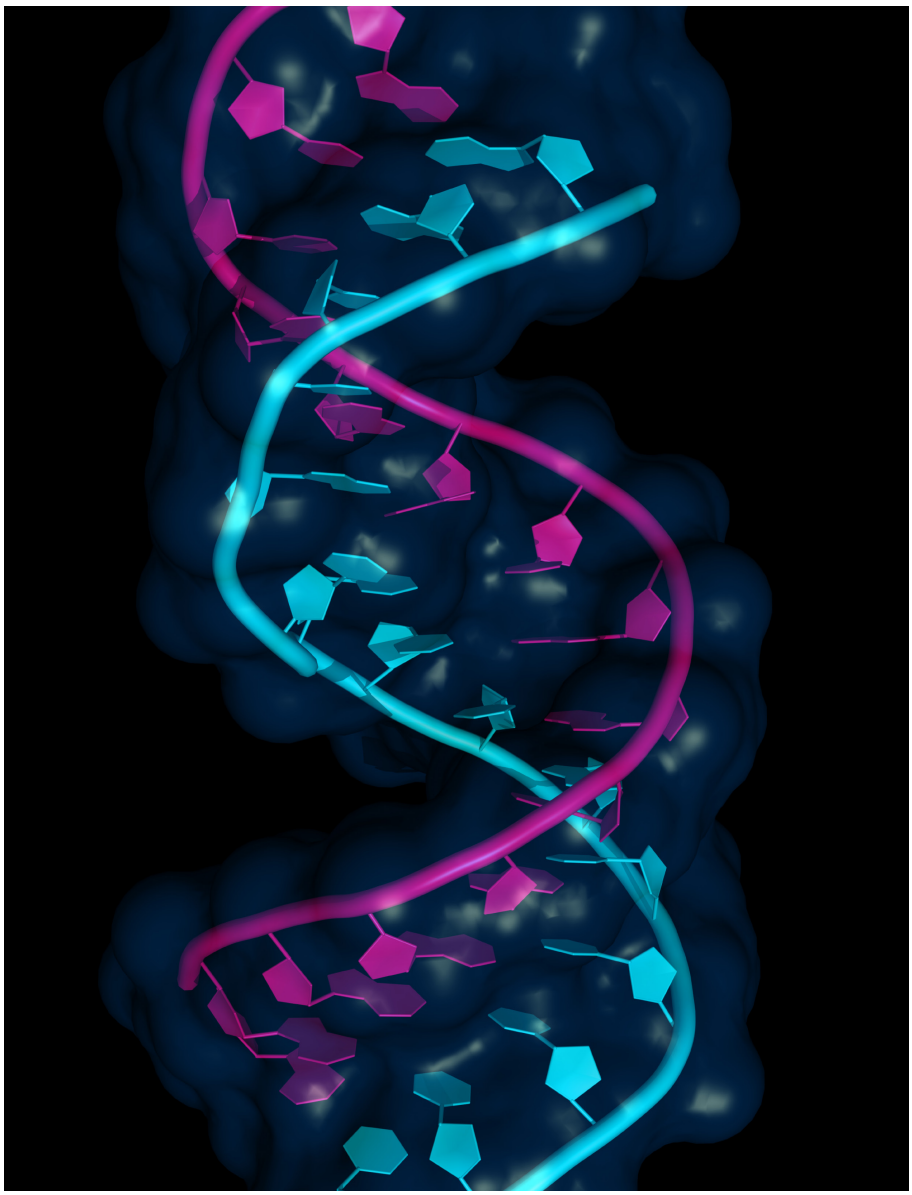

Cover image: petarg/Shutterstock.com

Citation: Nóbrega, C., Alves, S., eds (2018). Gene Silencing and Editing Strategies for Neurodegenerative Diseases. Lausanne: Frontiers Media.
doi: 10.3389/978-2-88945-551-5

Table of Contents

3.2 TO DEVELOP RESEARCH MODELS

frontiers in Neuroscience

EDITORIAL
published: 22 June 2018
doi: 10.3389/fnins.2018.00425

Editorial: Gene Silencing and Editing Strategies for Neurodegenerative Diseases

Clévio Nóbrega[1,2,3,4]* *and Sandro Alves*[5]*

[1] Department of Biomedical Sciences and Medicine, University of Algarve, Faro, Portugal, [2] Centre for Biomedical Research, University of Algarve, Faro, Portugal, [3] Algarve Biomedical Center, University of Algarve, Faro, Portugal, [4] Center for Neuroscience and Cell Biology, University of Coimbra, Coimbra, Portugal, [5] Brainvectis Therapeutics, Paris, France

Keywords: neurodegenerative diseases, gene silencing, gene editing, neurodegeneration, therapies

Editorial on the Research Topic

Gene Silencing and Editing Strategies for Neurodegenerative Diseases

The discovery of the RNA interference (RNAi) mechanism and the development of gene editing techniques such as TALENs or CRISPR/Cas9 opened a new avenue for the treatment and understanding of neurodegenerative diseases. If the main goal and most straightforward rationale is to use these systems to develop therapeutic options for neurodegenerative diseases, it is also clear that RNAi and editing strategies are valuable for research, as tools for the understanding of the molecular mechanisms implicated in these diseases or, alternatively, to develop research models for their study.

Recent studies have demonstrated that several biological networks implicated in the modulation of gene expression at transcriptional, post-transcriptional and epigenetic levels, are tightly regulated by multiple long non-coding RNAs (lncRNAs), some of them specifically expressed in the central nervous system (CNS). These lncRNAs may have an important role in the pathophysiology of neurodegenerative diseases. So far, deregulation of most lncRNAs is widely associated to the progression of neurodegenerative disorders like Alzheimer's (AD), Parkinson's (PD), and Huntington's (HD) diseases, as well as Amyotrophic Lateral Sclerosis (ALS). Quan et al. comprehensively discuss several lncRNAs-associated regulatory mechanisms, which may be involved in the pathophysiology of the above-mentioned diseases. They conclude that additional investigation of lncRNAs rolls has the potential to achieve increasing insights about their functions and therefore to better engineer therapeutic strategies based on lncRNAs modulation.

SILENCING AND EDITING STRATEGIES AS THERAPEUTIC APPROACHES

Recently, the toxicity at the RNA level emerged as a new important player in the pathogenesis of HD and other Polyglutamine (polyQ) disorders. Several studies have demonstrated cell degeneration and dysfunction associated to the expression of untranslated transcripts with expanded CAG repeats. Therefore, the development of editing strategies provided the tools and opportunity to directly target the mutant gene, thus preventing the formation of toxic RNA and the consequent cascade of pathological events. In line with this idea, Dabrowska et al. developed a CRISPR/Cas9 strategy based in the precise excision of the CAG tract using derived fibroblasts from several HD patients. This strategy was successful in excising the repeats leading to a safe and specific abolition of huntingtin synthesis. These important results if translated to *in vivo* studies could become a therapeutic option in future clinical trials for HD patients.

OPEN ACCESS

Edited and reviewed by:
Tibor Hortobágyi,
University of Debrecen, Hungary

***Correspondence:**
Clévio Nóbrega
cdnobrega@ualg.pt
Sandro Alves
sandro.alves@brainvectis.com

Specialty section:
This article was submitted to Neurodegeneration, a section of the journal Frontiers in Neuroscience

Received: *25 May 2018*
Accepted: *06 June 2018*
Published: *22 June 2018*

Citation:
Nóbrega C and Alves S (2018) Editorial: Gene Silencing and Editing Strategies for Neurodegenerative Diseases. Front. Neurosci. 12:425. doi: 10.3389/fnins.2018.00425

Another gene silencing-based therapy is the use of antisense oligonucleotides delivered by calcium-phosphate-lipid nanoparticles. The goal is to lower mutant superoxide dismutase I (SOD1), that abnormally accumulates in ALS motor neurons. Thus, SOD1 lowering could be an effective therapeutic strategy. To circumvent the short half-life of ASOs and the fact that they cannot cross the blood-brain-barrier, Chen et al. propose calcium phosphate lipid coated nanoparticles-based delivery of ASOs targeting SOD1 in motor neurons, as an effective and safe delivery system to the CNS. The authors also report for the first time the distribution of nanoparticles in the brain and spinal cord of zebrafish, a powerful animal model to develop therapies for ALS and other neurological disorders.

SILENCING AND EDITING STRATEGIES AS RESEARCH TOOL

To Understand the Molecular Mechanisms Underlying Neuronal Events

Methamphetamine (METH) is a stimulant drug that induce toxicity in the CNS, especially in dopaminergic neurons. Du et al. explored the effect of METH in astrocyte-related neuroinflammation, using siRNAs to block the expression of Caspase-11 and toll-like receptor (TLR4) in primary cultures of mouse astrocytes. They found that siRNA inhibition of Caspase-11 reduce the expression of pro-inflammatory cytokines, whereas TLR4 inhibition decrease the METH-induced activation of NF-kB and Caspse-11. These results highlight the importance of both Caspase-11 and TLR4 in the neuroinflammation induced by METH.

Inflammation is induced upon cerebral ischemia, with an activation of microglia and their phenotype alteration to M1 or M2, depending on the microenvironment stimuli. The study by Cheon et al. use siRNA-based strategies to study the involvement of signal-regulating kinase 1 (ASK1) in microglia function and its alterations upon ischemic stroke. The results show that ASK1 inhibition suppressed the expression of M1-associated genes (pro-inflammatory mediators), whereas augmented M2-associated genes expression (anti-inflammatory mediators). The authors propose that ASK1 modulation might constitute a new strategy for repair, targeting the microglia phenotype after an ischemic stroke.

Cholesterol metabolism has been widely associated to several neurodegenerative diseases including Alzheimer's disease. Despite this, lipid modifications associated to the disease progression, as well as the link between altered cholesterol levels and AD still remains poorly understood. In Ayciriex et al. the authors promoted the silencing of the *Cyp46a1* gene (which encodes the cholesterol 24-hydroxylase) in the mouse hippocampus and performed both targeted and non-targeted approaches by liquid chromatography coupled to high resolution mass spectroscopy to better understand lipid modifications associated to AD-like degeneration. The authors show that the cholesterol 24-hydroxylase silencing, key enzyme in cholesterol metabolism deregulates lipid homeostasis in brain, thus allowing dissecting the role of cholesterol metabolism in AD and other neurodegenerative diseases.

Mitochondrial dysfunction underlies the pathogenesis of several neurodegenerative diseases, including PD. Ye et al. use the RNAi pathway to inhibit peroxisome proliferator-activated receptor γ coactivator-1alpha (PGC-1α) in a PD cellular model. PGC-1α is implicated in the regulation of mitochondrial biogenesis and oxidative capacity. The use of siRNAs reducing the levels of PGC-1α led to a reduction of mitochondrial membrane potential, intracellular ATP content and intracellular H_2O_2 generation, thus establishing PGC-1α as an important modulator of mitochondria function.

In summary, all these studies highlight the importance of gene silencing strategies to achieve a better understanding of biological cellular mechanistic pathways.

To Develop Research Models

The development of research models is an essential tool for studying the molecular and cellular events underlying a pathogenesis and for testing new therapeutic approaches. Induced pluripotent stem cells (iPSCs), became one of the most popular research models, providing the opportunity to have customized models for diseases and patients. Szlachcic et al. developed a study aiming the development of HD iPS cells, where huntingtin was silenced by shRNAs. The authors achieved a stable silencing of huntingtin in different HD iPSc lines, remaining active until the differentiation in neural stem cells. The authors used the developed model to study the effect of huntingtin silencing in different signaling pathways, providing evidences for usefulness of the model to study the molecular processes underlying HD pathogenesis.

All these studies highlight that gene silencing and editing tools are powerful tools for research, allowing the development of advanced therapies based in gene and cell delivery, and importantly allowing the modulation of cellular pathways and functions as well as to develop new models to be used for research.

AUTHOR CONTRIBUTIONS

CN and SA contributed equally to this editorial, being both involved in the outline of the editorial, in its writing and scientific review.

FUNDING

The laboratory of CN is supported by the French Muscular Dystrophy Association (AFM-Téléthon), the Ataxia UK and the Fundação para a Ciência e Tecnologia, Portugal.

Conflict of Interest Statement: The authors declare that the research was conducted in the absence of any commercial or financial relationships that could be construed as a potential conflict of interest.

frontiers in Cellular Neuroscience

REVIEW
published: 30 June 2017
doi: 10.3389/fncel.2017.00175

Regulatory Roles of Long Non-Coding RNAs in the Central Nervous System and Associated Neurodegenerative Diseases

*Zhenzhen Quan, Da Zheng and Hong Qing**

School of Life Science, Beijing Institute of Technology, Beijing, China

Accumulating studies have revealed that the human genome encodes tens of thousands of long non-coding RNAs (lncRNAs), which participate in multiple biological networks modulating gene expression via transcriptional, post-transcriptional and epigenetic regulation. Strikingly, a large fraction of tissue-specific lncRNAs are expressed in the Central Nervous System (CNS) with precisely regulated temporal and spatial expression patterns. These brain-specific lncRNAs are also featured with the cell-type specificity, the highest signals of evolutionary conservation, and their preferential location adjacent to brain-expressed protein-coding genes. Mounting evidence has indicated dysregulation or mutations in lncRNA gene loci are associated with a variety of CNS-associated neurodegenerative disorders, such as Alzheimer's, Parkinson's, Huntington's diseases, Amyotrophic Lateral Sclerosis and others. However, how lncRNAs contribute to these disorders remains to be further explored and studied. In this review article, we systematically and comprehensively summarize the current studies of lncRNAs, demonstrate the specificity of lncRNAs expressed in the brain, their functions during neural development and expression profiles in major cell types of the CNS, highlight the regulatory mechanisms of several studied lncRNAs that may play essential roles in the pathophysiology of neurodegenerative diseases, and discuss the current challenges and future perspectives of lncRNA studies involved in neurodegenerative and other diseases.

Keywords: long non-coding RNAs (lncRNAs), central nervous system (CNS), neurodegenerative disease, gene expression, transcriptional regulation

OPEN ACCESS

Edited by:
Sandro Alves,
Brainvectis Therapeutics, France

Reviewed by:
Grzegorz Kreiner,
Institute of Pharmacology (PAS), Poland
Mark Verheijen,
VU University Amsterdam, Netherlands

****Correspondence:***
Hong Qing
hqing@bit.edu.cn

Received: *13 April 2017*
Accepted: *09 June 2017*
Published: *30 June 2017*

Citation:
Quan Z, Zheng D and Qing H (2017) Regulatory Roles of Long Non-Coding RNAs in the Central Nervous System and Associated Neurodegenerative Diseases. Front. Cell. Neurosci. 11:175. doi: 10.3389/fncel.2017.00175

INTRODUCTION

For decades, people have considered that "genes and gene-encoded proteins" play crucial roles in regulating diverse cellular processes. However, with the completion of the human genome project, it was observed that less than 5% of the genome is comprised of coding sequences, whereas the majority of human genes are non-protein-coding genes which basically include abundant pseudogenes and comparably numerous non-coding RNAs (ncRNAs; Lander et al., 2001; ENCODE Project Consortium, 2012; FANTOM Consortium and the RIKEN PMI and CLST (DGT), 2014). NcRNAs are broadly defined as all types of RNA that are not translated into proteins due to lack of open reading frames (ORFs). They are also considered to be generated from sections of pseudogenes, which are DNA copies of protein-coding genes with high sequence similarity but have lost at least some of the functions relative to

their parental genes over the course of evolution (Milligan and Lipovich, 2014; Ji et al., 2015).

Generally, ncRNAs can be classified into small ncRNAs and long ncRNAs (lncRNAs) based on whether their transcripts are less or larger than 200 nucleotides as a cutoff value (Elling et al., 2016). Small ncRNAs are usually defined as regulatory RNAs with a length ranging from 18 to 35 nucleotides. According to their diverse regulatory functions, small ncRNAs can be divided into several species, including transfer RNAs (tRNAs), ribosomal RNAs (rRNAs), small nuclear RNAs (snRNAs), small nucleolar RNAs (snoRNAs), piwi-interacting RNAs (piRNAs) and endogenous small interfering RNAs (siRNAs), as well as microRNAs (miRNAs; Lander et al., 2001; Costa, 2005; Grivna et al., 2006; Sosinska et al., 2015; Elling et al., 2016). For many short RNAs, their functions have been well-characterized in gene expression control. Apart from these, many of them have been shown to be involved in specific pathologies, including neurodegenerative diseases and cancers. An increasing number of studies have reported that short ncRNAs are involved in Alzheimer's, Parkinson's and Huntington's diseases (AD, PD and HD; Lee et al., 2011; Gstir et al., 2014).

LncRNAs are the largest class of longer ($\geq$200 nt) non-protein coding RNA and their gene number was recently estimated at approximately 9000 within the human genome according to the GENECODE project (ENCODE Project Consortium, 2012). Other lncRNA studies even suggested there are more than 50,000 in the human genome (Managadze et al., 2013). The discovery of large numbers of lncRNAs genes that are redefined as a gene into a transcriptional unit was initially described by the FANTOM Consortium on the mouse transcriptome study (Carninci et al., 2005). Later on, studies of metazoan lncRNA repertoires further demonstrated the ubiquity of lncRNAs, which are however relatively lower-expressed, more tissue-specific and with greater variability from one tissue to another in comparison to protein-coding genes (Derrien et al., 2012; Milligan and Lipovich, 2014). Roles performed by lncRNAs have been evidenced by their participation in multiple networks controlling gene expression in transcriptional, post-transcriptional or epigenetic levels (Batista and Chang, 2013; Kung et al., 2013; Qureshi and Mehler, 2013). However, the biological significance of the majority of lncRNAs is yet to be further elucidated.

It is well known that RNA biology is of foremost significance in the central neural system (CNS) since neural cells are highly transcriptionally active and exhibit a robust expression of ncRNAs (Cherubini et al., 2006; Kapranov et al., 2010; Qureshi and Mehler, 2012). Remarkably, the brain is the organ where a large proportion of tissue-specific lncRNAs are preferentially expressed in particular regions or different cell types (Mercer et al., 2008; Derrien et al., 2012). These lncRNAs in the CNS participate in many aspects of brain functions and their roles in the pathologies of brain-related neurodegenerative diseases have been intensively and comprehensively investigated (Qureshi and Mehler, 2012, 2013). In this review article, we systematically and comprehensively summarize the diverse mechanisms reported for lncRNAs, describe the specificity of lncRNAs expressed in the brain and their functions during neural development as well as their expression profile in major cell types of the CNS. Meanwhile, we present those intensively studied lncRNAs that may play essential roles in the pathophysiology of neurodegenerative diseases, and discuss current challenges and future perspectives of lncRNA studies that are involved in neurodegenerative and other diseases. Hopefully, this review will broaden insights for future research in the field of lncRNAs in the CNS and associated neurodegenerative diseases.

CHARACTERS AND FUNCTIONS OF LncRNAs

Basic Characters, Origins and Categories of LncRNAs

Studies by Derrien T and team (Derrien et al., 2012) aiming at analyzing of lncRNAs from GENCODE V7 catalog revealed that, lncRNAs are produced in a similar way as that of protein-coding genes, whereas they display a striking bias toward two-exon transcripts and they are predominately localized in the chromatin and nucleus, expressed at relatively low levels (Guttman et al., 2009; Quinn and Chang, 2016). In comparison to the protein-coding genes, lncRNAs are under secondary structure conservation, and therefore they are believed to have arisen from different evolutionary pathways (Ponting et al., 2009; Kaessmann, 2010). Yet, origins of lncRNAs are not well understood so far. Due to the fact that lncRNAs harbor low sequence conservations and rapid evolution among mammals, several evolutionary hypotheses could be proposed such as: (1) lncRNAs might be generated by the metamorphosis of protein-coding genes through a gene duplication process; (2) lncRNAs might have evolved from segmental or whole gene duplication of other ncRNA genes; (3) lncRNAs might have originated via *de novo* generation, such as alternations in genomes including chromosomal rearrangement, generation of splice sites and promoters might transform nonfunctional genomic sequences to functional lncRNAs; and (4) transposable elements (TEs) insertions might be another origin of lncRNAs (Ponting et al., 2009; Kaessmann, 2010; Kapusta et al., 2013; Kazemzadeh et al., 2015). However, it was observed that rarely or only a minority ($\sim$15%) of lncRNAs showed significant sequence similarity to other lncRNAs or protein-coding genes on positions other than the shared repetitive elements, suggesting that novel lncRNAs genes are basically originated rather from *de novo* non-exonic sequences and/or from TEs than duplication (Derrien et al., 2012; Kapusta et al., 2013).

LncRNAs and associated lncRNA transcripts have quite heterogeneousgenomic context, regulation, life cycles, mechanism of action and functional profiles. Broadly, lncRNAs can be classified based on their genomic localization and orientation relative to protein coding genes into several categories: (1) long intergenic noncoding RNAs (LincRNAs), consisting of separate transcript units that are located between but do not overlap with protein-coding genes; (2) intronic

transcripts, that are located within intron regions of protein-coding genes (sense or antisense); (3) overlapping lncRNAs that are overlapping with other genes either divergently or convergently transcribed; and (4) bidirectional ncRNAs (BincRNAs) with transcripts that are transcribed from divergent bidirectional promoters (see **Figure 1**; Guttman et al., 2009; Li and Ramchandran, 2010; Mattick and Rinn, 2015). Despite the diversities of lncRNAs, they share some common features, including: (1) most lncRNAs are transcribed by RNA polymerase II, spliced and modified with a 5′-cap and a poly-A tail, which makes them undistinguishable from protein-coding mRNAs; (2) they are poorly conserved at the sequence level, have a relatively low expression level and display a much more cell-tissue-specific pattern; and (3) they are generally regulated by transcription factors (Xiong et al., 2016). In addition, another subgroup of lncRNAs, the circular RNAs (circRNAs) have recently come into focus with the discovery of their pervasiveness and evolutionary conservation in mammalian and human cells (Jeck and Sharpless, 2014). Most circRNAs are generated during splicing either by spliceosomal machinery or by ribozymes I and II which thus splice out non-coding sequences from exons (exonic circRNAs), introns (intronic circRNAs), or a combination of introns and exons (exon-intron circRNAs; Abdelmohsen et al., 2015). CircRNAs can be differentiated from their linear counterparts by their adoption of a circular form and their lack of 5′ and 3′ ends (Vicens and Westhof, 2014).

General Functions of LncRNAs

LncRNAs have been best described for their participation in regulating gene and genome activity at various levels (see **Figure 2**). LncRNAs can regulate the expression of nearby genes on the same allele *in cis*, or *in trans* to control genes at other genomic locations on different chromosomes, through which they can regulate gene expression at diverse levels, such as transcription, RNA processing and translation (Elling et al., 2016). The majority of lncRNAs are localized in the nucleus, in which they can fulfill their regulatory functions via acting as scaffolds for chromatin modifiers by interacting with chromatin-modifying complexes or as transcriptional co-regulators by binding to transcription factors (Rinn and Chang, 2012; Ulitsky and Bartel, 2013).

The best-known case of lncRNA that regulates transcription mediated through chromatin modification is *Xist*, a 17 kb lincRNA generated from the inactive X-chromosome (Clemson et al., 1996). It mediates the silencing of the inactive X-chromosome in human female cells through recruiting Polycomb Repressive Complex 2 (PRC2) by the Repeat A motif (RepA) on *Xist* and thus initiating chromosome-wide silencing via catalyzing Lysine 27 trimethylation on histone H3 (H3K27; Pinter et al., 2012; Jiang et al., 2013; Bergmann and Spector, 2014). *Hotair*, a 2.2 kb conserved lncRNA transcribed from the human HOXC locus on chromosome 12, is involved in repressing transcription *in trans* across the HOXD locus. *Hotair* was shown to physically interact with PRC2 to ensure the PRC2 occupancy and histone H3 lysine-27 trimethylation of HOXD locus (Rinn et al., 2007). The lncRNA *Braveheart*, prominently expressed in the mouse heart, can interact with Suz12, a subunit of PRC2 (Klattenhoff et al., 2013). The lncRNA *Fendrr* (Fetal-lethal developmental regulatory RNA), that is also related

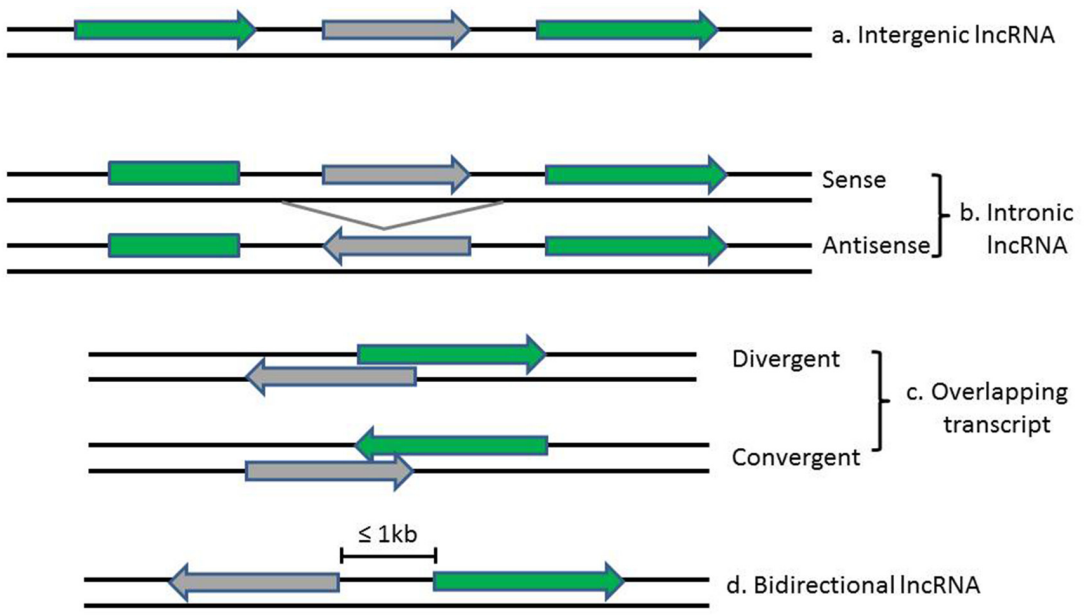

FIGURE 1 | Diagrams show the classification of lncRNAs (in *gray*) according to their position relative to neighboring protein-coding genes (in *green*). Arrows indicate direction of transcription.

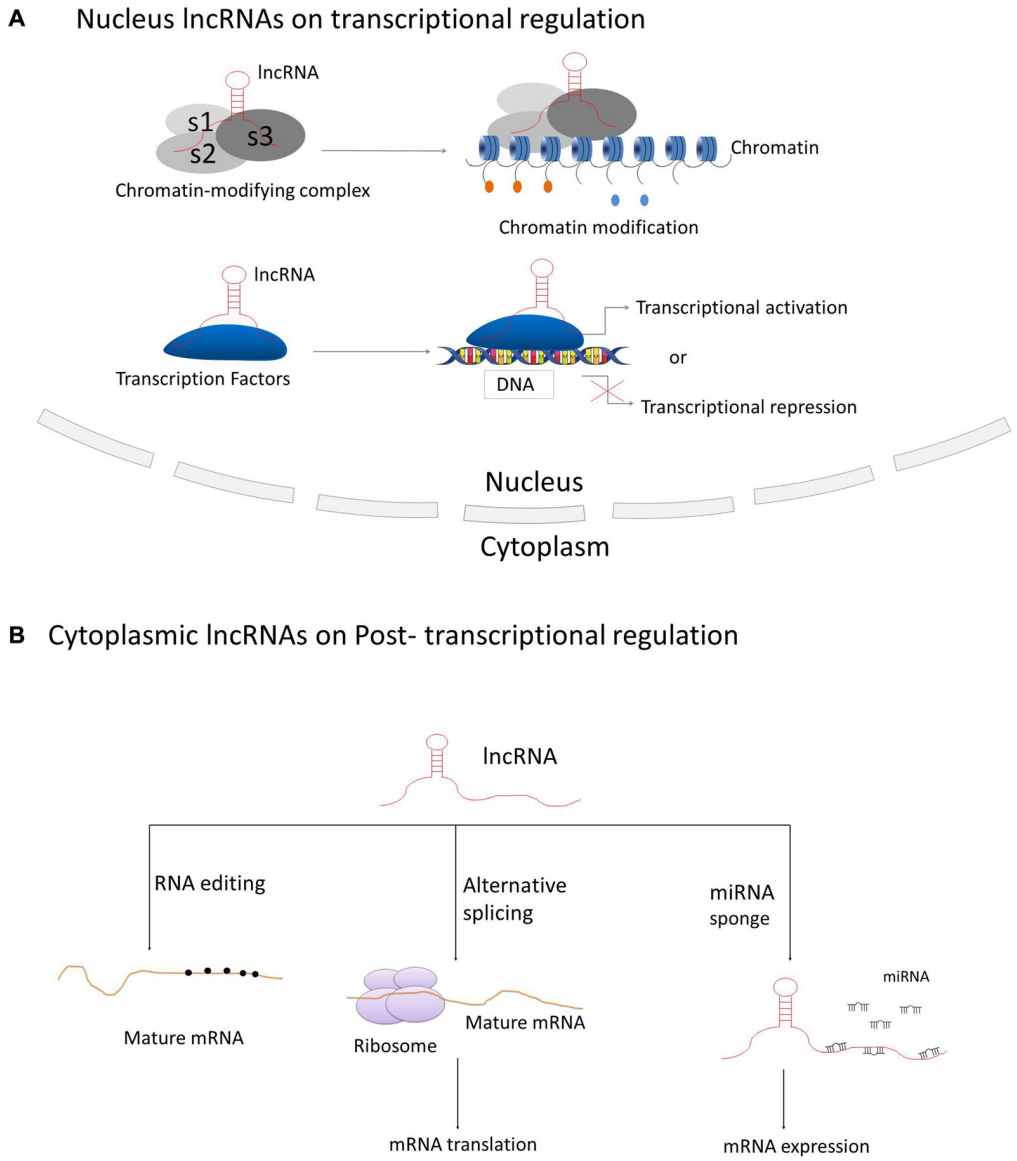

FIGURE 2 | Principle mechanisms of lncRNAs on regulation of gene and genome activity. **(A)** LncRNAs located in the nucleus are basically functioning in transcriptional regulation through interacting with chromatin-modifying complexes or transcription factors; **(B)** Cytoplasmic lncRNAs are generally acting as regulators on RNA processing, such as RNA editing, alternative splicing and miRNA-mediated mRNA expression.

to cardiac development and heart function, can bind to PRC2 and WDR5, a member of the MLL histone methyl-transferase complex (Grote and Herrmann, 2013; Grote et al., 2013).

There are also cases that many lncRNAs interact with transcription factors. The definitive endoderm-associated lncRNA1 (*DEANR1*) is crucial for human endoderm differentiation via interaction and upregulation of the endoderm factor FOXA2 (Jiang et al., 2015). The *lnc-DC* (*Lnc dendritic cells*) is a lncRNA exclusively expressed in human conventional dendritic cells. It was revealed that *lnc-DC* can bind to the transcription factor signal transducer and activator of transcription 3 (STAT3) directly in the cytoplasm and induce its phosphorylation on Tyrosine-75 by inhibiting its binding to and dephosphorylation by SHP1, thereby leading to the activation of STAT3 on dendritic cell differentiation (Wang et al., 2014). In addition, the lncRNA breast cancer anti-estrogen resistance 4 (*BCAR4*), functioning in breast cancer metastasis, was discovered to directly interact with Smad nuclear-interacting protein 1 (SNIP1) and Serine/threonine-protein phosphatase one regulatory subunit 10 (PPP1R10 or PNUTS), thus activating phosphor-GLI2 dependent gene expression (Xing et al., 2014).

Cytoplasmic lncRNAs are also acting as modulators on post-transcriptional regulation of genes through various mechanisms during RNA processing, such as mRNA editing,

alternative splicing and others. The antisense intronic lncRNA *prostate cancer antigen 3* (*PCA3*), acting as a dominant-negative oncogene, was demonstrated to interact with and down-regulate an as yet to be determined tumor suppressor gene *PRUNE2*, by the formation of *PRUNE2/PCA3* double-stranded RNAs that allow the adenosine deaminase to edit RNAs via adenosine to inosine editing (A-to-I editing; Salameh et al., 2015). Non-coding RNA activated by DNA damage (*NORAD*) is an abundant and highly conserved human lncRNA that acts as a multivalent binding platform for RNA binding proteins in the PUMILIO family in order to maintain genomic stability (Lee et al., 2016). Furthermore, the lncRNA-*asFGFR2* is an evolutionarily conserved nuclear antisense lncRNA that was generated from within the human FGFR2 locus. It was found to modulate the epithelial- specific alternative splicing of *FGFR2* by recruiting PRC2 and histone demethylase KDM2a in PNT2 cells (Gonzalez et al., 2015).

Recent studies also revealed certain lncRNAs acting as "miRNA sponges" that they have the potential to sponge and compete with miRNA target genes for the binding of miRNA response elements (MREs) to relieve miRNA-mediated target mRNA repression (Ebert and Sharp, 2010). The circRNA *ITCH* (*cir-ITCH*) was newly discovered to be functionally sponging miR-7, miR-17 and miR-214 and inducing the expression level of *ITCH*, which induced the ubiquitination and degradation of phosphorylated Dvl2 and thereby the inhibition of the Wnt/β-catenin pathway (Li et al., 2016). The lncRNA urothelial carcinoma-associated 1 (*UCA1*) was shown to work as an endogenous sponge that can down-regulate miR-216b expression by directly binding to miR-216b (Wang et al., 2015). The lncRNA human ovarian cancer-specific transcript 2 (*HOST2*) was verified to be a molecular sponge that can modulate the availability of miR let-7b (a potent tumor suppressor) and inhibit miR let-7b functions, thus post-transcriptionally suppressing target gene expressions (Gao et al., 2015).

LncRNAs PLAY CRUCIAL ROLES IN THE CNS

General Features of LncRNAs in Brain

Based on studies from the GENCODE project in 2012 that 10,000–50,000 lncRNAs in the human genome have been annotated to date, it was remarkably revealed that approximately 40% of lncRNAs (which is about 4000–20,000 lncRNAs) are tissue-specifically expressed in the brain (Derrien et al., 2012). This number is strikingly large in comparison to the number of protein-coding genes in human genome which is approximately 20,000–25,000 in general (Briggs et al., 2015). These brain-specific lncRNAs display the highest signals of evolutionary conservation in comparison with those expressed in other tissues. Studies also found that brain-expressed lncRNAs are enriched in predicted, conserved RNA structures and thus are more likely to possess conserved functions (Ponjavic et al., 2009). In addition, brain-expressed lncRNAs show greater brain region, temporal and spatial specificity than mRNAs. Numerous transcriptome analysis have revealed that various lncRNAs are expressed differentially over time and/or in those brain regions, such as cortex, cerebellum and hippocampus during development and adulthood (Lipovich et al., 2014; Kadakkuzha et al., 2015). LncRNAs are also found to be expressed in a more cell-type-specific manner than protein-coding genes. The transcriptome studies on cortical pyramidal neurons have uncovered 806 of 5195 lncRNAs have differential expression across neuronal types, of which, 55% of lncRNAs are annotated as cell-type signature cluster, 32% of lncRNAs are related to cell-type independent clusters, while around 10% of lncRNAs are found in the mixed cell-type clusters, indicating their role on the specification and maintenance of cell identity (Molyneaux et al., 2015). Another feature of brain-specific lncRNAs is their preferential location adjacent to brain-expressed protein-coding genes that are active in transcriptional modulation or in the nervous system development (Ponjavic et al., 2009). Transcriptome sequencing analysis in the corticogenesis displayed that most lncRNAs overlap with neurogenic genes and share with them a similar expression pattern, indicating that lncRNAs regulate corticogenesis through the tuning of the expression of nearby cell fate determinants (Aprea et al., 2013). Considering the complexity and heterogeneity of the mammalian CNS, the brain would be considered as the largest repertoire of lncRNAs in comparison to other somatic tissues and the tissue and cell-type specificity of these lncRNAs make them greatly contribute to cell fate, lineage specification and maintenance of cell identity during the development of the mammalian brain (Hart and Goff, 2016).

Molecular Mechanisms of LncRNAs in CNS Development

The development of the CNS is a complicated and highly stereotyped process that requires elaborate spatiotemporal regulation of stem/progenitor cell proliferation and differentiation. LncRNAs have been demonstrated to play indispensable roles in CNS development from early neural differentiation to late-stage synaptogenesis (see **Figure 3**; Briggs et al., 2015).

Accumulated studies have confirmed that dozens of lncRNAs are identified to be functional in establishing pluripotency or driving neural lineage entry in the widely used *in vitro* model systems—mouse embryonic stem cells (ESCs; Guttman et al., 2011; Ng et al., 2012). These lncRNAs are functional at various stages along the progression from pluripotent cells in the early embryo to the terminal cell types in the mature mammalian brain. The regulatory mechanisms are generally based on modulating these lncRNAs by canonical pluripotency transcription factors, which in turn perform their regulatory effects by directing transcription factors or chromatin remodeling complexes to specific lineage-specifying genes. For examples, the lncRNA Rhabdomyosarcoma 2-associated transcript (*Rmst*), specifically expressed in the brain and regulated by the transcription repressor REST, was found to modulate neural differentiation *in vitro*. It was shown that *Rmst* interacts with SOX2 to co-regulate a large pool of downstream genes (such as DLX1, HEY2 and SP8) implicated

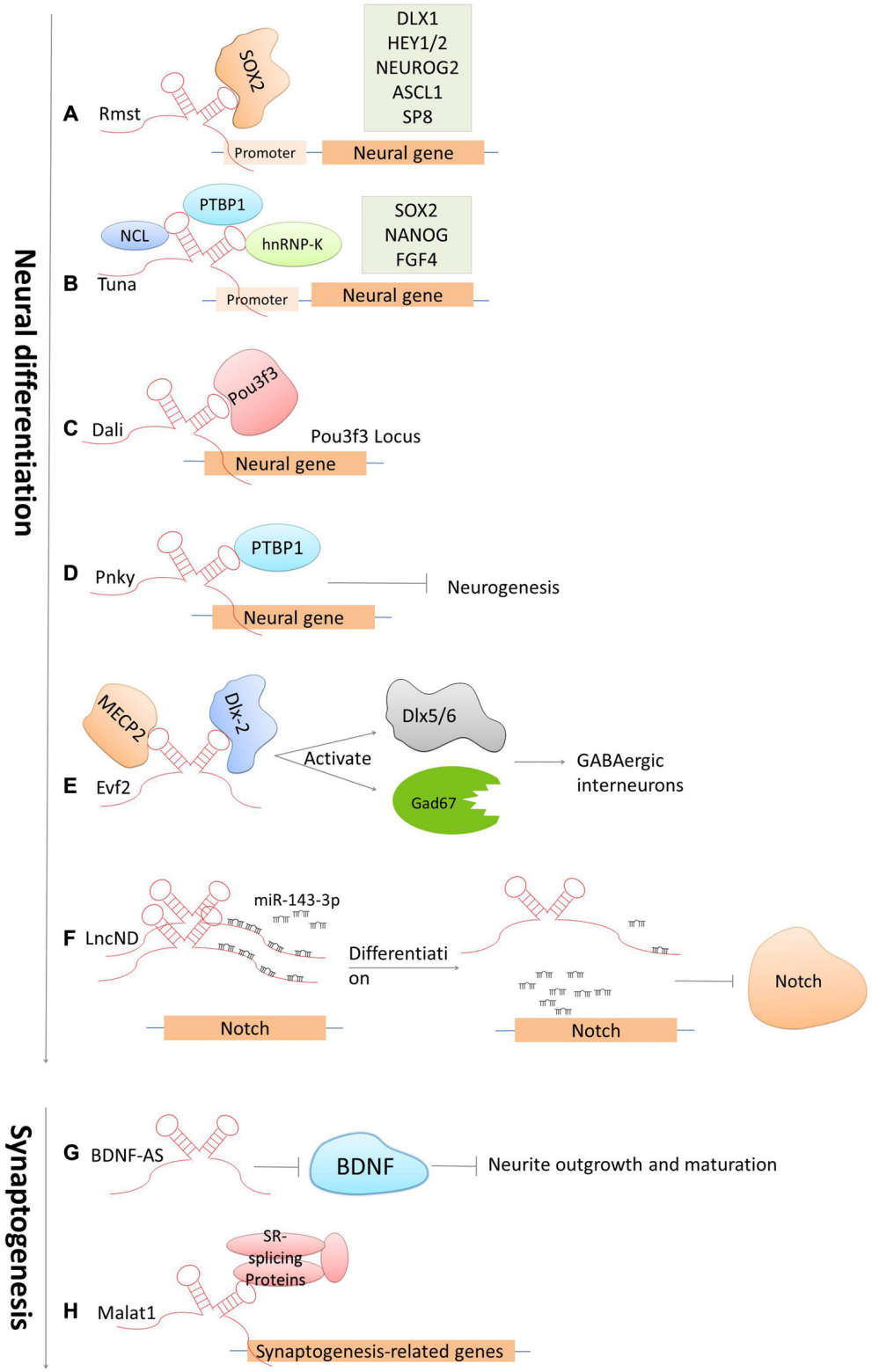

FIGURE 3 | Cases of lncRNAs functioning in neuronal development. **(A–F)** LncRNAs function in early neural commitment through the recruitment of the transcriptional machinery to regulate neural-related gene expressions (*Rmst, Tuna, Dali and Pnky*). *Evf2* is particularly acting in regulating GABAergic interneuron specification. *LncND* functions in regulating Notch signaling pathways via sequestering miR143-3p. **(G–H)** LncRNAs function in late developmental processes, such as neurite outgrowth and maturation mediated by *BDNF-AS*, synapse function by *Malat1*.

in neurogenesis. The absence of *Rmst* can block the exit from the ESC state and the initiation of neural differentiation (Ng et al., 2013). *Tuna*, is also a lncRNA that regulates neuronal gene expression in a similar mechanism as *Rmst*. *Tuna* interacts with three RNA-binding proteins (NCL, PTBP1 and hnRNP-K) and together target promoter regions of neural genes in differentiating mouse ESCs. The knockdown of *Tuna* or any of the three RNA-binding proteins can sufficiently suppress neural differentiation (Lin et al., 2014). This is also conserved from relatively related vertebrates, mice and zebrafish, indicating that the neural lineage commitment driven by lncRNAs displays the highly evolutionary conservation (Briggs et al., 2015). Furthermore, the lncRNA *Dali*, transcribed downstream of the transcription factor Pou3f3, was shown to drive the expression of an essential gene involved in neuronal differentiation in neuroblastoma cells. *Dali* can regulate transcription of the *Pou3f3* locus locally and physically interact with Pou3f3 protein to regulate the expression of neural differentiation genes distally (Chalei et al., 2014). *Paupar*, a chromatin-associated intergenic lncRNA expressed in the CNS, is divergently transcribed from a locus upstream from the gene encoding the transcription factor *Pax6*. It was shown that the knockdown of *Paupar* destroys the normal cell cycle profile of neuroblastoma cells, thus enhancing neuronal differentiation. The function of *Paupar* is performed via locally interacting with and transcriptionally regulating *Pax6*, as well as via distally controlling neural gene expression on a large scale (such as *SOX2*, *HES1* and *EVF2*), which in part requires physical association with Pax6 protein (Vance et al., 2014). Besides that, one of the latest studies has identified an lncRNA, termed *LncND* (Neurodevelopment) that harbors 16 miRNA response elements for miR-143-3p in primates. It performs its role in neuronal development by sequestering miR-143-3p, and in doing so, modulates Notch signaling pathways via regulating expression of Notch receptors, *NOTCH-1* and *NOTCH-2*. Also, *NOTCH-1* and *NOTCH-2* show the same expression pattern as *LncND* in early neurogenesis process when Notch expression is indispensable. While, later in neural differentiation process, reduction of *NOTCH* expression is followed by *LncND*, leading to the release of miR-143-3p and the decrease of Notch signaling specifically in *LncND*-expressing cells (Rani et al., 2016). Interestingly, knocking down *LncND* in neuroblastoma cells can inhibit *NOTCH-1* and *NOTCH-2* and make cells differentiate to neurons, which show similar phenotypes as what can be observed by miR-143-3p overexpression. These findings suggested a role of *LncND* in miR-mediated regulation of Notch signaling to sustain the neural progenitor pool during cerebral cortex expansion in primates (Rani et al., 2016).

There are also several important lncRNAs being identified to control stem cell turnover and the specification of particular lineages in the embryonic mouse brain *in vivo*. For example, *Evf2*, the firstly identified nervous system-specific lncRNA, has been shown to have a significant regulatory role in neural development. Depletion in *EVF2* can cause imbalance of the excitatory to inhibitory neurons in the postnatal hippocampus and dentate gyrus. This imbalance is caused by the failure of GABAergic interneuron specification (Bond et al., 2009). It was revealed that *Evf2* recruits DLX and methyl CpG-binding protein (MECP2) to modulate the transcriptional activity of two transcription factors Dlx5/6 and the glutamate decarboxylase 67 (Gad67, which is required for the conversion of glutamate to GABA), and thereby regulates the gene expression of GABAergic interneurons in the developing mouse forebrain (Feng et al., 2006; Bond et al., 2009). *Pnky* is an evolutionally conserved and neural-specific lncRNA that modulates neurogenesis of neural stem cells (NSC) in the embryonic and postnatal brain. The Ramos AD group (Ramos et al., 2013) has unveiled that knockdown of *Pnky* can increase neuronal differentiation and deplete the NSC population in the embryotic mouse cortex. In addition, it was shown that *Pnky* interacts with PTBP1, a splicing regulator expressed in NSCs that represses the inclusion of neural exons in non-neural cells. Knockdown of *PTBP1* also reinforce neurogenesis, indicating that *Pnky* and PTBP1 function similarly to modulate the alternative splicing of a group of transcripts that are involved with cellular phenotypes (Aprea and Calegari, 2015; Ramos et al., 2015). Together, these studies indicate that lncRNAs regulate cell-fate determination and progenitor cell turnover during neural development both *in vitro* and *in vivo*.

Another key process during CNS development is the late-stage synaptogenesis. Accordingly, several lncRNAs have been discovered to make great contributions to this process (Briggs et al., 2015). *Malat1* is a well-known lncRNA that have been implicated in the regulation of neurite elaboration. *Malat1* is expressed in multiple tissues but is highly abundant in neurons. It was revealed that *Malat1* can actively recruit SR-family splicing proteins to transcription sites in order to regulate synaptogenesis-related gene expression. The knockdown of *MALAT1* leads to a decreased level of synaptic density; while in contrast, overexpression can reciprocally increase synaptic density (Bernard et al., 2010). Primate-specific *BC200* RNA (Brain cytoplasmic RNA, 200 nt) and its rodent counterpart *BC1* are evolutionarily conserved lncRNAs that have been firstly identified to be expressed in both developing and adult nervous systems (Muslimov et al., 1997). Studies later reported that *BC200/BC1* is functional in the neuronal excitation-repression equilibria via protein-synthesis-dependent implementation (Zhong et al., 2009). In addition, several antisense lncRNAs have been recently presented as core protein regulators, for example Brain-derived neurotrophic factor (BDNF), glial-derived neurotrophic factor (GDNF) and ephrin receptor B2 (EPHB2) that control neurite elaboration. The expression of *BDNF* is repressed by its antisense lncRNA *BDNF-AS*. The inhibition of *BDNF-AS* can release and induce the expression of *BDNF* by 2- to 7-folds, which is in line with the reduction of EZH2 recruitment and an alternation of the chromatin state at the *BDNF* locus. This correspondingly induces neuronal outgrowth, differentiation, survival and proliferation both *in vitro* and *in vivo* (Modarresi et al., 2012). These observations, along with the current understanding of lncRNA mechanisms of action, imply that lncRNAs have a critical role in regulating neural gene expression and brain development.

Expression Profiles of LncRNAs in Major Cell Types of the CNS

LncRNAs have been proposed to play diverse roles in the CNS, such as in neural differentiation, in synaptogenesis and others. As a result, the expression profiles of lncRNAs in the CNS were recently studied. The CNS has prominent cellular diversities owning hundreds of distinct cell types. In particular, neurons and neuroglia cells (mainly including astrocytes and oligodendrocytes) are the major cell types. A recent study has successfully isolated nuclear RNAs from different CNS cell types (neurons, astrocytes and oligodendrocytes) and compared both protein-coding and noncoding nuclear transcriptome profiles in these three cell types (Reddy et al., 2017). For non-coding transcriptome, it was revealed that approximately 300 transcripts at a level of >5 CPM (counts per million) can be observed in one of the three different cell types, and the majority is transcribed at the level of >1 CPM. Several other highly expressed transcripts are also found in all three cell types, such as *Xist* and its regulators *Ftx* and *Jpx* (Tian et al., 2010; Chureau et al., 2011; Reddy et al., 2017). Nevertheless, 169 lincRNAs were shown to have a >10-fold difference in one of the pairwise comparisons, such as *Mirg* and other adjacent maternally expressed lncRNAs (*Meg3* and *Rian*) that are found to be highly enriched in neuronal nuclei. *Mirg* was found to be precisely localized within bright subnuclear puncta in neurons; the expression of *Meg3* was shown as neuronal selective that it was enhanced in gray matter where neurons are found but depleted from white matter areas where only glia are found; and *Rian* was found to have similar expression pattern as *Meg3* (Zhang et al., 2003; Balik et al., 2013; Reddy et al., 2017). In astrocytes, various transcripts were found but most of them do not possess known functions. Whereas, the lncRNA *Rmst*, a key co-regulator of neurogenesis with the SOX2 transcription factor, is an exception that it has been shown to be expressed robustly in the nuclei of astrocytes (Ng et al., 2013; Reddy et al., 2017). Meanwhile, it was shown that there are at least 16 lncRNAs with >5 CPM found in oligodendrocytes, such as *Neat1* and *DLeu2*. Notably, although *Neat1* was shown to have the highest expression level in oligodendrocytes, it was also present in astrocytes (Klein et al., 2010; Reddy et al., 2017). These data demonstrated different lncRNA expression patterns in three major cell types in the brain, providing a crucial clue for evaluating functions of various lncRNAs in the brain and CNS-associated disorders.

LncRNAs TIGHTLY ASSOCIATE WITH NEURODEGENERATIVE DISEASES

The importance of lncRNAs in the brain has been asserted by their association with various brain functions, including the maintenance of pluriotency, neuroectodermal differentiation, neuron-glial cell fate determination, synaptogenesis and so on (Roberts et al., 2014). Considering that, it is not surprising that dysregulation or mutation of lncRNAs is tightly related to various neurological disorders. Genome-wide association studies and comparative transcriptome analysis have implied that lncRNAs are involved in a variety of neurological disorders, such as psychiatric disorders, neurodegenerative diseases (like Alzheimer's disease-AD, Parkinson disease-PD, Huntington disease-HD, Frontotemporal lobar degeneration-FTLD and Amyotrophic lateral sclerosis-ALS, etc.), and others. Similarly, as described above, lncRNAs contribute to these diseases in diverse ways, from the regulation of transcription to the modulation of RNA processing and translation (see **Table 1**). Here, we briefly exemplified several studied cases of lncRNAs that have been identified to be associated with neurodegenerative diseases.

Huntingtin (HTT) is an essential gene for HD, a CAG trinucleotide repeat expansion in exon 1, and the main cause of HD. The *HTT antisense* (*HTT-AS*), a natural antisense transcript at the HD repeat locus containing the repeat tract, was identified and characterized with 5′ capped, poly A tailed, three exons maintained and alternatively being spliced into *HTTAS-v1* (exons 1 and 3) and *HTTAS-v2* (exons 2 and 3). Cell studies revealed that the overexpression of *HTTAS-v1* specifically decreases endogenous HTT transcript levels, whereas the siRNA knockdown of *HTTAS-v1* induces *HTT* transcript levels. What's more, *HTTAS-v1* expression was found to be downregulated in frontal cortex of HD patients, strongly suggesting the existence of a gene antisense to *HTT* acting as a regulator for its own expression and its contribution to the development of HD (Chung et al., 2011).

Beta-secretase 1 (BACE1) is the key enzyme that produces β-amyloid peptide (Aβ) which aggregates and forms into amyloid plaques as a main pathological hallmark of AD. Recent studies have identified a conserved noncoding antisense transcript of BACE1, *BACE1-AS*, that regulates *BACE1* mRNA and subsequently BACE1 protein expression both *in vivo* and *in vitro*. Studies have highlighted that the knockdown of *BACE1-AS* can reduce BACE1 levels, as well as Aβ1–40 and Aβ1–42 production correspondingly. Exposure to various cell stressors (including Aβ1–42) that have been implicated in the pathogenesis of AD, was found to induce *BACE1-AS* levels. This induction is led by the formation of a RNA duplex with *BACE1* mRNA, which in turn increases *BACE1* mRNA stability and BACE1 protein, and consequently generates additional Aβ1–42 through a post-transcriptional free-forward mechanism (Faghihi et al., 2008). Furthermore, it was found that increased *BACE1-AS* levels exist in various brain regions in subjects with AD in comparison to control individuals, indicating the possibility of *BACE1-AS* being a potential biomarker of AD (Faghihi et al., 2008; Modarresi et al., 2011).

Recently, *17A* was described as an antisense transcript of the human G-protein-coupled receptor 51 gene (GPR51, GABA B2 receptor) that is RNA polymerase III-dependent and embedded in the GPR5. In neuroblastoma cells, the stable expression of *17A* can promote the synthesis of an alternative splicing isoform for GABA R2, resulting in the elimination of GABA B2 intracellular signaling and the enhancement of Aβ secretion and the ratio of Aβ42/Aβ40. Furthermore, *17A* is expressed in the human brain and upregulated in cerebral tissues derived from AD patients, indicating its potential contribution to the development of AD (Massone et al., 2011).

TABLE 1 | Cases of neurodegenerative diseases-associated lncRNAs.

Regulatory functions	lncRNAs	Targets	Regulating	Related pathologies	In which regions/cells	Diseases involved	References
Transcription	*HTT-AS*	HTT	Downregulated	Regulates HTT expression	Frontal cortex	HD	Chung et al. (2011)
Transcription	*C9ORF72*	Yet to be determined	Upregulated	Containing the G_4C_2 expansion	Frontal and motor cortex, hippocampus, spinal cord neurons	ALS/FTLD	Zu et al. (2013)
Transcription	*NEAT1–2*	TDP-43; FUS/TLS	Upregulated	Regulate the transcription or transcript stability of lncRNAs	Spinal motor neuron	ALS/FTLD	Nishimoto et al. (2013)
Transcription	*GDNFOS1*	GDNF	Upregulated		Middle temporal gyrus	AD	Airavaara et al. (2011)
mRNA stability	*BACE1-AS*	BACE1	Upregulated	Induces Aβ40 and Aβ42 production	Prefrontal cortex, striatum, cerebellum, hippocampus anterior & posterior,	AD	Faghihi et al. (2008); Modarresi et al. (2011)
Alternative splicing	*17A*	GPR51	Upregulated	Abolishes GABA B2 intracellular signaling and increase Aβ secretion	Cerebral Cortex	AD	Massone et al. (2011)
Post-transcriptional	*NAT-Rad18*	Rad18	Upregulated	Affects ability of neuron and their apoptosis susceptibility	Cortical neuron	AD	Parenti et al. (2007); Wu et al. (2013)
miRNA sponge	*ciRS-7*	UBE2A	Upregulated	Regulated AD-associated targets	Hippocampal CA1	Sporadic AD	Cogswell et al. (2008); Hansen et al. (2013); Lukiw (2013)
Translation	*BC200*	SYNCRIP	Upregulated	Regulates dendritic mislocalization	Brodmann's area 9	AD	Muddashetty et al. (2002); Mus et al. (2007); Duning et al. (2008)
Translation	*Uchl1-AS*	Uchl1	Downregulated	Regulates protein synthesis of Uchl1	Dopaminergic neurons	PD	Carrieri et al. (2012)

NAT-Rad18, a natural antisense transcript against *Rad18* (a gene encoding DNA repair protein), was investigated and considered to play potential roles in the DNA damage repair system in AD. RNA quantitative and immunohistochemistry analysis revealed that *NAT-Rad18* is widely distributed in the adult rat brain, but with high levels in the cerebellum, brainstem and cortex where neurons are specifically expressed. Upon Aβ-induced apoptosis in cortical neurons, the expression of *NAT-Rad18* was shown to be up-regulated, whereas *Rad18* was post-transcriptionally down-regulated. This observation suggested NAT-Rad18 might reduce the ability of neurons and increase their apoptosis susceptibility via the post-transcriptional modulation of *Rad18* to reduce their response to DNA damage stress (Parenti et al., 2007; Wu et al., 2013).

GDNFOS, transcribed from the opposite strand of GDNF, was demonstrated to be associated with neurodegenerative diseases, like AD. *GDNFOS* contains four exons that therefore are spliced into different isoforms, including *GDNFOS1/2* acting as *lncRNAs* and *GDNFOS3* encoding a protein of 105 amino acids (Airavaara et al., 2011). It was revealed that the mature GDNF peptide was reduced while the transcript *GDNFOS1* upregulated in the postmortem middle temporal gyrus of patients suffering from AD when compared with those of normal controls, indicating the dysregulation of *GDNF* and *GDNFOS* might further implicate in other human brain diseases (Airavaara et al., 2011).

One brain-specific circRNA, *ciRS-7* (circular RNA sponge for miR-7), also known as *CDR1as*, is transcribed antisense to the cerebellar degeneration-related protein 1 transcript (*CDR1*) that is highly expressed (even more than the sense transcript) in the mouse and human CNS. The *ciRS-7* functions as a miR-7 sponge that strongly quenches miR-7 activity, thus causing induced levels of miR-7 targets. Recent studies also indicated an endogenous interaction between *ciRS-7* and miR-7 based on the observation of the co-expression of *ciRS-7* and miR-7 in the mouse brain (Hansen et al., 2013; Memczak et al., 2013). The *ciRS-7* has been identified to be related to the sporadic AD, that dysregulation of *ciRS-7* was evidenced in the hippocampal CA1 region of the sporadic AD (Lukiw, 2013). The *ciRS-7* deficiency was expected to induce ambient miR-7 levels in AD-affected brain cells, which is probably responsible for down-regulating AD-associated targets, such as, the ubiquitin protein ligase A (UBE2A; Cogswell et al., 2008; Lukiw, 2013).

BC200 RNA is tightly related to AD development and its expression has been demonstrated to be substantially up-regulated in tested AD brain tissues (Brodmann's area 9) in comparison to that in age-matched normal brain samples (Mus et al., 2007). Further analysis also demonstrated that the increase in levels of *BC200* RNA only occurs in specific regions of the AD-brain and is accompanied by changes in *BC200* RNA neuronal distribution, including dendritic mislocalization and gradual accumulation of *BC200* RNA to the perikaryon (Mus et al., 2007). The role of *BC200* RNA in regulating gene expression at translational level during the development of AD has been reported in many studies as being through mechanisms of interaction with many different proteins. It was shown that *BC200* RNA interacts with the human synaptotagmin-binding

cytoplasmic RNA interacting protein (SYNCRIP), a component of large mRNA transport granules in neurons and functioning in local protein synthesis at post-synaptic sites, through mediation by the N-terminal RNA recognition motifs and the central A-rich region of *BC200* RNA (Duning et al., 2008). In addition, the polyA-binding protein (PABP1), a regulator of translation initiation, was also identified to bind to *BC200* RNA mediated by its central A-rich region, leading to the hypothesis that *BC200* RNA is associated with protein translation in neuronal dendrites (Muddashetty et al., 2002). The interactions between *BC200* RNA and proteins involved in local protein synthesis in neurons indicated the important role of *BC200* RNA in AD pathology.

The Uchl1-AS is a nuclear-enriched lncRNA that is transcribed antisense to the mouse ubiquitin carboxy-terminal hydrolase L1 (Uchl1). Uchl1 is a neuron-restricted protein acting as a de-ubiquitinating enzyme or a monoubiquitin stabilizer. *UCHL1* gene mutations have been discovered to be related to familial PD, and the oxidative inactivation of Uchl1 protein has been reported in PD and AD brains (Choi et al., 2004; Barrachina et al., 2006). *Uchl1-AS* can increase the protein synthesis of *UCHL1* at post-transcriptional level, which depends on the combined activities of two domains, the 5′ antisense region that provides specificity for the sense target gene and the embedded repetitive SINEB2 element (short interspersed nuclear element of B3 subclass) that confers the protein synthesis activation domain (Nishihara et al., 2006; Carrieri et al., 2012). In addition, the activity of *Uchl1-AS* is under the control of signaling pathways. Uchl1 mRNA is predominantly localized in the cytoplasm while *Uchl1-AS* is abundant in the nucleus of dopaminergic neurons. Intriguingly, the mTOR inhibitor-Rapamycin treatment resulted in the induction of Uchl1 protein by association of shuttling *Uchl1-AS* from the nucleus to the cytoplasm, indicating the interplay among Uchl1-ncRNA-mTOR might be crucial for the development of PD (Carrieri et al., 2012; Vučičevič et al., 2014).

C9ORF72, chromosome 9 ORF72, contains a hexanucleotide (GGGGCC, G_4C_2) repeat expansion in its non-coding region, which was found as the causative mutation for both ALS and FTLD (DeJesus-Hernandez et al., 2011). The *C9ORF72* expansion mutation can be transcribed bidirectionally that produces unexpected proteins via repeat-associated non-ATG (RAN) translational mechanism. Recent discovery found that antisense *C9ORF72* transcripts containing the G_4C_2 expansion are increased in ALS patients' brains (Zu et al., 2013), indicating the vital role of antisense *C9ORF72* transcripts on fundamental pathologies of ALS/FTLD.

In addition, the lncRNA nuclear-enriched abundant transcript 1–2 (*NEAT1-2*), containing nuclear bodies named as "paraspeckles", has also been shown to be associated with ALS/FTLD. TAR DNA binding protein 43 (TDP-43) inclusions or that are fused in sarcoma/translocated in liposarcoma (FUS/TLS) are displayed and characterized as the major pathology of ALS/FTLD (Nishimoto et al., 2010). Studies revealed that TDP-43 and FUS/TLS are enriched in paraspeckles and bound to NEAT1-2 directly. Furthermore, the expression of *NEAT1-2* was shown to be enriched and the specific assembly of NEAT1-2 as paraspeckles be formed in spinal motor neurons at an early stage of the ALS pathogenesis (Nishimoto et al., 2013; Lourenco et al., 2015). These suggested *NEAT1-2* might be functional in modulation of ALS-associated RNA-binding proteins at the early stage of ALS.

CHALLENGES AND PERSPECTIVES

Along with intensive studies of lncRNAs, there are still challenges for our understanding of lncRNAs. On one side, most investigations of lncRNA are limited to single studies, and some of them are only an *in vitro* study. Kohtz (2014) has stated that the roles of lncRNAs in cell lines can be distinguished with the ones examined in animal models (*in vivo*). Taking *Evf2* as an example, *Evf2* cell line assays indicated the *in trans* mechanism of lncRNA functioning as activation enhancers, whereas the knockdown of *Evf2* in $Evf2^{TS/TS}$ mice associated lncRNA with repression *in cis* (Feng et al., 2006; Bond et al., 2009). On the other side, some lncRNAs are only studied in mouse models with genomic deletions. With respect to the characters of lncRNAs that are located in the nucleus and chromatin-associated that might be *cis*-acting transcriptional regulators, or in cytoplasm that might be predicted to act *in trans*, the phenotypes produced by deletion of an entire genomic locus apparently cannot be equivalently the same as the loss of lncRNA *per se* or as the associated loss of other overlapping DNA regulatory elements (Bassett et al., 2014). In these cases, it will be difficult to distinguish from the effects caused by loss of a lncRNA transcript to the general effects caused by the loss of the genomic region itself (Kohtz, 2014; Aprea and Calegari, 2015). Considering these challenges, researchers have proposed the importance of optimizing currently employed techniques along with developing advanced ones as tools to help differentiating between the influences of lncRNAs when they act as molecular species compared to when they act as gene regulatory elements. For example, fluorescent *in situ* hybridization (FISH) has been widely applied for the analysis of lncRNA localization in tissues and subcellular levels (Chakraborty et al., 2012). Also, a series of interaction assays for the identification of protein or nucleic acids with lncRNAs are applied, such as protein-RNA (crosslinking immunoprecipitation, CLIP), RNA-RNA (crosslinking analysis of synthetic hybrids, CLASH) or RNA-DNA (capture hybridization analysis of RNA targets, CHART; Helwak et al., 2013; Huppertz et al., 2014; Vance and Ponting, 2014). Apart from these technical updates, the Clustered regularly interspersed palindromic repeats (CRISPR/Cas9) system, functioning as a mechanistic tool, is popularly used for targeted genome engineering (Cheng et al., 2013; Bassett et al., 2014). With regards to this, the landscape of lncRNAs with proven functions in various biological processes have been substantially increasing and this range is expected to be further expanding in the coming years.

The brain is the organ where more lncRNAs are abundantly expressed, comprising the highest proportion of brain-specific lncRNAs (Derrien et al., 2012). Although limited numbers of lncRNAs have been identified to be associated with the

complexity of the brain functions, lncRNAs are involved in brain functions in both a normal and diseased state. It is implied that brain-specific lncRNAs may be innovatively evolved, involved in human brain development and related to neurodegenerative diseases (Vučičevič et al., 2014). Based on studies of lncRNAs functioning in brain development and pathophysiology of neurological disorders, the definition criteria include: (1) genetic variation in lncRNA genes leads to disease and influences susceptibility; (2) epigenetic deregulation of lncRNAs is associated with disease; (3) genomic context binds lncRNAs to disease-related genes and pathways; and (4) lncRNAs are interconnected with known pathogenic mechanisms (Qureshi and Mehler, 2013). However, it is worth noting that phenomena, like some lncRNAs either might show different expression levels in healthy brains compared to diseased brains, or they might interact with certain proteins that function in brain disorders, could be a result of multiple reasons that are not related to the disease or caused by unspecific side effects (Vučičevič et al., 2014). Apart from studies of lncRNA functions in cell lines that would reveal basic molecular mechanisms of lncRNAs, the generation of lncRNAs-knockdown or mutation in mouse models would be more effective to study the functional relevance of lncRNAs during brain development and in the physiological conditions of neurodegenerative disease.

In fact, as proposed by many studies, more and more attention has been given to lncRNAs as being disease biomarkers or potential targets for therapeutic strategies. Indeed, several commercial entities (e.g., OPKO-CURNA and RaNA therapeutics), which target lncRNAs have been developed to design and develop oligoneucleotide therapeutics for the treatment of CNS-related neurological disorders (Qureshi and Mehler, 2013). However, due to the large size of many lncRNAs, it became evident that the crossing of lncRNAs through the blood-brain barrier (BBB) will be a significant issue to be considered. Exosomes, 20–100 nm membrane nanovesicles of endocytic origin secreted by most cell types *in vivo* and *in vitro*, are shown to be natural carriers of functional RNAs (such as mRNA, miRNA, rRNA and lncRNAs) and proteins (Raposo et al., 1996; Valadi et al., 2007). Exosomes can also transfer these genetic materials between cells and subsequently modulate the functions of targeted cells. These characteristics indicate their important role in communications between cells, and therefore make them great potentials for therapeutic delivery (Kawikova and Askenase, 2015; Barile and Vassalli, 2017). Moreover, exosomes were found to have an impact on the pathophysiology of the brain due to the fact that they can also be released by CNS cells (Faure et al., 2006; Kawikova and Askenase, 2015). As suggested, utilization of exosomes as delivery cargo would be an efficient strategy for helping to bypass the BBB (Lakhal and Wood, 2011; Katakowski et al., 2013). Hereby, further investigation on the role of lncRNAs will provide a better understanding of how the brain functions and how diseases develop, and lead to greater insights into further therapeutic development for neurodegenerative diseases based on manipulations of lncRNA functions.

AUTHOR CONTRIBUTIONS

ZQ and HQ organized the article and ZQ drafted the manuscript; ZQ and DZ designed the pictures and prepared the draft; ZQ and HQ approved the final version.

ACKNOWLEDGMENTS

This work is funded by the National Natural Science Foundation of China under grant No. 81671268 and the China Postdoctoral Science Foundation under grant No. 2016M600931. We are grateful to Dr. Zhang N, Dr. Dikicioglu D, Zhao J, Xu Y, Qazi T J and Duru L for their valuable comments and language editing of this manuscript.

REFERENCES

Abdelmohsen, K., Panda, A. C., De, S., Grammatikakis, I., Kim, J., Ding, J., et al. (2015). Circular RNAs in monkey muscle: age-dependent changes. *Aging (Albany NY)* 7, 903–910. doi: 10.18632/aging.100834

Airavaara, M., Pletnikova, O., Doyle, M. E., Zhang, Y. E., Troncoso, J. C., and Liu, Q. R. (2011). Identification of novel GDNF isoforms and cis-antisense GDNFOS gene and their regulation in human middle temporal gyrus of Alzheimer disease. *J. Biol. Chem.* 286, 45093–45102. doi: 10.1074/jbc.M111.310250

Aprea, J., and Calegari, F. (2015). Long non-coding RNAs in corticogenesis: deciphering the non-coding code of the brain. *EMBO J.* 34, 2865–2884. doi: 10.15252/embj.201592655

Aprea, J., Prenninger, S., Dori, M., Ghosh, T., Monasor, L. S., Wessendorf, E., et al. (2013). Transcriptome sequencing during mouse brain development identifies long non-coding RNAs functionally involved in neurogenic commitment. *EMBO J.* 32, 3145–3160. doi: 10.1038/emboj.2013.245

Balik, V., Srovnal, J., Sulla, I., Kalita, O., Foltanova, T., Vaverka, M., et al. (2013). MEG3: a novel long noncoding potentially tumour-suppressing RNA in meningiomas. *J. Neurooncol.* 112, 1–8. doi: 10.1007/s11060-012-1038-6

Barile, L., and Vassalli, G. (2017). Exosomes: therapy delivery tools and biomarkers of diseases. *Pharmacol. Ther.* 174, 63–78. doi: 10.1016/j.pharmthera.2017.02.020

Barrachina, M., Castaño, E., Dalfó, E., Maes, T., Buesa, C., and Ferrer, I. (2006). Reduced ubiquitin C-terminal hydrolase-1 expression levels in dementia with Lewy bodies. *Neurobiol. Dis.* 22, 265–273. doi: 10.1016/j.nbd.2005.11.005

Bassett, A. R., Akhtar, A., Barlow, D. P., Bird, A. P., Brockdorff, N., Duboule, D., et al. (2014). Considerations when investigating lncRNA function *in vivo*. *Elife* 3:e03058. doi: 10.7554/eLife.03058

Batista, P. J., and Chang, H. Y. (2013). Long noncoding RNAs: cellular address codes in development and disease. *Cell* 152, 1298–1307. doi: 10.1016/j.cell.2013.02.012

Bergmann, J. H., and Spector, D. L. (2014). Long non-coding RNAs: modulators of nuclear structure and function. *Curr. Opin. Cell Biol.* 26, 10–18. doi: 10.1016/j.ceb.2013.08.005

Bernard, D., Prasanth, K. V., Tripathi, V., Colasse, S., Nakamura, T., Xuan, Z., et al. (2010). A long nuclear-retained non-coding RNA regulates synaptogenesis by modulating gene expression. *EMBO J.* 29, 3082–3093. doi: 10.1038/emboj.2010.199

Bond, A. M., Vangompel, M. J., Sametsky, E. A., Clark, M. F., Savage, J. C., Disterhoft, J. F., et al. (2009). Balanced gene regulation by an embryonic brain ncRNA is critical for adult hippocampal GABA circuitry. *Nat. Neurosci.* 12, 1020–1027. doi: 10.1038/nn.2371

Briggs, J. A., Wolvetang, E. J., Mattick, J. S., Rinn, J. L., and Barry, G. (2015). Mechanisms of long non-coding RNAs in mammalian nervous

system development, plasticity, disease, and evolution. *Neuron* 88, 861–877. doi: 10.1016/j.neuron.2015.09.045

Carninci, P., Kasukawa, T., Katayama, S., Gough, J., Frith, M. C., Maeda, N., et al. (2005). The transcriptional landscape of the mammalian genome. *Science* 309, 1559–1563. doi: 10.1126/science.1112014

Carrieri, C., Cimatti, L., Biagioli, M., Beugnet, A., Zucchelli, S., Fedele, S., et al. (2012). Long non-coding antisense RNA controls Uchl1 translation through an embedded SINEB2 repeat. *Nature* 491, 454–457. doi: 10.1038/nature 11508

Chakraborty, D., Kappei, D., Theis, M., Nitzsche, A., Ding, L., Paszkowski-Rogacz, M., et al. (2012). Combined RNAi and localization for functionally dissecting long noncoding RNAs. *Nat. Methods* 9, 360–362. doi: 10.1038/nmeth.1894

Chalei, V., Sansom, S. N., Kong, L., Lee, S., Montiel, J. F., Vance, K. W., et al. (2014). The long non-coding RNA Dali is an epigenetic regulator of neural differentiation. *Elife* 3:e04530. doi: 10.7554/eLife.04530

Cheng, A. W., Wang, H., Yang, H., Shi, L., Katz, Y., Theunissen, T. W., et al. (2013). Multiplexed activation of endogenous genes by CRISPR-on, an RNA-guided transcriptional activator system. *Cell Res.* 23, 1163–1171. doi: 10.1038/cr. 2013.122

Cherubini, E., Gustincich, S., and Robinson, H. (2006). The mammalian transcriptome and the cellular complexity of the brain. *J. Physiol.* 575, 319–320. doi: 10.1113/jphysiol.2006.118364

Choi, J., Levey, A. I., Weintraub, S. T., Rees, H. D., Gearing, M., Chin, L. S., et al. (2004). Oxidative modifications and down-regulation of ubiquitin carboxyl-terminal hydrolase L1 associated with idiopathic Parkinson's and Alzheimer's diseases. *J. Biol. Chem.* 279, 13256–13264. doi: 10.1074/jbc. M314124200

Chung, D. W., Rudnicki, D. D., Yu, L., and Margolis, R. L. (2011). A natural antisense transcript at the Huntington's disease repeat locus regulates HTT expression. *Hum. Mol. Genet.* 20, 3467–3477. doi: 10.1093/ hmg/ddr263

Chureau, C., Chantalat, S., Romito, A., Galvani, A., Duret, L., Avner, P., et al. (2011). Ftx is a non-coding RNA which affects Xist expression and chromatin structure within the X-inactivation center region. *Hum. Mol. Genet.* 20, 705–718. doi: 10.1093/hmg/ddq516

Clemson, C. M., McNeil, J. A., Willard, H. F., and Lawrence, J. B. (1996). XIST RNA paints the inactive X chromosome at interphase: evidence for a novel RNA involved in nuclear/chromosome structure. *J. Cell Biol.* 132, 259–275. doi: 10.1083/jcb.132.3.259

Cogswell, J. P., Ward, J., Taylor, I. A., Waters, M., Shi, Y., Cannon, B., et al. (2008). Identification of miRNA changes in Alzheimer's disease brain and CSF yields putative biomarkers and insights into disease pathways. *J. Alzheimers Dis.* 14, 27–41. doi: 10.3233/jad-2008-14103

Costa, F. F. (2005). Non-coding RNAs: new players in eukaryotic biology. *Gene* 357, 83–94. doi: 10.1016/j.gene.2005.06.019

DeJesus-Hernandez, M., Mackenzie, I. R., Boeve, B. F., Boxer, A. L., Baker, M., Rutherford, N. J., et al. (2011). Expanded GGGGCC hexanucleotide repeat in noncoding region of C9ORF72 causes chromosome 9p-linked FTD and ALS. *Neuron* 72, 245–256. doi: 10.1016/j.neuron.2011.09.011

Derrien, T., Johnson, R., Bussotti, G., Tanzer, A., Djebali, S., Tilgner, H., et al. (2012). The GENCODE v7 catalog of human long noncoding RNAs: analysis of their gene structure, evolution and expression. *Genome Res.* 22, 1775–1789. doi: 10.1101/gr.132159.111

Duning, K., Buck, F., Barnekow, A., and Kremerskothen, J. (2008). SYNCRIP, a component of dendritically localized mRNPs, binds to the translation regulator BC200 RNA. *J. Neurochem.* 105, 351–359. doi: 10.1111/j.1471-4159.2007. 05138.x

Ebert, M. S., and Sharp, P. A. (2010). Emerging roles for natural microRNA sponges. *Curr. Biol.* 20, R858–R861. doi: 10.1016/j.cub.2010.08.052

Elling, R., Chan, J., and Fitzgerald, K. A. (2016). Emerging role of long noncoding RNAs as regulators of innate immune cell development and inflammatory gene expression. *Eur. J. Immunol.* 46, 504–512. doi: 10.1002/eji.201 444558

ENCODE Project Consortium. (2012). An integrated encyclopedia of DNA elements in the human genome. *Nature* 489, 57–74. doi: 10.1038/nature11247

Faghihi, M. A., Modarresi, F., Khalil, A. M., Wood, D. E., Sahagan, B. G., Morgan, T. E., et al. (2008). Expression of a noncoding RNA is elevated in Alzheimer's disease and drives rapid feed-forward regulation of beta-secretase. *Nat. Med.* 14, 723–730. doi: 10.1038/nm1784

FANTOM Consortium and the RIKEN PMI and CLST (DGT), Forrest, A. R., Kawaji, H., Rehli, M., Baillie, J. K., de Hoon, M. J., et al. (2014). A promoter-level mammalian expression atlas. *Nature* 507, 462–470. doi: 10.1038/nature13182

Faure, J., Lachenal, G., Court, M., Hirrlinger, J., Chatellard-Causse, C., Blot, B., et al. (2006). Exosomes are released by cultured cortical neurones. *Mol. Cell. Neurosci.* 31, 642–648. doi: 10.1016/j.mcn.2005.12.003

Feng, J., Bi, C., Clark, B. S., Mady, R., Shah, P., and Kohtz, J. D. (2006). The Evf-2 noncoding RNA is transcribed from the Dlx-5/6 ultraconserved region and functions as a Dlx-2 transcriptional coactivator. *Genes Dev.* 20, 1470–1484. doi: 10.1101/gad.1416106

Gao, Y., Meng, H., Liu, S., Hu, J., Zhang, Y., Jiao, T., et al. (2015). LncRNA-HOST2 regulates cell biological behaviors in epithelial ovarian cancer through a mechanism involving microRNA let-7b. *Hum. Mol. Genet.* 24, 841–852. doi: 10.1093/hmg/ddu502

Gonzalez, I., Munita, R., Agirre, E., Dittmer, T. A., Gysling, K., Misteli, T., et al. (2015). A lncRNA regulates alternative splicing via establishment of a splicing-specific chromatin signature. *Nat. Struct. Mol. Biol.* 22, 370–376. doi: 10.1038/nsmb.3005

Grivna, S. T., Beyret, E., Wang, Z., and Lin, H. (2006). A novel class of small RNAs in mouse spermatogenic cells. *Genes Dev.* 20, 1709–1714. doi: 10.1101/gad. 1434406

Grote, P., and Herrmann, B. G. (2013). The long non-coding RNA Fendrr links epigenetic control mechanisms to gene regulatory networks in mammalian embryogenesis. *RNA Biol.* 10, 1579–1585. doi: 10.4161/ rna.26165

Grote, P., Wittler, L., Hendrix, D., Koch, F., Währisch, S., Beisaw, A., et al. (2013). The tissue-specific lncRNA Fendrr is an essential regulator of heart and body wall development in the mouse. *Dev. Cell* 24, 206–214. doi: 10.1016/j.devcel. 2012.12.012

Gstir, R., Schafferer, S., Scheideler, M., Misslinger, M., Griehl, M., Daschil, N., et al. (2014). Generation of a neuro-specific microarray reveals novel differentially expressed noncoding RNAs in mouse models for neurodegenerative diseases. *RNA* 20, 1929–1943. doi: 10.1261/rna.047225.114

Guttman, M., Amit, I., Garber, M., French, C., Lin, M. F., Feldser, D., et al. (2009). Chromatin signature reveals over a thousand highly conserved large non-coding RNAs in mammals. *Nature* 458, 223–227. doi: 10.1038/nature07672

Guttman, M., Donaghey, J., Carey, B. W., Garber, M., Grenier, J. K., Munson, G., et al. (2011). lincRNAs act in the circuitry controlling pluripotency and differentiation. *Nature* 477, 295–300. doi: 10.1038/nature10398

Hansen, T. B., Jensen, T. I., Clausen, B. H., Bramsen, J. B., Finsen, B., Damgaard, C. K., et al. (2013). Natural RNA circles function as efficient microRNA sponges. *Nature* 495, 384–388. doi: 10.1038/nature 11993

Hart, R. P., and Goff, L. A. (2016). Long noncoding RNAs: central to nervous system development. *Int. J. Dev. Neurosci.* 55, 109–116. doi: 10.1016/j.ijdevneu. 2016.06.001

Helwak, A., Kudla, G., Dudnakova, T., and Tollervey, D. (2013). Mapping the human miRNA interactome by CLASH reveals frequent noncanonical binding. *Cell* 153, 654–665. doi: 10.1016/j.cell.2013.03.043

Huppertz, I., Attig, J., D'Ambrogio, A., Easton, L. E., Sibley, C. R., Sugimoto, Y., et al. (2014). iCLIP: protein-RNA interactions at nucleotide resolution. *Methods* 65, 274–287. doi: 10.1016/j.ymeth.2013.10.011

Jeck, W. R., and Sharpless, N. E. (2014). Detecting and characterizing circular RNAs. *Nat. Biotechnol.* 32, 453–461. doi: 10.1038/nbt.2890

Ji, Z., Song, R., Regev, A., and Struhl, K. (2015). Many lncRNAs, 5'UTRs and pseudogenes are translated and some are likely to express functional proteins. *Elife* 4:e08890. doi: 10.7554/eLife.08890

Jiang, J., Jing, Y., Cost, G. J., Chiang, J. C., Kolpa, H. J., Cotton, A. M., et al. (2013). Translating dosage compensation to trisomy 21. *Nature* 500, 296–300. doi: 10.1038/nature12394

Jiang, W., Liu, Y., Liu, R., Zhang, K., and Zhang, Y. (2015). The lncRNA DEANR1 facilitates human endoderm differentiation by activating FOXA2 expression. *Cell Rep.* 11, 137–148. doi: 10.1016/j.celrep.2015. 03.008

Kadakkuzha, B. M., Liu, X. A., McCrate, J., Shankar, G., Rizzo, V., Afinogenova, A., et al. (2015). Transcriptome analyses of adult mouse brain reveal enrichment of lncRNAs in specific brain regions and neuronal populations. *Front. Cell. Neurosci.* 9:63. doi: 10.3389/fncel.2015.00063

Kaessmann, H. (2010). Origins, evolution, and phenotypic impact of new genes. *Genome Res.* 20, 1313–1326. doi: 10.1101/gr.101386.109

Kapranov, P., St Laurent, G., Raz, T., Ozsolak, F., Reynolds, C. P., Sorensen, P. H., et al. (2010). The majority of total nuclear-encoded non-ribosomal RNA in a human cell is 'dark matter' un-annotated RNA. *BMC Biol* 8:149. doi: 10.1186/1741-7007-8-149

Kapusta, A., Kronenberg, Z., Lynch, V. J., Zhuo, X., Ramsay, L., Bourque, G., et al. (2013). Transposable elements are major contributors to the origin, diversification, and regulation of vertebrate long noncoding RNAs. *PLoS Genet.* 9:e1003470. doi: 10.1371/journal.pgen.1003470

Katakowski, M., Buller, B., Zheng, X., Lu, Y., Rogers, T., Osobamiro, O., et al. (2013). Exosomes from marrow stromal cells expressing miR-146b inhibit glioma growth. *Cancer Lett.* 335, 201–204. doi: 10.1016/j.canlet.2013.02.019

Kawikova, I., and Askenase, P. W. (2015). Diagnostic and therapeutic potentials of exosomes in CNS diseases. *Brain Res.* 1617, 63–71. doi: 10.1016/j.brainres.2014.09.070

Kazemzadeh, M., Safaralizadeh, R., and Orang, A. V. (2015). LncRNAs: emerging players in gene regulation and disease pathogenesis. *J. Genet.* 94, 771–784. doi: 10.1007/s12041-015-0561-6

Klattenhoff, C. A., Scheuermann, J. C., Surface, L. E., Bradley, R. K., Fields, P. A., Steinhauser, M. L., et al. (2013). Braveheart, a long noncoding RNA required for cardiovascular lineage commitment. *Cell* 152, 570–583. doi: 10.1016/j.cell.2013.01.003

Klein, U., Lia, M., Crespo, M., Siegel, R., Shen, Q., Mo, T., et al. (2010). The DLEU2/miR-15a/16–1 cluster controls B cell proliferation and its deletion leads to chronic lymphocytic leukemia. *Cancer Cell* 17, 28–40. doi: 10.1016/j.ccr.2009.11.019

Kohtz, J. D. (2014). Long non-coding RNAs learn the importance of being *in vivo*. *Front. Genet.* 5:45. doi: 10.3389/fgene.2014.00045

Kung, J. T., Colognori, D., and Lee, J. T. (2013). Long noncoding RNAs: past, present, and future. *Genetics* 193, 651–669. doi: 10.1534/genetics.112.146704

Lakhal, S., and Wood, M. J. (2011). Exosome nanotechnology: an emerging paradigm shift in drug delivery: exploitation of exosome nanovesicles for systemic *in vivo* delivery of RNAi heralds new horizons for drug delivery across biological barriers. *Bioessays* 33, 737–741. doi: 10.1002/bies.201100076

Lander, E. S., Linton, L. M., Birren, B., Nusbaum, C., Zody, M. C., Baldwin, J., et al. (2001). Initial sequencing and analysis of the human genome. *Nature* 409, 860–921. doi: 10.1038/35057062

Lee, S. T., Chu, K., Im, W. S., Yoon, H. J., Im, J. Y., Park, J. E., et al. (2011). Altered microRNA regulation in Huntington's disease models. *Exp. Neurol.* 227, 172–179. doi: 10.1016/j.expneurol.2010.10.012

Lee, S., Kopp, F., Chang, T. C., Sataluri, A., Chen, B., Sivakumar, S., et al. (2016). Noncoding RNA NORAD regulates genomic stability by sequestering PUMILIO proteins. *Cell* 164, 69–80. doi: 10.1016/j.cell.2015.12.017

Li, K., and Ramchandran, R. (2010). Natural antisense transcript: a concomitant engagement with protein-coding transcript. *Oncotarget* 1, 447–452. doi: 10.18632/oncotarget.178

Li, J., Tian, H., Yang, J., and Gong, Z. (2016). Long noncoding RNAs regulate cell growth, proliferation, and apoptosis. *DNA Cell Biol.* 35, 459–470. doi: 10.1089/dna.2015.3187

Lin, N., Chang, K. Y., Li, Z., Gates, K., Rana, Z. A., Dang, J., et al. (2014). An evolutionarily conserved long noncoding RNA TUNA controls pluripotency and neural lineage commitment. *Mol. Cell* 53, 1005–1019. doi: 10.1016/j.molcel.2014.01.021

Lipovich, L., Tarca, A. L., Cai, J., Jia, H., Chugani, H. T., Sterner, K. N., et al. (2014). Developmental changes in the transcriptome of human cerebral cortex tissue: long noncoding RNA transcripts. *Cereb. Cortex* 24, 1451–1459. doi: 10.1093/cercor/bhs414

Lourenco, G. F., Janitz, M., Huang, Y., and Halliday, G. M. (2015). Long noncoding RNAs in TDP-43 and FUS/TLS-related frontotemporal lobar degeneration (FTLD). *Neurobiol. Dis.* 82, 445–454. doi: 10.1016/j.nbd.2015.07.011

Lukiw, W. J. (2013). Circular RNA (circRNA) in Alzheimer's disease (AD). *Front. Genet.* 4:307. doi: 10.3389/fgene.2013.00307

Managadze, D., Lobkovsky, A. E., Wolf, Y. I., Shabalina, S. A., Rogozin, I. B., and Koonin, E. V. (2013). The vast, conserved mammalian lincRNome. *PLoS Comput. Biol.* 9:e1002917. doi: 10.1371/journal.pcbi.1002917

Massone, S., Vassallo, I., Fiorino, G., Castelnuovo, M., Barbieri, F., Borghi, R., et al. (2011). 17A, a novel non-coding RNA, regulates GABA B alternative splicing and signaling in response to inflammatory stimuli and in Alzheimer disease. *Neurobiol. Dis.* 41, 308–317. doi: 10.1016/j.nbd.2010.09.019

Mattick, J. S., and Rinn, J. L. (2015). Discovery and annotation of long noncoding RNAs. *Nat. Struct. Mol. Biol.* 22, 5–7. doi: 10.1038/nsmb.2942

Memczak, S., Jens, M., Elefsinioti, A., Torti, F., Krueger, J., Rybak, A., et al. (2013). Circular RNAs are a large class of animal RNAs with regulatory potency. *Nature* 495, 333–338. doi: 10.1038/nature11928

Mercer, T. R., Dinger, M. E., Sunkin, S. M., Mehler, M. F., and Mattick, J. S. (2008). Specific expression of long noncoding RNAs in the mouse brain. *Proc. Natl. Acad. Sci. U S A* 105, 716–721. doi: 10.1073/pnas.0706729105

Milligan, M. J., and Lipovich, L. (2014). Pseudogene-derived lncRNAs: emerging regulators of gene expression. *Front. Genet.* 5:476. doi: 10.3389/fgene.2014.00476

Modarresi, F., Faghihi, M. A., Lopez-Toledano, M. A., Fatemi, R. P., Magistri, M., Brothers, S. P., et al. (2012). Inhibition of natural antisense transcripts *in vivo* results in gene-specific transcriptional upregulation. *Nat. Biotechnol.* 30, 453–459. doi: 10.1038/nbt.2158

Modarresi, F., Faghihi, M. A., Patel, N. S., Sahagan, B. G., Wahlestedt, C., and Lopez-Toledano, M. A. (2011). Knockdown of BACE1-AS nonprotein-coding transcript modulates beta-amyloid-related hippocampal neurogenesis. *Int. J. Alzheimers Dis.* 2011:929042. doi: 10.4061/2011/929042

Molyneaux, B. J., Goff, L. A., Brettler, A. C., Chen, H. H., Brown, J. R., Hrvatin, S., et al. (2015). DeCoN: genome-wide analysis of *in vivo* transcriptional dynamics during pyramidal neuron fate selection in neocortex. *Neuron* 85, 275–288. doi: 10.1016/j.neuron.2014.12.024

Muddashetty, R., Khanam, T., Kondrashov, A., Bundman, M., Iacoangeli, A., Kremerskothen, J., et al. (2002). Poly(A)-binding protein is associated with neuronal BC1 and BC200 ribonucleoprotein particles. *J. Mol. Biol.* 321, 433–445. doi: 10.1016/s0022-2836(02)00655-1

Mus, E., Hof, P. R., and Tiedge, H. (2007). Dendritic BC200 RNA in aging and in Alzheimer's disease. *Proc. Natl. Acad. Sci. U S A* 104, 10679–10684. doi: 10.1073/pnas.0701532104

Muslimov, I. A., Santi, E., Homel, P., Perini, S., Higgins, D., and Tiedge, H. (1997). RNA transport in dendrites: a cis-acting targeting element is contained within neuronal BC1 RNA. *J. Neurosci.* 17, 4722–4733.

Ng, S. Y., Bogu, G. K., Soh, B. S., and Stanton, L. W. (2013). The long noncoding RNA RMST interacts with SOX2 to regulate neurogenesis. *Mol. Cell* 51, 349–359. doi: 10.1016/j.molcel.2013.07.017

Ng, S. Y., Johnson, R., and Stanton, L. W. (2012). Human long non-coding RNAs promote pluripotency and neuronal differentiation by association with chromatin modifiers and transcription factors. *EMBO J.* 31, 522–533. doi: 10.1038/emboj.2011.459

Nishihara, H., Smit, A. F., and Okada, N. (2006). Functional noncoding sequences derived from SINEs in the mammalian genome. *Genome Res.* 16, 864–874. doi: 10.1101/gr.5255506

Nishimoto, Y., Ito, D., Yagi, T., Nihei, Y., Tsunoda, Y., and Suzuki, N. (2010). Characterization of alternative isoforms and inclusion body of the TAR DNA-binding protein-43. *J. Biol. Chem.* 285, 608–619. doi: 10.1074/jbc.M109.022012

Nishimoto, Y., Nakagawa, S., Hirose, T., Okano, H. J., Takao, M., Shibata, S., et al. (2013). The long non-coding RNA nuclear-enriched abundant transcript 1_2 induces paraspeckle formation in the motor neuron during the early phase of amyotrophic lateral sclerosis. *Mol. Brain* 6:31. doi: 10.1186/1756-6606-6-31

Parenti, R., Paratore, S., Torrisi, A., and Cavallaro, S. (2007). A natural antisense transcript against Rad18, specifically expressed in neurons and upregulated during beta-amyloid-induced apoptosis. *Eur. J. Neurosci.* 26, 2444–2457. doi: 10.1111/j.1460-9568.2007.05864.x

Pinter, S. F., Sadreyev, R. I., Yildirim, E., Jeon, Y., Ohsumi, T. K., Borowsky, M., et al. (2012). Spreading of X chromosome inactivation via a hierarchy of defined Polycomb stations. *Genome Res.* 22, 1864–1876. doi: 10.1101/gr.133751.111

Ponjavic, J., Oliver, P. L., Lunter, G., and Ponting, C. P. (2009). Genomic and transcriptional co-localization of protein-coding and long non-coding RNA pairs in the developing brain. *PLoS Genet.* 5:e1000617. doi: 10.1371/journal.pgen.1000617

Ponting, C. P., Oliver, P. L., and Reik, W. (2009). Evolution and functions of long noncoding RNAs. *Cell* 136, 629–641. doi: 10.1016/j.cell.2009.02.006

Quinn, J. J., and Chang, H. Y. (2016). Unique features of long non-coding RNA biogenesis and function. *Nat. Rev. Genet.* 17, 47–62. doi: 10.1038/nrg.2015.10

Qureshi, I. A., and Mehler, M. F. (2012). Emerging roles of non-coding RNAs in brain evolution, development, plasticity and disease. *Nat. Rev. Neurosci.* 13, 528–541. doi: 10.1038/nrn3234

Qureshi, I. A., and Mehler, M. F. (2013). Long non-coding RNAs: novel targets for nervous system disease diagnosis and therapy. *Neurotherapeutics* 10, 632–646. doi: 10.1007/s13311-013-0199-0

Ramos, A. D., Andersen, R. E., Liu, S. J., Nowakowski, T. J., Hong, S. J., Gertz, C. C., et al. (2015). The long noncoding RNA Pnky regulates neuronal differentiation of embryonic and postnatal neural stem cells. *Cell Stem Cell* 16, 439–447. doi: 10.1016/j.stem.2015.02.007

Ramos, A. D., Diaz, A., Nellore, A., Delgado, R. N., Park, K. Y., Gonzales-Roybal, G., et al. (2013). Integration of genome-wide approaches identifies lncRNAs of adult neural stem cells and their progeny *in vivo*. *Cell Stem Cell* 12, 616–628. doi: 10.1016/j.stem.2013.03.003

Rani, N., Nowakowski, T. J., Zhou, H., Godshalk, S. E., Lisi, V., Kriegstein, A. R., et al. (2016). A primate lncRNA mediates notch signaling during neuronal development by sequestering miRNA. *Neuron* 90, 1174–1188. doi: 10.1016/j.neuron.2016.05.005

Raposo, G., Nijman, H. W., Stoorvogel, W., Liejendekker, R., Harding, C. V., Melief, C. J., et al. (1996). B lymphocytes secrete antigen-presenting vesicles. *J. Exp. Med.* 183, 1161–1172. doi: 10.1084/jem.183.3.1161

Reddy, A. S., O'Brien, D., Pisat, N., Weichselbaum, C. T., Sakers, K., Lisci, M., et al. (2017). A comprehensive analysis of cell type-specific nuclear RNA from neurons and glia of the brain. *Biol. Psychiatry* 81, 252–264. doi: 10.1016/j.biopsych.2016.02.021

Rinn, J. L., and Chang, H. Y. (2012). Genome regulation by long noncoding RNAs. *Annu. Rev. Biochem.* 81, 145–166. doi: 10.1146/annurev-biochem-051410-092902

Rinn, J. L., Kertesz, M., Wang, J. K., Squazzo, S. L., Xu, X., Brugmann, S. A., et al. (2007). Functional demarcation of active and silent chromatin domains in human HOX loci by noncoding RNAs. *Cell* 129, 1311–1323. doi: 10.1016/j.cell.2007.05.022

Roberts, T. C., Morris, K. V., and Wood, M. J. (2014). The role of long non-coding RNAs in neurodevelopment, brain function and neurological disease. *Philos. Trans. R. Soc. Lond. B Biol. Sci.* 369:20130507. doi: 10.1098/rstb.2013.0507

Salameh, A., Lee, A. K., Cardó-Vila, M., Nunes, D. N., Efstathiou, E., Staquicini, F. I., et al. (2015). PRUNE2 is a human prostate cancer suppressor regulated by the intronic long noncoding RNA PCA3. *Proc. Natl. Acad. Sci. U S A* 112, 8403–8408. doi: 10.1073/pnas.1507882112

Schmitz, S. U., Grote, P., and Herrmann, B. G. (2016). Mechanisms of long noncoding RNA function in development and disease. *Cell. Mol. Life Sci.* 73, 2491–2509. doi: 10.1007/s00018-016-2174-5

Sosinska, P., Mikula-Pietrasik, J., and Ksiazek, K. (2015). The double-edged sword of long non-coding RNA: the role of human brain-specific BC200 RNA in translational control, neurodegenerative diseases, and cancer. *Mutat. Res. Rev. Mutat. Res.* 766, 58–67. doi: 10.1016/j.mrrev.2015.08.002

Tian, D., Sun, S., and Lee, J. T. (2010). The long noncoding RNA, Jpx, is a molecular switch for X chromosome inactivation. *Cell* 143, 390–403. doi: 10.1016/j.cell.2010.09.049

Ulitsky, I., and Bartel, D. P. (2013). lincRNAs: genomics, evolution, and mechanisms. *Cell* 154, 26–46. doi: 10.1016/j.cell.2013.06.020

Valadi, H., Ekstrom, K., Bossios, A., Sjostrand, M., Lee, J. J., and Lötvall, J. O. (2007). Exosome-mediated transfer of mRNAs and microRNAs is a novel mechanism of genetic exchange between cells. *Nat. Cell Biol.* 9, 654–659. doi: 10.1038/ncb1596

Vance, K. W., and Ponting, C. P. (2014). Transcriptional regulatory functions of nuclear long noncoding RNAs. *Trends Genet.* 30, 348–355. doi: 10.1016/j.tig.2014.06.001

Vance, K. W., Sansom, S. N., Lee, S., Chalei, V., Kong, L., Cooper, S. E., et al. (2014). The long non-coding RNA Paupar regulates the expression of both local and distal genes. *EMBO J.* 33, 296–311. doi: 10.1002/embj.201386225

Vicens, Q., and Westhof, E. (2014). Biogenesis of circular RNAs. *Cell* 159, 13–14. doi: 10.1016/j.cell.2014.09.005

Vučičevič, D., Schrewe, H., and Orom, U. A. (2014). Molecular mechanisms of long ncRNAs in neurological disorders. *Front. Genet.* 5:48. doi: 10.3389/fgene.2014.00048

Wang, F., Ying, H. Q., He, B. S., Pan, Y. Q., Deng, Q. W., Sun, H. L., et al. (2015). Upregulated lncRNA-UCA1 contributes to progression of hepatocellular carcinoma through inhibition of miR-216b and activation of FGFR1/ERK signaling pathway. *Oncotarget* 6, 7899–7917. doi: 10.18632/oncotarget.3219

Wang, P., Xue, Y., Han, Y., Lin, L., Wu, C., Xu, S., et al. (2014). The STAT3-binding long noncoding RNA lnc-DC controls human dendritic cell differentiation. *Science* 344, 310–313. doi: 10.1126/science.1251456

Wu, P., Zuo, X., Deng, H., Liu, X., Liu, L., and Ji, A. (2013). Roles of long noncoding RNAs in brain development, functional diversification and neurodegenerative diseases. *Brain Res. Bull.* 97, 69–80. doi: 10.1016/j.brainresbull.2013.06.001

Xing, Z., Lin, A., Li, C., Liang, K., Wang, S., Liu, Y., et al. (2014). lncRNA directs cooperative epigenetic regulation downstream of chemokine signals. *Cell* 159, 1110–1125. doi: 10.1016/j.cell.2014.10.013

Xiong, X. D., Ren, X., Cai, M. Y., Yang, J. W., Liu, X., and Yang, J. M. (2016). Long non-coding RNAs: an emerging powerhouse in the battle between life and death of tumor cells. *Drug Resist. Updat.* 26, 28–42. doi: 10.1016/j.drup.2016.04.001

Zhang, X., Zhou, Y., Mehta, K. R., Danila, D. C., Scolavino, S., Johnson, S. R., et al. (2003). A pituitary-derived MEG3 isoform functions as a growth suppressor in tumor cells. *J. Clin. Endocrinol. Metab.* 88, 5119–5126. doi: 10.1210/jc.2003-030222

Zhong, J., Chuang, S. C., Bianchi, R., Zhao, W., Lee, H., Fenton, A. A., et al. (2009). BC1 regulation of metabotropic glutamate receptor-mediated neuronal excitability. *J. Neurosci.* 29, 9977–9986. doi: 10.1523/JNEUROSCI.3893-08.2009

Zu, T., Liu, Y., Bañez-Coronel, M., Reid, T., Pletnikova, O., Lewis, J., et al. (2013). RAN proteins and RNA foci from antisense transcripts in C9ORF72 ALS and frontotemporal dementia. *Proc. Natl. Acad. Sci. U S A* 110, E4968–E4977. doi: 10.1073/pnas.1315438110

Conflict of Interest Statement: The authors declare that the research was conducted in the absence of any commercial or financial relationships that could be construed as a potential conflict of interest.

frontiers in Neuroscience

ORIGINAL RESEARCH
published: 26 February 2018
doi: 10.3389/fnins.2018.00075

Precise Excision of the CAG Tract from the Huntingtin Gene by Cas9 Nickases

Magdalena Dabrowska[1], *Wojciech Juzwa*[2], *Wlodzimierz J. Krzyzosiak*[3] and *Marta Olejniczak*[1]*

[1] Department of Genome Engineering, Institute of Bioorganic Chemistry, Polish Academy of Sciences, Poznan, Poland, [2] Department of Biotechnology and Food Microbiology, Poznan University of Life Sciences, Poznan, Poland, [3] Department of Molecular Biomedicine, Institute of Bioorganic Chemistry, Polish Academy of Sciences, Poznan, Poland

Huntington's disease (HD) is a progressive autosomal dominant neurodegenerative disorder caused by the expansion of CAG repeats in the first exon of the huntingtin gene (*HTT*). The accumulation of polyglutamine-rich huntingtin proteins affects various cellular functions and causes selective degeneration of neurons in the striatum. Therapeutic strategies used to date to silence the expression of mutant *HTT* include antisense oligonucleotides, RNA interference-based approaches and, recently, genome editing with the CRISPR/Cas9 system. Here, we demonstrate that the CAG repeat tract can be precisely excised from the *HTT* gene with the use of the paired Cas9 nickase strategy. As a model, we used HD patient-derived fibroblasts with varied numbers of CAG repeats. The repeat excision inactivated the *HTT* gene and abrogated huntingtin synthesis in a CAG repeat length-independent manner. Because Cas9 nickases are known to be safe and specific, our approach provides an attractive treatment tool for HD that can be extended to other polyQ disorders.

Keywords: genome editing, CRISPR/Cas9, neurodegenerative diseases, repeat expansion, engineered nucleases, Huntington's disease, nonsense-mediated decay

OPEN ACCESS

Edited by:
Sandro Alves,
Brainvectis Therapeutics, France

Reviewed by:
Nicole Déglon,
Centre Hospitalier Universitaire Vaudois (CHUV), Switzerland
Panchanan Maiti,
University of California, Los Angeles, United States

***Correspondence:**
Marta Olejniczak
marta.olejniczak@ibch.poznan.pl

Specialty section:
This article was submitted to Neurodegeneration, a section of the journal Frontiers in Neuroscience

Received: *28 November 2017*
Accepted: *29 January 2018*
Published: *26 February 2018*

Citation:
Dabrowska M, Juzwa W, Krzyzosiak WJ and Olejniczak M (2018) Precise Excision of the CAG Tract from the Huntingtin Gene by Cas9 Nickases. Front. Neurosci. 12:75. doi: 10.3389/fnins.2018.00075

INTRODUCTION

Expansions of short tandem repeat sequences in functionally unrelated genes are causative factors of numerous human hereditary neurological diseases. Currently, there are nine known neurodegenerative disorders caused by the expansion of CAG repeats within the coding regions of associated genes. These disorders include Huntington's disease (HD) (Bates et al., 2015); spinocerebellar ataxia types 1, 2, 3, 6, 7, and 17 (SCA) (Paulson et al., 2017); spinal-bulbar muscular atrophy (SBMA) (Spada et al., 1991); and dentatorubral-pallidoluysian atrophy (DRPLA) (Koide et al., 1994). A positive correlation exists between the size of the expansion and the severity of symptoms, which usually appear during the 4th-5th decade of life and lead to patient's death (Duyao et al., 1993).

HD is caused by the expansion of CAG repeats in exon 1 of the *HTT* gene, which encodes huntingtin (HTT), a large protein of more than 3,000 amino acids (Saudou and Humbert, 2016). Expanded polyglutamine (polyQ) protein may form intracellular aggregates and affects numerous cellular activities inducing pathogenesis *via* a gain of toxic function. Despite many years of research on an effective treatment method, HD and other polyQ diseases are incurable, and only their symptoms can be controlled. Several different strategies have already been employed in cellular and animal models of polyQ diseases to achieve the desired therapeutic effects

(Wild and Tabrizi, 2017). These strategies include the silencing of both HTT alleles in a non-allele-selective strategy and the targeting of single-nucleotide polymorphisms (SNPs) linked to repeat expansions. The repeat region itself may be targeted in an allele selective and non-selective manner (Fiszer et al., 2012; Keiser et al., 2016; Esteves et al., 2017). RNA interference and antisense oligonucleotide technologies, which have been used for many years in experimental therapy for polyQ diseases, are currently complemented with genome editing systems such as the CRISPR/Cas9 (Shin et al., 2016; Kolli et al., 2017; Merienne et al., 2017; Monteys et al., 2017; Yang et al., 2017).

Zinc finger nucleases (ZFNs) and transcription activator-like effector-based nucleases (TALENs) were the first tools that provided proof of principle for the idea of targeted inactivation of the expanded CAG repeats at a disease *loci* (Mittelman et al., 2009; Richard et al., 2014). In one of the first studies, preceding the CRISPR/Cas9 technology development, Isalan group used zinc finger proteins (ZFPs) to selectively bind and repress expanded CAG repeats in the R6/2 mouse model of HD (Garriga-Canut et al., 2012). In other approach expanded CAG repeat tracts were replaced with a normal CAG length by inducing homologous recombination in induced pluripotent stem cells (iPSCs) derived from HD patient fibroblasts (An et al., 2012). The efficiency of homologous recombination was further increased by using CRISPR/Cas9 (An et al., 2014).

The CRISPR-Cas9 system uses a small guide RNA (sgRNA) containing a 20 nt sequence complementary to the target DNA and Cas9 nuclease for site-specific cleavage of a genomic target containing a protospacer-adjacent motif (PAM) (Jinek et al., 2012). Double-strand breaks (DSBs) are repaired mainly by error-prone non-homologous end joining (NHEJ), resulting in mutations that may cause frame-shifts in open reading frames, premature translation termination and transcript degradation by nonsense-mediated decay (NMD). To increase specificity and reduce off-targeting, one of two cleavage domains in the Cas9 protein was mutated to act as a nickase (Cas9n) (Cho et al., 2014; Trevino and Zhang, 2014). Nickases generate single strand breaks (SSBs) that are repaired with high fidelity. Paired sgRNA/Cas9 nickases targeted to the opposite DNA strands enable genome editing via homology-directed repair (HDR) and have been shown to reduce off-targeting by 5- to 1.500-fold compared to wild-type Cas9 (wt Cas9) (Ran et al., 2013; Cho et al., 2014). Therefore, the paired Cas9 nickase strategy can be useful in applications that require precise genome editing such as gene and cell therapy.

To date, the CRISPR/Cas9 system has been used to selectively inactivate mutant *HTT* genes by using PAM sites generated by SNP alleles (Shin et al., 2016; Monteys et al., 2017). Although this strategy is very promising, it requires a comprehensive analysis of the *HTT* gene haplotype structure. In addition, the non-allele selective approach has been used to inactivate the *HTT* gene by using a pair of sgRNAs flanking CAG repeats and wt Cas9 in a transgenic mouse model of HD (Yang et al., 2017). Non-allele selective supression of *HTT* gene expression was achieved also by using CRISPR interference strategy (CRISPRi) in HEK293T cells (Heman-Ackah et al., 2016). In this approach nuclease null, dead Cas9 (dCas9) and sgRNAs targeting *HTT* transcription start site were used.

In this study, we examined paired Cas9 nickase strategy to inactivate the *HTT* gene by targeting sequences directly flanking the CAG repeat tract. We demonstrate that precise excision of the CAG repeats from the *HTT* gene results in the abrogation of protein synthesis in all investigated fibroblast cell lines derived from HD patients. Importantly, we also show that this specific and safe strategy leads to preservation of repeat-deficient transcript level, suggesting that the transcript may escape from NMD pathway.

MATERIALS AND METHODS

Cell Culture and Transfection

Fibroblasts (GM04208, 21/44 CAG in the *HTT* gene; GM04281, 17/68 CAG in the *HTT* gene; GM09197, 21/151 CAG in the *HTT* gene) were obtained from the Coriell Cell Repositories (Camden, New Jersey, USA) and grown in minimal essential medium (Lonza; Basel, Switzerland) supplemented with 10% fetal bovine serum (Sigma-Aldrich; St. Louis, MO, USA), antibiotics (Sigma-Aldrich, A5955) and non-essential amino acids (Sigma-Aldrich, M7145). HEK293T cells (16/17 CAG in the *HTT* gene) were grown in Dulbecco's modified Eagle's medium (Lonza; Basel, Switzerland) supplemented with 10% fetal bovine serum (Sigma-Aldrich), antibiotics (Sigma-Aldrich) and L-glutamine (Sigma-Aldrich). HEK293T transfections were performed using calcium phosphate method with 10 μg of plasmid DNA for 3×10^5 cells (Jordan et al., 1996). Fibroblasts were electroporated with the NeonTM Transfection System (Invitrogen, Carlsbad, CA, USA). Briefly, 1×10^6 to 5×10^5 cells were harvested, resuspended in PBS and electroporated with 10 μg of plasmid DNA (5 μg of each plasmid from a HTT_sgRNA/Cas9n pair) in 100 μl tips using the following parameters: 1.350 V, 30 ms, 1 pulse. Fibroblasts were sorted by flow cytometry (BD Biosciences, BD FACS AriaIII) 48 h post electroporation and collected for genomic DNA, RNA and protein extraction.

Plasmids

Guide RNA sequences for the CRISPR/Cas9 system were designed as described in Ran et al. with the use of CRISPOR software (http://crispor.tefor.net/crispor.py; Haeussler et al., 2016). Briefly, the top and bottom strand of 20-nt guide RNA were synthesized (IBB, Warsaw), annealed and ligated into the pair of FastDigest BsmBI (Thermo Fisher Scientific, Waltham, MA, USA) cut plasmids, namely, pSpCas9(BB)-2A-GFP (PX458) (Addgene, Cambridge, MA, USA) and its nickase version (D10A nickase mutant; pSpCas9n(BB)-2A-GFP (PX461)) from *S. pyogenes* (Ran et al., 2013). Ligated products were transformed into chemically competent E. coli GT116 cells (InvivoGen, San Diego, CA, USA), and the cells were plated onto ampicillin selection plates (100 μg/mL ampicillin) and incubated at 37°C overnight. Plasmid DNA was isolated using the Gene JET Plasmid Miniprep kit (Thermo Scientific) and verified with Sanger sequencing. For larger scale plasmid preparations, the Qiagen Midi kit was used (Qiagen, Hilden, Germany). The sgRNA oligonucleotide sequences are presented in **Table S1**.

DNA Extraction and Analysis of Genome Editing Efficiency

Genomic DNA from the HD fibroblast and HEK293T cell lines was extracted using the Cells and Tissue DNA Isolation Kit (Norgen, Biotek Corp., Schmon Pkwy, ON, Canada) according to manufacturer's instructions and quantified using a spectrophotometer/fluorometer (DeNovix, Wilmington, DE, USA). For the T7E1 mismatch analysis, genomic DNA was amplified using Phusion High-Fidelity PCR Master Mix (Thermo Fisher) with primers HD1F and HD1R spanning CAG repeats in exon 1 of the *HTT* gene. The two-step PCR amplification program was used as follows: an initial denaturation at 98°C for 3 min; 12 cycles at 98°C for 15 s, 72°C for 15 s; 21 cycles at 98°C for 15 s, 62°C for 15 s, and 72°C for 15 s; and a final elongation at 72°C for 5 min. PCR products were purified using the GeneJET PCR Purification Kit (Thermo Fisher). 400 ng of the purified PCR product was used in an annealing reaction and enzymatic digestion with the T7E1 enzyme (New England Biolabs, Ipswich, MA, USA). Cleavage products were separated in 1.3% agarose gels and detected using G-BOX. Band intensities were analyzed with GelPro software (Media Cybernetics, Rockville, MD, USA). Indel occurrence was estimated with an analysis of signal loss from the main PCR products. Briefly, the main band intensities from HTT_sgRNA-treated samples were compared to the same bands from control samples treated with the empty plasmid. Genes selected for off-target analysis were PCR-amplified with specific primer pairs (**Table S1**) using Phusion High-Fidelity PCR Master Mix (Thermo Fisher) and the following program: an initial denaturation at 95°C for 3 min; 30 cycles at 95°C for 15 s, 62°C for 15 s, and 72°C for 15 s; and a final elongation at 72°C for 5 min. T7E1 analysis was performed as described for the *HTT* gene.

RNA Isolation and Reverse Transcription-Polymerase Chain Reaction

Total RNA was isolated from fibroblast cells using the TRI Reagent (BioShop; Burlington, Canada) according to the manufacturer's instructions. The RNA concentration was measured using spectrophotometer (DeNovix). A total of 700 ng of RNA was reverse transcribed at 55°C using Superscript III (Life Technologies) and random hexamer primers (Promega; Madison, WI, USA). The quality of the reverse transcription (RT) reaction was assessed through polymerase chain reaction (PCR) amplification of the GAPDH gene. Complementary DNA (cDNA) was used for quantitative polymerase chain reaction (qPCR) using SsoAdvanced™ Universal SYBR® Green Supermix (BIO-RAD, Hercules, CA, USA) with denaturation at 95°C for 30 s followed by 40 cycles of denaturation at 95°C for 15 s and annealing at 60°C for 30 s. The melt curve protocol was subsequently performed for 5 s at 65°C followed by 5 s increments at 0.5°C from 65°C to 95°C with *HTT*- or *GAPDH*-specific primers (sequences are listed in **Table S1**) on the CFX Connect™ Real-Time PCR Detection System (BIO-RAD). In order to avoid generation of two PCR products with different number of CAG repeats (two alleles of HD), primers used in qRT-PCR (HD_F and HD_R) were design to cover the HTT region downstream the CAG repeat tract. Data preprocessing and normalization were performed using BIO-RAD CFX Manager software (BIO-RAD). To confirm that the HTT transcript from the Cas9n-treated fibroblasts did not contain CAG repeats, cDNA was amplified with cDNAF and cDNAR primers flanking the repeat tract.

Western Blot Analysis

A total of 30 μg of protein was resolved on a Tris-acetate SDS-polyacrylamide gel (3–8%, NuPAGE™, Invitrogen, Carlsbad, CA, USA) in Tris-Acetate SDS Running buffer (Novex, Carlsbad, CA, USA) at 170 V at 4°C. After electrophoresis, the proteins were wet-transferred overnight to a nitrocellulose membrane (Sigma–Aldrich). The primary antibodies, namely, anti-huntingtin (1:1000, MAB2166, Millipore, Burlington, MA, USA) and anti-plectin (1:1000, ab83497, Abcam, Cambridge, UK), and the secondary antibodies, namely, the anti-mouse HRP conjugate (1:2000, A9917, Sigma–Aldrich) and anti-rabbit HRP conjugate (1:2000, 711-035-152, Jackson ImmunoResearch, West Grove, PA, USA) were used in a TBS/0.1% Tween-20 buffer containing 2.5% non-fat milk. The immunoreaction was detected using Western Bright Quantum HRP Substrate (Advansta, Menlo Park, CA, USA). The protein bands were scanned directly from the membrane using a camera and quantified using Gel-Pro Analyzer (Media Cybernetics).

Sanger Sequencing

DNA obtained from cell cultures transfected with plasmids was sequenced using a forward primer (HD1F). PCR products from DNA treated with Cas9 nickase pairs were separated in 1% agarose gel. Bands were extracted using the GeneJET Gel Extraction Kit (Thermo Scientific) and sequenced with the same HD1F primer.

Statistical Analysis

Statistical analysis was performed using GraphPad Prism v. 5.0 software. Data were analyzed using one-way ANOVA followed by Bonferroni's *post hoc* test ($^{***}P < 0.0001$) with an arbitrary value of 1 assigned to the cells treated with the empty control plasmid.

RESULTS

Pre-screening of HTT_sgRNA Activity in HEK293T Cells

We designed 3 sgRNAs using *S. pyogenes* PAM sequences (NGG) located within the sequences flanking the CAG repeat tract in the *HTT* gene (HTT_sgRNA1, HTT_sgRNA3 and HTT_sgRNA4) and one sgRNA (HTT_sgRNA2) directly targeting the CAG repeats (**Figure 1A**). HTT_sgRNA2 was designed to use a non-canonical NAG PAM sequence that is known to be recognized by *S. pyogenes* Cas9 (Hsu et al., 2013; Zhang et al., 2014; Leenay et al., 2016). The first screening of the sgRNA activities was performed in easy-to-transfect HEK293T cells. The cells were transfected with plasmids expressing both the wt Cas9 protein and HTT_sgRNA (**Figure 1B**). The transfection efficiency, expressed as GFP-positive cells, was ∼80% (data not shown), and genomic

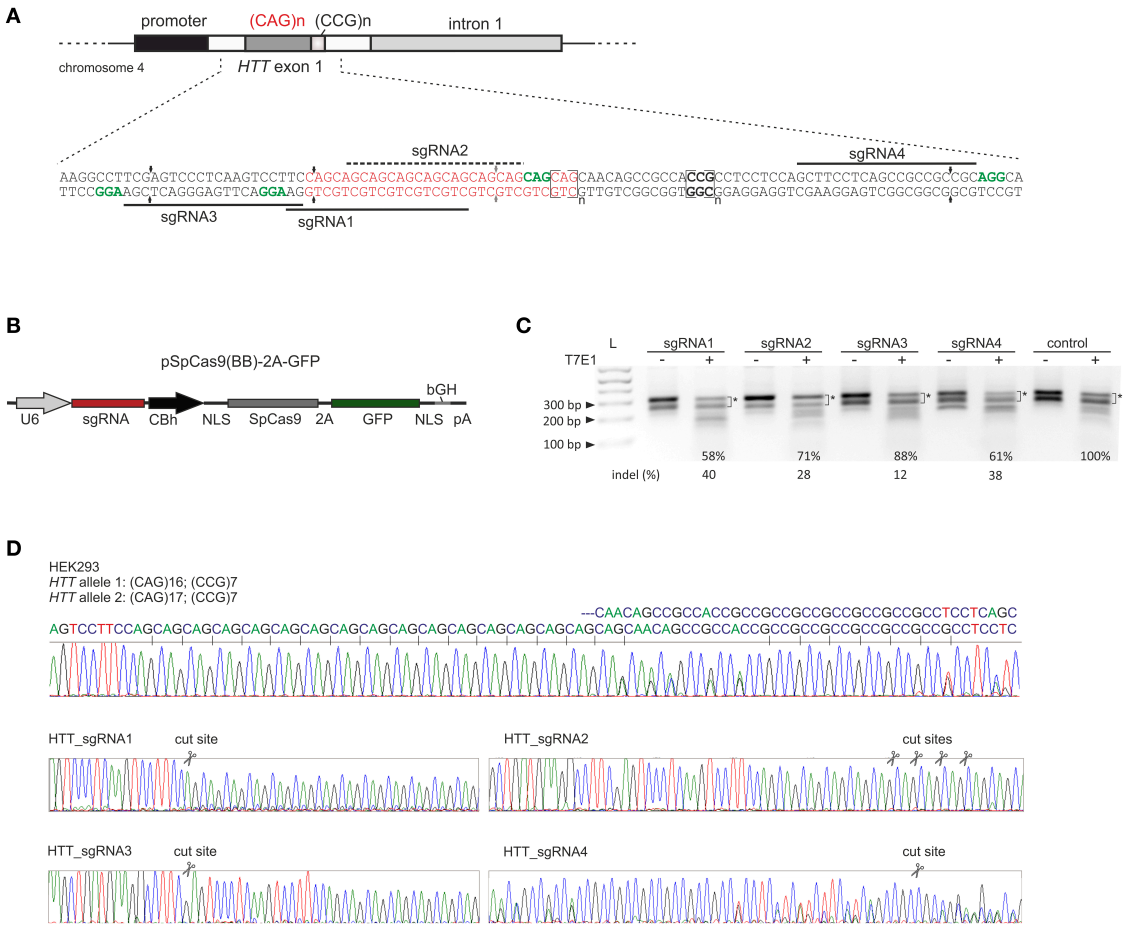

FIGURE 1 | Pre-screening of HTT_sgRNAs activity in HEK293T cells. **(A)** Polymorphic CAG repeats and the following CCG repeats are located in exon 1 of the *HTT* gene. sgRNA1, sgRNA3 and sgRNA4 were designed to target the 5′- and 3′-repeat flanking sequences, respectively. Appropriate PAM sequences are highlighted in green. SgRNA2 uses a non-canonical NAG PAM sequence and targets CAG repeats directly. **(B)** Illustration depicting the CRISPR/Cas9 expression plasmid used to co-express the SpCas9 protein together with the GFP reporter marker and sgRNA under the U6 promoter. NLS, nuclear localization signal. **(C)** Analysis of HTT_sgRNA and wt Cas9 activity in HEK293T cells by T7E1 mismatch assays. The signal intensities of the two main bands (marked with an asterisk) was measured. The loss of this signal in relation to the control (100%) was used to calculate the indel frequency (%) in the samples treated with T7E1 (+). The length of the main PCR product is ∼ 305 bp. Additional, faster migrating bands in samples non treated with T7E1 enzyme are secondary structure forms of the main product and their contribution is significantly reduced after denaturation of a sample directly before gel electrophoresis (see **Figure S1**). **(D)** Sanger sequencing of the *HTT* gene fragment included the CAG repeat tract. HEK293T cells are heterozygous in this locus with two alleles containing 16 and 17 CAG repeats. After *HTT* gene editing with CRISPR/Cas9, the sequence trace after the break site comprised a mixture of signals derived from the unmodified and modified DNA.

DNA was isolated 48 h post-transfection from unsorted cells. PCR amplification of the *HTT* gene region, including the CAG repeats, and subsequent T7E1 analysis resulted in the generation of multiple bands in both the treated and untreated control cells (**Figure 1C**). The HEK293T cells contain 16 and 17 CAG repeats in the two alleles of the *HTT* gene (**Figure 1D**). In addition, PCR products containing long stretches of repeated sequences may form various secondary structures (e.g., hairpins) in non-denaturing conditions (agarose gel electrophoresis) (**Figure S1**). Therefore, a determination of the exact indels frequency in this polymorphic, highly repetitive gene region was difficult using methods based on heteroduplex recognition by nucleases. However, Sanger sequencing (**Figure 1D**) and T7E1 analysis of the PCR products from a pool of transfected and non-transfected cells revealed that HTT_sgRNA1, HTT_sgRNA4 and HTT_sgRNA2 efficiently edited the *HTT* gene (∼40, 38, and ∼28% of indels, respectively) whereas HTT_sgRNA3 was the least active (∼12%) (**Figure 1C**). This result was consistent with the fact that the sequence composition of sgRNA (GC:AT content) may influence the editing efficiency (Moreno-Mateos MA 2015). The GC content for HTT_sgRNAs ranges from 57% for the least active HTT_sgRNA3 to 81% for HTT_sgRNA4.

Next, we analyzed the activities of the HTT_sgRNA pairs with the Cas9 nickase protein. HEK293T cells were transfected with a pair of plasmids encoding HTT_sgRNA1 and HTT_sgRNA2, HTT_sgRNA1 and HTT_sgRNA4, and HTT_sgRNA3 and HTT_sgRNA4. T7E1 analysis (**Figure 2A**) and Sanger sequencing (**Figure 2B**) confirmed that except for HTT_sgRNA1+2, the sgRNAs functioned in pairs and generated

shorter bands corresponding to HTT amplicons with 107-bp and 125-bp deletions for HTT_sgRNA1+4 and HTT_sgRNA3+4 pairs, respectively. As a result of the CAG repeat excision and frameshift mutation premature-translation-termination codon, PTC (TGA) was generated in the 3' region of *HTT* exon 1 (e.g., at the 44th codon of the 50-codon exon 1 for Cas9n_sgRNA1+4-treated cells) (**Figure S2**).

Analysis of Paired HTT_sgRNA/Cas9n Activity in Patient-Derived Fibroblasts

The most active pair of HTT_sgRNAs (sgRNA1 and sgRNA4) was electroporated into HD fibroblasts containing varied lengths of the CAG repeat tract: 21/44 CAGs, 17/68 CAGs and 21/151 CAGs. GFP-positive cells were sorted by FACS before DNA, RNA and protein isolation. We confirmed by PCR and Sanger sequencing of the PCR products that Cas9 nickase with the HTT_sgRNA1+4 pair efficiently excised the targeted region of *HTT* exon 1 in the patient-derived cell lines (**Figure S3**). The lengths of the excised DNA fragments were between 119 and 188 bp for both alleles of the GM04208 cell line, 107 and 260 bp for GM04281 and 119 and 509 for the GM09197 cell line. As expected, the HTT transcript also did not contain the targeted sequence, which was specifically excised from the DNA by the HTT_sgRNA1+4 Cas9 nickases (**Figure 3A**). A shorter, 545-bp PCR product was present in the three patients-derived cell lines; however, the editing efficiency was different, with the highest observed for the GM04281 cell line. Interestingly, the level of the HTT transcript did not change in the cells treated with paired nickases, suggesting that the transcript may have escaped the nonsense-mediated mRNA decay pathway (**Figure 3B**). Notably, the newly generated stop codon (UGA) was localized ∼20 bp from the exon/exon junction and may have been occupied by the exon-exon junction complex (EJC) (**Figure S2**). Despite the presence of a shortened HTT transcript, the HTT protein level was efficiently reduced by 82% in the GM04281 cell line, 68% in the GM04208 cell line, and 71% in the GM09197 cell line (**Figures 3C,D**). This data accurately reflects the results of the RT-PCR analysis (**Figure 3A**) and indicates that the length of the CAG repeat tract does not influence the excision efficiency of Cas9n. The prematurely terminated translation product (43 amino-acid protein) was not detected with the use of the N-terminal huntingtin antibody by western blot (data not shown).

Assessment of Off-Target Effects

In silico analysis using the CRISPOR tool (Haeussler et al., 2016) predicted 13 exonic off-target sites for HTT_sgRNA1 (with score > 10.00), 18 sites for HTT_sgRNA3 and 196 for HTT_sgRNA4. Notably, more than 98% of the exonic HTT_sgRNA4 off-targets had 3 to 4 mismatches with the target sequence (**Table S2**). Specificity score that measures the uniqueness of a guide in the genome is low for HTT_sgRNAs, because target sequence is composed of repetitive sequences (6 for HTT_sgRNA1, 66 for HTT_sgRNA3 and 40 for HTT_sgRNA4). HTT_sgRNA2 with a non-canonical NAG PAM comprised a repeated sequence and theoretically targeted every CAG repeat tract longer than

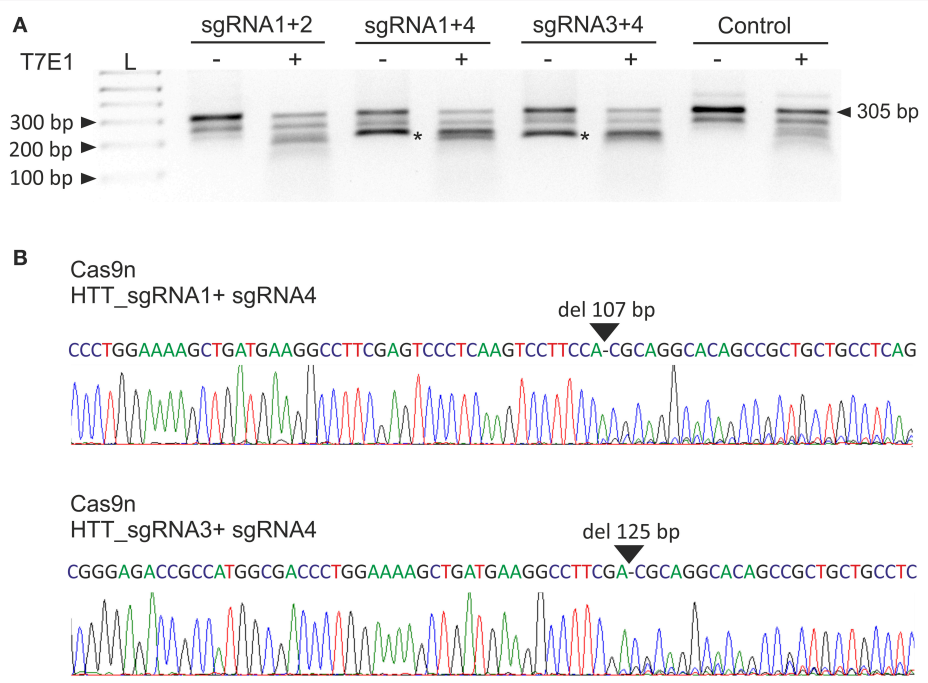

FIGURE 2 | Excision of the CAG repeats from the HTT gene with paired Cas9 nickases. **(A)** DNA from HEK293T cells treated with Cas9 nickase and the HTT_sgRNA pairs was PCR amplified and subjected to T7E1 analysis. The length of the unmodified PCR fragment is 305 bp, whereas the edited products are shortened to < 200 bp (marked with an asterisk). **(B)** A representative Sanger sequencing electropherogram showing the deletion of 107 and 125 bp in HTT_sgRNA1+4- and HTT_sgRNA1+3-treated cells, respectively (marked with an arrow).

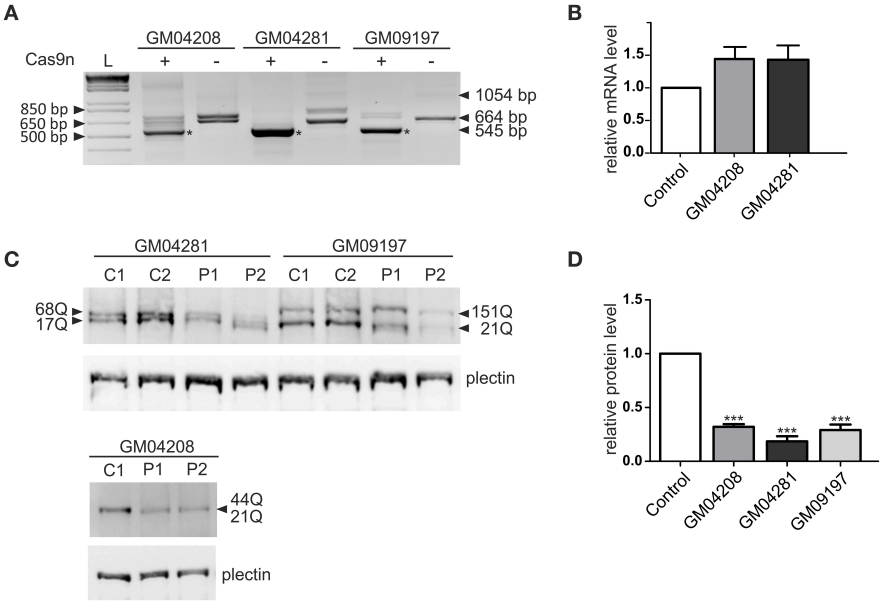

FIGURE 3 | Huntingtin inactivation via the Cas9 nickase pair in patient-derived fibroblasts. **(A)** RT-PCR analysis of the Cas9n/HTT_sgRNA1+4-edited (+) and non-edited (–) *HTT* gene product in the three human HD cell lines containing 21/44 (GM04208), 17/68 (GM04281) and 21/151 (GM09197) CAG repeats. As a result of repeat excision, shorter PCR products (∼545 bp, marked with an asterisk) are present. **(B)** RT-qPCR analysis of the HTT mRNA levels in the human fibroblast cell lines transfected with the Cas9n/HTT_sgRNA1 and sgRNA4 plasmid pairs. All samples are normalized to human GAPDH, and the results are the mean (± SEM) relative to the cells transfected with the control Cas9n plasmid (one-way ANOVA followed by Bonferroni's *post hoc* test; the difference was non-significant). **(C)** Representative western blots showing the HTT protein levels in the control fibroblasts treated with the empty Cas9n plasmids, expressing only Cas9 protein and not sgRNA (C1 and C2) and in the Cas9n/HTT_sgRNA1+4-treated cells (P1 and P2). Plectin was used as the loading control. The lengths of the polyQ tracts in both alleles of the HTT protein in each cell line are marked with an arrow. **(D)** The quantification of the huntingtin levels in the three human HD cell lines transfected with the Cas9n/HTT_sgRNA1+4 plasmid pair relative to the plectin levels. The results indicate the mean (± SEM) relative to the cells transfected with the control Cas9n plasmid ($n = 3$; one way ANOVA followed by Bonferroni's *post hoc* test; ***$p < 0.0001$).

7 units. Notably, these predictions generally applied to the wt CRISPR/Cas9 activity since Cas9 nickases cut only one DNA strand that is faithfully repaired by HDR. In addition, the maximal cleavage efficiency of paired Cas9 nickases has previously been observed at sites with the tail-to-tail orientation separated by 10–30 bp (Shen et al., 2014). Potential off-target activity for Cas9n/HTT_sgRNA1+4 pair was expected to be rare as similar sequences were unlikely to occur close together elsewhere in the genome. Nonetheless, the 4 selected off-target regions for each HTT_sgRNA were PCR-amplified and analyzed with T7E1 assays (**Figure S4**). The *TEX13A* and *ZFHX3* genes and *TJP2* and *FBXW7* genes were tested for HTT_sgRNA1 and HTT_sgRNA4, respectively. We used DNA from HEK293T cells treated with plasmids expressing the HTT_sgRNA1+4 Cas9 nickase pair and wt Cas9/sgRNAs. Non-specific activity of the CRISPR/Cas9 system was not detected in any of the tested off-target sites.

DISCUSSION

To date, multiple therapeutic approaches have been described for the treatment of HD and other polyQ diseases' however, these approaches suffer from specific limitations that hinder their introduction to the clinic (reviewed in Keiser et al., 2016; Esteves et al., 2017; Wild and Tabrizi, 2017). In addition, the role of huntingtin in cell physiology and pathology is not fully understood (Saudou and Humbert, 2016), and therefore, strategies using selective silencing of the mutant allele alone and non-allele-selective silencing of both alleles are being developed in parallel. It has been shown using RNAi and antisense oligonucleotides that the knockdown of huntingtin, either the mutant or both mutant and normal is beneficial in mouse models of HD (Harper et al., 2005; Boudreau et al., 2009; Kordasiewicz et al., 2012). Recently, the CRISPR/Cas9 system was used to permanently inactivate the *HTT* gene, by using a pair of sgRNAs flanking the CAG/CTG repeats in a transgenic mouse model of HD (HD140Q knock-in) (Yang et al., 2017). Stereotactic injection of AAVs expressing sgRNAs and SpCas9 into the striata of adult mice resulted in the depletion of huntingtin aggregates in the brain, thereby alleviating motor deficits and neuropathological symptoms.

In our study, we present another repeat-depletion strategy to inactivate the *HTT* gene in which we further improve the approach by using a nickase version of Cas9 that is known to be more specific and safe than the wt Cas9. The efficiency of paired Cas9 nickase editing depends on the activity of two sgRNAs and the length of the target sequence between the two sgRNAs (Mali et al., 2013; Ran et al., 2013). We demonstrate that the pair of HTT_sgRNA/Cas9n is able to efficiently and specifically excise the repeat-containing fragment of exon 1 in three HD

patient-derived cell lines differing in CAG repeat length. We show that the CAG repeat length did not influence the cutting efficiency and specificity, and the HTT protein level is reduced by ∼70% in all tested models. Notably, in the case of the GM09197 cell line containing 151 CAG repeats in the mutant allele, the HTT_sgRNAs were separated by nearly 500 bp. We confirmed the specificity and safety of the paired nickase strategy by testing selected off-target loci with T7E1 mismatch detection assays.

The mechanism of this precise repeat excision and DNA repair (without scars), atypical for NHEJ is poorly known and needs further studies. However, it has been reported previously that DSBs generated by CRISPR/Cas9 near a long stretch of CTG/CAG repeats in myotonic dystrophy type 1 (DM1) locus can induce deletion of the entire repeat region (Van Agtmaal et al., 2017). Even single DSB in the region flanking the repeated sequence was sufficient to generate clean loss of repeats. Contraction of CAG/CTG repeats was also observed for ZFN and TALEN—treated human and yeast cells (Mittelman et al., 2009; Richard et al., 2014).

Interestingly, in our study the level of the shortened HTT transcript did not change, suggesting that the transcript may be NMD-resistant. The *HTT* gene contains 67 exons and has three isoforms of mRNA transcripts (Romo et al., 2017); the two predominant forms are 10,366 and of 13,711 bp (Lin et al., 1993). The longer transcript differs by an additional 3′ UTR sequence of 3,360 bp that affects mRNA localization, stability, and translation (Di Giammartino et al., 2011). A previous report showed that targeting the HTT exon 1-intron junction with CRISPR/Cas9 reduced the mRNA level by ∼50% in BM-MSCs derived from the YAC128 mouse model (Kolli et al., 2017). In another study, a large deletion of approximately 44 kb of DNA using wt Cas9 and a pair of sgRNAs targeting the upstream promoter region and intron 3 resulted in the complete abrogation of mRNA and HTT protein synthesis (Shin et al., 2016). HTT mRNA resistance to NMD, observed in our study, may result from the specific localization of CRISPR/Cas9n-generated PTC in exon 1 of the multi-exonic *HTT* gene. In addition, a UGA stop codon is localized to position occupied by the EJC (∼20–24 nt upstream of the exon/exon junction), which serves to orient the NMD machinery and may be masked during the "pioneer round" of translation (Popp and Maquat, 2016). A previous report showed that β-globin transcript containing PTCs in exon 1 of three-exonic gene is NMD–resistant; however, the influence of the nonsense codon localization within transcripts needs to be clarified (Thermann et al., 1998; Inácios et al., 2004; Peixeiro et al., 2011).

Genome editing with the use of a more universal CAG repeat-targeting strategy is still challenging due to the lack of specific PAM recognized by targeted nucleases, off-targeting induced by sgRNA comprising repeats and problems with the selective inactivation of mutant alleles alone. Similar problems have already been overcome by antisense and RNAi technologies (Hu et al., 2009; Yu et al., 2012; Fiszer et al., 2013). In our study CAG repeat targeting with Cas9n and HTT_sgRNA pair composed of sgRNA2 (non-canonical NAG PAM) and sgRNA1 was ineffective. However, the in-frame shortening of the CAG repeat tract with the use of genome editing tools would be the most desired and universal approach and is our goal for future studies.

AUTHOR CONTRIBUTIONS

MO and MD contributed to the study design. MD, MO, and WJ performed experiments. MO, MD, and WK contributed to the data analysis, writing, and editing of the manuscript.

ACKNOWLEDGMENTS

This work was supported by a grant from the National Science Center (2015/18/E/NZ2/00678) and from the quality-promoting subsidy under the Leading National Research Center (KNOW) program for 2014–2018.

SUPPLEMENTARY MATERIAL

The Supplementary Material for this article can be found online at: https://www.frontiersin.org/articles/10.3389/fnins.2018.00075/full#supplementary-material

REFERENCES

An, M. C., O'Brien, R. N., Zhang, N., Patra, B. N., De La Cruz, M., Ray, A., et al. (2014). Polyglutamine disease modeling: epitope based screen for homologous recombination using CRISPR/Cas9 System. *PLoS Curr*. 6:ecurrents.hd.0242d2e7ad72225efa72f6964589369a. doi: 10.1371/currents.hd.0242d2e7ad72225efa72f6964589369a

An, M. C., Zhang, N., Scott, G., Montoro, D., Wittkop, T., Mooney, S., et al. (2012). Genetic correction of huntington's disease phenotypes in induced pluripotent stem cells. *Cell Stem Cell* 11, 253–263. doi: 10.1016/j.stem.2012.04.026

Bates, G. P., Dorsey, R., Gusella, J. F., Hayden, M. R., Kay, C., Leavitt, B. R., et al. (2015). Huntington disease. *Nat. Rev. Dis. Prim*. 1:15005. doi: 10.1038/nrdp.2015.5

Boudreau, R. L., McBride, J. L., Martins, I., Shen, S., Xing, Y., Carter, B. J., et al. (2009). Nonallele-specific silencing of mutant and wild-type Huntingtin demonstrates therapeutic efficacy in Huntington's disease mice. *Mol. Ther*. 17, 1053–1063. doi: 10.1038/mt.2009.17

Cho, S. W., Kim, S., Kim, Y., Kweon, J., Kim, H. S., Bae, S., et al. (2014). Analysis of off-target effects of CRISPR/Cas-derived RNA-guided endonucleases and nickases. *Genome Res*. 24, 132–141. doi: 10.1101/gr.162339.113

Di Giammartino, D. C., Nishida, K., Manley, J. L. L., Di Giammartino, D. C., Nishida, K., and Manley, J. L. L. (2011). Mechanisms and consequences of alternative polyadenylation. *Mol. Cell* 43, 853–866. doi: 10.1016/j.molcel.2011.08.017

Duyao, M., Ambrose, C., Myers, R., Novelletto, A., Persichetti, F., Frontali, M., et al. (1993). Trinucleotide repeat length instability and age of onset in Huntington's disease. *Nat. Genet*. 4, 387–392. doi: 10.1038/ng0893-387

Esteves, S., Duarte-Silva, S., and Maciel, P. (2017). Discovery of therapeutic approaches for polyglutamine diseases: a summary of recent efforts. *Med. Res. Rev*. 37, 860–906. doi: 10.1002/med.21425

Fiszer, A., Olejniczak, M., Galka-Marciniak, P., Mykowska, A., and Krzyzosiak, W. J. (2013). Self-duplexing CUG repeats selectively inhibit mutant huntingtin expression. *Nucleic Acids Res*. 41, 10426–10437. doi: 10.1093/nar/gkt825

Fiszer, A., Olejniczak, M., Switonski, P. M., Wroblewska, J. P., Wisniewska-Kruk, J., Mykowska, A., et al. (2012). An evaluation of oligonucleotide-based therapeutic strategies for polyQ diseases. *BMC Mol. Biol*. 13:6. doi: 10.1186/1471-2199-13-6

Garriga-Canut, M., Agustín-Pavón, C., Herrmann, F., Sánchez, A., Dierssen, M., Fillat, C., et al. (2012). Synthetic zinc finger repressors reduce mutant

huntingtin expression in the brain of R6/2 mice. *Proc. Natl. Acad. Sci. U.S.A.* 109, E3136–E3145. doi: 10.1073/pnas.1206506109

Haeussler, M., Schönig, K., Eckert, H., Eschstruth, A., Mianné, J., Renaud, J. B., et al. (2016). Evaluation of off-target and on-target scoring algorithms and integration into the guide RNA selection tool CRISPOR. *Genome Biol.* 17:148. doi: 10.1186/s13059-016-1012-2

Harper, S. Q., Staber, P. D., He, X., Eliason, S. L., Martins, I. H., Mao, Q., et al. (2005). RNA interference improves motor and neuropathological abnormalities in a Huntington's disease mouse model. *Proc. Natl. Acad. Sci. U.S.A.* 102, 5820–5825. doi: 10.1073/pnas.0501507102

Heman-Ackah, S. M., Bassett, A. R., and Wood, M. J. A. (2016). Precision modulation of neurodegenerative disease-related gene expression in human iPSC-derived neurons. *Sci. Rep.* 6:28420. doi: 10.1038/srep28420

Hsu, P. D., Scott, D. A., Weinstein, J. A., Ran, F. A., Konermann, S., Agarwala, V., et al. (2013). DNA targeting specificity of RNA-guided Cas9 nucleases. *Nat. Biotechnol.* 31, 827–832. doi: 10.1038/nbt.2647

Hu, J., Matsui, M., Gagnon, K. T., Schwartz, J. C., Gabillet, S., Arar, K., et al. (2009). Allele-specific silencing of mutant huntingtin and ataxin-3 genes by targeting expanded CAG repeats in mRNAs. *Nat. Biotechnol.* 27, 478–484. doi: 10.1038/nbt.1539

Inácios, Â., Silva, A. L., Pinto, J., Ji, X., Morgado, A., Almeida, F., et al. (2004). Nonsense mutations in close proximity to the initiation codon fail to trigger full nonsense-mediated mRNA decay. *J. Biol. Chem.* 279, 32170–32180. doi: 10.1074/jbc.M405024200

Jinek, M., Chylinski, K., Fonfara, I., Hauer, M., Doudna, J. A., and Charpentier, E. (2012). A programmable dual-RNA-guided DNA endonuclease in adaptive bacterial immunity. *Science* 337, 816–821. doi: 10.1126/science.1225829

Jordan, M., Schallhorn, A., and Wurm, F. M. (1996). Transfecting mammalian cells: optimization of critical parameters affecting calcium-phosphate precipitate formation. *Nucleic Acids Res.* 24, 596–601. doi: 10.1093/nar/24.4.596

Keiser, M. S., Kordasiewicz, H. B., and McBride, J. L. (2016). Gene suppression strategies for dominantly inherited neurodegenerative diseases: lessons from Huntington's disease and spinocerebellar ataxia. *Hum. Mol. Genet.* 25, R53–R64. doi: 10.1093/hmg/ddv442

Koide, R., Ikeuchi, T., Onodera, O., Tanaka, H., Igarashi, S., Endo, K., et al. (1994). Unstable expansion of CAG repeat in hereditary dentatorubral-pallidoluysian atrophy (DRPLA). *Nat. Genet.* 6, 9–13. doi: 10.1038/ng0194-9

Kolli, N., Lu, M., Maiti, P., Rossignol, J., and Dunbar, G. L. (2017). CRISPR-Cas9 mediated gene-silencing of the mutant Huntingtin gene in an *in vitro* model of Huntington's disease. *Int. J. Mol. Sci.* 18:754. doi: 10.3390/ijms18040754

Kordasiewicz, H. B., Stanek, L. M., Wancewicz, E. V., Mazur, C., McAlonis, M. M., Pytel, K. A., et al. (2012). Sustained therapeutic reversal of Huntington's disease by transient repression of Huntingtin synthesis. *Neuron* 74, 1031–1044. doi: 10.1016/j.neuron.2012.05.009

Leenay, R. T., Maksimchuk, K. R., Slotkowski, R. A., Agrawal, R. N., Gomaa, A. A., Briner, A. E., et al. (2016). Identifying and visualizing functional PAM diversity across CRISPR-cas systems. *Mol. Cell* 62, 137–147. doi: 10.1016/j.molcel.2016.02.031

Lin, B., Rommens, J. M., Graham, R. K., Kalchman, M., Macdonald, H., Nasir, J., et al. (1993). Differential 3' polyadenylation of the huntington disease gene results in two mRNA species with variable tissue expression. *Hum. Mol. Genet.* 2, 1541–1545. doi: 10.1093/hmg/2.10.1541

Mali, P., Aach, J., Stranges, P. B., Esvelt, K. M., Moosburner, M., Kosuri, S., et al. (2013). CAS9 transcriptional activators for target specificity screening and paired nickases for cooperative genome engineering. *Nat. Biotechnol.* 31, 833–838. doi: 10.1038/nbt.2675

Merienne, N., Vachey, G., de Longprez, L., Meunier, C., Zimmer, V., Perriard, G., et al. (2017). The self-inactivating KamiCas9 system for the editing of CNS disease genes. *Cell Rep.* 20, 2980–2991. doi: 10.1016/j.celrep.2017.08.075

Mittelman, D., Moye, C., Morton, J., Sykoudis, K., Lin, Y., Carroll, D., et al. (2009). Zinc-finger directed double-strand breaks within CAG repeat tracts promote repeat instability in human cells. *Proc. Natl. Acad. Sci. U.S.A.* 106, 9607–9612. doi: 10.1073/pnas.0902420106

Monteys, A. M., Ebanks, S. A., Keiser, M. S., and Davidson, B. L. (2017). CRISPR/Cas9 editing of the mutant huntingtin allele *in vitro* and *in vivo*. *Mol. Ther.* 25, 12–23. doi: 10.1016/j.ymthe.2016.11.010

Paulson, H. L., Shakkottai, V. G., Clark, H. B., and Orr, H. T. (2017). Polyglutamine spinocerebellar ataxias — from genes to potential treatments. *Nat. Rev. Neurosci.* 18, 613–626. doi: 10.1038/nrn.2017.92

Peixeiro, I., Silva, A. L., and Romão, L. (2011). Control of human β-globin mRNA stability and its impact on beta-thalassemia phenotype. *Haematologica* 96, 905–913. doi: 10.3324/haematol.2010.039206

Popp, M. W., and Maquat, L. E. (2016). Leveraging rules of nonsense-mediated mRNA decay for genome engineering and personalized medicine. *Cell* 165, 1319–1332. doi: 10.1016/j.cell.2016.05.053

Ran, F. A., Hsu, P. D., Lin, C. Y., Gootenberg, J. S., Konermann, S., Trevino, A. E., et al. (2013). Double nicking by RNA-guided CRISPR cas9 for enhanced genome editing specificity. *Cell* 154, 1380–1389. doi: 10.1016/j.cell.2013.08.021

Richard, G. F., Viterbo, D., Khanna, V., Mosbach, V., Castelain, L., and Dujon, B. (2014). Highly specific contractions of a single CAG/CTG trinucleotide repeat by TALEN in yeast. *PLoS ONE* 9:e95611. doi: 10.1371/journal.pone.0095611

Romo, L., Ashar-Patel, A., Pfister, E., and Aronin, N. (2017). Alterations in mRNA 3′ UTR isoform abundance accompany gene expression changes in human Huntington's disease brains. *Cell Rep.* 20, 3057–3070. doi: 10.1016/j.celrep.2017.09.009

Saudou, F., and Humbert, S. (2016). The biology of Huntingtin. *Neuron* 89, 910–926. doi: 10.1016/j.neuron.2016.02.003

Shen, B., Zhang, W., Zhang, J., Zhou, J., Wang, J., Chen, L., et al. (2014). Efficient genome modification by CRISPR-Cas9 nickase with minimal off-target effects. *Nat. Methods* 11, 399–402. doi: 10.1038/nmeth.2857

Shin, J. W., Kim, K.-H., Chao, M. J., Atwal, R. S., Gillis, T., MacDonald, M. E., et al. (2016). Permanent inactivation of Huntington's disease mutation by personalized allele-specific CRISPR/Cas9. *Hum. Mol. Genet.* 25, 4566–4576. doi: 10.1093/hmg/ddw286

Spada, A. R., La Wilson, E. M., Lubahn, D. B., Harding, A. E., and Fischbeck, K. H. (1991). Androgen receptor gene mutations in X-linked spinal and bulbar muscular atrophy. *Nature* 352, 77–79. doi: 10.1038/352077a0

Thermann, R., Neu-Yilik, G., Deters, A., Frede, U., Wehr, K., Hagemeier, C., et al. (1998). Binary specification of nonsense codons by splicing and cytoplasmic translation. *EMBO J.* 17, 3484–3494. doi: 10.1093/emboj/17.12.3484

Trevino, A. E., and Zhang, F. (2014). Genome editing using cas9 nickases. *Methods Enzymol.* 546, 161–174. doi: 10.1016/B978-0-12-801185-0.00008-8

Van Agtmaal, E. L., André, L. M., Willemse, M., Cumming, S. A., Van Kessel, I. D. G., Van Den Broek, W. J. A. A., et al. (2017). CRISPR/Cas9-Induced (CTG,CAG) n repeat instability in the myotonic dystrophy type 1 locus: implications for therapeutic genome editing. *Mol. Ther.* 25, 24–43. doi: 10.1016/j.ymthe.2016.10.014

Wild, E. J., and Tabrizi, S. J. (2017). Therapies targeting DNA and RNA in Huntington's disease. *Lancet Neurol.* 16, 837–847. doi: 10.1016/S1474-4422(17)30280-6

Yang, S., Chang, R., Yang, H., Zhao, T., Hong, Y., Kong, H. E., et al. (2017). CRISPR/Cas9-mediated gene editing ameliorates neurotoxicity in mouse model of Huntington's disease. *J. Clin. Invest.* 127, 2719–2724. doi: 10.1172/JCI92087

Yu, D., Pendergraff, H., Liu, J., Kordasiewicz, H. B., Cleveland, D. W., Swayze, E. E., et al. (2012). Single-stranded RNAs use RNAi to potently and allele-selectively inhibit mutant huntingtin expression. *Cell* 150, 895–908. doi: 10.1016/j.cell.2012.08.002

Zhang, Y., Ge, X., Yang, F., Zhang, L., Zheng, J., Tan, X., et al. (2014). Comparison of non-canonical PAMs for CRISPR/Cas9-mediated DNA cleavage in human cells. *Sci. Rep.* 4:5405. doi: 10.1038/srep05405

Conflict of Interest Statement: The authors declare that the research was conducted in the absence of any commercial or financial relationships that could be construed as a potential conflict of interest.

frontiers in Neuroscience

ORIGINAL RESEARCH
published: 30 August 2017
doi: 10.3389/fnins.2017.00476

Improving the Delivery of SOD1 Antisense Oligonucleotides to Motor Neurons Using Calcium Phosphate-Lipid Nanoparticles

Liyu Chen[1,2†], Clare Watson[1,2†], Marco Morsch[3], Nicholas J. Cole[3], Roger S. Chung[3], Darren N. Saunders[4], Justin J. Yerbury[2] and Kara L. Vine[1,2]*

[1] Illawarra Health and Medical Research Institute, Wollongong, NSW, Australia, [2] Science Medicine and Health Faculty, Centre for Medical and Molecular Bioscience, School of Biological Sciences, University of Wollongong, Wollongong, NSW, Australia, [3] Department of Biomedical Sciences, Faculty of Medicine and Health Sciences, Macquarie University, Sydney, NSW, Australia, [4] School of Medical Sciences, University of New South Wales, Sydney, NSW, Australia

OPEN ACCESS

Edited by:
Sandro Alves,
Brainvectis Therapeutics, France

Reviewed by:
Patrizia Longone,
Fondazione Santa Lucia (IRCCS), Italy
Jenny Sassone,
Vita-Salute San Raffaele University, Italy

***Correspondence:**
Kara L. Vine
kara@uow.edu.au

[†] *These authors have contributed equally to this work.*

Specialty section:
This article was submitted to Neurodegeneration, a section of the journal Frontiers in Neuroscience

Received: *01 June 2017*
Accepted: *10 August 2017*
Published: *30 August 2017*

Citation:
Chen L, Watson C, Morsch M, Cole NJ, Chung RS, Saunders DN, Yerbury JJ and Vine KL (2017) Improving the Delivery of SOD1 Antisense Oligonucleotides to Motor Neurons Using Calcium Phosphate-Lipid Nanoparticles. Front. Neurosci. 11:476. doi: 10.3389/fnins.2017.00476

Amyotrophic Lateral Sclerosis (ALS) is a fatal neurodegenerative disease affecting the upper and lower motor neurons in the motor cortex and spinal cord. Abnormal accumulation of mutant superoxide dismutase I (SOD1) in motor neurons is a pathological hallmark of some forms of the disease. We have shown that the orderly progression of the disease may be explained by misfolded SOD1 cell-to-cell propagation, which is reliant upon its active endogenous synthesis. Reducing the levels of SOD1 is therefore a promising therapeutic approach. Antisense oligonucleotides (ASOs) can efficiently silence proteins with gain-of-function mutations. However, naked ASOs have a short circulation half-life and are unable to cross the blood brain barrier (BBB) warranting the use of a drug carrier for effective delivery. In this study, calcium phosphate lipid coated nanoparticles (CaP-lipid NPs) were developed for delivery of SOD1 ASO to motor neurons. The most promising nanoparticle formulation (Ca/P ratio of 100:1), had a uniform spherical core–shell morphology with an average size of 30 nm, and surface charge (ζ-potential) of −4.86 mV. The encapsulation efficiency of ASO was 48% and stability studies found the particle to be stable over a period of 20 days. *In vitro* experiments demonstrated that the negatively charged ASO-loaded CaP-lipid NPs could effectively deliver SOD1-targeted ASO into a mouse motor neuron-like cell line (NSC-34) through endocytosis and significantly down-regulated SOD1 expression in HEK293 cells. The CaP-lipid NPs exhibited a pH-dependant dissociation, suggesting that that the acidification of lysosomes is the likely mechanism responsible for facilitating intracellular ASO release. To demonstrate tissue specific delivery and localization of these NPs we performed *in vivo* microinjections into zebrafish. Successful delivery of these NPs was confirmed for the zebrafish brain, the blood stream, and the spinal cord. These results suggest that CaP-lipid NPs could be an effective and safe delivery system for the improved delivery of SOD1 ASOs to motor neurons. Further *in vivo* evaluation in transgenic mouse models of SOD1 ALS are therefore warranted.

Keywords: amyotrophic lateral sclerosis, motor neurone disease, drug delivery, calcium phosphate nanoparticle, antisense oligonucleotide, SOD1, therapeutic intervention, zebrafish

INTRODUCTION

Amyotrophic lateral sclerosis (ALS) is an incurable neurodegenerative disease that is associated with protein misfolding and aggregation. Accumulation of toxic proteinaceous aggregates in the upper and lower motor neurons of the motor cortex and spinal cord over time is associated with motor neuron death, leading to loss of muscle control, muscle atrophy, and invariably death (Brettschneider et al., 2014). The causes of most ALS cases remain undefined, however ∼5–10% are inherited (Majoor-Krakauer et al., 2003). Mutations in genes known to cause ALS are growing and include, F*US/TLS, VAPB, TARDBP, OPTN, VCP, SQSTM1, UBQLN2, CCNF, PFN1, MATR3,* and hexanucleotide repeat expansions in *C9ORF72* (Renton et al., 2014). Due to its early discovery in 1993, the best-studied mutation associated with the familial form of ALS (fALS) is in the gene encoding copper/zinc superoxide dismutase (Cu/Zn SOD, SOD1) (Rosen et al., 1993).

SOD1 is a 32-kDa homodimeric metalloenzyme, found primarily in the nucleus, plasma membrane, and cytosol. It contains an active site that binds a catalytic copper ion and a structural zinc ion where it serves to catalyze the dismutation of superoxide radical to dioxygen and hydrogen peroxide (Perry et al., 2010). The correctly folded and active form of the SOD1 enzyme is obtained through several post-translational modifications such as the acquisition of zinc and copper ions, disulfide bond formation, and dimerization (Arnesano et al., 2004). However, mutations that lead to the dissociation of metal ions, and reduction of the intramolecular disulfide bond are known to decrease its conformational stability and promote misfolding. It is well accepted that mutations in SOD1 cause ALS through a toxic gain of function rather than a loss of its native function. Over 180 mutations in the *SOD1* gene that impact upon its structural stability have now been identified (http://alsod.iop.kcl.ac.uk/Overview/gene.aspx?gene_id=SOD1).

A common pathological hallmark in SOD1-ALS cases is the abnormal accumulation of mutant SOD1 in motor neurons of the affected nervous tissues. Our group has recently reported that misfolded SOD1 is present in sporadic disease as well as SOD1-linked fALS, and can propagate cell-to-cell in a prion-like fashion potentially contributing to the orderly progression of the disease (Grad et al., 2014). In addition, we have shown that this cell-to-cell transmission of SOD1 protein aggregates is dependent on fluid-phase endocytosis pathways, primarily via stimulated macropinocytosis (Zeineddine et al., 2015), and relies on active SOD1 synthesis and its presence in a form readily incorporated into aggregates in recipient cells (Grad et al., 2014). Reducing the levels of monomeric and/or misfolded SOD1 is therefore a promising therapeutic target for familial and potentially some sporadic SOD1-related forms of ALS.

Considering the key role copper plays in regulating SOD1 protein stability and function and that low levels have been associated with SOD1 misfolding (Bourassa et al., 2014), a novel ALS treatment based on the concept of copper supplementation to motor neurons has recently been suggested. In the $SOD1^{G93A}$ transgenic mouse model of ALS, the administration of CuATSM, a compound capable of transporting copper into the brain, extended the lives of ALS rodents by 18 months (Soon et al., 2011). Furthermore, restoring copper homeostasis with CuATSM treatment was found to rescue neurons from their symptomatic stage. The effect of CuATSM in patients with familial SOD1-ALS is currently being examined in a Phase I clinical trial (NCT03136809). Another approach currently under clinical investigation involves intraventricular or intrathecal delivery of antisense oligonucleotide against SOD1 for patients with SOD1 fALS (Smith et al., 2006). In a Phase I, randomized, first-in-man study, Miller et al. reported a reduction of SOD1 concentrations in brain tissue, and that this correlates with reduced SOD1 in the CSF (Miller et al., 2013). Although these data strongly support use of SOD1 antisense oligonucleotide as a therapy, the route of administration is invasive by nature and poses a greater risk of post-surgery complications, particularly for repeat dosing.

Nanomedicine is a rapidly growing field that has produced several drug delivery vehicles, such as lipid and polymeric-based nanoparticles, able to deliver genes, and other therapeutics to tissues including the brain and spinal cord (Soppimath et al., 2001; Vieira and Gamarra, 2016). Mechanistically, a drug poorly distributed to the brain can be loaded on/into a nanocarrier system which interacts with the endothelial cells at the blood brain barrier (BBB) to produce higher drug concentrations in brain parenchyma. These nanocarriers can be further modified with targeting moieties to preferentially bind to putative receptors or transporters expressed at the BBB for enhanced CNS selectivity, permeability, and drug trafficking. For example, liposomes surface functionalized with apoE fragments, folate, transferrin or anti-transferrin receptor (anti-TfR) antibody have been shown to cross the BBB by transcytosis and deliver genes to the nervous system, including neurons, with little toxicity (Mc Carthy et al., 2015). In ALS, only one preclinical study has used nanoparticles (glutathione functionalized liposomes) to transport a drug across the BBB, and increase its availability in the CNS, but disappointingly failed to deliver cargo into neurons (Evans et al., 2014). Herein we report the manufacture and biophysical characterization of solid core calcium phosphate lipid nanoparticles (CaP-lipid NPs) that can encapsulate antisense oligonucleotide directed to SOD1 (**Figure 1A**). We also describe for the first time nanoparticle distribution in the brain, spinal cord, and blood circulation of zebrafish, a powerful experimental vertebrate model for studying ALS. We propose that CaP-lipid NPs can increase the successful delivery of oligonucleotide in ALS.

MATERIALS AND METHODS

Reagents and Chemicals

Cholesterol, dioleoylphosphatydic acid (DOPA), 1,2-dioleoyl-3-trimethylammonium-propane chloride salt (DOTAP), 1,2-dipalmitoyl-sn-glycero-3-phosphoethanolamine-N-(lissaminerhodamine B sulfonyl) (ammonium salt) (LissRdB-DSPE), and 1,2-distearoryl-sn-glycero-3-phosphoethanolamine-N-[methoxy-(polyethyleneglycol-2000) ammonium salt (DSPE-PEG) were purchased from Avanti Polar Lipids, Inc. (Alabaster, AL). All other chemicals were obtained from

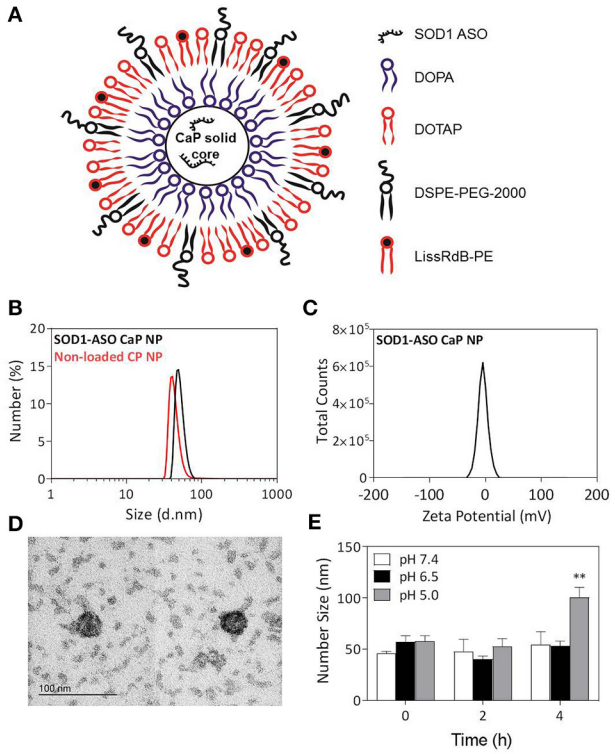

FIGURE 1 | Physical properties of SOD1-ASO-loaded CaP-lipid NPs with a Ca/P ratio 100:1. Schematic representation of SOD1-ASO loaded CaP-lipid NP formulation **(A)**, particle size (d.nm) of SOD1-ASO loaded (black) and non-loaded (red) CaP-lipid NPs determined by DLS **(B)**, zeta potential of SOD1-ASO CaP-lipid NP **(C)**, transmission electron micrograph (TEM) of SOD1-ASO CaP-lipid NPs visualized by negative staining **(D)**, pH-sensitivity as indicated by change in number size (d.nm) of CaP-lipid NPs in PBS at pH 7.4, 6.5, and 5.0 following incubation at 37°C for up to 4 h **(E)**. $^{**}P < 0.01$.

Sigma-Aldrich (St. Louis, MO) without further purification. SOD1 antisense oligonucleotide (target sequence 5′-CCG TCG CCC TTC AGC ACG CA-3′) (Patent US 20120214865 A1) and a scrambled negative control oligonucleotide (target sequence 5'-GCC AGC CTA CGA CTC CGC TC-3′) were synthesized by GeneWorks. The scrambled control sequence was generated using an online tool provided by GenScript, USA (https://www.genscript.com/ssl-bin/app/scramble).

Preparation of Oligonucleotide-Loaded CaP Lipid Nanoparticles

Non-loaded or SOD1 antisense oligonucleotide (ASO)-loaded calcium phosphate lipid nanoparticles (CaP-lipid NPs) were prepared as described by Li et al. (Schneider et al., 2012) with minor modifications. The anionic lipid coating CaP core were firstly prepared by a water-in-oil micro-emulsion method. Briefly, 300 μL of 500 mM $CaCl_2$ and 50 μL of 2 mg/mL SOD1 antisense oligonucleotide were added in 15 mL cyclohexane/Igepal CO-520 (70/30 v/v) solution to form a very well dispersed water-in-oil reverse micro-emulsion. To form the phosphate phase, 300 μL of 5 mM Na_2HPO_4 (pH = 9.0), 50 μL of 2 mg/mL SOD1 antisense oligonucleotide and 200 μL of 20 mg/mL dioleoylphosphatydicacid (DOPA) in chloroform were dispersed in another 15 mL cyclohexane/Igepal solution. Then, the phosphate phase was added to the calcium phase in a dropwise manner. The solution was stirred for 20 min to form the CaP cores encapsulating SOD1 ASO. The micro-emulsion was divided equally in to two 50 mL falcon tubes for the purpose of centrifugation. Absolute ethanol (15 mL) was added to each tube before centrifugation at 9,000 × g for 30 min in Heraeus Megafuge X3R (Thermo Scientific, USA). The pellet of CaP cores was washed and rinsed with ethanol 3 times centrifuging as above each time. The pellet was resuspended in 1 mL chloroform and stored in a small glass vial for subsequently lipid coating. The final CaP lipid-coated nanoparticles were prepared by the thin film hydration method. Briefly, to 500 μL of CaP cores, 50 μL 10 mM DOTAP/Cholesterol (1:1) and 50 μL 3 mM DSPE-PEG-2000 were added. For cellular uptake studies, LissRdB-DSPE (12.5 μL of a 16 mM stock solution) was also added. The solution was transferred to a round bottom flask and the chloroform was evaporated off using a rotary evaporator (Büchi, Switzerland). Tris-HCl buffer (1 mL; 5 mM; pH 7.4) was then added into the round bottom flask to rehydrate the lipid film, and the solution was gently sonicated for 5 min. The final CaP-lipid NPs were sterile filtered (0.22 μm) and stored at 4°C for subsequent characterization and biological evaluation.

Particle Characterization

Zeta (ζ) potential of CaP-lipid NPs was measured using a Malvern Zetasizer ZS (Malvern, CA), while size was determined by dynamic light scattering (DLS) using a Malvern Zetasizer APS instrument (Malvern, CA). NanoSight (LM14, NanoSight, UK) was used to calculate particle concentration. Specifically, particles were diluted to between 10^8–10^{10} particles/mL particles (∼1:500 dilution of particles in Milli-Q water) before observing via conventional optical microscope equipped with a CCD camera at room temperature. The particle motion (20–100 particles per field of view) was recorded at 30 frames for 60 s. Particle concentration was then calculated via the NanoSight software (NTA 2.3, UK). To visualize the morphology of CaP-lipid NPs we used transmission electron microscopy (TEM). The nanoparticle suspension was dropped onto a 200 mesh carbon coated copper grid and stained with 1% phosphotungstic acid (PTA). The stained suspension was washed using Milli-Q water and dried at room temperature before observing on a transmission electron microscope (TEM; Gantan, Inc.). TEM was carried out using a JEOL 2010 instrument operating at 200 kV. Bright field images were captured with an objective aperture inserted to enhance diffraction contrast. Images were recorded using a Gatan Orius camera coupled to Gatan's Digital Micrograph software. Oligonucleotide loading was determined using the propidium iodide (PI) staining method whereby the final SOD1 ASO-loaded CaP-lipid NPs were dissolved in an equal volume of lysis buffer (2 mM EDTA and 0.05% Triton X-100 in pH 7.8 Tris buffer) and heated at 65°C for 20 min to release the entrapped SOD1 ASO for fluorometric measurement. To each 100 μL sample, PI (1 μL; 1 μg/μL) was added and fluorescence (RFLU) was measured using a FLUOstar plate reader (BMG

Labtech, Germany) (Ex = 540 nm; Em = 620 nm). The amount of SOD1 ASO loaded into CaP-lipid NPs was then determined by interpolation of RFLU from a SOD1 ASO standard curve. The stability of SOD1-loaded CaP-lipid NPs was assessed via the change in particle size (number peak area) over time measured by DLS. Briefly, 100 μL SOD1 CaP-lipid NP suspension was incubated at 4°C under sterile conditions, and the peak area of particles measured at the following time points 0, 4, 8, 12, 16, 20, 24, and 28 days. For pH-responsive studies, the particles were diluted 10 times (v/v) in PBS (pH 7.4, 6.5, or 5), and incubated for 2 and 4 h at 37°C with constant shanking at 200 RPM. The change in particle size (number peak area) was recorded by DLS. The corresponding anti-dilution ability was also detected to ensure that the CaP-NPs retain their size upon dilution in complete DMEM media supplemented with 10% FCS.

Cell Lines and Culture Conditions

The mouse motor neuron-like cell line (NSC-34), a hybrid cell line produced by fusion of neuroblastoma with mouse motor neuron-enriched primary spinal cord cell (Cashman et al., 1992), was routinely cultured in DMEM/F12 supplemented with 10% (v/v) FBS. The human embryonic kidney (HEK293) cell line, which has been used extensively as an expression tool to study recombinant proteins, was cultured in the same media. Cells were maintained in an incubator at 37°C under a humidified atmosphere containing 5% (v/v) CO_2. When 80% confluence was reached, cells were detached by incubation with 5 mM Trypsin-EDTA and harvested after centrifugation in a Heraeus Megafuge 1.0 (Thermo Scientific, USA) at 1,200 rpm for 5 min at RT. Cells were resuspended in media, and viable cells counted using a hemocytometer and trypan blue staining. Cells were confirmed free of Mycoplasma contamination.

In vitro Cellular Uptake

NSC-34 cells were seeded at 75,000 cells/cm^2 into eight well-chamber slides, and incubated overnight at 37°C before the addition of sterile filtered (0.22 μm) non-loaded CaP-lipid NPs containing LissRdB-DSPE (1:5 or 1:10 v/v). Cells were then incubated for a further 30, 60, or 90 min at 37°C to measure cellular uptake over time. Media was removed and cells were washed in chilled 1 × PBS before being imaged using a Leica TCS SPII laser scanning confocal microscope (Heidelberg, Germany). Internalization was quantified by calculating the mean fluorescence per cell from five images per treatment using ImageJ (Schneider et al., 2012). This represents a minimum of 100 cells analyzed per treatment. To confirm the mechanism of particle uptake, LysoTracker Green DND-26 (Life Technologies, Mulgrave, VIC) was used to stain for acidic compartments, lysosomes and endosomes. NSC-34 cells were incubated at 37°C with Lysotracker Green DND-26 for 30 min, before the addition of LissRdB-DSPE CaP-lipid NPs and incubation for a further 30 min. Imaging of live cells was carried out as described above.

In vitro Transfection and Gene Silencing

HEK293 cells were seeded in 6-well plates at a density of 20 × 10^4 cells/well. After reaching 60% confluency, the cells were treated with SOD1-loaded CaP-lipid NPs, and incubated at 37°C for 72 h. Control treatments included non-loaded CaP-lipid NPs, SOD1 ASO or scrambled negative control with Lipofectamine® 2,000 Transfection Reagent (ThermoFisher Scientific, Rockford, IL, USA) and non-loaded CaP-lipid NPs with SOD1 ASO free in solution. Each treatment delivered an equivalent amount of ASO. Cells were washed twice with chilled PBS and harvested with 0.05% Trypsin-EDTA. Cell lysates were collected after adding RIPA lysis buffer (25 mM pH7.6 Tris-HCl, 150 mM NaCl, 1% Triton X-100, 1% Na-deoxycholate and 1% SDS) supplemented with HALT Protease Inhibitor Cocktail (1% protease inhibitor and 1% EDTA; ThermoFisher Scientific). The final protein extracts were obtained after centrifuging (12,000 × g, 5 min) the aspirated cell lysates. Total protein concentration in the lysate was determined by Bio-RAD Assay according to manufacturer's instructions using a protein assay kit (Micro BCA™ Protein Assay Kit, Pierce).

Total protein (15 μg) was loaded on a pre-cast sodium dodecyl sulfate polyacrylamide gel (Bio-Rad, Gladesville, NSW) and electrophoresed at 150 mV for 45 min. The proteins were transferred to a pure nitrocellulose blotting membrane at 1.0A and 25 V for 30 min using the Bio-Rad Trans-Blot Turbo system. The membrane was blocked with 5% skim milk in TBST on a horizontal shaker overnight at 4°C. The membrane was incubated with 1:1000 sheep polyclonal antibody to SOD1 (ab8866; Abcam, Melbourne, VIC) for 1 h at 37°C on an orbital shaker followed by incubation with HRP-conjugated donkey anti-sheep IgG secondary antibody (AB324P; Merck Millipore, Bayswater, VIC) for 1.5 h at room temperature on a horizontal shaker. Finally, SuperSignal West Pico Chemiluminescent Substrate (ThermoFisher Scientific) was added to the membrane and it was exposed using an Amersham 600RGB Imager (GE).

In vivo Delivery and Visualization of CaP Nanoparticles

Zebrafish (Danio rerio) at an age of 4–6 days post fertilization (dpf) were used for the injection studies. Experimental protocols were approved by Macquarie University Animal Ethics Committee (using zebrafish to understand how the central nervous system responds to neuronal stress and death caused by neurodegenerative diseases; protocol no. 2015/033). Zebrafish were maintained at 28°C in a 13 h light and 11 h dark cycle. Embryos were collected by natural spawning and raised at 28.5°C in E3 and PTU (1-phenyl-2-thiourea) solution according to standard protocols (Westerfield, 2000; Morsch et al., 2015). For *in vivo* studies, sterile filtered non ASO-loaded CaP-lipid NPs containing LissRdB-DSPE (stock, 1:5 or 1:10 v/v) were used for injections into the zebrafish. Borosilicate capillary glass needles with filament (WPI Inc.) were pulled to a resistance between 2 and 7 MΩ and filled with 4 μL of non-loaded CaP-lipid NPs containing LissRdB injection solution. A microinjection apparatus (WPI Inc.; Picospritzer II, General Valve Corporation) was used under control of a stereo dissection microscope (Leica, M165FC) to deliver the NPs into the area of interest (∼1–2 nL per injection). To ensure precise injection anesthetized zebrafish were mounted into low-melting agarose (Fisher-Scientific) at

a concentration of 1–1.5% according to established protocols (Morsch et al., 2017). Control injections were performed with the same dilution of free LissRdB and fish were imaged under the same imaging conditions. Imaging was performed at various time-points (immediately after injections, 2 and 24 h post injection) using a compound microscope (Leica DMI300b), a structured illumination microscope (Zeiss ApoTome), or a confocal microscope (Leica SP5) as described previously (Morsch et al., 2015). To confirm localization of NPs in the zebrafish spinal cord and brain, injections were performed into transgenic lines with fluorescent labeling of neurons [motor neurons: Tg(-3mnx1:TagBFP); pan-neuronal: Tg(isl1:GFP)] (Don et al., 2017). Localization in the brain and vasculature was confirmed with transgenic lines labeling CNS astrocytes [Tg(GFAP:EGFP)] or the entire vasculature [Tg(fli1a:EGFP)], respectively.

Statistical Analysis

Data are presented as the mean ± standard deviation based on triplicate values from two or more independent experiments ($n > 6$). Student's *t*-test or one-way analysis of variance (ANOVA) using a Tukey's multiple comparisons *post-test* were used to determine statistical significance (GraphPad Prism 6 software). $P < 0.05$ was considered statistically significant.

RESULTS

Preparation and Characterization of SOD1-ASO CaP-Lipid Nanoparticles

Previous studies have demonstrated that the stoichiometry of calcium to phosphate can influence the size, encapsulation efficiency, and polydispersity of CaP nanoparticles (Olton et al., 2007; Tang et al., 2015). In this study, the physical properties of SOD1-ASO CaP-lipid NPs were optimized through variation of the Ca/P ratio from 20:1 to 100:1, by changing either the concentration of $CaCl_2$ or Na_2HPO_4. Particle size decreased with increasing concentration of $CaCl_2$ (100–500 mM) (**Table 1**). Increasing the Ca/P ratio to 200:1 and 400:1, with the corresponding concentration of $CaCl_2$ at 1000 and 2000 mM, respectively, lead to poor nanoparticle re-hydration (data not shown). An inverse trend in particle size was obtained when increasing the concentration of Na_2HPO_4 from 5 mM to 25 mM, whilst keeping the concentration of $CaCl_2$ at 500 mM (**Table 1**). The encapsulation efficiency (EE) of ASO was also influenced by the concentration of $CaCl_2$ and Na_2HPO_4. We used an encapsulation method for SOD1-ASO analogous to that reported by Tang et al. where half of the ASO was mixed with the calcium and the phosphate solutions to yield a significantly greater EE than if the ASO was loaded into the calcium or phosphate phases alone (Tang et al., 2015) (Figure S1). The EE decreased from 69.09 ± 2.7 to 47.87 ± 5.6% when increasing the Ca/P ratio from 20:1 to 100:1, respectively. However, the difference in EE between 50:1 and 100:1 Ca/P formulations was not significant as determined by one-way ANOVA (**Table 1**). Conversely, the EE of the SOD1-ASO CaP-NPs peaked at 47.87 ± 2.8% and displayed a declining trend as the content of Na_2HPO_4 increased, when the concentration of $CaCl_2$ was fixed at 500 mM. The EE appeared to be independent of particle concentration. All ASO-loaded particles were slightly negatively charged, likely due to the anionic lipid DOPA in the inner lipid layer and the DSPE-PEG-2000 in the outer lipid layer which has a net negative charge at pH 7.4. Encapsulation of SOD1 ASO into CaP-lipid NPs with a Ca/P ratio of 100:1 significantly decreased the zeta potential from −03 ± 0.03 to −4.9 ± 0.1 mV. Free SOD1 ASO was −50.1 ± 1.8 mV (Figure S2). In light of the optimal particle size, concentration and charge that would be required for crossing the BBB in future studies, we chose the nanoparticle formulation with a Ca/P ratio of 100:1 for all subsequent experiments. Full physicochemical data of this formulation including size, zeta potential, and morphology using TEM is presented in **Figures 1B–D**.

pH Sensitivity of CaP-ASO-Nanoparticles

The disassembly of CaP-lipid NPs at low pH allows for the release of the encapsulated ASO from acidic compartments into the cytoplasm. The lead CaP-lipid NP formulation (Ca/P ratio of 100:1) displayed pH-dependant dissolution after 4 h (**Figure 1E**). No significant difference in particle size was observed when the particles were incubated at 37°C in PBS at pH 7.4, and pH 6.5, however, particle size increased sharply to 84.8 nm 4 h post incubation at pH 5, indicating particle disassembly. The results suggest that CaP-lipid NPs exhibit good pH-responsive release of cargo under acidic conditions with sufficient incubation time. Stability studies found the particles to be stable in Tris buffer over a period of 20 days (Figure S3). With respect to the stability of particles upon dilution, which would occur if using a systemic route of administration, the CaP-lipid NPs exhibited a robust anti-dilution effect. No significant change in particle size was detected when CaP-lipid NPs were diluted 1:10 and 1:50 in complete DMEM supplemented with 10% FCS (Figure S4), indicating the as-prepared CaP-lipid NPs are likely to retain colloidal stability in circulation when delivered systemically in future *in vivo* studies.

CaP-Lipid Nanoparticle Uptake into NSC-34 Motor Neuron-Like Cells Is Time Dependent

It is well known that CaP NPs in the size range of 25–40 nm can be internalized by various cell lines (Li et al., 2012; Tang et al., 2015). Here we sought to determine if our CaP-lipid NPs could be internalized by motor neuron-like cells. Nanoparticles containing LissRdB-DSPE were added to the media of NSC-34 motor neuron-like cells at two dilutions (1:5 or 1:10, total particle concentration $2.69 \times 10^{11}.mL^{-1}$ and $1.35 \times 10^{11}.mL^{-1}$, respectively). The fluorescent properties of LissRdB-DSPE allowed us to monitor uptake of the nanoparticles in live cells. Following incubation for 30–60 min, confocal microscopy confirmed close association of our nanoparticles with NSC-34 cells (**Figures 2A,C**), indicating that nanoparticles were entering the cytoplasm, and accumulating in florescent foci, but were absent in the nucleus (**Figure 2**). There was minimal auto fluorescence from NSC-34 cells (**Figure 2C,** Figure S5), allowing us to easily distinguish, and quantify cellular uptake of fluorescent CaP-lipid NPs. After 30 min,

TABLE 1 | Particle size, Zeta (ζ)-potential, polydispersity index, and encapsulation effiency of SOD1 antisense oligonucleotide calcium phosphate-lipid nanoparticles (SOD1-ASO CaP-lipid NPs) prepared at different $CaCl_2$, and Na_2HPO_4 concentrations.

$CaCl_2$ (mM)	100	250	500	500	500
Na_2HPO_4 (mM)	5	5	5	10	25
CaP Ratio	20/1	50/1	100/1	1/50	1/20
No. Size (nm)	61.0 ± 13.7	52.3 ± 14.7	31.0 ± 2.2	39.9 ± 3.3	50.4 ± 7.6
Zeta Potential (mV)	−6.3 ± 0.2	−7.2 ± 0.2	−4.9 ± 0.1	−6.6 ± 0.51	−6.4 ± 0.25
Polydispersity Index (PDI)	0.2 ± 0.019	0.2 ± 0.005	0.3 ± 0.006	0.2 ± 0.014	0.2 ± 0.007
Encapsulation Effiencicy (%)	69.1 ± 2.7	51.1 ± 2.56	47.9 ± 5.6	34.3 ± 4.15	16.1 ± 2.07
Particle Concentration (per mL)	0.7 E^{11}	2.6 E^{11}	11.9 E^{11}	2.6 E^{11}	5.3 E^{11}

Data is presented as the average ± SD (n = 5).

a proportion of the CaP-lipid NP signal was co-localized to acidic compartments, late endosomes, and lysosomes (Figure S6). The uptake of nanoparticles was dependent upon time, with a significant increase in fluorescence after 90 min of incubation (**Figures 2B,C**).

ASO Delivered by CaP Nanoparticles Decreases SOD1 Levels *in vitro*

SOD1 ASO infused directly into brains via the lateral ventricle has been used in preclinical models, including rats, and Rhesus monkeys (Smith et al., 2006). It has also been shown to significantly reduce SOD1 levels in human fibroblasts after transfection (Smith et al., 2006). Here we compared the *in vitro* efficacy of SOD1 knockdown by free ASO to our SOD1-ASO-CaP-lipid NPs. Due to the ASO being directed toward human SOD1, our knockdown experiments were performed in the HEK293t cell line as they are human derived. Cells were incubated with either empty CaP-lipid NPs, empty CaP-lipid NPs + free (un-encapsulated) SOD1 ASO, or SOD1-ASO-CaP-lipid NPs. Compared to empty nanoparticles alone, there was a small decrease in SOD1 levels after incubation with free SOD1 ASO (**Figure 2D**). Incubation with SOD1 ASO encapsulated within CaP-lipid NPs resulted in an 8× reduction in SOD1 levels, compared with free SOD1 ASO (**Figure 2D**). While naked ASO can enter cells inefficiently and interact with mRNA after infusion into the CNS (Smith et al., 2006), our data shows a significantly increased SOD1 knockdown through our CaP-lipid NP drug delivery system.

In vivo Distribution of CaP-Lipid Nanoparticles in Zebrafish

To test the delivery of the nanoparticles *in vivo* we microinjected small volumes (1–2 nL) of empty CaP-lipid NPs into living zebrafish larvae. Our CaP-lipid NPs were able to diffuse throughout the brain, and spinal cord after direct injection. Injections into the brain, the bloodstream and the spinal cord resulted in characteristic accumulation of speckle-like structures (**Figures 3**, **4**) compared to the free fluorescent reporter (Figure S7). Retro-orbital injections into the zebrafish eye (Pugach et al., 2009) or injections into the posterior cardinal vein, representing systemic routes of delivery, resulted in distinctive uptake of fluorescent NPs into the bloodstream within minutes after injection (**Figures 3A–C**). The particles were detectable with high fluorescence emission within the vasculature of the zebrafish 2 h post administration (Video S1). After injection into the zebrafish brain we observed rapid NP accumulation along the ventricle and throughout the whole brain (**Figure 4B**). Injections directly into the spinal cord of the living zebrafish showed accumulation of the CaP-lipid NPs around neurons and occasionally co-localized with neuronal labeling within 2 h of injection (**Figure 4A**). Altogether, our *in vivo* application via microinjections revealed an efficient delivery method for these nanoparticles in order to test their potential in disease modification in the future.

DISCUSSION

Gene therapies (mostly antisense oligonucleotides; ASO) are in use for a range of disorders where increasing or decreasing the production of a specific gene is of therapeutic benefit. A number of gene therapies are already in clinical use for various cancers, Gaucher's disease and Rheumatoid Arthritis reviewed in Stein and Castanotto (2017). While there are no approved gene therapy products on the market for ALS, multiple oligonucleotide-based compounds are under development for the treatment of brain disorders by direct delivery inside the BBB. Notably, the first new central nervous system (CNS)-targeted oligonucleotide-based drug (nusinersen/Spinraza) was approved by the US Food and Drug Administration (FDA) in late 2016 for spinal muscular atrophy (SMA) in pediatric and adult patients and several compounds are beginning to be trialed in a range of other neurodegenerative diseases (O'Connor and Boulis, 2015; Khorkova and Wahlestedt, 2017). So far there have been three gene therapy clinical trials in ALS based on either expressing growth factors (VEGF and HGF) or ASOs to knockdown SOD1 reviewed in Scarrott et al. (2015). To date, clinical trials in ALS have identified that gene therapies are tolerable, and safe; however more work is needed to understand the specific advantages and disadvantages of the delivery methods. For example, while SOD1 ASOs hold great promise, they are unable to cross the BBB and as such rely on intraventricular or intrathecal infusion, an invasive surgical procedure whereby ASO

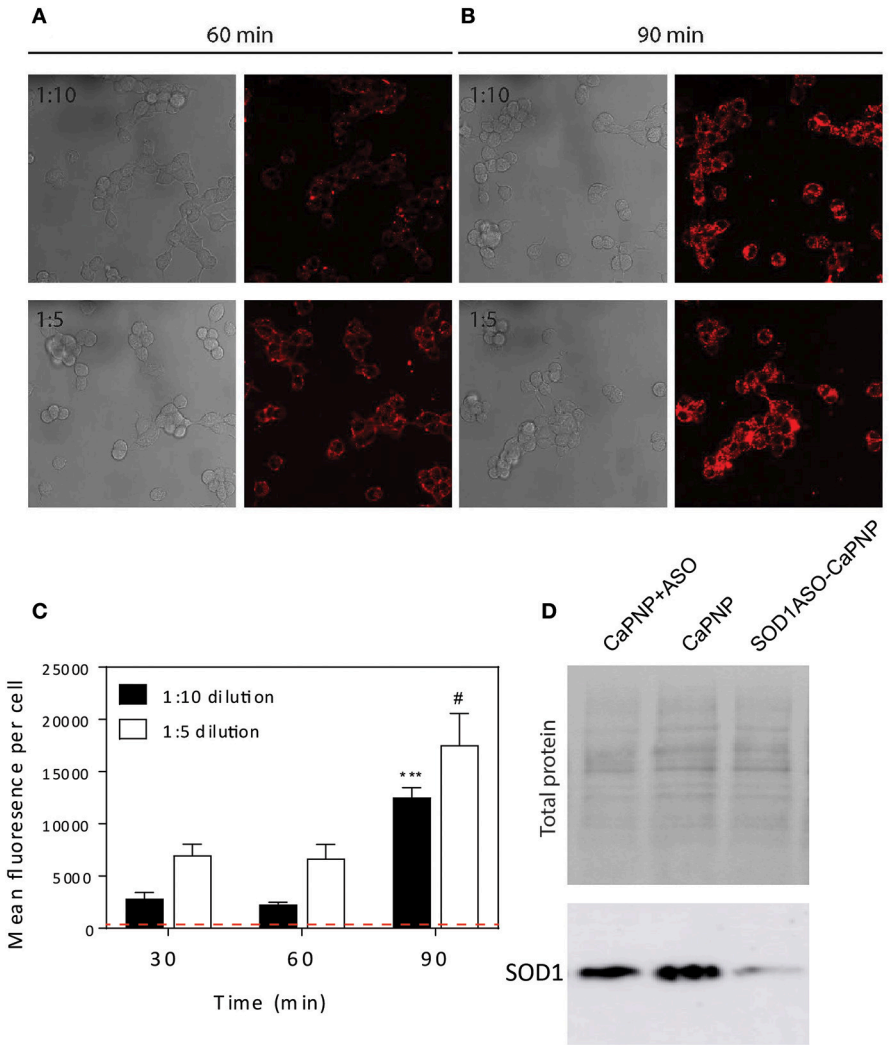

FIGURE 2 | Internalization of CaP-lipid NPs into NSC-34 cells and knockdown of SOD1 protein expression in HEK293 cells. The CaP nanoparticles contained LissRdB-DSPE (Ex = 560 nm; Em = 583 nm) in the outer lipid layer. NSC-34 cells were incubated at 37°C with LissRdB-DSPE CaP-lipid NPs diluted either 1:5 or 1:10 (v/v) for 30, 60 **(A)** and 90 min **(B)**. Images were acquired with a 63 × objective (512 × 512 pixels; physical length 246.03 μm × 246.03 μm). Change in average cell fluorescence over 90 min incubation period **(C)**. Red dotted line represents auto fluorescence of NSC-34 cells for comparison. ***$P < 0.001$ and #$P < 0.05$ signifies significant difference compared to respective 30 min data. HEK293 cells were treated with SOD1-ASO CaP-lipid NPs for 72 h at 37°C (Lane 3). Control treatments included non-loaded CaP-lipid NPs (Lane 2) and non-loaded CaP-lipid NPs with SOD1-ASO free in solution (Lane 1). Controls using Lipofectamine 2000 Transfection Reagent with SOD1-ASO or scrambled negative SOD1 oligonucleotide are not shown here. The change in SOD1 protein expression (16 kDa) was visualized sing SuperSignal West Pico Chemiluminescent Substrate and exposed using an Amersham 600RGB Imager **(D)**.

is delivered directly to the CNS. Furthermore, initial clinical trials involving SOD1 ASO infusion did not reduce SOD1 levels in the CNS at the dose trialed in humans (Scarrott et al., 2015). In this study, we encapsulated SOD1 ASO in an optimized formulation of CaP-lipid NPs and examined their biophysical properties, effectiveness of ASO delivery *in vitro* and biodistribution *in vivo*.

The stoichiometry of calcium to phosphate has been reported to influence the size, encapsulation efficiency (EE), and polydispersity of CaP nanoparticles (Olton et al., 2007; Tang et al., 2015). In this study, the EE decreased as the ratio of Na_2HPO_4 increased. This is likely due to the fact that the ionic crosslinking of negatively charged phosphates of the ASO with positively charged Ca^{2+} ions would decrease if more PO_4^{3-} ions were present during the co-precipitation step (Truong-Le et al., 1999; Uskoković and Uskoković, 2011). In contrast, the size of the particles varied such that the largest particles were observed when prepared using the highest, and lowest ratios of Ca/P, a phenomenon similarly described by Tang et al. (2015). The smallest particles were made using a Ca/P ratio of 100:1. In general, for optimal cell uptake via receptor mediated endocytosis, particles should be smaller than the clatherin coated vesicle size (i.e., <200 nm) (Traub, 2009). Of particular interest here is that small particle size is always preferred for brain-drug delivery due to the rigorous restriction of the BBB

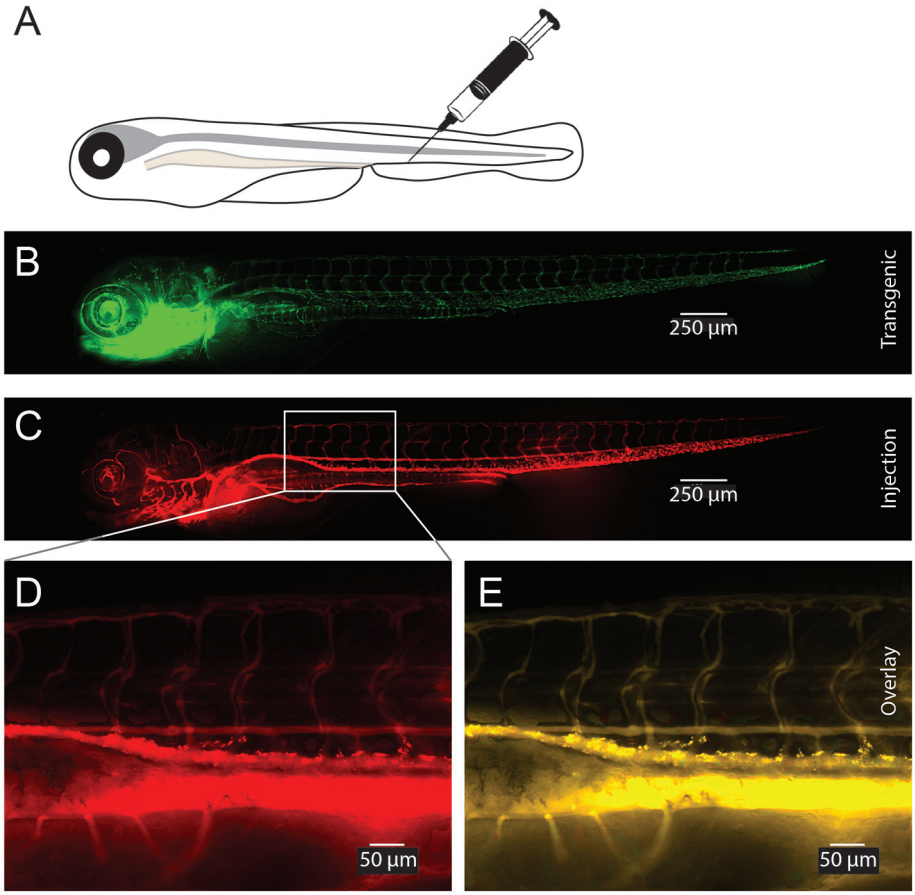

FIGURE 3 | Visualization of CaP-lipid NPs after tail vein injection in transgenic zebrafish. Sterile filtered non ASO-loaded CaP-lipid NPs containing LissRdB-DSPE (stock, 1:5 or 1:10 v/v) was injected into the vein of zebrafish expressing a green fluorescent reporter in their vasculature (Tg(fli1a:EGFP)). Schematic illustration of the route of injection **(A)**. Expression of EGFP in transgenic fish highlighting the blood vessels **(B)**. Visualization of CaP-lipid NP in 6-day-old transgenic zebrafish 2 h after injection **(C)**. Zoomed image of the treated zebrafish from area indicated by white box, showing distribution and accumulation of CaP-lipid NP in and around blood vessels **(D)**. Overlay of transgenic EGFP expression and CaP-lipid NP distribution **(E)**.

(Silva et al., 2017). In addition, Lockman et al. highlights the importance of nanoparticle surface charge (ζ-potential) on the integrity, and crossing of the BBB, with neutral and anionic nanoparticles preferable over cationic particles as colloidal drug carriers to the brain (Lockman et al., 2004). Taken together, the properties of nanoparticle size, charge, encapsulation efficiency, and polydispersity index (PDI) led us to select the SOD1-ASO CaP-lipid NPs with Ca/P molar ratio of 100:1 (500 mM $CaCl_2$ and 5 mM Na_2HPO_4) as our lead formulation.

Previous work has shown that CaP NPs in the size range of 25–40 nm can be efficiently internalized by various cell lines (Li et al., 2012; Tang et al., 2015). Our results suggest that our CaP-lipid NPs (31.0 $\pm$ 2.2 nm) are rapidly taken up by motor neuron-like NSC-34 cells in a time and concentration dependent manner. At least partial overlap with a lysotracker dye suggests trafficking of the CaP-lipid NPs to acidic compartments, likely late endosomes and lysosomes (Liu et al., 2014). Our optimized CaP-lipid NPs were stable in solutions of neutral pH for at least 20 days, but broke down at pH 5 in as little as 4 h. Once a CaP NP has dissolved it is thought that the released calcium and phosphate ions cause changes in osmotic pressure across the lysosomal membrane causing rupture of the vesicle (Neumann et al., 2009) and release of the ASO. This principle has for many years been used to transfect mammalian cells with plasmid DNA. In this study, the efficiency of ASO delivery in cell culture was increased through CaP-lipid NP encapsulation, and resulted in significant reduction in SOD1 protein expression. This is likely due to the pH sensitivity, lysosomal membrane rupture, and cytoplasmic delivery of ASO. Importantly, CaP transfection methods have been successfully used on primary neurons for decades (Dudek et al., 1997), suggesting that CaP-lipid NPs are a viable system for the delivery of DNA/RNA to neurons in the brain. CaP has primarily been used as a transfection agent because it is inexpensive and easy to use, biocompatible, bioactive, and can alter the osmotic properties of the lysosome. While there have been reports that transfection with CaP can cause large-scale lysosome rupture and subsequent necrosis (Liu et al., 2014), packaging CaP into nanoparticles

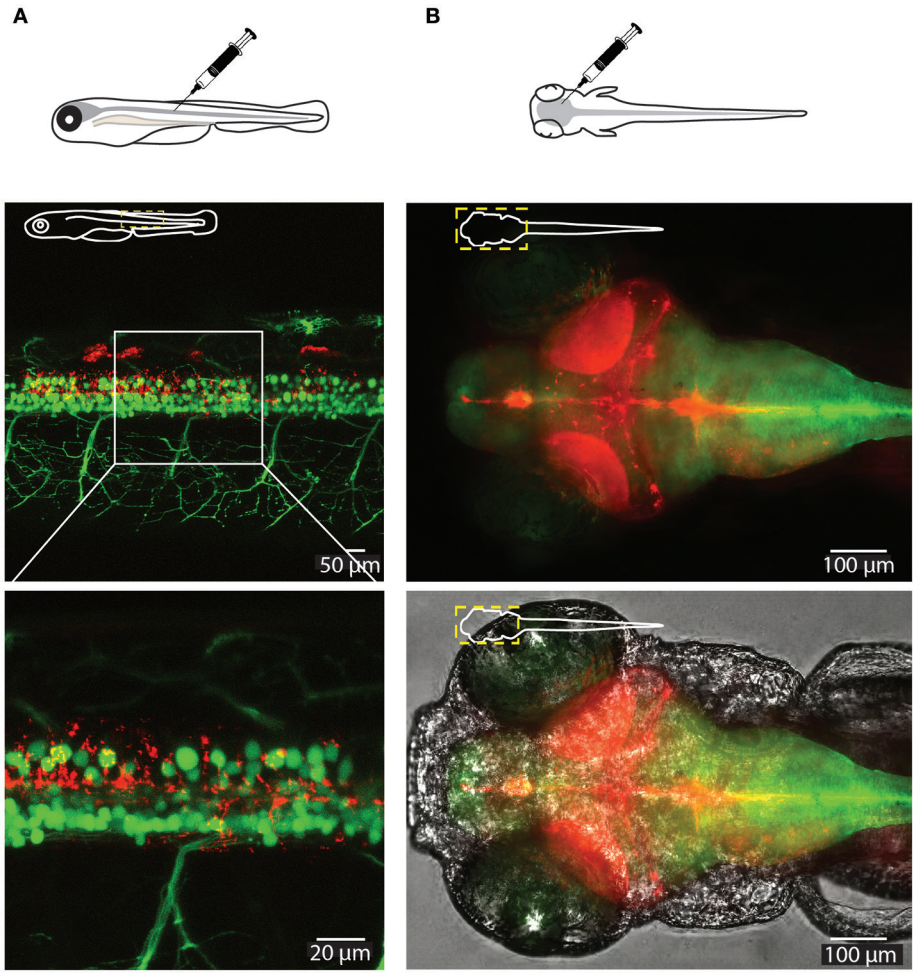

FIGURE 4 | Visualization of CaP-lipid NPs and neurons in the spinal cord and brain of a 6-dpf zebrafish. Sterile filtered non ASO-loaded CaP-lipid NPs containing LissRdB-DSPE (red) were micro injected into the zebrafish spinal cord **(A)** and brain **(B)**. **(A)** Visualization of CaP- lipid NPs containing LissRdB-DSPE (red; injections) within the spinal cord neurons (green; transgenic expression) of a 6-day-old transgenic zebrafish. Zoomed image of the treated zebrafish from area indicated by white box, showing distribution of the CaP-lipid NPs within GFP-expressing spinal cord neurons. **(B)** Expression of brain-injected CaP-lipid NPs (red) in a transgenic zebrafish expressing astrocyte-specific GFP [green; Tg(GFAP:GFP)] to highlight the brain-specific delivery of these particles. The bottom image overlays the bright-field channel for better visualization of the CNS. The schematic inserts in panels depict the orientation of the fish and outline the presented area.

suppresses this toxicity (Neumann et al., 2009), making it safe for intracellular delivery. Moreover, CaP NPs are thought to have a high loading capacity when compared to other inorganic particles, and provide several advantages over viral delivery systems, including low immunogenicity, and the ability to switch off or modify therapeutic dose.

Some genetic lesions associated with ALS result in toxic gain-of-function and have been the traditional targets for genetic therapeutic strategies (Foust et al., 2013). In particular, the largest known genetic causes of ALS, mutations in SOD1, and C9ORF72, are both thought to be gain of toxic function mechanisms, making genetic knockdown a relevant, and important avenue for research. Yet this strategy has achieved only modest outcomes to date in preclinical development. For example, knockdown of SOD1 using viral delivered shRNA in the $SOD1^{G93A}$ ALS mouse model found only 8% of neurons had been successfully targeted in 3 week old mice (Foust et al., 2013). Non-viral vectors are therefore gaining traction as alternative delivery systems due to their potential safety advantages, ease of manufacture, customization, BBB targeting potential, and ability to deliver all nucleic acid varieties [reviewed in Niidome and Huang (2002) and Pack et al. (2005)]. The BBB presents both a physical and electrostatic barrier to limit brain permeation of therapeutics. Previous work has demonstrated that nanoparticles can overcome the physical barrier and deliver genes to the nervous system including neurons, by utilizing transcytosis pathways when functionalized with various ligands including apoE fragments, folate, transferrin or anti-transferrin receptor (anti-TfR) antibodies (Mc Carthy et al., 2015). This surface functionalization could also be applied to CaP-lipid NPs and has been successfully demonstrated after i.v. administration in rodent models (Shi and Pardridge, 2000; Shi et al., 2001; da Cruz

et al., 2005; Re et al., 2011; Qiao et al., 2012). In ALS preclinical models, the only nanoparticle so far used has been glutathione functionalized liposomes that targeted methylprednisolone (a glucocorticoid) across the BBB, and increased its availability in the CNS (Evans et al., 2014). Two of the main reasons for a lack of effective neuroprotective therapy for ALS can be attributed to a number of key challenges including ineffective targeting and delivery of therapeutic agents specifically to the diseased CNS site and/or cell type of interest (Scarrott et al., 2015). However, targeted delivery across the BBB and concomitant internalization by cells of the brain, in particular motor neurons using such nanotechnology has so far not been developed for ALS.

Zebrafish are emerging as a powerful model organism to study neurodegenerative diseases. This is primarily due to features such as experimentally feasible (short) developmental life time, external fertilization, well established methods of transgenesis, and importantly transparent bodies that allow imaging of the living nervous system (Westerfield, 2000; Morsch et al., 2017). In the context of ALS, zebrafish models have been used to study familial forms, and recapitulate some aspects of ALS pathology, including loss of motor neurons (Hogan et al., 2017), making them a useful system for gene therapy testing. In addition, the ability to generate compound transgenic zebrafish permits strategies to track and follow different cell types and different pathogenic proteins concomitantly, making them a valuable addition to current model systems for study of ALS. Previous work has shown the utility of the fluorescently labeled cell populations and simultaneous delivery of therapeutic cargo encapsulated in fluorescent nanoparticles (Fenaroli et al., 2014). The work presented here demonstrates that our CaP-lipid NPs circulate freely within the bloodstream following systemic delivery in an experimental zebrafish model and were detectable immediately after and up to 29 h post injection. This prolonged circulation time is owed to the hydrophilic nature of PEG within our formulation. PEGylation of particles is well known to create a protective water shell around the particle thereby protecting it against enzymatic degradation, decreasing clearance by the mononuclear phagocyte system and retarding renal clearance, increasing the residence time in the bloodstream (Suk et al., 2016). Finally, our CaP-lipid NPs were able to diffuse throughout the brain and spinal cord after direct injection, demonstrating the usefulness of zebrafish in the study of nanoparticle delivery of therapeutic cargo in ALS. It will be interesting to test the efficacy of our ASO encapsulated CaP-lipid NPs in zebrafish and mammalian models of SOD1 ALS in the future. Taken together, our data suggest that CaP-lipid NPs establish a useful tool to increase gene therapy delivery, and thus efficacy in ALS.

AUTHOR CONTRIBUTIONS

JY, KV, DS, MM, LC, CW, and RC contributed to the conception or design of the work and/or purchased consumables. JY, KV, CW, LC, and MM acquired, analyzed and interpreted data. JY, KV, DS, MM, LC, CW, and RC drafted the work and/or revised it critically for important intellectual content. All Authors have approved the final version to be published and agree to be accountable for all aspects of the work.

FUNDING

Funding from the US Department of Defense (AL150057) and Motor Neuron Disease Research Institute of Australia (Cunningham Family MND Research Grant, GIA1656) is gratefully acknowledged. JY is the recipient of an NHMRC Career Development Fellowship (APP1084144).

ACKNOWLEDGMENTS

We thank Mr. Tony Romeo and Dr. David Mitchell (University of Wollongong, Electron Microscopy Unit) for performing TEM imaging.

SUPPLEMENTARY MATERIAL

The Supplementary Material for this article can be found online at: http://journal.frontiersin.org/article/10.3389/fnins.2017.00476/full#supplementary-material

REFERENCES

Arnesano, F., Banci, L., Bertini, I., Martinelli, M., Furukawa, Y., and O'Halloran, T. V. (2004). The unusually stable quaternary structure of human Cu,Zn-superoxide dismutase 1 is controlled by both metal occupancy and disulfide status. *J. Biol. Chem.* 279, 47998–48003. doi: 10.1074/jbc.M406021200

Bourassa, M. W., Brown, H. H., Borchelt, D. R., Vogt, S., and Miller, L. M. (2014). Metal-deficient aggregates and diminished copper found in cells expressing SOD1 mutations that cause ALS. *Front. Aging Neurosci.* 6:110. doi: 10.3389/fnagi.2014.00110

Brettschneider, J., Arai, K., Del Tredici, K., Toledo, J. B., Robinson, J. L., Lee, E. B., et al. (2014). TDP-43 pathology and neuronal loss in amyotrophic lateral sclerosis spinal cord. *Acta Neuropathol.* 128, 423–437. doi: 10.1007/s00401-014-1299-6

Cashman, N. R., Durham, H. D., Blusztajn, J. K., Oda, K., Tabira, T., Antel, J. P. et al. (1992). Neuroblastoma x spinal cord (NSC) hybrid cell lines resemble developing motor neurons. *Dev. Dyn.* 194, 209–221. doi: 10.1002/aja.1001940306

da Cruz, M. T., Cardoso, A. L., de Almeida, L. P., Simoes, S., and de Lima, M. C. (2005). Tf-lipoplex-mediated NGF gene transfer to the CNS: neuronal protection and recovery in an excitotoxic model of brain injury. *Gene Ther.* 12, 1242–1252. doi: 10.1038/sj.gt.3302516

Don, E. K., Isabel, F., Andrew, P. B., Thomas, E. H., Marco Morsch, E. H., Alison Hogan, S. C., et al. (2017). A Tol2 gateway-compatible toolbox for the study of the nervous system and neurodegenerative disease. *Zebrafish* 14, 69–72. doi: 10.1089/zeb.2016.1321

Dudek, H., Datta, S. R., Franke, T. F., Birnbaum, M. J., Yao, R., Greenberg, M. E., et al. (1997). Regulation of neuronal survival by the serine-threonine protein kinase Akt. *Science* 275, 661–665. doi: 10.1126/science.275.5300.661

Evans, M. C., Gaillard, P. J., de Boer, M., Appeldoorn, C., Dorland, R., Stolp, H. B., et al. (2014). CNS-targeted glucocorticoid reduces pathology in mouse model of amyotrophic lateral sclerosis. *Acta Neuropathol. Commun.* 2:66. doi: 10.1186/2051-5960-2-66

Fenaroli, F., David Westmoreland, J. B., Terje Kolstad, F. M. S., van der Vaart, M. A., Ulanova, L., Roos, N., et al. (2014). Nanoparticles as

drug delivery system against tuberculosis in zebrafish embryos: direct visualization and treatment. *ACS Nano* 8, 7014–7026. doi: 10.1021/nn5019126

Foust, K. D., Salazar, D. L., Likhite, S., Ferraiuolo, L., Ditsworth, D., Kaspar, B. K., et al. (2013). Therapeutic AAV9-mediated suppression of mutant SOD1 slows disease progression and extends survival in models of inherited ALS. *Mol. Ther.* 21, 2148–2159. doi: 10.1038/mt.2013.211

Grad, L. I., Yerbury, J. J., Turner, B. J., Guest, W. C., Pokrishevsky, E., O'Neill, M. A., et al. (2014). Intercellular propagated misfolding of wild-type Cu/Zn superoxide dismutase occurs via exosome-dependent and -independent mechanisms. *Proc. Natl. Acad. Sci. U.S.A.* 111, 3620–3625. doi: 10.1073/pnas.1312245111

Hogan, A. L., Don, E. K., Rayner, S. L., Lee, A., Laird, A. S., Watchon, M., et al. (2017). Expression of ALS/FTD-linked mutant CCNF in zebrafish leads to increased cell death in the spinal cord and an aberrant motor phenotype. *Hum. Mol. Genet.* 26, 2616–2626. doi: 10.1093/hmg/ddx136

Khorkova, O., and Wahlestedt, C. (2017). Oligonucleotide therapies for disorders of the nervous system. *Nat. Biotechnol.* 35, 249–263. doi: 10.1038/nbt.3784

Li, J., Yang, Y., and Huang, L. (2012). Calcium phosphate nanoparticles with an asymmetric lipid bilayer coating for siRNA delivery to the tumor. *J. Control. Release* 158, 108–114. doi: 10.1016/j.jconrel.2011.10.020

Liu, Z., Xiao, Y., Chen, W., Wang, Y., Wang, B., Wang, G., et al. (2014). Calcium phosphate nanoparticles primarily induce cell necrosis through lysosomal rupture: the origination of material cytotoxicity. *J. Mater. Chem. B* 2, 3480–3489. doi: 10.1039/c4tb00056k

Lockman, P. R., Koziara, J. M., Mumper, R. J., and Allen, D. D. (2004). Nanoparticle surface charges alter blood-brain barrier integrity and permeability. *J. Drug Target.* 12, 635–641. doi: 10.1080/10611860400015936

Majoor-Krakauer, D., Willems, P. J., and Hofman, A. (2003). Genetic epidemiology of amyotrophic lateral sclerosis. *Clin. Genet.* 63, 83–101. doi: 10.1046/j.0009-9163.2002.00001.x

Mc Carthy, D. J., Malhotra, M., O'Mahony, A. M., Cryan, J. F., and O'Driscoll, C. M. (2015). Nanoparticles and the blood-brain barrier: advancing from *in-vitro* models towards therapeutic significance. *Pharm. Res.* 32, 1161–1185. doi: 10.1007/s11095-014-1545-6

Miller, T. M., Pestronk, A., David, W., Rothstein, J., Simpson, E., Appel, S. H., et al. (2013). An antisense oligonucleotide against SOD1 delivered intrathecally for patients with SOD1 familial amyotrophic lateral sclerosis: a phase 1, randomised, first-in-man study. *Lancet Neurol.* 12, 435–442. doi: 10.1016/S1474-4422(13)70061-9

Morsch, M., Radford, R. A. W., Don, E. K., Lee, A., Hortle, E., Cole, N. J., et al. (2017). Triggering cell stress and death using conventional UV laser confocal microscopy. *J. Vis. Exp.* e54983. doi: 10.3791/54983

Morsch, M., Radford, R., Lee, A., Don, E. K., Badrock, A. P., Chung, R., et al. (2015). *In vivo* characterization of microglial engulfment of dying neurons in the zebrafish spinal cord. *Front. Cell. Neurosci.* 9:321. doi: 10.3389/fncel.2015.00321

Neumann, S., Kovtun, A., Dietzel, I. D., Epple, M., and Heumann, R. (2009). The use of size-defined DNA-functionalized calcium phosphate nanoparticles to minimise intracellular calcium disturbance during transfection. *Biomaterials* 30, 6794–6802. doi: 10.1016/j.biomaterials.2009.08.043

Niidome, T., and Huang, L. (2002). Gene therapy progress and prospects: nonviral vectors. *Gene Ther.* 9, 1647–1652. doi: 10.1038/sj.gt.3301923

O'Connor, D. M., and Boulis, N. M. (2015). Gene therapy for neurodegenerative diseases. *Trends Mol. Med.* 21, 504–512. doi: 10.1016/j.molmed.2015.06.001

Olton, D., Li, J., Wilson, M., E., Rogers, T., Close, J., Sfeir, C., et al. (2007). Nanostructured calcium phosphates (NanoCaPs) for non-viral gene delivery: influence of the synthesis parameters on transfection efficiency. *Biomaterials* 28, 1267–1279. doi: 10.1016/j.biomaterials.2006.10.026

Pack, D. W., Hoffman, A. S., Pun, S., and Stayton, P. S. (2005). Design and development of polymers for gene delivery. *Nat. Rev. Drug Discov.* 4, 581–593. doi: 10.1038/nrd1775

Perry, J. J., Shin, D. S., Getzoff, E. D., and Tainer, J. A. (2010). The structural biochemistry of the superoxide dismutases. *Biochim. Biophys. Acta* 1804, 245–262. doi: 10.1016/j.bbapap.2009.11.004

Pugach, E. K., Li, P., White, R., and Zon, L. (2009). Retro-orbital injection in adult zebrafish. *J. Vis. Exp.* e1645. doi: 10.3791/1645

Qiao, R., Jia, Q., Huwel, S., Xia, R., Liu, T., Gao, F., et al. (2012). Receptor-mediated delivery of magnetic nanoparticles across the blood-brain barrier. *ACS Nano* 6, 3304–3310. doi: 10.1021/nn300240p

Re, F., Cambianica, I., Zona, C., Sesana, S., Gregori, M., Rigolio, R., et al. (2011). Functionalization of liposomes with ApoE-derived peptides at different density affects cellular uptake and drug transport across a blood-brain barrier model. *Nanomedicine* 7, 551–559. doi: 10.1016/j.nano.2011.05.004

Renton, A. E., Chio, A., and Traynor, B. J. (2014). State of play in amyotrophic lateral sclerosis genetics. *Nat. Neurosci.* 17, 17–23. doi: 10.1038/nn.3584

Rosen, D. R., Siddique, T., Patterson, D., Figlewicz, D., A., Sapp, P., Hentati, A., et al. (1993). Mutations in Cu/Zn superoxide dismutase gene are associated with familial amyotrophic lateral sclerosis. *Nature* 362, 59–62. doi: 10.1038/362059a0

Scarrott, J. M., Herranz-Martin, S., Alrafiah, A. R., Shaw, P. J., and Azzouz, M. (2015). Current developments in gene therapy for amyotrophic lateral sclerosis. *Expert Opin. Biol. Ther.* 15, 935–947. doi: 10.1517/14712598.2015.1044894

Schneider, C. A., Rasband, W. S., and Eliceiri, K. W. (2012). NIH Image to ImageJ: 25 years of image analysis. *Nat. Methods* 9:671. doi: 10.1038/nmeth.2089

Shi, N., and Pardridge, W. M. (2000). Noninvasive gene targeting to the brain. *Proc. Natl. Acad. Sci. U.S.A.* 97, 7567–7572. doi: 10.1073/pnas.130187497

Shi, N., Zhang, Y., Zhu, C., Boado, R. J., and Pardridge, W. M. (2001). Brain-specific expression of an exogenous gene after i.v. administration. *Proc. Natl. Acad. Sci. U.S.A.* 98, 12754–12759. doi: 10.1073/pnas.221450098

Silva, A. D., Aguirre-Cruz, L., Guevara, J., and Ortiz-Islas, E. (2017). Nanobiomaterials' applications in neurodegenerative diseases. *J. Biomater. Appl.* 31:2. doi: 10.1177/0885328216659032

Smith, R. A., Miller, T. M., Yamanaka, K., Monia, B. P., Condon, T. P., Hung, G., et al. (2006). Antisense oligonucleotide therapy for neurodegenerative disease. *J. Clin. Invest.* 116, 2290–2296. doi: 10.1172/JCI25424

Soon, C. P., Donnelly, P. S., Turner, B. J., Hung, L. W., Crouch, P. J., Sherratt, N. A., et al. (2011). Diacetylbis(N-methylthiosemicarbazonato) copper(II) (CuII(atsm)) protects against peroxynitrite-induced nitrosative damage and prolongs survival in amyotrophic lateral sclerosis mouse model. *J. Biol. Chem.* 286, 44035–44044. doi: 10.1074/jbc.M111.274407

Soppimath, K. S., Tejraj Aminabhavi, M., Anandrao Kulkarni, R., and Walter Rudzinski, E. (2001). Biodegradable polymeric nanoparticles as drug delivery devices. *J. Control. Release* 70, 1–20. doi: 10.1016/S0168-3659(00)00339-4

Stein, C. A., and Castanotto, D. (2017). FDA-approved oligonucleotide therapies in 2017. *Mol. Ther.* 25, 1069–1075. doi: 10.1016/j.ymthe.2017.03.023

Suk, J. S., Qingguo, X., Namho Kim, J. H., and Laura Ensign, M. (2016). PEGylation as a strategy for improving nanoparticle-based drug and gene delivery. *Adv. Drug Deliv. Rev.* 99, 28–51. doi: 10.1016/j.addr.2015.09.012

Tang, J., Li, L., Howard, C. B., Mahler, S. M., Huang, L., and Xu, Z. P. (2015). Preparation of optimized lipid-coated calcium phosphate nanoparticles for enhanced *in vitro* gene delivery to breast cancer cells. *J. Mater. Chem. B Mater. Biol. Med.* 3, 6805–6812. doi: 10.1039/C5TB00912J

Traub, L. M. (2009). Clathrin couture: fashioning distinctive membrane coats at the cell surface. *PLoS Biol.* 7:e1000192. doi: 10.1371/journal.pbio.1000192

Truong-Le, V. L., Walsh, S. M., Schweibert, E., Mao, H. Q., Guggino, W. B., Leong, K. W., et al. (1999). Gene transfer by DNA-gelatin nanospheres. *Arch. Biochem. Biophys.* 361, 47–56. doi: 10.1006/abbi.1998.0975

Uskoković, V., and Uskoković, D. P. (2011). Nanosized hydroxyapatite and other calcium phosphates: chemistry of formation and application as drug and

gene delivery agents. *J. Biomed. Mater. Res.* 96, 152–191. doi: 10.1002/jbm.b.31746

Vieira, D. B., and Gamarra, L. F. G. (2016). Getting into the brain: liposome-based strategies for effective drug delivery across the blood–brain barrier. *Int. J. Nanomed.* 11, 5381–5414. doi: 10.2147/IJN.S117210

Westerfield, M. (2000). *The Zebrafish Book. A Guide for the Laboratory Use of Zebrafish (Danio rerio), 4th Edn*. Eugene, OR: University of Oregon Press.

Zeineddine, R., Pundavela, J. F., Corcoran, L., Stewart, E. M., Do-Ha, D., Bax, M., et al. (2015). SOD1 protein aggregates stimulate macropinocytosis in neurons to facilitate their propagation. *Mol. Neurodegener.* 10:57. doi: 10.1186/s13024-015-0053-4

Conflict of Interest Statement: The authors declare that the research was conducted in the absence of any commercial or financial relationships that could be construed as a potential conflict of interest.

frontiers in Molecular Neuroscience

ORIGINAL RESEARCH
published: 12 December 2017
doi: 10.3389/fnmol.2017.00409

Toll-Like Receptor 4 Mediates Methamphetamine-Induced Neuroinflammation through Caspase-11 Signaling Pathway in Astrocytes

Si-Hao Du[1†], Dong-Fang Qiao[1†], Chuan-Xiang Chen[1], Si Chen[1], Chao Liu[2], Zhoumeng Lin[3], Huijun Wang[1] and Wei-Bing Xie[1*]*

[1]School of Forensic Medicine, Southern Medical University, Guangzhou, China, [2]Guangzhou Forensic Science Institute, Guangzhou, China, [3]Department of Anatomy and Physiology, Institute of Computational Comparative Medicine (ICCM), College of Veterinary Medicine, Kansas State University, Manhattan, KS, United States

OPEN ACCESS

Edited by:
Sandro Alves,
Brainvectis Therapeutics, France

Reviewed by:
Jee Hyun Kim,
Florey Institute of Neuroscience and Mental Health, Australia
Françoise Piguet,
UMR7104 Institut de Génétique et de Biologie Moléculaire et Cellulaire (IGBMC), France

***Correspondence:**
Huijun Wang
hjwang@smu.edu.cn
Wei-Bing Xie
xwb@smu.edu.cn

[†]These authors have contributed equally to this work.

Received: 12 September 2017
Accepted: 27 November 2017
Published: 12 December 2017

Citation:
Du S-H, Qiao D-F, Chen C-X, Chen S, Liu C, Lin Z, Wang H and Xie W-B (2017) Toll-Like Receptor 4 Mediates Methamphetamine-Induced Neuroinflammation through Caspase-11 Signaling Pathway in Astrocytes.
Front. Mol. Neurosci. 10:409.
doi: 10.3389/fnmol.2017.00409

Methamphetamine (METH) is an amphetamine-typed stimulant drug that is increasingly being abused worldwide. Previous studies have shown that METH toxicity is systemic, especially targeting dopaminergic neurons in the central nervous system (CNS). However, the role of neuroinflammation in METH neurotoxicity remains unclear. We hypothesized that Toll-like receptor 4 (TLR4) and Caspase-11 are involved in METH-induced astrocyte-related neuroinflammation. We tested our hypothesis by examining the changes of TLR4 and Caspase-11 protein expression in primary cultured C57BL/6 mouse astrocytes and in the midbrain and striatum of mice exposed to METH with western blot and double immunofluorescence labeling. We also determined the effects of blocking Caspase-11 expression with wedelolactone (a specific inhibitor of Caspase-11) or siRNA on METH-induced neuroinflammation in astrocytes. Furthermore, we determined the effects of blocking TLR4 expression with TAK-242 (a specific inhibitor of TLR4) or siRNA on METH-induced neuroinflammation in astrocytes. METH exposure increased Caspase-11 and TLR4 expression both *in vitro* and *in vivo*, with the effects *in vitro* being dose-dependent. Inhibition of Caspase-11 expression with either wedelolactone or siRNAs reduced the expression of inflammasome NLRP3 and pro-inflammatory cytokines. In addition, blocking TLR4 expression inhibited METH-induced activation of NF-κB and Caspase-11 *in vitro* and *in vivo*, suggesting that TLR4-Caspase-11 pathway is involved in METH-induced neuroinflammation. These

Abbreviations: ASC, apoptosis-associated speck-like protein containing CARD; CNS, central nervous system; DAB, 3,3′-diaminobenzidine; DAPI, 4′,6′-diamidino-2-phenylindole; DMEM, Dulbecco's modified Eagle's medium; FBS, Fetal bovine serum; IFN, Interferon; IL, Interleukin; IRAK, Interleukin-1 receptor-associated kinase; LPS, lipopolysaccharides; METH, Methamphetamine; NLRP3, nucleotide-binding oligomerization domain-like receptor family pyrin domain containing 3; PVDF, Polyvinylidenedifluoride; SDS-PAGE, Sodium dodecyl sulfate polyacrylamide gel; TLR4, Toll-like receptor 4; TRAM, TRIF-related adaptor molecule; Wed, Wedelolactone.

results indicate that Caspase-11 and TLR4 play an important role in METH-induced neuroinflammation and may be potential gene targets for therapeutics in METH-caused neurotoxicity.

Keywords: methamphetamine, Caspase-11, Toll-like receptor 4 (TLR4), neuroinflammation, inflammasome, astrocyte

BACKGROUND

Methamphetamine (METH) is one of the most widely abused drugs and the most commonly synthesized illegal drug worldwide (Kiyatkin and Sharma, 2009; Cai et al., 2016; Li et al., 2017). A major target of METH is the central nervous system (CNS), especially the central dopaminergic circuitries (Carmena et al., 2015; Huang et al., 2015; Chen et al., 2016; Mendieta et al., 2016). Previous studies have demonstrated that short-term exposure to METH can cause widespread brain damage and long-term exposure to METH can lead to CNS neurodegeneration (Wu et al., 2014; Andres et al., 2015). Accumulating evidence suggests that METH exposure can alter the functions of glial cells and activate astrocytes (Granado et al., 2011; Loftis and Janowsky, 2014; Fernandes et al., 2016; Bortell et al., 2017). Activated astrocytes play important roles in METH-induced neurotoxicity (Hebert and O'Callaghan, 2000; Abdul Muneer et al., 2011; Carmena et al., 2015). However, the underlying mechanisms of how astrocytes mediate METH-induced neurotoxicity remain to be elucidated.

Astrocytes represent the largest population of glial cells in the CNS and have a variety of functions, including maintenance of brain homeostasis, storage of energy substrates, and as a major component of the blood-brain barrier and the synapses (Liu et al., 2017; Singh and Abraham, 2017). Neuroinflammation is a process mediated by microglia, astrocytes, neurons, T cells, neutrophils, mast cells and inflammatory mediators released from these cells (Shabab et al., 2017). Astrocytes can mediate neuroinflammation by secreting specific signaling molecules, such as pro-inflammatory cytokines and anti-inflammatory cytokines, including interleukin (IL), interferon (IFN), chemokines and tumor necrosis factor (Whitney et al., 2009; Granado et al., 2011). Activation of microglia and astrocytes is initially a normal compensatory neuroinflammatory response to brain injury, but excessive neuroinflammation can lead to further brain damage (Whitney et al., 2009; Kempuraj et al., 2016; Pal et al., 2016).

Toll-like receptors (TLRs) are a class of immunological pattern recognition receptors (Krawczyk-Michalak et al., 2008; Shirjang et al., 2017). In mammals, 13 TLRs have been identified that can recognize different endogenous ligands or exogenous pathogens from protozoa, bacteria, fungi or viruses. Toll-like receptor 4 (TLR4) is one of the most widely studied receptors in the TLR family because it is the only one that can active both of the following two pathways: Myd88-dependent and non Myd88-dependent pathways (Billod et al., 2016). In the Myd88-dependent pathway, Myd88 induces the downstream tumor necrosis factor receptor-associated factor 6, interleukin-1 receptor-associated kinase (IRAK) activation and then induces NF-κB activation, thereby mediating inflammatory and pro-inflammatory cytokine production (Shen et al., 2016). In the non Myd88-dependent pathway, TLR4 triggers the activation of the TRIF-related adaptor molecule (TRAM), followed by the activation of interferon regulatory factor 3, which induces the production of IFN-γ. In the later inflammatory response process, TRAM can also activate NF-κB, inducing inflammatory factor expression and activation (Brempelis et al., 2017; Yan et al., 2017).

Caspase-11 is a member of the caspase family, which is a group of structurally related cysteine proteases (Roberts and Yilmaz, 2015). Caspase-11 plays an important role in apoptosis, inflammation and cell migration (Coutermarsh-Ott et al., 2016; Zanoni et al., 2016). In our previous study, we found that neuronal apoptosis in METH-treated rats was associated with Caspase-11 activation (Huang et al., 2015). Other studies have shown that Caspase-11 can be induced by lipopolysaccharides (LPS) secreted by gram-negative bacteria, leading to inflammation, and this reaction is closely related to the activation of Caspase-1 (Kayagaki et al., 2015). Caspase-1 and inflammasome adaptor protein apoptosis-associated speck-like protein containing CARD (ASC) together participate in the assembly of inflammasomes, and mediate the expression of downstream inflammatory factors. Previous studies have shown that the activation of inflammasome nucleotide-binding oligomerization domain-like receptor family pyrin domain containing 3 (NLRP3) is mediated by the activation of Caspase-1, which promotes the pro-inflammatory cytokine secretion (Meng et al., 2014; Zhu et al., 2016). Therefore, specific inhibition of inflammasome NLRP3 activation pathway maybe is a potential strategy to the therapeutic treatment of related diseases. Inflammatory cytokines and inflammation play an important role in many diseases. Our previous work and other studies have confirmed that METH induces dopamine neuronal damage through apoptosis, autophagy, oxidative stress and other mechanisms (Krasnova and Cadet, 2009; Abdul Muneer et al., 2011; Qiao et al., 2014; Wu et al., 2014). However, the role of glial cells and its possible molecular mechanisms in METH neurotoxicity are still unclear, which is important and warrants further study.

The objective of this study was to investigate the role of TLR4 and Caspase-11 in METH-induced neuroinflammation. To this end, we determined changes of TLR4 and Caspase-11 expression and the levels of inflammatory factors in primary cultured astrocytes, and the corpus striatum and midbrain of mice exposed to METH. We found that METH exposure increased Caspase-11 and TLR4 expression; inhibition of Caspase-11 or TLR4 reduced Caspase-1 and ASC activation and pro-inflammatory cytokine production *in vitro* and *in vivo*. Our

results indicate that both TLR4 and Caspase-11 play a crucial role in METH-induced neuroinflammation and these proteins may be potential therapeutic targets for neuronal injury caused by METH.

MATERIALS AND METHODS

Materials

Cell culture reagents, including Dulbecco's modified Eagle's medium/F12 (DMEM/F12) medium, fetal bovine serum (FBS) and trypsin were purchased from Gibco (Carlsbad, CA, USA). METH (>99% purity) was obtained from the National Institutes for the Control of Pharmaceutical and Biological Products (Beijing, China). Anti-Myd88, anti-Caspase-1 and anti-rabbit and mouse IgG (H + L), F(ab')2 fragment (Alexa Fluor 555 conjugate) were purchased from the Cell Signaling Technology (Boston, MA, USA). Anti-GFAP was purchased from Arigo Biolaboratories. Anti-NF-κB, anti-TLR4, anti-IL-1β, anti-TIRAP, anti-TRIF and anti-IL-18 were purchased from ABclonal Inc. (College Park, MD, USA). Anti-β-actin and goat anti-mouse and rabbit IgG (H + L)-HRP were purchased from Beijing Ray Antibody Biotech (Beijing, China). Anti-NLRP3, anti-Caspase-11 and anti-ASC were purchased from Bioss (Beijing, China). Fluorescein (FITC)-conjugated goat anti-mouse and rabbit IgG were purchased from DingGuo (Beijing, China). siRNAs for TLR4, Myd88, TRIF, TIRAP, Caspase-11 and NF-κB were purchased from the Shanghai GenePharma Company Limited (Shanghai, China). TAK-242 ($C_{15}H_{17}ClFNO_4S$; a specific inhibitor of TLR4) was purchased from Sigma-Aldrich (St.Louis, MO, USA). Wedelolactone (Wed; a specific inhibitor of Caspase-11) was purchased from Aladdin (Shanghai, China). Super ECL Assay was purchased from KeyGEN Biotech (Nanjing, China). Other chemicals or reagents, unless specifically mentioned below, were purchased from Sigma-Aldrich (St. Louis, MO, USA).

Animal Protocol

Healthy adult male C57BL/6 mice (18–22 g, 6–8 weeks old) were purchased from Laboratory Animal Center of Southern Medical University (Guangzhou, China) and were singly housed in tub cages in a temperature-controlled (approximately 22°C) room with a 12 h light/dark cycle. Animal care and experimental procedures were approved by the Institutional Animal Care and Use Committee at the Southern Medical University and followed the latest NIH Guidelines for the Care and Use of Laboratory Animals (NIH in 2011). The animals were habituated to the animal facility for 1 week before use. The mice were divided randomly into four groups (n = 3/group): saline control group, METH subacute exposure group, TAK-242 exposure group and METH + TAK-242 exposure group. METH was dissolved in saline. The mice in the subacute exposure group received eight intraperitoneal (i.p.) injections of METH (15 mg/kg/injection) at 12 h intervals. This exposure paradigm was chosen based on our and other previous studies to mimic human METH abuse (Cadet et al., 2003; Krasnova and Cadet, 2009; Qiao et al., 2014; Xu et al., 2017). This exposure paradigm is relevant to human exposure because the measured concentrations of METH in the blood and brain (∼0.1–1.1 μg/ml in blood and ∼0.4–1.8 μg/g in brain; **Table 1**) of mice at 2 h after the last injection were in the range of reported blood concentrations in METH abusers (0.6–5 μg/ml [4–30 μM]; Winek et al., 2001; Huang et al., 2015). The saline control group (vehicle group) mice received a similar volume of physiological 0.9% saline via i.p. injections according to the same schedule as the subacute exposure group. TAK-242 was initially dissolved in DMSO, and then further diluted in saline. In the TAK-242 exposure group, TAK-242 was administered i.p. once per day for 5 days (3 mg/kg/injection; Fang et al., 2014). In the METH + TAK-242 exposure group, TAK-242 was given i.p. daily for 5 days, and beginning from the second day METH was given i.p. for eight injections at 12 h intervals. All animals survived throughout the study period. Mice were euthanized (CO_2; followed by decapitation) at 2 h after the last injection. Brain samples were rapidly removed, and the midbrain and striatum were dissected on an ice-cold glass plate, rapidly frozen and stored at −80°C until analysis.

TABLE 1 | Methamphetamine (METH) concentrations in the blood and brain of vehicle-treated and METH-exposed mice at 2 h after the last injection.

Control			METH-treated		
No	Blood (ng/ml)	Brain (ng/g)	No	Blood (ng/ml)	Brain (ng/g)
1	<0	<0	1	110	397.04
2	<0	<0	2	660	528.24
3	<0	<0	3	1050	1797.82

METH Concentrations in Mice Brain and Blood

Blood and brain samples of vehicle-treated and METH-treated mice were collected at 2 h after the last injection. Brains were homogenated in PBS. Then, we measured METH concentrations using a previously reported LC-MS/MS (AB4000Q, USA) protocol and the concentrations were calculated based on a standard curve (Huang et al., 2015).

Cell Culture

Primary astrocytes were cultured in DMEM/F12 medium supplemented with 10% FBS, 50 units/ml penicillin G, and 50 mg/ml streptomycin sulfate at 37°C in a humidified atmosphere of 5% CO_2. The cells were passaged every 6 days. Isolation and identification of mouse primary astrocytes were performed as previously described (Zhang et al., 2017a,b).

METH and Inhibitor Treatment

Once cells reached about 80% in 6-well plates, medium was changed to non-serum medium and cells were exposed to 0, 0.5, 1.0, 1.5, 2.0 or 2.5 mM METH in primary astrocytes for 24 h. This concentration range was selected based on the results of LC25 (data not shown), and this concentration is similar to the concentrations used in other studies (Huang et al., 2009; Cisneros and Ghorpade, 2014; Zhang et al., 2015; Cao et al., 2016). According to the western blot results, at the 2.0 mM METH treatment, the expressions of IL-1β and IL-18

TABLE 2 | The sequences of small interfering RNAs (siRNAs) used in the present study.

Gene	Number	The sequence of siRNA (5′–3′)
TLR4	1	GCAUAGAGGUAGUUCCUAA TT
Myd88	1	CCUUUACAGGUGGCCA GAGUGGAAA
Myd88	2	GGUCCAUUGCCAGCGAGCUAAUUGA
NF-κB	1	GAAGAUUCAUCUGGGUGAAGAUUUA
TRIF	1	CCACGUCCUACACGGAAG AUGAUUU
TRIF	2	UCUAUCGCAUGAGACAUCAUUACAA
Caspase-11	1	GGAACAGCUGGGCAAAGAATT
Caspase-11	2	CCACCAUGGUGAAGCUAAUTT
ASC	1	GCUACUAUCUGGAGUCGUATT
ASC	2	CCCUUGCACAGCCUAUCUUTT
NC	1	UUCU CCGAACGUGUCACGUTT

were the highest. In the experiments with inhibitors, the cells were pre-cultured for 3 h with 100 nM TAK-242 or 30 μM wedelolactone and then incubated with 2.0 mM METH for 24 h. The concentrations of TAK-242 and wedelolactone were selected based on earlier studies (Ii et al., 2006; Matsunaga et al., 2011; Huang et al., 2015) and the results of LC25 (data not shown), and these concentrations had optimal inhibition effects in our experimental model.

siRNA and Transfection

Small interfering RNA (siRNA) was synthesized by GenePharma (Shanghai, China). The sequences of siRNA are shown in **Table 2**. Primary astrocytes were seeded onto a 6-well plate (4×10^5 cells/well). When cells reached 80% confluence, 5 μl Lipofectamine 3000 (Invitrogen, Carlsbad, CA, USA) reagent and 20 μmol siRNA or siNC were added in opti-MEM medium (Gibco BRL, Paisley, UK). The mixed solution was incubated at room temperature for 20 min, and then siRNA mixture was added gently and slowly in each well, and then 1 ml complete medium was added in each well. After 6 h incubation, all supernatant was discarded and then 2 ml complete medium was added in each well.

Western Blot Analysis

Primary cultured astrocytes and brain samples from mice exposed to vehicle or METH were lysed in ice-cold RIPA buffer with protease inhibitors. Protein concentrations were determined with the BCA-100 Protein Quantitative Analysis kit (Biocolors, Shanghai, China). Protein samples were separated by 10–15% sodium dodecyl sulfate polyacrylamide gel (SDS-PAGE) and transferred onto 0.22 μm polyvinylidenedifluoride (PVDF) membranes (Millipore, Billerica, MA, USA). The membranes were incubated at room temperature for 2 h in 5% nonfat milk blocking buffer. After blocking, membranes were incubated with primary antibodies overnight at 4°C (1:500–1000). After the membranes were washed three times with TBST, they were incubated with an anti-rabbit or mouse IgG horseradish peroxidase (1:10,000) for 1 h at room temperature. The membranes were developed with Super ECL Western blotting detection reagents. The signal of band intensities was quantitated by Gel-Pro analyzer (Media Cybernetics, Inc., Rockville, MD, USA). Expression of the housekeeping gene β-actin was used as a reference control.

Double Immunofluorescence Labeling

To determine TLR4 and NF-κB expression levels in primary cultured astrocytes and mouse midbrain samples, we performed double immunofluorescence labeling on cells and frozen sections of adult mouse midbrains. For immunolabeling, all incubation solutions were prepared using PBS supplemented with 10% normal goat serum and 0.05% Triton X-100. These antibodies were used together with DAPI nuclear labeling. The frozen tissue sections were incubated with blocking buffer (10% BSA in PBS) for 30 min at room temperature, with the primary antibody (anti-GFAP dilution of 1:500, anti-TLR4 dilution of 1:100, or anti-NF-κB dilution of 1:100) overnight at 4°C, and then with the secondary antibody for 1 h at room temperature (FITC conjugated anti-mouse or rabbit IgG dilution of 1:50, Alexa Fluor 555 conjugated anti-mouse or rabbit IgG dilution of 1:200). Microphotographs were taken using fluorescence microscopy (A1+/A1R+; Nikon). All digital images were processed using the same settings to improve the contrast.

Immunohistochemistry

Brain tissue samples were fixed in 4% formalin, embedded in paraffin and sectioned at 3 μm thickness. Brain sections were treated with xylene to remove the paraffin and then were rehydrated. Prior to staining heat-induced antigen retrieval was performed by placing the slides into 0.01 M citrate buffer solution (pH6.0), and subjected to microwave heating three times for 5 min. Then the sections were incubated with 3% H_2O_2 for 10 min at room temperature and washed three times with PBS, followed by incubation with serum for 30 min. Samples were incubated with the indicated primary antibodies (e.g., anti-GFAP dilution of 1:500) overnight at 4°C. After washing with PBS, the slices were incubated with secondary antibodies for 0.5 h at 37°C. After staining with 3,3′-diaminobenzidine (DAB), the sections were observed under optical microscope.

Statistical Analysis

Data given in the text are expressed as mean ± standard deviation (SD) of at least three independent replicates. Data were analyzed with Student's *t*-test, one-way analysis of variance (ANOVA), 2 × 2 factorial ANOVA or two-way ANOVA (as appropriate) followed by LSD *post hoc* analyses using SPSS 20.0 software (IBM Corporation, Armonk, NY, USA). The value of $P < 0.05$ was considered statistically significant.

RESULTS

Methamphetamine Increases the Expression of Proinflammatory Cytokines IL-1β and IL-18 in Astrocytes

To determine whether astrocytes are activated after METH exposure, a mouse model treated with METH (8 injections, 15 mg/kg/injection, at 12 h intervals) was used. Immunohistochemistry staining results showed the size of astrocyte cell body and the number of bulges were increased in the striatum and midbrain, suggesting that METH treatment activates astrocytes (**Figure 1A**). In order to further examine the

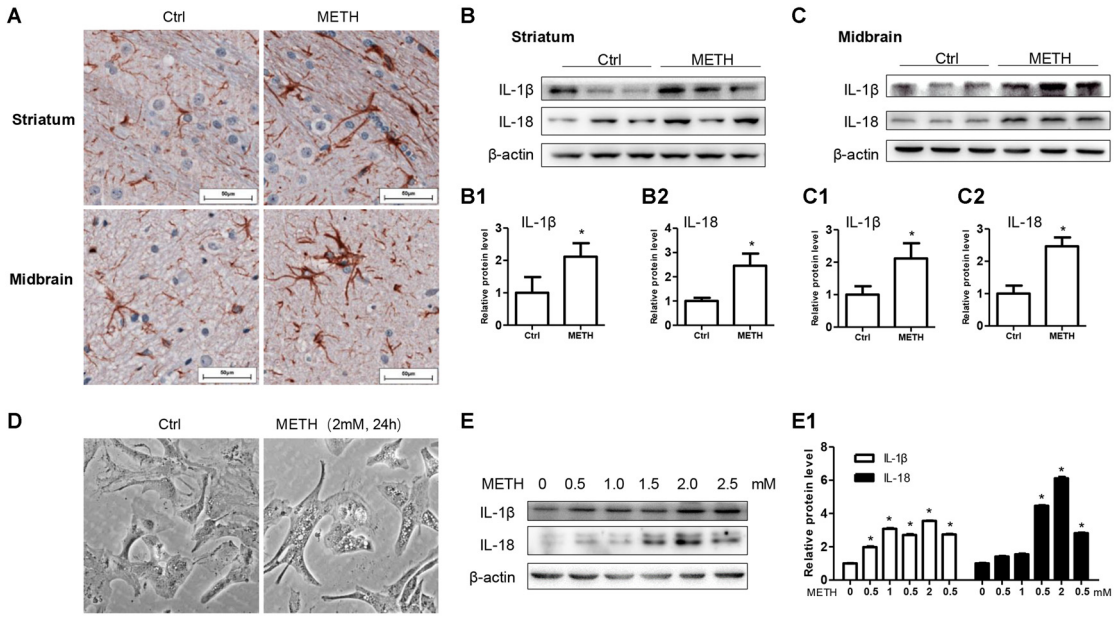

FIGURE 1 | Astrocytes are activated after Methamphetamine (METH) exposure *in vitro* and *in vivo*. Male C57BL/6 mice were divided randomly into control and experiment groups (n = 5). Animals were injected intraperitoneally with saline or METH (15 mg/kg/injection, 8 injections, at 12 h intervals). **(A)** Immunohistochemical staining of GFAP in the striatum and midbrain. Scale bar, 50 μm. Western blot **(B,C)** and quantitative analyses **(B1–C2)** were performed to determine IL-1β and IL-18 protein expression in the striatum and midbrain. Primary cultured astrocytes were exposed to 0.5, 1.0, 1.5, 2.0 and 2.5 mM METH for 24 h. **(D)** Morphological changes were observed. Western blot **(E)** and quantitative analyses **(E1)** were performed to determine IL-1β and IL-18 protein expression. β-actin was used as a loading control. Fold induction relative to vehicle-treated group is shown. $^*p < 0.05$ vs. vehicle-treated group. Data were analyzed with Student's t-test or one-way analyses of variance (ANOVA) followed by LSD *post hoc* analysis. Data are expressed as mean ± standard deviation (SD).

inflammatory response of the mouse brain after the treatment of METH, we used the inflammatory indicators of IL-1β and IL-18. IL-1β and IL-18 are proinflammatory cytokines that play a major role in the inflammatory response *in vivo*. Western blot results revealed that the expressions of IL-1β ($t_{(4)}$ = 3.027, P = 0.0389) and IL-18 ($t_{(4)}$ = 2.799, P = 0.0489) were increased in the corpus striatum (**Figures 1B–B2**) of METH-exposed mice compared to the control group. The expressions of IL-1β ($t_{(4)}$ = 3.603, P = 0.0227) and IL-18 ($t_{(4)}$ = 6.825, P = 0.0024) were also increased in the midbrain (**Figures 1C–C2**). Furthermore, the morphology of primary cultured astrocytes was significantly changed after METH exposure. Specifically, vacuole-like secretory vesicles were observed in the cell body of METH-treated astrocytes (**Figure 1D**). IL-1β ($F_{(1,17)}$ = 1966, $P < 0.0001$) and IL-18 ($F_{(1,17)}$ = 5616, $P < 0.0001$) protein expression was also significantly increased in a dose-dependent manner in primary cultured astrocytes (**Figures 1E,E1**). Taken together, these data demonstrated that METH exposure activates astrocytes and induces the expression of proinflammatory factors *in vivo* and *in vitro*.

Caspase-11 Mediates IL-1β and IL-18 Expression in METH-Exposed Astrocytes

To assess the role of Caspase-11 in METH-caused neuroinflammation in astrocytes, primary cultured astrocytes were exposed to METH for 24 h with or without siCaspase-11. Western blot results showed that the expression level of Caspase-11 was increased by METH in a dose-dependent manner (**Figure 2A**). Caspase-11 protein level was 2.8-fold higher in the 2.0 mM METH-treated primary cultured astrocytes than in the control (group effect: $F_{(1,17)}$ = 20.62, $P < 0.0001$; METH 2.0 mM: $t_{(3)}$ = 7.916, $P < 0.001$; **Figure 2A1**). This increase was normalized after co-treatment with either one of the siCaspase-11 s ($F_{(1,11)}$ = 63.638, $P < 0.001$; mean difference of siRNA#1 = 1.7850, $P < 0.001$; mean difference of siRNA#2 = 1.3632, $P < 0.001$; **Figures 2B,B1**). These results suggest that both of the two siRNAs can effectively knockdown Caspase-11 expression.

Next, we evaluated whether silencing of Caspase-11 can reduce the expression of METH-induced proinflammatory cytokines in astrocytes. Western blot results showed that IL-1β ($F_{(1,11)}$ = 63.068, $P < 0.001$; mean difference of siRNA#1 = 1.8308, $P < 0.001$; mean difference of siRNA#2 = 1.4752, $P < 0.001$; **Figure 2B2**) and IL-18 ($F_{(1,11)}$ = 90.282, $P < 0.001$; mean difference of siRNA#1 = 4.3131, $P < 0.001$; mean difference of siRNA#2 = 3.5472, $P < 0.001$; **Figure 2B3**) expression was significantly decreased after Caspase-11 knockdown in METH-treated primary cultured astrocytes. To confirm this result, we also used Wed, a specific inhibitor of Caspase-11, to block Caspase-11 expression and then examined the expression of IL-1β and IL-18. The expression of Caspase-11 was significantly decreased ($F_{(1,11)}$ = 33.394, $P < 0.001$). Consistent with the above-described results, Wed inhibited the expression of

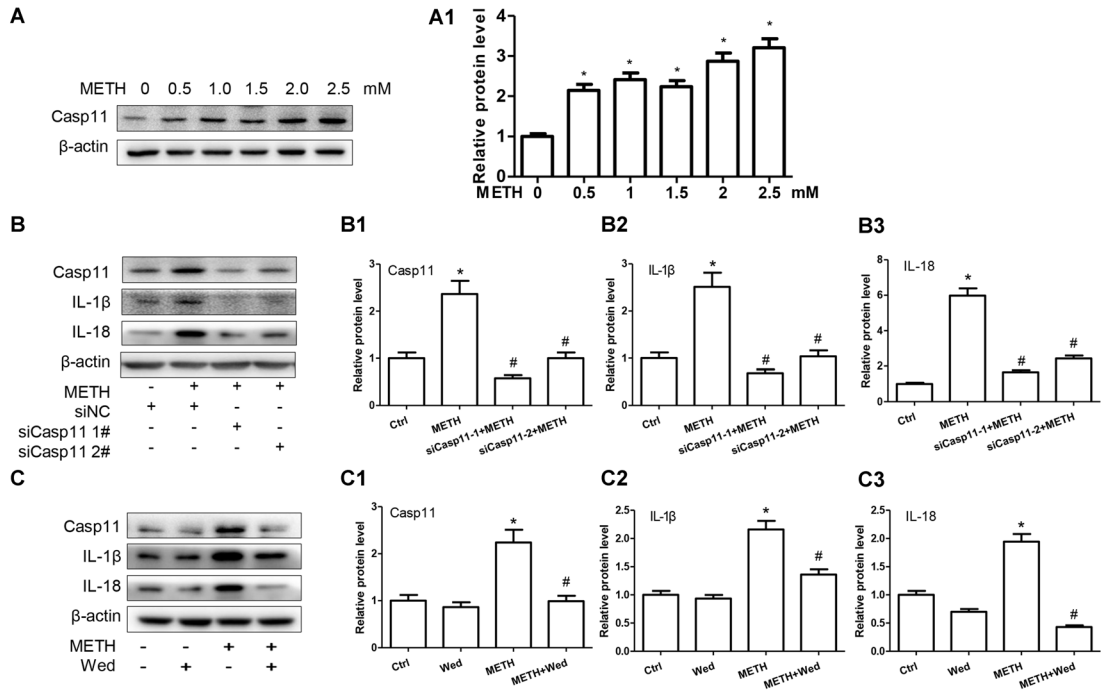

FIGURE 2 | Caspase-11 mediates IL-1β and IL-18 expression in METH-exposed astrocytes. **(A,A1)** Primary cultured astrocytes were exposed to 0.5, 1.0, 1.5, 2.0 and 2.5 mM METH for 24 h. **(B–B3)** Primary cultured astrocytes were transfected with siRNAs targeting Caspase-11 or control siRNA for 24 h followed by METH (2 mM) treatment for 24 h. **(C–C3)** Primary cultured astrocytes were exposed to Wed (30 μM) for 2 h prior to METH (2 mM) treatment as indicated. Western blot **(A–C)** and quantitative analyses were performed to determine Caspase-11, IL-1β and IL-18 protein expression. All the experiments were repeated three times. Data are expressed as mean ± SD. $^{*}p < 0.05$ vs. non-METH-treated group. $^{\#}p < 0.05$ vs. the scrambled + METH treated group. Data in **(A)** were analyzed with one-way ANOVA followed by LSD *post hoc* analyses; data in **(B)** were analyzed with two-way ANOVA followed by LSD *post hoc* analyses; data in **(C)** was analyzed with 2 × 2 factorial ANOVA followed by LSD *post hoc* analyses.

IL-1β ($F_{(1,11)} = 13.470$, $P < 0.001$) and IL-18 ($F_{(1,11)} = 56.288$, $P < 0.001$) induced by METH (**Figures 2C–C3**). These results suggest that METH exposure induces Caspase-11 protein expression and its activation is involved in METH-caused increased expression of IL-1β and IL-18.

Inflammasome NLRP3 Is Involved in Caspase-11 Mediated Neuroinflammation Signaling Pathways Caused by METH in Astrocytes

Previous studies demonstrated that Caspase-11 could mediate the expression of IL-1β and IL-18 via NLRP3/ASC/Caspase-1 signal axis (Zanoni et al., 2016). To examine whether the NLRP3/ASC/Caspase-1 complex is involved in Caspase-11- mediated METH-induced IL-1β and IL-18 expression, we determined the changes on NLRP3, ASC and Caspase-1 protein levels in METH-treated and untreated primary cultured astrocytes by Western blot analysis. The results showed that the expression level of NLRP3 was not changed significantly ($F_{(1,17)} = 2.753$, $P = 0.0699$), but the expression levels of ASC ($F_{(1,17)} = 30.61$, $P < 0.0001$) and Caspase-1 ($F_{(1,17)} = 13.05$, $P = 0.002$) were increased in a dose-dependent manner (**Figures 3A,A1**).

To further assess whether elevation of ASC and Caspase-1 is involved in Caspase-11-mediated induction of IL-1β and IL-18 by METH, we used siRNAs or specific inhibitor (Wed) to block Caspase-11 expression and then observed the expression changes on ASC and Caspase-1 before and after Caspase-11 silencing. Western blot results showed decreased expression of Caspase-1 and ASC after Caspase-11 expression knockdown (Caspase-1: $F_{(1,11)} = 69.870$, $P < 0.001$; mean difference of siRNA#1 = 1.6883, $P < 0.001$; mean difference of siRNA#2 = 1.3302, $P < 0.001$; ASC: $F_{(1,11)} = 27.891$, $P < 0.001$; mean difference of siRNA#1 = 0.8521, $P < 0.001$; mean difference of siRNA#2 = 0.5150, $P < 0.001$) or inhibitor (Caspase-1: $F_{(1,11)} = 72.187$, $P < 0.001$; ASC: $F_{(1,11)} = 22.810$, $P = 0.001$) in METH-treated primary cultured astrocytes (**Figures 3B–B2,C–C3**). In addition, we used siRNAs targeting ASC to silence ASC expression and then examined the effects on METH-caused neuroinflammation in primary cultured astrocytes. Western blot results showed that both of siRNAs could effectively knockdown ASC expression, with siRNA #1 being more effective ($F_{(1,11)} = 77.319$, $P < 0.001$; mean difference of siRNA#1 = 2.4278, $P < 0.001$; mean difference of siRNA#2 = 1.2030, $P = 0.001$). The ASC silence significantly decreased the expression of IL-1β ($F_{(1,11)} = 36.266$, $P < 0.001$; mean difference of siRNA#1 = 1.3684, $P < 0.001$; mean difference

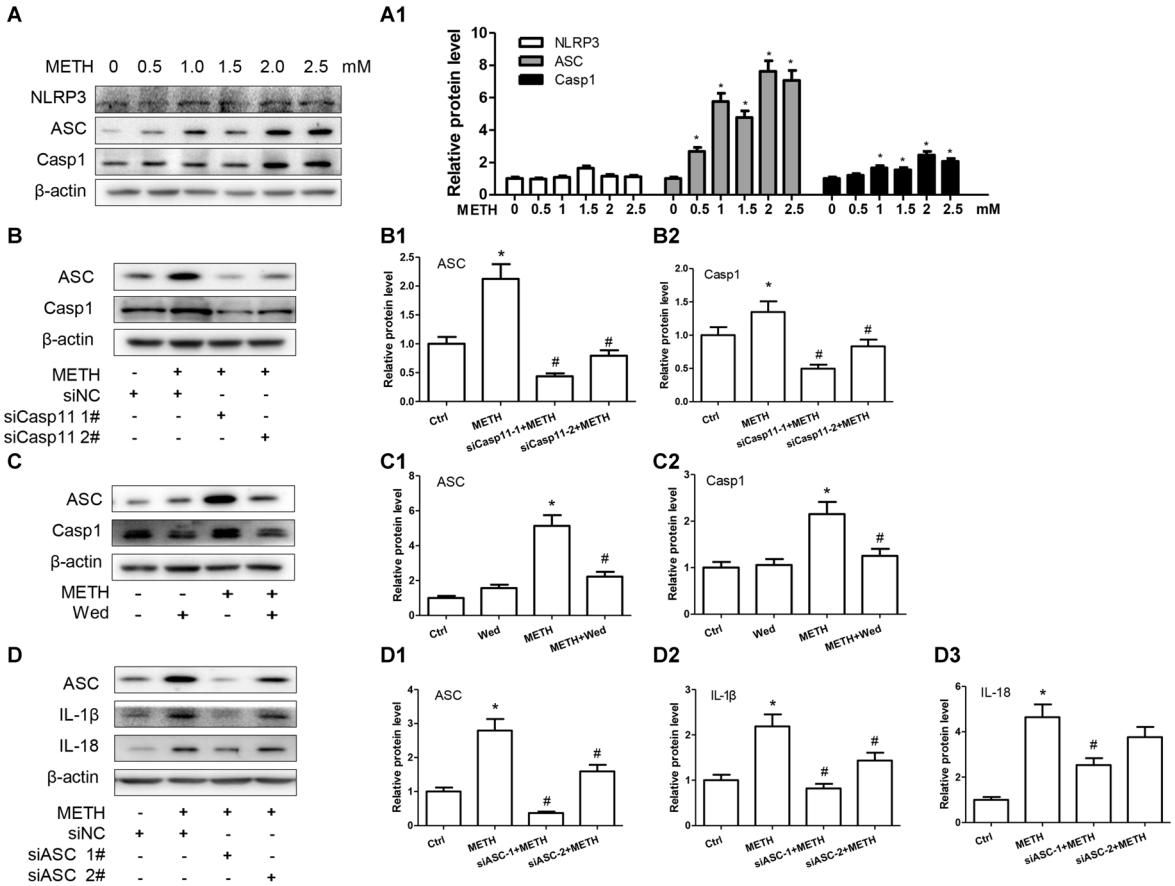

FIGURE 3 | Inflammasomes are involved in Caspase-11-mediated IL-1β and IL-18 protein expression caused by METH in astrocytes. **(A,A1)** Primary cultured astrocytes were exposed to 0.5, 1.0, 1.5, 2.0 and 2.5 mM METH for 24 h. **(B–B2)** Cells were transfected with siRNAs targeting Caspase-11 or control siRNA for 24 h followed by METH (2 mM) treatment for 24 h. **(C–C2)** Cells were exposed to Wed (30 μM) for 2 h prior to METH (2 mM) treatment as indicated. **(D–D3)** Cells were transfected with siRNAs targeting apoptosis-associated speck-like protein containing CARD (ASC) or control siRNA for 24 h followed by METH (2 mM) treatment for 24 h. Western blot **(A–D)** and quantitative analyses were performed to determine Caspase-11, NLRP3, ASC, Caspase-1, IL-1β and IL-18 protein expression. All the experiments were repeated three times. Data are expressed as mean ± SD. $^{*}p < 0.05$ vs. non-METH-treated group. $^{\#}p < 0.05$ vs. the scrambled + METH treated group. Data in **(A)** were analyzed with one-way ANOVA followed by LSD *post hoc* analyses; data in **(B,D)** were analyzed with two-way ANOVA followed by LSD *post hoc* analyses; data in **(C)** were analyzed with 2 × 2 factorial ANOVA followed by LSD *post hoc* analyses.

of siRNA#2 = 0.7536, $P = 0.005$) and IL-18 ($F_{(1,11)} = 48.380$, $P < 0.001$; mean difference of siRNA#1 = 2.1178, $P = 0.001$; mean difference of siRNA#2 = 0.8849, $P = 0.151$; **Figures 3D–D3**). Taken together, these results suggest that Caspase-11 mediates METH-induced neuroinflammation through NLRP3/ASC/Caspase-1 signaling pathway in astrocytes.

TLR4 Is Necessary for METH-Induced IL-1β and IL-18 Expression in Astrocytes

TLR4, a receptor located in the cell membrane, is the first line of defense of innate immunity system. In the present study, we found that TLR4 protein expression was increased after treatment with METH in primary cultured astrocytes in a dose-dependent manner ($F_{(1,17)} = 12.41$, $P < 0.001$; **Figures 4A,A1**). After silencing TLR4 with siRNA ($F_{(1,11)} = 20.278$, $P = 0.002$), the METH-caused increased expression of IL-1β ($F_{(1,11)} = 1678.59$, $P < 0.001$) and IL-18 ($F_{(1,11)} = 162.589$, $P < 0.001$) was substantially ameliorated (**Figures 4B–B3**). To confirm these results, we also used a specific inhibitor of TLR4, bromomethyl acetate (TAK-242), to inhibit the expression of TLR4 and then examined the effect on expression of IL-1β and IL-18 in astrocytes. Western blot (**Figures 4C,C1**) and immunofluorescence staining (**Figure 4D**) results showed that TAK-242 pretreatment attenuated METH-induced TLR4 expression in primary cultured astrocytes ($F_{(1,11)} = 24.026$, $P < 0.001$). Similar results were observed in the midbrain of METH-treated C57BL/6 mice with or without TAK-242 co-treatment (**Figure 4E**). Consistent with the results of silencing TLR4 expression by siRNA, we observed that inhibition of TLR4 expression by TAK-242 also reduced the expression of IL-1β ($F_{(1,11)} = 38.922$, $P < 0.001$) and IL-18 ($F_{(1,11)} = 260.665$, $P < 0.001$) induced by METH in astrocytes (**Figures 4C2,C3**). These results suggest that METH exposure

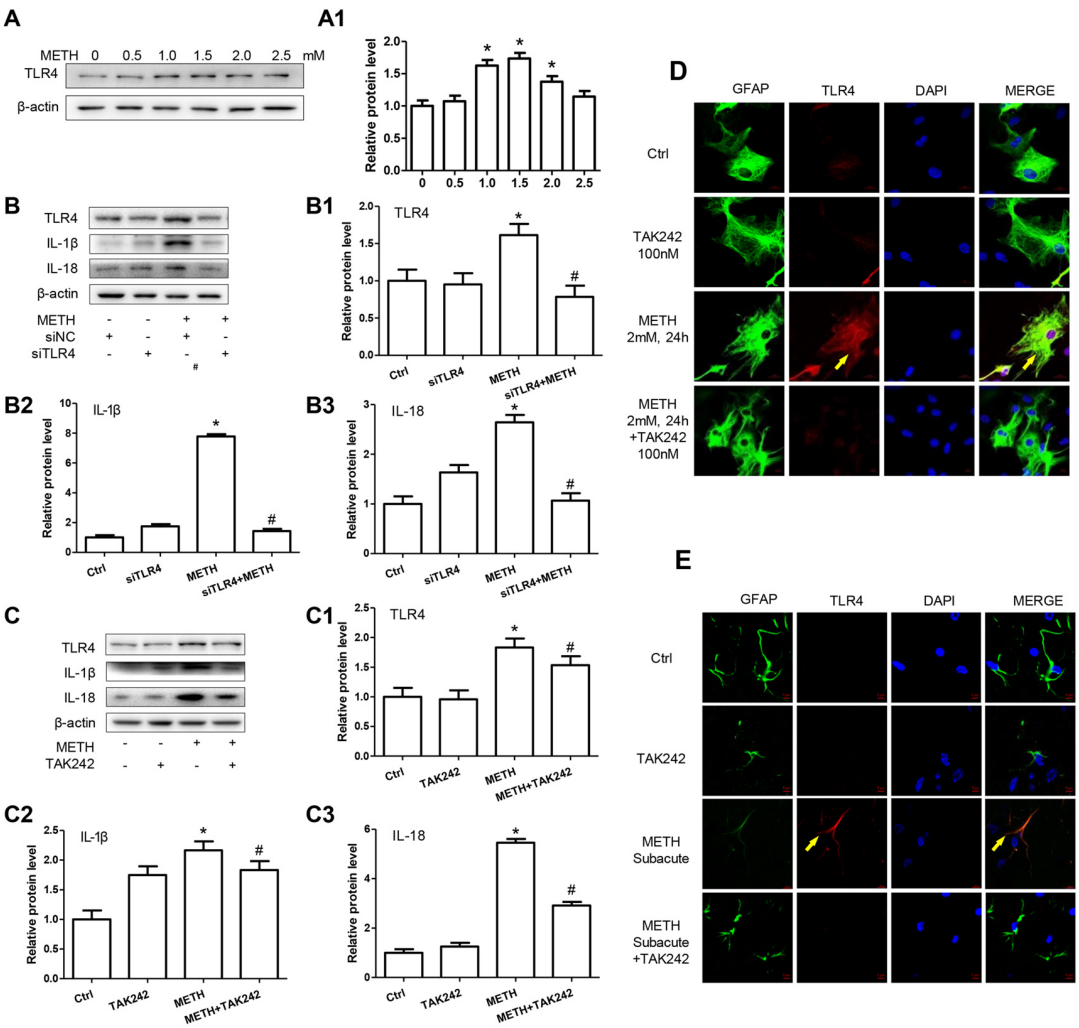

FIGURE 4 | Toll-like receptor 4 (TLR4) is necessary for METH-induced IL-1β and IL-18 expression in astrocytes. **(A,A1)** Primary cultured astrocytes were exposed to 0.5, 1.0, 1.5, 2.0 and 2.5 mM METH for 24 h. **(B–B3)** Cells were transfected with siRNAs targeting TLR4 or control siRNA for 24 h followed by METH (2 mM) treatment for 24 h. **(C–C3,D)** Cells were exposed to TAK-242 (100 nM) for 2 h prior to METH (2 mM) treatment. Western blot **(A–C)** and quantitative analyses were performed to determine TLR4, IL-1β and IL-18 protein expression. Immunolabeling and confocal imaging analysis **(D)** showed elevated TLR4 expression in the cells treated with METH compared with controls. **(E)** Male C57BL/6 mice were divided randomly into control, METH, TAK-242 and METH + TAK-242 groups (n = 3/group). TAK-242 was injected intraperitoneally with DMSO and saline (3 mg/kg/injection, five injections, at 24 h intervals). At the 2nd day, animals were injected intraperitoneally with saline or METH (15 mg/kg/injection, eight injections, at 12 h intervals). Midbrain tissues were harvested at 2 h after the last dosing. Immunolabeling and confocal imaging analysis showed elevated TLR4 expression in the midbrain of METH-exposed mice compared with controls. Yellow arrow refers to TLR4. Cell experiments were repeated three times. Data are expressed as mean ± SD. $^{*}p < 0.05$ vs. non-METH-treated group. $^{\#}p < 0.05$ vs. the scrambled + METH treated group. Data in **(A)** were analyzed with one-way ANOVA followed by LSD *post hoc* analyses; data in **(B,C)** were analyzed with 2 × 2 factorial ANOVA followed by LSD *post hoc* analyses.

induces TLR4 protein expression and this activation is involved in the METH-induced expression of IL-1β and IL-18 in astrocytes.

Caspase-11 Is Involved in TLR4-Mediated IL-1β and IL-18 Expression in METH-Exposed Astrocytes

According to the above-described results, both Caspase-11 and TLR4 mediate METH-induced expression of IL-1β and IL-18 in astrocytes, but the relation between Caspase-11 and TLR4 is still not clear. To address this, we determined the effect on TLR4 expression after blocking Caspase-11 expression by siRNAs or specific inhibitor targeting Caspase-11. Western blot results showed that blockade of Caspase-11 expression by siRNAs ($F_{(1,11)}$ = 12.158, P = 0.002; mean difference of siRNA#1 = −0.3007, $P > 0.05$; mean difference of siRNA#2 = −0.4628, $P > 0.05$) or Wed ($F_{(1,11)}$ = 2.185, P = 0.178) had no effects on TLR4 expression (**Figures 5A,A1,B,B1**), suggesting that TLR4 is not the downstream target of Caspase-11. Conversely, we found that METH-induced expression of

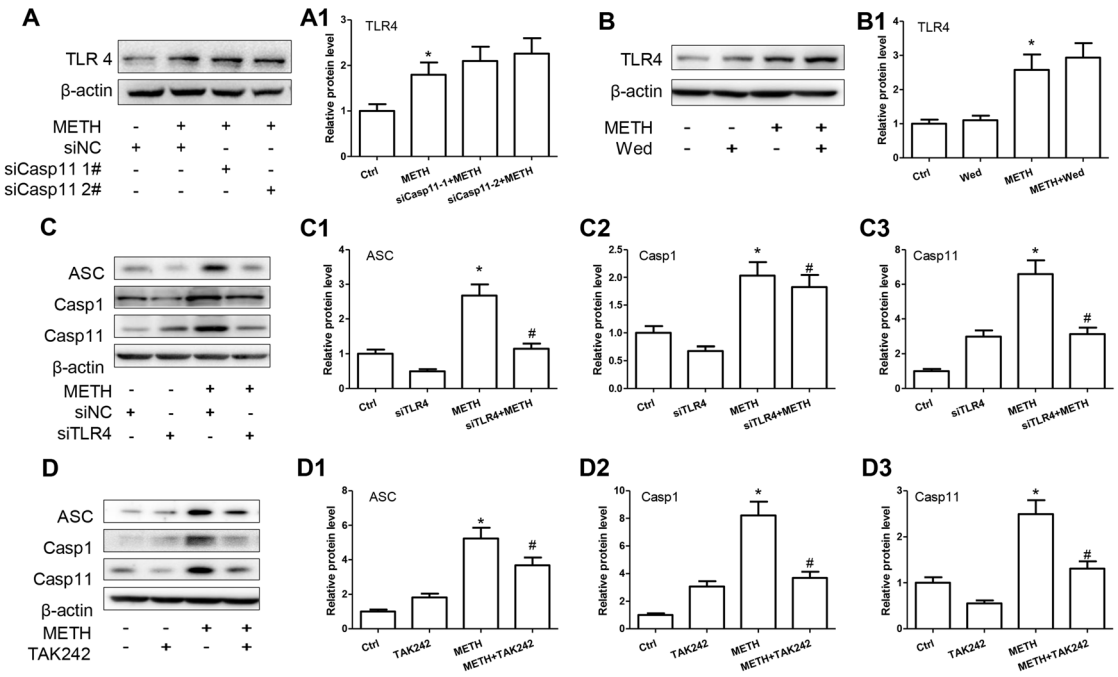

FIGURE 5 | Caspase-11 is involved in TLR4-mediated IL-1β and IL-18 expression in METH-exposed astrocytes. Primary cultured astrocytes transfected with siRNAs targeting Caspase-11 **(A,A1)**, TLR4 **(C–C3)** or control siRNA for 24 h followed by METH (2 mM) treatment for 24 h. Cells were exposed to Wed (30 μM) **(B,B1)** or TAK-242 (100 nM) **(D–D3)** for 2 h prior to METH (2 mM) treatment as indicated. Western blot **(A–D)** and quantitative analyses were performed to determine TLR4, Caspase-11, ASC and Caspase-1 protein expression. All the experiments were repeated three times. Data are expressed as mean ± SD. $^{*}p < 0.05$ vs. non-METH-treated group. $^{\#}p < 0.05$ vs. the scrambled + METH treated group. Data in **(A)** were analyzed with two-way ANOVA followed by LSD *post hoc* analyses; data in **(B–D)** were analyzed with 2 × 2 factorial ANOVA followed by LSD *post hoc* analyses.

Caspase-11 was significantly attenuated after TLR4 silencing by siRNAs ($F_{(1,11)} = 97.975$, $P < 0.001$) or TAK-242 ($F_{(1,11)} = 12.284$, $P < 0.001$; **Figures 5C,C3,D,D3**), which indicates that TLR4 can regulate Caspase-11 expression. Notably, we also observed that the expression of ASC and Caspase-1 were decreased significantly after blockade of TLR4 expression by siRNA (ASC: $F_{(1,11)} = 22.297$, $P = 0.001$; Caspase-1: $F_{(1,11)} = 39.431$, $P < 0.001$) or TAK-242 (ASC: $F_{(1,11)} = 25.985$, $P < 0.001$; Caspase-1: $F_{(1,11)} = 98.882$, $P < 0.001$; **Figures 5C1,C2,D1,D2**). These results indicate that TLR4 mediates METH-induced expression of IL-1β and IL-18 through Caspase-11/ASC/Caspase-1 signal axis in astrocytes.

TLR4 Induces Translocation of NF-κB into the Nucleus, Leading to an Increase of Caspase-11 Transcription in METH-Exposed Astrocytes

We have demonstrated that TLR4 mediates METH-induced expression of IL-1β and IL-18 via Caspase-11-mediated Caspase-1-dependent pathway. The next question is to clarify how TLR4 regulates the expression of Caspase-11. Previous studies have shown that NF-κB, a well-known downstream target of TLR4, can bind to promoter of Caspase-11 and activate Caspase-11 expression (Dolunay et al., 2017). We hypothesized that TLR4 regulates the expression of Caspase-11 through NF-κB signaling axis. To test this hypothesis, we used siRNA targeting to NF-κB to silence the expression of NF-κB and then determined the effect on Caspase-11 expression in astrocytes after METH exposure. The results showed that siRNA can effectively knockdown METH-induced NF-κB expression ($F_{(1,11)} = 17.625$, $P = 0.003$), and METH-induced expression of Caspase-11 was significantly decreased after silencing NF-κB ($F_{(1,11)} = 36.680$, $P < 0.001$; **Figures 6A–A2**). This result suggests that NF-κB regulates METH-caused increased expression of Caspase-11. To further clarify the mechanisms of how TLR4 regulates the expression of Caspase-11 via NF-κB, we observed the location changes of NF-κB after METH exposure with or without TAK-242 pre-treatment. We extracted nucleus and cytoplasm proteins separately from METH-treated astrocytes with or without TAK-242 pre-treatment, and then measured NF-κB protein level in the nucleus and cytoplasm. Western blot results showed that METH exposure increased the expression of NF-κB both in the cytoplasm ($F_{(1,11)} = 23.819$, $P < 0.001$) and nucleus ($F_{(1,11)} = 23.606$, $P < 0.001$); and this effect was significantly mitigated by co-treatment with TAK-242 (**Figures 6B,B1,C,C1**). To confirm the results, we also performed the immunofluorescence staining. Results showed that METH exposure increased the expression of

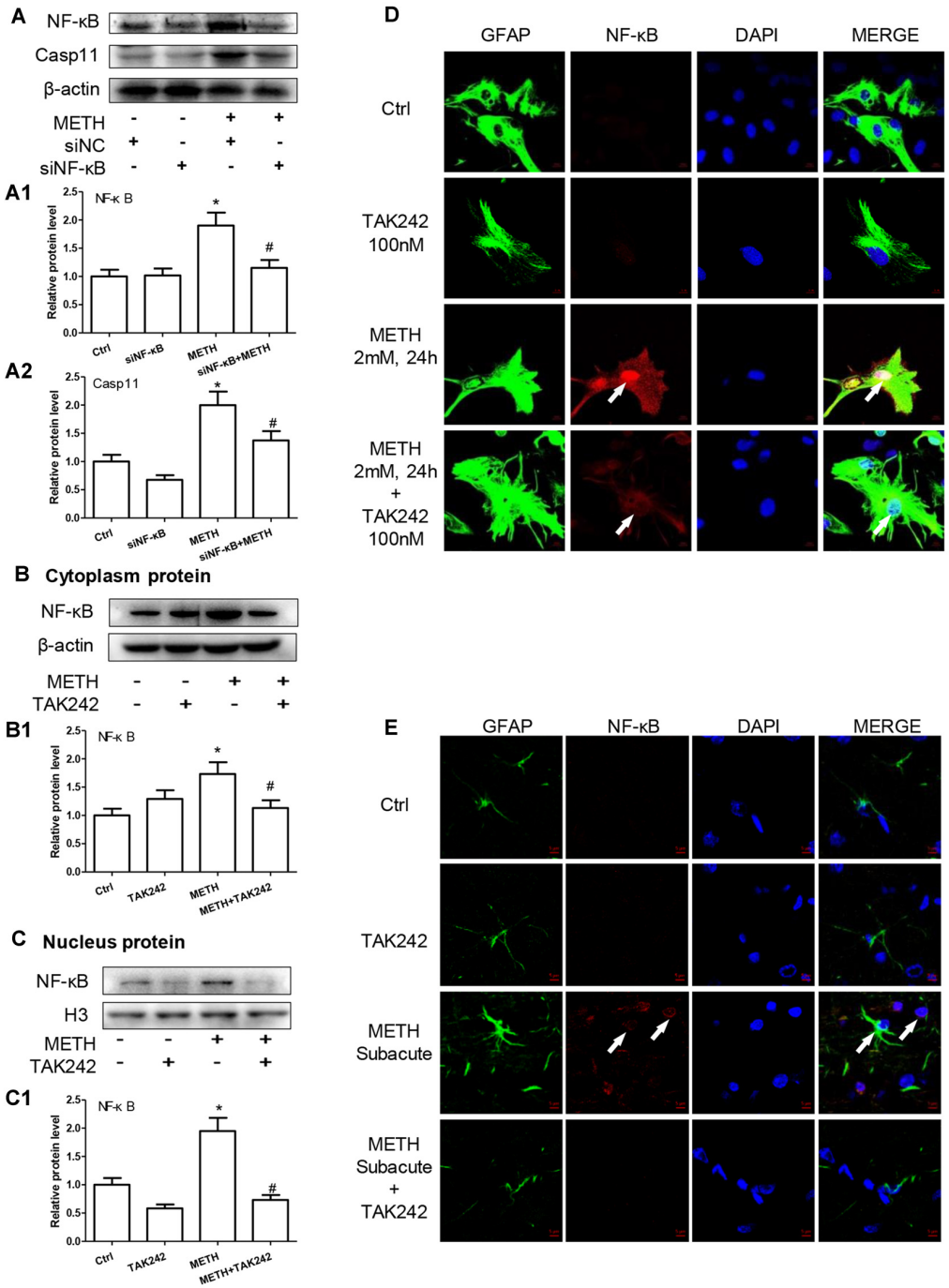

FIGURE 6 | TLR4 induces translocation of NF-κB into the nucleus, leading to an increase of Caspase-11 transcription in METH-exposed astrocytes. **(A–A2)** Primary cultured astrocytes were transfected with siRNAs targeting NF-κB or control siRNA for 24 h followed by METH (2 mM) treatment for 24 h. **(B–D)** Cells were exposed to TAK-242 (100 nM) for 2 h prior to METH (2 mM) treatment as indicated, nucleus proteins **(C,C1)** and cytoplasm **(B,B1)** proteins were extracted separately. Western blot **(A–C)** and quantitative analyses were performed to determine NF-κB, and Caspase-11 protein expression. H3 was used as the loading control of nucleus proteins. Immunolabeling and confocal imaging analysis **(D)** showed elevated NF-κB expression in the METH-treated cells compared with controls. **(E)** The animal exposure paradigms were the same as described in **Figure 4**. Immunolabeling and confocal imaging analysis showed elevated NF-κB expression in the midbrain of METH-exposed mice compared with controls. White arrow refers to NF-κB. Cell experiments were repeated three times. Data are expressed as mean ± SD. $^{*}p < 0.05$ vs. non-METH-treated group. $^{\#}p < 0.05$ vs. the scrambled + METH treated group. Data were analyzed with 2 × 2 factorial ANOVA followed by LSD *post hoc* analyses.

NF-κB, particularly in the nucleus, and this effect was significantly mitigated by pre-treatment with the TAK-242 (**Figure 6D**). Similar results were observed in the midbrain of METH-treated C57BL/6 mice with or without TAK-242 pre-treatment (**Figure 6E**). Taken together, these results suggest that TLR4 regulates the expression of Caspase-11 via NF-κB.

TLR4 Mediates METH-Induced IL-1β and IL-18 Expression through Both Myd88-Dependent and Myd88-Independent Signaling Pathways

TLR4 regulates the NF-κB expression through two-independent signal axes: one is TRIF signaling axis and the other is TIRAP/Myd88/IRAK4 signal axis (Van Acker et al., 2014; Planès et al., 2016). To explore whether TLR4 regulates NF-κB expression through TIRAP/Myd88/IRAK4 axis and/or TRIF axis in METH-exposed astrocytes, we used siRNA and TAK-242 to silence TLR4 expression and then examined the protein levels of TIRAP, Myd88 and NF-κB. Western blot results showed that TRIF, Myd88 and NF-κB protein levels were significantly increased in METH-treated astrocytes compared with control cells and then significantly decreased after inhibiting TLR4 expression by siRNA (TIRAP: $F_{(1,11)} = 18.088$, $P = 0.003$; Myd88: $F_{(1,11)} = 83.986$, $P < 0.001$; NF-κB: $F_{(1,11)} = 116.232$, $P < 0.001$) or TAK-242 (TIRAP: $F_{(1,11)} = 14.603$, $P < 0.001$; Myd88: $F_{(1,11)} = 37.914$, $P < 0.001$; NF-κB: $F_{(1,11)} = 59.806$, $P < 0.001$; **Figures 7A–A3,B–B3**), suggesting that both TRIF axis and TIRAP/Myd88/IRAK4 axis were activated in METH-treated astrocytes.

To assess whether activated TRIF axis and TIRAP/Myd88/IRAK4 axis are involved in TLR4-mediated METH-induced expression of IL-1β and IL-18, we designed siRNAs targeting TRIF and Myd88, respectively, to inhibit their expression and block the two pathways. For TRIF axis, Western blot analysis showed that both of two siRNAs can effectively knockdown METH-induced TRIF expression ($F_{(1,11)} = 46.137$, $P < 0.001$; mean difference of siRNA#1 = 0.9489, $P < 0.001$; mean difference of siRNA#2 = 1.3343, $P < 0.001$), and as we expected, silencing of TRIF expression had no effect on the expression of TLR4 ($F_{(1,11)} = 41.028$, $P < 0.001$; mean difference of siRNA#1 = 0.1537, $P > 0.05$; mean difference of siRNA#2 = −0.6282, $P = 0.716$), TIRAP ($F_{(1,11)} = 9.750$, $P = 0.005$; mean difference of siRNA#1 = 0.0093, $P > 0.05$; mean difference of siRNA#2 = −0.2144, $P > 0.05$), and Myd88 ($F_{(1,11)} = 17.865$, $P = 0.001$; mean difference of siRNA#1 = −0.1990, $P > 0.05$; mean difference of siRNA#2 = −0.4939, $P = 0.131$), but significantly decreased the expression of Caspase-11 ($F_{(1,11)} = 27.421$, $P < 0.001$; mean difference of siRNA#1 = 0.5428, $P = 0.001$; mean difference of siRNA#2 = 0.9130, P = < 0.001) and IL-1β ($F_{(1,11)} = 36.249$, $P < 0.001$; mean difference of siRNA#1 = 0.8943, $P < 0.001$; mean difference of siRNA#2 = 1.064, $P < 0.001$; **Figures 7C–C6**). These results indicate that TRIF can regulate the expression of IL-1β through Caspase-11.

For TIRAP/Myd88/IRAK4 axis, the two Myd88 siRNAs can effectively knockdown METH-induced Myd88 expression ($F_{(1,11)} = 16.972$, $P = 0.001$; mean difference of siRNA#1 = 0.6301, $P = 0.012$; mean difference of siRNA#2 = 0.7037, $P = 0.006$), as shown in **Figures 7D–D6**. Furthermore, we found that silencing Myd88 expression inhibited METH-induced expression of Caspase-11 ($F_{(1,11)} = 24.584$, $P < 0.001$; mean difference of siRNA#1 = 0.8441, $P = 0.002$; mean difference of siRNA#2 = 0.4460, $P = 0.048$) and IL-1β ($F_{(1,11)} = 46.602$, $P < 0.001$; mean difference of siRNA#1 = 0.6738, $P = 0.001$; mean difference of siRNA#2 = 1.1653, $P < 0.001$), while had no effect on the expression of TLR4 ($F_{(1,11)} = 31.889$, $P < 0.001$; mean difference of siRNA#1 = 0.1242, $P > 0.05$; mean difference of siRNA#2 = −0.1581, $P > 0.05$), TRIAP ($F_{(1,11)} = 15.216$, $P = 0.001$; mean difference of siRNA#1 = −0.032, $P > 0.05$; mean difference of siRNA#2 = 0.1140, $P > 0.05$) and TRIF ($F_{(1,11)} = 14.190$, $P = 0.001$; mean difference of siRNA#1 = 0.9489, $P < 0.001$; mean difference of siRNA#2 = 1.3343, $P < 0.001$). These results indicate that the Myd88-dependent downstream signaling pathway of TLR4 might also be the pathway through which Caspase-11 mediates the expression of inflammatory factors. These results suggest that both TRIF axis and TIRAP/Myd88/IRAK4 axis can regulate Caspase-11 expression and lead to increased expression of IL-1β after METH exposure.

Silencing of TLR4 Expression Reduces METH-Induced IL-1β and IL-18 Expression *in Vivo*

To confirm the role of TLR4 in METH-induced IL-1β and IL-18 expression *in vivo*, TAK-242, a specific inhibitor of TLR4, was injected to the mice to inhibit TLR4 expression in the brain. After TAK-242 pre-treatment, mice were treated with saline or METH (n = 3/group). Western blot analysis showed METH exposure significantly induced TLR4 protein expression; and this effect was substantially attenuated by pre-treatment with TAK-242 in the striatum ($F_{(1,11)} = 8.407$, $P = 0.02$) and midbrain ($F_{(1,11)} = 80.867$, $P < 0.001$; **Figures 8A,A1,B,B1**). Previously, we demonstrated that IL-1β and IL-18 were regulated by TLR4 *in vitro* (**Figures 4B,C**). Next, we explored whether silencing TLR4 can decrease METH-induced neuroinflammation in the mouse striatum and midbrain. We measured IL-1β and IL-18 protein expression in each treatment group. We found that METH-induced expression of IL-1β (striatum: $F_{(1,11)} = 6.752$, $P = 0.032$; midbrain: $F_{(1,11)} = 13.907$, $P = 0.006$) and IL-18 (striatum: $F_{(1,11)} = 23.073$, $P = 0.001$; midbrain: $F_{(1,11)} = 6.8389$, $P = 0.031$) both were decreased after pre-treatment with TAK-242 (**Figures 8A5,A6,B5,B6**). These results were consistent with those *in vitro*. To further affirm the relationship of Caspase-11 and TLR4, NF-κB and ASC protein expression was measured with Western blot. Decreased expression after inhibiting TLR4 expression with TAK-242 was detected for NF-κB (striatum: $F_{(1,11)} = 7.736$, $P = 0.024$; midbrain: $F_{(1,11)} = 47.831$, $P < 0.001$), Caspase-11 (striatum: $F_{(1,11)} = 6.361$, $P = 0.036$; midbrain: $F_{(1,11)} = 97.043$, $P < 0.001$) and ASC (striatum:

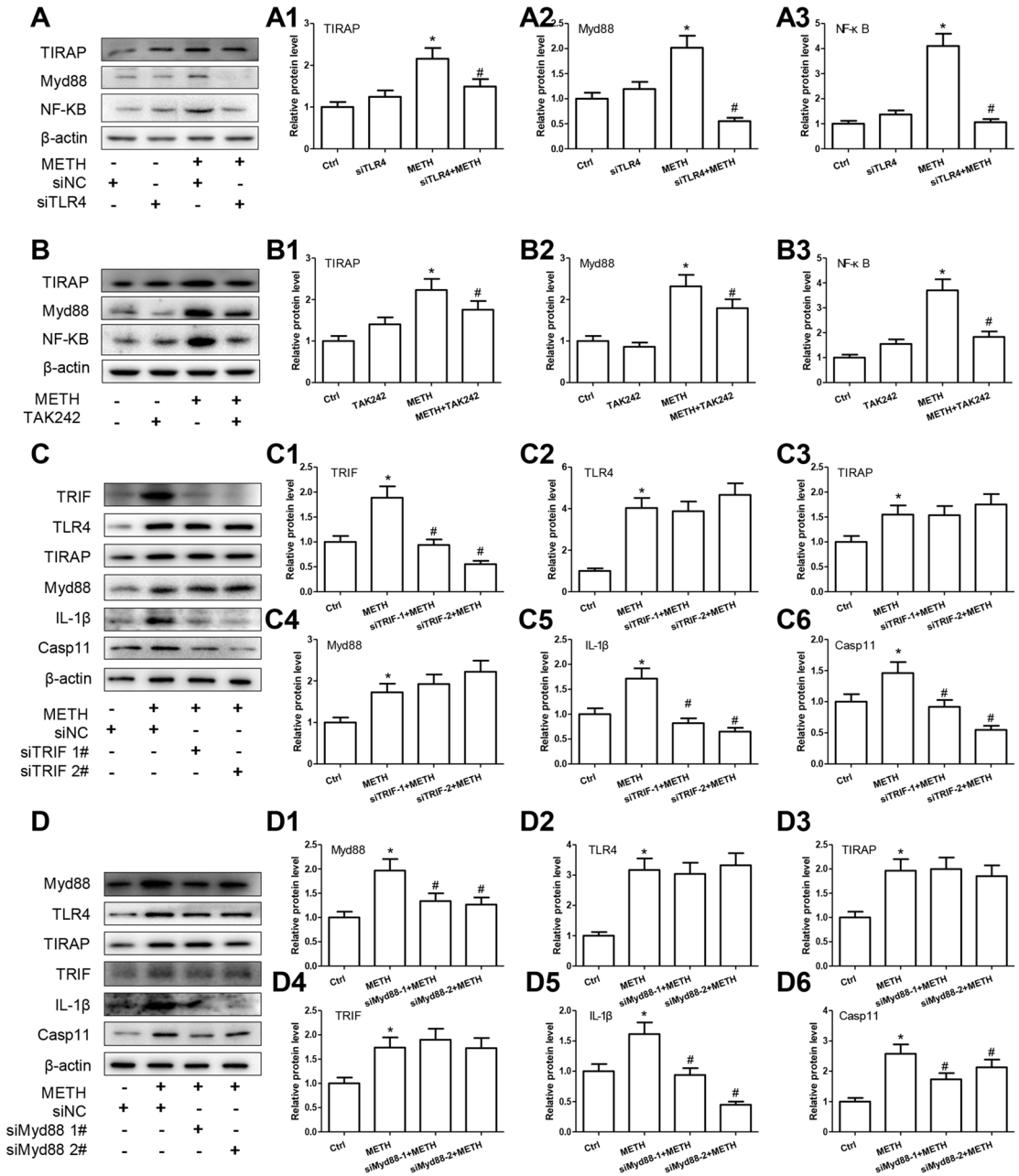

FIGURE 7 | TLR4 mediates METH-induced IL-1β and IL-18 expression through both Myd88-dependent and Myd88-independent signaling pathways. Primary cultured astrocytes transfected with siRNAs targeting TLR4 **(A–A3)**, TRIF **(C–C6)**, Myd88 **(D–D6)** or control siRNA for 24 h followed by METH (2 mM) treatment for 24 h. Cells were exposed to TAK-242 (100 nM) **(B–B3)** for 2 h prior to METH (2 mM) treatment as indicated. Western blot **(A–D)** and quantitative analyses were performed to determine TLR4, TRIF, TIRAP, Myd88, NF-κB, Caspase-11 and/or IL-1β protein expression. All the experiments were repeated three times. Data are expressed as mean ± SD. $^{*}p < 0.05$ vs. non-METH-treated group. $^{\#}p < 0.05$ vs. the scrambled + METH treated group. Data in **(A,B)** were analyzed with 2 × 2 factorial ANOVA followed by LSD *post hoc* analyses; data in **(C,D)** were analyzed with two-way ANOVA followed by LSD *post hoc* analyses.

$F_{(1,11)} = 10.593$, $P = 0.012$; midbrain: $F_{(1,11)} = 15.005$, $P = 0.005$; **Figures 8A2–A4,B2–B4**). These results indicate that the Caspase-11 pathway is involved in TLR4-mediated METH-induced neuroinflammation *in vivo*.

DISCUSSION

Recent studies have demonstrated that METH can stimulate glial cells in the CNS, suggesting that neurotoxicity of METH

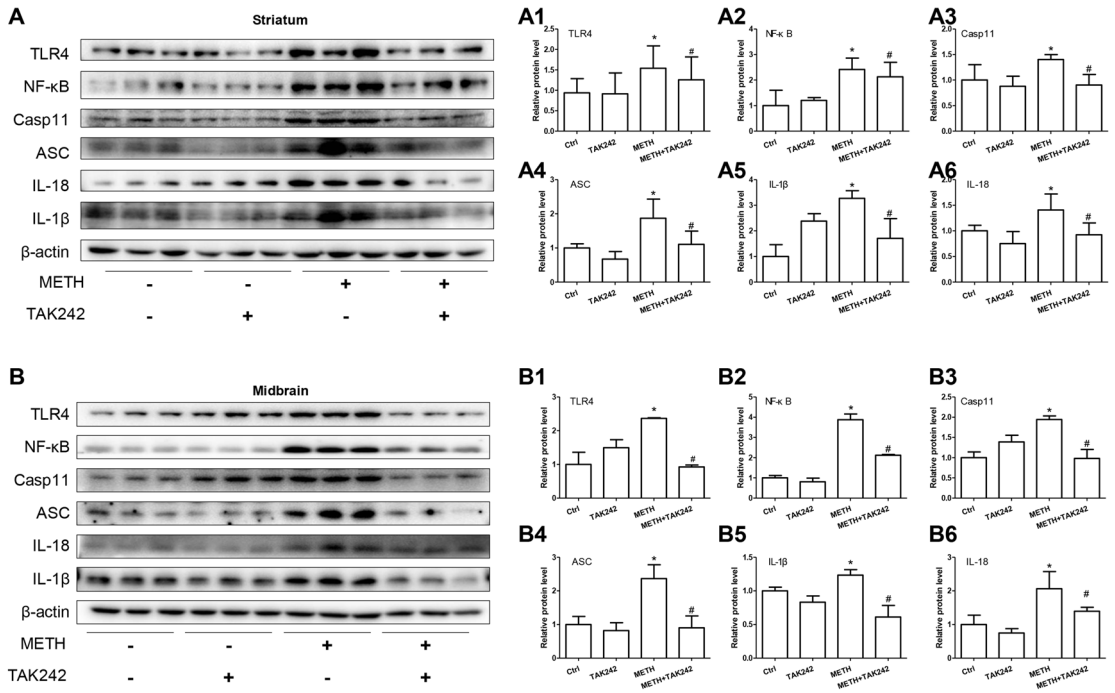

FIGURE 8 | Silencing of TLR4 expression reduces METH-induced IL-1β and IL-18 expression *in vivo*. Mice were exposed to saline vehicle, METH, TAK-242, or METH + TAK-242 as described in the methods section and in **Figure 4** legend. Striatum and midbrain tissues were harvested at 24 h after the last dosing. Western blot **(A,B)** and quantitative analyses **(A1–A6,B1–B6)** were performed to determine TLR4, NF-κB, Caspase-11, ASC, IL-18 and IL-1β protein expression. Data are expressed as mean ± SD. $^{*}p < 0.05$ vs. non-METH-treated group. $^{\#}p < 0.05$ vs. METH-treated group. Data were analyzed with 2 × 2 factorial ANOVA followed by LSD *post hoc* analyses.

could be partially due to neuroinflammation response, which includes astrocyte activation (Cisneros and Ghorpade, 2014; Borgmann and Ghorpade, 2015). In the present study, we report that TLR4 expression is increased after METH exposure *in vivo* and *in vitro*. Furthermore, we for the first time demonstrate that Caspase-11 plays an important role in METH-induced astrocyte stimulation and the NLRP3 inflammasome promotes the pro-inflammatory cytokine expression.

As the most abundant cell type in the brain, the primary roles of astrocytes include the protection of neurons, participation in myelination, expression of glutamate transporters, involvement of glutamate transport in the CNS, and a part of inflammation effects (Loftis and Janowsky, 2014; Zhang et al., 2017a). The results of inflammatory response are generally harmful, including regulation of microglia activation and the expression of inflammatory factors that could directly damage the neurons. Activation of astrocytes has a dual effect. Astrocyte hyperplasia can beneficially provide nutritional support for neurons and maintain the steady balance of the surrounding environment (Loftis and Janowsky, 2014; Singh and Abraham, 2017). While the hyperactive astrocytes may cause neuroinflammation, leading to an increase release of pro-inflammatory cytokines. In this study, we found that 2.0 mM of METH could increase the secretion of pro-inflammatory cytokines in astrocytes, and upregulate the expression of pro-inflammatory cytokines in the midbrain and striatum of C57BL/6 mice. Studies have shown that METH-treated astrocytes can produce neuroinflammation, oxidative stress and excitotoxicity, as well as morphological changes of the blood-brain barrier (Cisneros and Ghorpade, 2014; Loftis and Janowsky, 2014). However, the relationship between METH-induced astrocyte activation and production of proinflammatory cytokines remains to be investigated.

TLR4 is one type of immune pattern recognition receptors, which are the first defense of the body's immune response (Krawczyk-Michalak et al., 2008; Matsunaga et al., 2011; Fang et al., 2013; Shirjang et al., 2017). Studies have reported that heroin can induce the activation of TLR4 on the cell surface, which in turn mediates the occurrence of inflammatory responses (Theberge et al., 2013). Here, we demonstrate that METH exposure induces the expression of TLR4 and TLR4 promotes the expression of NF-κB through both the TRIF signaling axis (Myd88 independent pathway) and the TIRAP/Myd88/IRAK4 signaling axis (Myd88 dependent pathway), leading to increased nuclear transcription of inflammatory cytokines. Specifically, following METH exposure, the expression levels of TRIF (the key protein of the Myd88 independent pathway) and Myd88 (the key protein of the Myd88 dependent pathway) were both increased; and these effects were normalized or significantly attenuated after inhibiting TLR4 expression by siRNA or TAK-242. Of

note, the expression of NF-κB was also increased by METH, and this effect was significantly attenuated after inhibiting TLR4 expression by siRNA or TAK-242. These results suggest that the activation of NF-κB by METH may be through the TLR4 pathway.

The present study revealed the important role of TLR4 in astrocytes in METH-induced neuroinflammation, but TLR4 is not unique to astrocytes in the brain. In this study, we determined the co-localization of TLR4 expression in different brain cell types. We observed that METH treatment induced the expression of TLR4 and co-localization of TLR4 with GFAP (marker of astrocytes) and Iba1 (marker of microglia). We also observed that part of the NeuN (marker of neurons) expression was co-localized with TLR4 (methods and results provided in the Supplementary Figure S1). Studies of other neurological disease models have shown that TLR4 plays an important role in the pathogenesis of a variety of neuro-inflammation and is expressed in microglia and neurons (Wang et al., 2014; Baek et al., 2017; Chen et al., 2017; Lawrimore and Crews, 2017; Rocha Sobrinho et al., 2017). Our results suggest that METH treatment could also induce TLR4 activation in microglia and neurons. The role of microglia in METH-induced neuro-inflammation and the interactions of astrocytes with microglia and neurons in METH neurotoxicity are a direction of future research.

Caspase-11 mediates non-classical inflammatory responses and increases the release of pro-inflammatory cytokines, which has been demonstrated in other immune cell models (Viganò and Mortellaro, 2013; Coutermarsh-Ott et al., 2016). While previous studies mainly focused on macrophages (Viganò and Mortellaro, 2013), in this study, we used primary cultured astrocytes to mimic the response of astrocytes *in vivo* and to reveal the regulatory mechanism of Caspase-11. Previous studies of Caspase-11 mainly demonstrated that it was stimulated by LPS or other extracellular stimuli, resulting in the occurrence of inflammatory response (Kayagaki et al., 2011, 2013, 2015; Shi et al., 2015). Our studies showed that METH could also cause inflammatory response through Caspase-11. The expression of Caspase-11 decreased after silencing of TLR4, while the expression of TLR4 had no change after Caspase-11 silencing. Besides, the expression of Caspase-11 decreased after silencing of Myd88 and TRIF, indicating that the expression of Caspase-11 is activated by both Myd88-dependent and independent pathways of TLR4.

There is also an interesting finding in this study that the NLRP3 inflammasome is involved in Caspase-11-

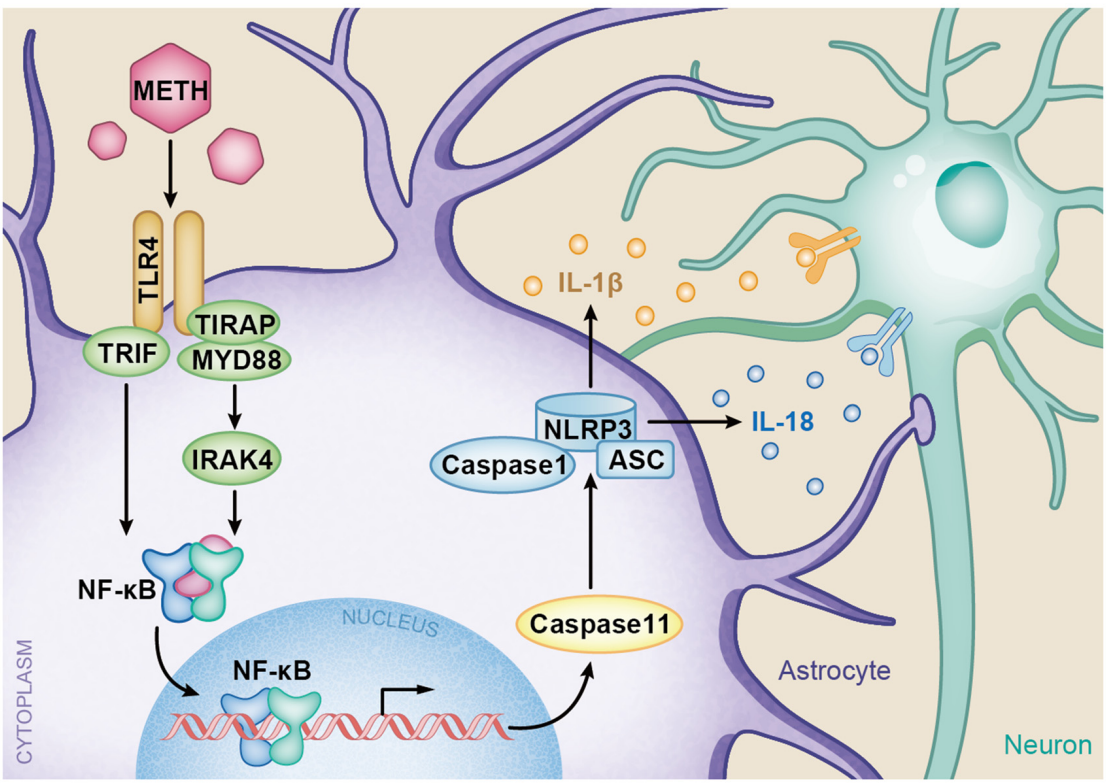

FIGURE 9 | A schematic depicting the role of TLR4-NFkB-Caspase-11 signaling pathway in METH-induced astrocyte-related neuroinflammation. Briefly, TLR4 expression is increased following METH treatment. Increased TLR4 upregulates the expression of Myd88 and TRIF. The Myd88-dependent and Myd88-independent pathways upregulate the expression of transcription factor NF-κB. Then NF-κB elevates Caspase-11 expression, which mediates the inflammasome NLRP3 pathway by upregulating the expression of Caspase-1 and ASC. The increased NLRP3 inflammasomes induce the expression of pro-inflammatory cytokines IL-1β and IL-18.

mediated neuroinflammation caused by METH in astrocytes. Caspase-11-dependent NLRP3 inflammasome activation was also reported during gram-negative bacterial infection (Rathinam et al., 2012). This indicates that METH might cause neuroinflammation through Caspase-11-mediated non-classical inflammatory pathway. However, we found that METH could only increase ASC and Caspase-1 expression, while NLRP3 expression was not changed. This may be due to that fact that a higher proportion of Caspase-1 is involved in the composition of the inflammasome complex (Wang et al., 1998; Man et al., 2017) and METH may primarily activate Caspase-1, rather than increase the overall expression of inflammasome NLRP3 itself, thereby inducing an increase in downstream inflammatory factors. Of note, there is also a classical pathway in which the increased expression of inflammatory factors can be induced by Caspase-1 directly (Youm et al., 2013; Man et al., 2017). Further studies are needed to determine whether Caspase-11 plays a role in the non-inflammasome NLRP3 pathway in the METH-induced astrocyte activation.

CONCLUSION

In summary, the present study provides insights into the molecular mechanisms of TLR4 and Caspase-11-mediated METH-induced neuroinflammation in astrocytes. A schematic depicting the proposed mechanisms of METH-induced astrocyte neuroinflammation is provided in **Figure 9**. Specifically, METH can increase TLR4 and Caspase-11 expression *in vitro* and *in vivo*, and TLR4 plays an important role in astrocyte neuroinflammation induced by METH. The increased activation of the TLR4-regulated neuroinflammation is through both Myd88-dependent and independent pathways. As a transcription factor, NF-κB upregulates the expression of Caspase-11, resulting in upregulation of NLRP3 inflammasome, which mediates the increased expression levels of IL-1β and IL-18 after METH exposure. However, the underlying mechanisms of whether or not Caspase-11 could directly regulate pro-inflammatory cytokine expression need further research. Further studies are also needed to determine the exact mechanisms of neuronal apoptosis and autophagy regulated by astrocyte-related neuroinflammation in METH acute exposure models.

ETHICS STATEMENT

All procedures involving animals were performed in accordance with the ethical standards of Ethics Committee of Nanfang Hospital, Southern Medical University and with the 1964 Helsinki Declaration and its later amendments or comparable ethical standards. This article does not contain any studies with humans performed by any of the authors.

AVAILABILITY OF DATA AND MATERIAL

The authors declare that the data supporting the findings of this study are available within the article.

AUTHOR CONTRIBUTIONS

S-HD and D-FQ conducted all the experiments with the help of C-XC and SC. W-BX and HW designed the research. W-BX, S-HD, CL and ZL analyzed and interpreted the results. W-BX and S-HD wrote the manuscript with the help of ZL.

FUNDING

This work was supported by the Natural Science Foundation of China (Grant No. 81430045 to HW and Grant No. 81370227 to W-BX).

ACKNOWLEDGMENTS

The authors thank Prof. Ande Ma and Dr. Juan Du for their help of the mass spectrometry analysis of METH. The authors also thank Guangzhou Sagene Biotech Co., Ltd. for their help of pattern diagram making.

SUPPLEMENTARY MATERIAL

The Supplementary Material for this article can be found online at: https://www.frontiersin.org/articles/10.3389/fnmol.2017.00409/full#supplementary-material

REFERENCES

Abdul Muneer, P. M., Alikunju, S., Szlachetka, A. M., and Haorah, J. (2011). Methamphetamine inhibits the glucose uptake by human neurons and astrocytes: stabilization by acetyl-L-carnitine. *PLoS One* 6:e19258. doi: 10.1371/journal.pone.0019258

Andres, M. A., Cooke, I. M., Bellinger, F. P., Berry, M. J., Zaporteza, M. M., Rueli, R. H., et al. (2015). Methamphetamine acutely inhibits voltage-gated calcium channels but chronically up-regulates L-type channels. *J. Neurochem.* 134, 56–65. doi: 10.1111/jnc.13104

Baek, H., Shin, H. J., Kim, J. J., Shin, N., Kim, S., Yi, M. H., et al. (2017). Primary cilia modulate TLR4-mediated inflammatory responses in hippocampal neurons. *J. Neuroinflammation* 14:189. doi: 10.1186/s12974-017-0958-7

Billod, J. M., Lacetera, A., Guzmán-Caldentey, J., and Martín-Santamaria, S. (2016). Computational approaches to toll-like receptor 4 modulation. *Molecules* 21:E994. doi: 10.3390/molecules21080994

Borgmann, K., and Ghorpade, A. (2015). HIV-1, methamphetamine and astrocytes at neuroinflammatory Crossroads. *Front. Microbiol.* 6:1143. doi: 10.3389/fmicb.2015.01143

Bortell, N., Basova, L., Semenova, S., Fox, H. S., Ravasi, T., and Marcondes, M. C. G. (2017). Astrocyte-specific overexpressed gene signatures in response to methamphetamine exposure *in vitro*. *J. Neuroinflammation* 14:49. doi: 10.1186/s12974-017-0825-6

Brempelis, K. J., Yuen, S. Y., Schwarz, N., Mohar, I., and Crispe, I. N. (2017). Central role of the TIR-domain-containing adaptor-inducing interferon-β (TRIF) adaptor protein in murine sterile liver injury. *Hepatology* 65, 1336–1351. doi: 10.1002/hep.29078

Cadet, J. L., Jayanthi, S., and Deng, X. (2003). Speed kills: cellular and molecular bases of methamphetamine-induced nerve terminal degeneration and neuronal apoptosis. *FASEB J.* 17, 1775–1788. doi: 10.1096/fj.03-0073rev

Cai, D., Huang, E., Luo, B., Yang, Y., Zhang, F., Liu, C., et al. (2016). Nupr1/Chop signal axis is involved in mitochondrion-related endothelial cell apoptosis induced by methamphetamine. *Cell Death Dis.* 7:e2161. doi: 10.1038/cddis.2016.67

Cao, L., Fu, M., Kumar, S., and Kumar, A. (2016). Methamphetamine potentiates HIV-1 gp120-mediated autophagy via Beclin-1 and Atg5/7 as a pro-survival response in astrocytes. *Cell Death Dis.* 7:e2425. doi: 10.1038/cddis.2016.317

Carmena, A., Granado, N., Ares-Santos, S., Alberquilla, S., Tizabi, Y., and Moratalla, R. (2015). Methamphetamine-induced toxicity in indusium griseum of mice is associated with astro- and microgliosis. *Neurotox. Res.* 27, 209–216. doi: 10.1007/s12640-014-9505-9

Chen, T., Li, H., Yin, Y., Zhang, Y., Liu, Z., and Liu, H. (2017). Interactions of Notch1 and TLR4 signaling pathways in DRG neurons of *in vivo* and *in vitro* models of diabetic neuropathy. *Sci. Rep.* 7:14923. doi: 10.1038/s41598-017-15053-w

Chen, C., Qincao, L., Xu, J., Du, S., Huang, E., Liu, C., et al. (2016). Role of PUMA in methamphetamine-induced neuronal apoptosis. *Toxicol. Lett.* 240, 149–160. doi: 10.1016/j.toxlet.2015.10.020

Cisneros, I. E., and Ghorpade, A. (2014). Methamphetamine and HIV-1-induced neurotoxicity: role of trace amine associated receptor 1 cAMP signaling in astrocytes. *Neuropharmacology* 85, 499–507. doi: 10.1016/j.neuropharm.2014.06.011

Coutermarsh-Ott, S. L., Doran, J. T., Campbell, C., Williams, T. M., Lindsay, D. S., and Allen, I. C. (2016). Caspase-11 modulates inflammation and attenuates toxoplasma gondii pathogenesis. *Mediators Inflamm.* 2016:9848263. doi: 10.1155/2016/9848263

Dolunay, A., Senol, S. P., Temiz-Resitoglu, M., Guden, D. S., Sari, A. N., Sahan-Firat, S., et al. (2017). Inhibition of NLRP3 inflammasome prevents LPS-induced inflammatory hyperalgesia in mice: contribution of NF-κB, caspase-1/11, ASC, NOX, and NOS isoforms. *Inflammation* 40, 366–386. doi: 10.1007/s10753-016-0483-3

Fang, H., Chen, J., Lin, S., Wang, P., Wang, Y., Xiong, X., et al. (2014). CD36-mediated hematoma absorption following intracerebral hemorrhage: negative regulation by TLR4 signaling. *J. Immunol.* 192, 5984–5992. doi: 10.4049/jimmunol.1400054

Fang, H., Wang, P. F., Zhou, Y., Wang, Y. C., and Yang, Q. W. (2013). Toll-like receptor 4 signaling in intracerebral hemorrhage-induced inflammation and injury. *J. Neuroinflammation* 10:27. doi: 10.1186/1742-2094-10-27

Fernandes, N. C., Sriram, U., Gofman, L., Cenna, J. M., Ramirez, S. H., and Potula, R. (2016). Methamphetamine alters microglial immune function through P2X7R signaling. *J. Neuroinflammation* 13:91. doi: 10.1186/s12974-016-0553-3

Granado, N., Lastres-Becker, I., Ares-Santos, S., Oliva, I., Martin, E., Cuadrado, A., et al. (2011). Nrf2 deficiency potentiates methamphetamine-induced dopaminergic axonal damage and gliosis in the striatum. *Glia* 59, 1850–1863. doi: 10.1002/glia.21229

Hebert, M. A., and O'Callaghan, J. P. (2000). Protein phosphorylation cascades associated with methamphetamine-induced glial activation. *Ann. N Y Acad. Sci.* 914, 238–262. doi: 10.1111/j.1749-6632.2000.tb05200.x

Huang, Y. N., Wu, C. H., Lin, T. C., and Wang, J. Y. (2009). Methamphetamine induces heme oxygenase-1 expression in cortical neurons and glia to prevent its toxicity. *Toxicol. Appl. Pharmacol.* 240, 315–326. doi: 10.1016/j.taap.2009.06.021

Huang, W., Xie, W., Qiao, D., Qiu, P., Huang, E., Li, B., et al. (2015). Caspase-11 plays an essential role in methamphetamine-induced dopaminergic neuron apoptosis. *Toxicol. Sci.* 145, 68–79. doi: 10.1093/toxsci/kfv014

Ii, M., Matsunaga, N., Hazeki, K., Nakamura, K., Takashima, K., Seya, T., et al. (2006). A novel cyclohexene derivative, ethyl (6*R*)-6-[*N*-(2-Chloro-4-fluorophenyl)sulfamoyl] cyclohex-1-ene-1-carboxylate (TAK-242), selectively inhibits toll-like receptor 4-mediated cytokine production through suppression of intracellular signaling. *Mol. Pharmacol.* 69, 1288–1295. doi: 10.1124/mol.105.019695

Kayagaki, N., Stowe, I. B., Lee, B. L., O'Rourke, K., Anderson, K., Warming, S., et al. (2015). Caspase-11 cleaves gasdermin D for non-canonical inflammasome signalling. *Nature* 526, 666–671. doi: 10.1038/nature15541

Kayagaki, N., Warming, S., Lamkanfi, M., Vande Walle, L., Louie, S., Dong, J., et al. (2011). Non-canonical inflammasome activation targets caspase-11. *Nature* 479, 117–121. doi: 10.1038/nature10558

Kayagaki, N., Wong, M. T., Stowe, I. B., Ramani, S. R., Gonzalez, L. C., Akashi-Takamura, S., et al. (2013). Noncanonical inflammasome activation by intracellular LPS independent of TLR4. *Science* 341, 1246–1249. doi: 10.1126/science.1240248

Kempuraj, D., Thangavel, R., Natteru, P. A., Selvakumar, G. P., Saeed, D., Zahoor, H., et al. (2016). Neuroinflammation induces neurodegeneration. *J. Neurol. Neurosurg. Spine* 1:1003.

Kiyatkin, E. A., and Sharma, H. S. (2009). Acute methamphetamine intoxication: brain hyperthermia, blood-brain barrier, brain edema, and morphological cell abnormalities. *Int. Rev. Neurobiol.* 88, 65–100. doi: 10.1016/S0074-7742(09)88004-5

Krasnova, I. N., and Cadet, J. L. (2009). Methamphetamine toxicity and messengers of death. *Brain Res. Rev.* 60, 379–407. doi: 10.1016/j.brainresrev.2009.03.002

Krawczyk-Michalak, K., Glapiński, A., and Brzezińska-Baszczyk, E. (2008). Toll-like receptors and their role in regulation of the inflammatory response in sepsis. *Anestezjol. Intens. Ter.* 40, 253–259.

Lawrimore, C. J., and Crews, F. T. (2017). Ethanol, TLR3, and TLR4 agonists have unique innate immune responses in neuron-like SH-SY5Y and microglia-like BV2. *Alcohol. Clin. Exp. Res.* 41, 939–954. doi: 10.1111/acer.13368

Li, B., Chen, R., Chen, L., Qiu, P., Ai, X., Huang, E., et al. (2017). Effects of DDIT4 in methamphetamine-induced autophagy and apoptosis in dopaminergic neurons. *Mol. Neurobiol.* 54, 1642–1660. doi: 10.1007/s12035-015-9637-9

Liu, B., Teschemacher, A. G., and Kasparov, S. (2017). Astroglia as a cellular target for neuroprotection and treatment of neuro-psychiatric disorders. *Glia* 65, 1205–1226. doi: 10.1002/glia.23136

Loftis, J. M., and Janowsky, A. (2014). Neuroimmune basis of methamphetamine toxicity. *Int. Rev. Neurobiol.* 118, 165–197. doi: 10.1016/B978-0-12-801284-0.00007-5

Man, S. M., Karki, R., Briard, B., Burton, A., Gingras, S., Pelletier, S., et al. (2017). Differential roles of caspase-1 and caspase-11 in infection and inflammation. *Sci. Rep.* 7:45126. doi: 10.1038/srep45126

Matsunaga, N., Tsuchimori, N., Matsumoto, T., and Ii, M. (2011). TAK-242 (resatorvid), a small-molecule inhibitor of Toll-like receptor (TLR) 4 signaling, binds selectively to TLR4 and interferes with interactions between TLR4 and its adaptor molecules. *Mol. Pharmacol.* 79, 34–41. doi: 10.1124/mol.110.068064

Mendieta, L., Granado, N., Aguilera, J., Tizabi, Y., and Moratalla, R. (2016). Fragment C domain of tetanus toxin mitigates methamphetamine neurotoxicity and its motor consequences in mice. *Int. J. Neuropsychopharmacol.* 19:pyw021. doi: 10.1093/ijnp/pyw021

Meng, X. F., Tan, L., Tan, M. S., Jiang, T., Tan, C. C., Li, M. M., et al. (2014). Inhibition of the NLRP3 inflammasome provides neuroprotection in rats following amygdala kindling-induced status epilepticus. *J. Neuroinflammation* 11:212. doi: 10.1186/s12974-014-0212-5

Pal, R., Tiwari, P. C., Nath, R., and Pant, K. K. (2016). Role of neuroinflammation and latent transcription factors in pathogenesis of Parkinson's disease. *Neurol. Res.* 38, 1111–1122. doi: 10.1080/01616412.2016.1249997

Planès, R., Ben Haij, N., Leghmari, K., Serrero, M., BenMohamed, L., and Bahraoui, E. (2016). HIV-1 tat protein activates both the MyD88 and TRIF pathways to induce tumor necrosis factor α and interleukin-10 in human monocytes. *J. Virol.* 90, 5886–5898. doi: 10.1128/JVI.00262-16

Qiao, D., Xu, J., Le, C., Huang, E., Liu, C., Qiu, P., et al. (2014). Insulin-like growth factor binding protein 5 (IGFBP5) mediates methamphetamine-induced dopaminergic neuron apoptosis. *Toxicol. Lett.* 230, 444–453. doi: 10.1016/j.toxlet.2014.08.010

Rathinam, V. A., Vanaja, S. K., Waggoner, L., Sokolovska, A., Becker, C., Stuart, L. M., et al. (2012). TRIF licenses caspase-11-dependent NLRP3 inflammasome activation by gram-negative bacteria. *Cell* 150, 606–619. doi: 10.1016/j.cell.2012.07.007

Roberts, J. S., and Yilmaz, Ö. (2015). Dangerous liaisons: caspase-11 and reactive oxygen species crosstalk in pathogen elimination. *Int. J. Mol. Sci.* 16, 23337–23354. doi: 10.3390/ijms161023337

Rocha Sobrinho, H. M. D., Silva, D. J. D., Gomides, L. F., Dorta, M. L., Oliveira, M. A. P., and Ribeiro-Dias, F. (2017). TLR4 and TLR2 activation is differentially associated with age during Parkinson's disease. *Immunol. Invest.* 27, 1–18. doi: 10.1080/08820139.2017.1379024

Shabab, T., Khanabdali, R., Moghadamtousi, S. Z., Kadir, H. A., and Mohan, G. (2017). Neuroinflammation pathways: a general review. *Int. J. Neurosci.* 127, 624–633. doi: 10.1080/00207454.2016.1212854

Shen, Y., Qin, H., Chen, J., Mou, L., He, Y., Yan, Y., et al. (2016). Postnatal activation of TLR4 in astrocytes promotes excitatory synaptogenesis in hippocampal neurons. *J. Cell Biol.* 215, 719–734. doi: 10.1083/jcb.201605046

Shi, J., Zhao, Y., Wang, K., Shi, X., Wang, Y., Huang, H., et al. (2015). Cleavage of GSDMD by inflammatory caspases determines pyroptotic cell death. *Nature* 526, 660–665. doi: 10.1038/nature15514

Shirjang, S., Mansoori, B., Solali, S., Hagh, M. F., and Shamsasenjan, K. (2017). Toll-like receptors as a key regulator of mesenchymal stem cell function: an up-to-date review. *Cell. Immunol.* 315, 1–10. doi: 10.1016/j.cellimm.2016.12.005

Singh, A., and Abraham, W. C. (2017). Astrocytes and synaptic plasticity in health and disease. *Exp. Brain Res.* 235, 1645–1655. doi: 10.1007/s00221-017-4928-1

Theberge, F. R., Li, X., Kambhampati, S., Pickens, C. L., St Laurent, R., Bossert, J. M., et al. (2013). Effect of chronic delivery of the Toll-like receptor 4 antagonist (+)-naltrexone on incubation of heroin craving. *Biol. Psychiatry* 73, 729–737. doi: 10.1016/j.biopsych.2012.12.019

Van Acker, T., Eyckerman, S., Vande Walle, L., Gerlo, S., Goethals, M., Lamkanfi, M., et al. (2014). The small GTPase Arf6 is essential for the Tram/Trif pathway in TLR4 signaling. *J. Biol. Chem.* 289, 1364–1376. doi: 10.1074/jbc.M113.499194

Viganò, E., and Mortellaro, A. (2013). Caspase-11: the driving factor for noncanonical inflammasomes. *Eur. J. Immunol.* 43, 2240–2245. doi: 10.1002/eji.201343800

Wang, S., Miura, M., Jung, Y. K., Zhu, H., Li, E., and Yuan, J. (1998). Murine caspase-11, an ICE-interacting protease, is essential for the activation of ICE. *Cell* 92, 501–509. doi: 10.1016/s0092-8674(00)80943-5

Wang, X., Wang, C., Wang, J., Zhao, S., Zhang, K., Wang, J., et al. (2014). Pseudoginsenoside-F11 (PF11) exerts anti-neuroinflammatory effects on LPS-activated microglial cells by inhibiting TLR4-mediated TAK1/IKK/NF-κB, MAPKs and Akt signaling pathways. *Neuropharmacology* 79, 642–656. doi: 10.1016/j.neuropharm.2014.01.022

Whitney, N. P., Eidem, T. M., Peng, H., Huang, Y., and Zheng, J. C. (2009). Inflammation mediates varying effects in neurogenesis: relevance to the pathogenesis of brain injury and neurodegenerative disorders. *J. Neurochem.* 108, 1343–1359. doi: 10.1111/j.1471-4159.2009.05886.x

Winek, C. L., Wahba, W. W., Winek, C. L. Jr., and Balzer, T. W. (2001). Drug and chemical blood-level data 2001. *Forensic Sci. Int.* 122, 107–123. doi: 10.1016/s0379-0738(01)00483-2

Wu, X. F., Wang, A. F., Chen, L., Huang, E. P., Xie, W. B., Liu, C., et al. (2014). S-Nitrosylating protein disulphide isomerase mediates α-synuclein aggregation caused by methamphetamine exposure in PC12 cells. *Toxicol. Lett.* 230, 19–27. doi: 10.1016/j.toxlet.2014.07.026

Xu, X., Huang, E., Tai, Y., Zhao, X., Chen, X., Chen, C., et al. (2017). Nupr1 modulates methamphetamine-induced dopaminergic neuronal apoptosis and autophagy through CHOP-Trib3-mediated endoplasmic reticulum stress signaling pathway. *Front. Mol. Neurosci.* 10:203. doi: 10.3389/fnmol.2017.00203

Yan, B., Wang, D., Dong, S., Cheng, Z., Sang, M., Yang, H., et al. (2017). Palmatine inhibits TRIF-dependent NF-κB pathway against inflammation induced by LPS in goat endometrial epithelial cells. *Int. Immunopharmacol.* 45, 194–200. doi: 10.1016/j.intimp.2017.02.004

Youm, Y. H., Grant, R. W., McCabe, L. R., Albarado, D. C., Nguyen, K. Y., Ravussin, A., et al. (2013). Canonical Nlrp3 inflammasome links systemic low-grade inflammation to functional decline in aging. *Cell Metab.* 18, 519–532. doi: 10.1016/j.cmet.2013.09.010

Zanoni, I., Tan, Y., Di Gioia, M., Broggi, A., Ruan, J., Shi, J., et al. (2016). An endogenous caspase-11 ligand elicits interleukin-1 release from living dendritic cells. *Science* 352, 1232–1236. doi: 10.1126/science.aaf3036

Zhang, Y., He, X., Meng, X., Wu, X., Tong, H., Zhang, X., et al. (2017a). Regulation of glutamate transporter trafficking by Nedd4–2 in a Parkinson's disease model. *Cell Death Dis.* 8:e2574. doi: 10.1038/cddis.2016.454

Zhang, Y., He, X., Wu, X., Lei, M., Wei, Z., Zhang, X., et al. (2017b). Rapamycin upregulates glutamate transporter and IL-6 expression in astrocytes in a mouse model of Parkinson's disease. *Cell Death Dis.* 8:e2611. doi: 10.1038/cddis.2016.491

Zhang, Y., Lv, X., Bai, Y., Zhu, X., Wu, X., Chao, J., et al. (2015). Involvement of sigma-1 receptor in astrocyte activation induced by methamphetamine via up-regulation of its own expression. *J. Neuroinflammation* 12:29. doi: 10.1186/s12974-015-0250-7

Zhu, K., Mu, H., and Pi, B. (2016). Regulatory effect of caspase-11 on interleukin-1β in the fungal keratitis. *Pak. J. Pharm. Sci.* 29, 2327–2334.

Conflict of Interest Statement: The authors declare that the research was conducted in the absence of any commercial or financial relationships that could be construed as a potential conflict of interest.

frontiers in Molecular Neuroscience

ORIGINAL RESEARCH
published: 14 August 2017
doi: 10.3389/fnmol.2017.00261

Regulation of Microglia and Macrophage Polarization via Apoptosis Signal-Regulating Kinase 1 Silencing after Ischemic/Hypoxic Injury

*So Yeong Cheon[1,2], Eun Jung Kim[1,2], Jeong Min Kim[1,2], Eun Hee Kam[1,2], Byung Woong Ko[1] and Bon-Nyeo Koo[1,2]**

[1] Department of Anesthesiology and Pain Medicine, Yonsei University College of Medicine, Seoul, South Korea, [2] Anesthesia and Pain Research Institute, Yonsei University College of Medicine, Seoul, South Korea

Inflammation is implicated in ischemic stroke and is involved in abnormal homeostasis. Activation of the immune system leads to breakdown of the blood–brain barrier and, thereby, infiltration of immune cells into the brain. Upon cerebral ischemia, infiltrated macrophages and microglia (resident CNS immune cell) are activated, change their phenotype to M1 or M2 based on the microenvironment, migrate toward damaged tissue, and are involved in repair or damage. Those of M1 phenotype release pro-inflammatory mediators, which are associated with tissue damage, while those of M2 phenotype release anti-inflammatory mediators, which are related to tissue recovery. Moreover, late inflammation continually stimulates immune cell infiltration and leads to brain infarction. Therefore, regulation of M1/M2 phenotypes under persistent inflammatory conditions after cerebral ischemia is important for brain repair. Herein, we focus on apoptosis signal-regulating kinase 1 (ASK1), which is involved in apoptotic cell death, brain infarction, and production of inflammatory mediators after cerebral ischemia. We hypothesized that ASK1 is involved in the polarization of M1/M2 phenotype and the function of microglia and macrophage during the late stage of ischemia/hypoxia. We investigated the effects of ASK1 in mice subjected to middle cerebral artery occlusion and on BV2 microglia and RAW264.7 macrophage cell lines subjected to oxygen-glucose deprivation. Our results showed that ASK1 silencing effectively reduced Iba-1 or CD11b-positive cells in ischemic areas, suppressed pro-inflammatory cytokines, and increased anti-inflammatory mediator levels at 7 days after cerebral ischemia. In cultured microglia and macrophages, ASK1 inhibition, induced by NQDI-1 drug, decreased the expression and release of M1-associated factors and increased those of M2-associated factors after hypoxia/reperfusion (H/R). At the gene level, ASK1 inhibition suppressed M1-associated genes and augmented M2-associated genes. In gap closure assay, ASK1 inhibition reduced the migration rate of microglia and macrophages after H/R. Taken together, our results provide new

OPEN ACCESS

Edited by:
Clevio Nobrega, University of Algarve, Portugal

Reviewed by:
Tobias Engel, Royal College of Surgeons in Ireland, Ireland
Albert Quintana, Universitat Autònoma de Barcelona, Spain
Liliana Simões Mendonça, Centro de Neurociências e Biologia Celular (CNC), Portugal

***Correspondence:**
Bon-Nyeo Koo
koobn@yuhs.ac

Received: *31 May 2017*
Accepted: *31 July 2017*
Published: *14 August 2017*

Citation:
Cheon SY, Kim EJ, Kim JM, Kam EH, Ko BW and Koo B-N (2017) Regulation of Microglia and Macrophage Polarization via Apoptosis Signal-Regulating Kinase 1 Silencing after Ischemic/Hypoxic Injury. Front. Mol. Neurosci. 10:261. doi: 10.3389/fnmol.2017.00261

information that suggests ASK1 controls the polarization of M1/M2 and the function of microglia and macrophage under sustained-inflammatory conditions. Regulation of persistent inflammation via M1/M2 polarization by ASK1 is a novel strategy for repair after ischemic stroke.

Keywords: apoptosis signal-regulating kinase 1 (ASK1), M1/M2 polarization, BV2 microglia cell line, RAW264.7 macrophage cell line, cerebral ischemia, hypoxia, late inflammation, ischemic stroke

INTRODUCTION

Inflammation is a key contributor to the pathophysiology of ischemic stroke and is responsible for abnormal homeostasis (Amantea et al., 2009; Denes et al., 2010; Iadecola and Anrather, 2011). After ischemic insults, activation of the immune system causes leakiness of the blood–brain barrier (BBB), and immune cells such as macrophages, neutrophils and leukocytes, infiltrate the lesion area via the disrupted BBB (Amantea et al., 2009; Denes et al., 2010; Iadecola and Anrather, 2011). Recruitment of immune cells results in initiation of inflammatory processes in the brain parenchyma, which include both tissue damage and repair (Fu et al., 2015). Although inflammation is involved in all phases of ischemic cascade (Iadecola and Anrather, 2011), late inflammation in the brain, particularly after ischemic stroke, provokes persistent immune cell recruitment and eventually aggravates cerebral infarcts (Mena et al., 2004; Vogelgesang et al., 2014). Therefore, regulation of late inflammation in ischemic stroke is considered important to prevent development of subsequent brain damage.

Once activated, microglia and infiltrated macrophages are able to modify their morphology and function by switching between M1 and M2 phenotypes (Tugal et al., 2013; Sica et al., 2015). A classical (M1) polarized phenotype secretes Th1 cytokines and pro-inflammatory mediators, such as interleukin (IL)-6, IL-1β, and tumor necrosis factor (TNF)-α, which are involved in tissue damage and prolong the neuro-inflammatory response (Tugal et al., 2013; Sica et al., 2015; Qin et al., 2016). The alternative (M2) phenotype releases Th2 cytokines and anti-inflammatory mediators including transforming growth factor (TGF)-β, IL-4, IL-10, and arginase (arg-1), which are associated with prevention of inflammation, tissue repair, and neuro-protection (Tugal et al., 2013; Sica et al., 2015; Qin et al., 2016). Although little is known about the relationship between the chronic phase of cerebral ischemia and immune cell phenotype modulating the exaggerated inflammatory environment after ischemic stroke via regulation of M1/M2 polarization could be a therapeutic aim.

After I/R injury, the excessive accumulation of reactive oxygen species (ROS) in cells induces oxidative stress and subsequent damage (Cheon et al., 2013). ROS is a key player in the pathophysiology of cerebral ischemia and ASK1 is known as the initial responder of ROS (Kim et al., 2011; Cheon et al., 2016b). Also, ASK1 is activated by various stimuli, such as oxidative stress, calcium overload, and receptor-mediated inflammatory signals (Hayakawa et al., 2006; Takeda et al., 2008). After ischemic insult, ASK1 immediately promotes intracellular signaling and induces apoptotic cell death, and down-regulation of ASK1 diminishes cell death and cerebral infarct. Previous studies demonstrated that ASK1 is associated with brain edema (Kim et al., 2011; Song et al., 2015). In addition, in mammals, ASK1 has been shown to modify innate immunity and to be required for inflammatory response (Matsukawa et al., 2004; Hayakawa et al., 2006; Takeda et al., 2008). ASK1 deficiency leads to suppression of lipopolysaccharide (LPS)-induced inflammatory cytokine production, such as IL-6, IL-1β, and TNF-α in splenocytes and bone marrow-derived dendritic cells (BMDCs). Also, in an LPS-induced sepsis model, ASK1-deficient mice shows resistance against LPS injury (Matsukawa et al., 2004; Takeda et al., 2008). Further, in primary microglia cell culture, ASK1 is found to be closely related to TNF-α and iNOS production (Katome et al., 2013). Class A scavenger receptor suppresses M1 macrophages, thereby reducing IL-6, IL-1β, and TNF-α in accordance with the dampening of ASK1/p38/NF-κB pathway (Hu et al., 2011). In this study, we focused on ASK1 and we hypothesized that ASK1 is likely to affect inflammation via modulation of M1/M2 polarization after I/R injury. Therefore, we examined whether ASK1 could modulate polarization of microglia and macrophage in mice after ischemic injury and in cultured BV2 microglia and RAW264.7 macrophage cell lines after hypoxic injury.

MATERIALS AND METHODS

Mouse Focal Cerebral Ischemia Model

All animal experiments in this study were conducted in accordance by the Guide for the Care and Use of Laboratory Animal Care and were approved by Institutional Animal Care and Use Committee (IACUC) in Yonsei University. Mice were provided free access to chow and water under a 12-h dark and light cycle. A total of 52, adult male C57BL/6 mice aged 8–12 weeks (Orient, Seongnam, Korea) were used in this study. To mimic ischemic stroke, we utilized a middle cerebral occlusion (MCAO) model. Anesthesia was induced with 5% isoflurane and maintained with 2% isoflurane in mixed gas. Mice were placed onto a homeothermic blanket, and a longitudinal incision was made along the midline of the neck. MCA was occluded with a 6-0 blue nylon suture for 1 h and mice were reperfused for 7 days. At 7 days after MCAO, Zoletil mixture (30 mg/kg; active ingredient: Zolezepam and Tiletamin; Virbac Laboratories, Carros, France) was injected intraperitoneally. Mice were cardiac-perfused with saline, and brains were isolated for immunohistochemistry and ELISA assay. The mice were divided into three groups: normal group (control), ischemia/reperfusion (I/R) group, and ischemia/reperfusion + si-ASK1 treated (I/R+si-ASK1) group.

siRNA Experiment

ASK1-siRNA was purchased from Ambion [Austin, TX, United States; sense, 5′-GCUGGUAAUUUAUACACuGtt-3′; antisense, 5′-CAGUGUAUAAAUUACGAGCtt–3′; conc, 5 μM (178.5–192.3 nM/g)] (Cheon et al., 2016b; Cho et al., 2016). Based on a previous study, a 100-μl solution mixed with siPORT*NeoFX* (Ambion) and ASK1-siRNA was administrated into the left ventricle of the mice by an osmotic pump with a brain infusion kit (Alzet, Cupertino, CA, United States) for 3 days before MCAO. The osmotic pump was planted subcutaneously on the dorsal side, and brain infusion cannula connected to the osmotic pump was placed on the left ventricle (mediolateral 1.0 mm, anteroposterior 0.2 mm, dorsoventral 3.0 mm). The hole in the skull was made by using a drill (Cheon et al., 2016b; Cho et al., 2016).

BV2 Microglia and RAW 264.7 Macrophage Cell Cultures

Murine brain microglia (BV2 cell line) were cultured with RPMI 1640 (Hyclone^{TM}, GE Healthcare Life Sciences, Logan, UT, United States) containing 10% fetal bovine serum (FBS, GE Healthcare Life Sciences) and 1% penicillin-streptomycin solution (Thermo Scientific, Waltham, MA, United States). Murine macrophages (RAW 264.7cell line) were cultured with DMEM high glucose cultured media (Hyclone^{TM}, GE Healthcare Life Sciences) containing 10% FBS (GE Healthcare Life Sciences) and 1% penicillin-streptomycin solution (Thermo Scientific) at 37°C. The cultured cells were incubated in a humid atmosphere under the presence of 5% CO_2 at 37°C.

Oxygen/Glucose Deprivation

To induce oxygen and glucose deprivation, microglia and macrophage cultures were transferred to an anaerobic chamber after being washed with phosphate buffer saline (PBS). Transferred cells were then cultured in deoxygenated glucose-free balanced solution (BSS_0) containing 5.36 mM KCl, 0.81 mM NaH_2PO_4, 0.81 mM $MgSO_4$, and116 mM NaCl, and incubated for 4 h in a 37°C anaerobic chamber. After 4 h, the cells were washed with PBS, the cultured media was changed, and cells were incubated for 24 h under the presence of 5% CO_2 at 37°C. To inhibit ASK1, the ASK1 inhibitor NQDI-1 drug (600 nM, Tocris Bioscience, Bristol, United Kingdom) was used in this study and was applied 1 h before hypoxia and 4 h during hypoxia.

Immunofluorescence Staining

Mice were cardiac-perfused with 4% formaldehyde, and brains specimens were fixed with 4% formaldehyde for 24 h. Fixed brains were immersed in 30% sucrose for 2 days and then frozen with OCT compound (Sakura Finetek Japan Co., Ltd., Tokyo, Japan) at −70°C in a deep freezer. Frozen brain tissues were sectioned coronally with a cryotome with 20-μm thickness and onto coated slide glass. After drying the slide at room temperature, sections were treated with Trion-X 100 (0.3%) for permeability over 1 h and treated blocking solution [5% bovine serum albumin (BSA)] at room temperature for 1 h. After washing with PBS, primary antibodies such as anti-Iba-1 (Abcam, Cambridge, United Kingdom), anti-CD11b (Millipore, Bedford, MA, United States), anti-CD206 (Abcam), and anti-ASK1 (Santa Cruz Biotechnology, Santa Cruz, CA, United States) were incubated, respectively, overnight at 4°C. Secondary antibody conjugated FITC or Rhodamine (Jackson ImmunoResearch Laboratories, West Grove, PA, United States) was used and incubated for 1 h at room temperature after washing with PBS. Slides were mounted with Vectashield with DAPI (Vector Laboratories Inc., Burlingame, CA, United States). The specimens were observed by using an LSM 700 confocal microscope (Carl Zeiss, Thornwood, NY, United States) and microscope (Olympus, Tokyo, Japan). Immunoreactivities for CD11b, Iba-1, CD206, and ASK1 were measured using ImageJ (ImageJ, Bethesda, MD, United States) and Zen 2010 software (Carl Zeiss) by analyzing the mean intensities, which apply a manual threshold above the background intensity. The mean intensities were analyzed by average intensity, obtained from three slice of each mouse. Three fields of the cortex, striatum, and hippocampus were randomly chosen from each specimen.

Cresyl Violet Staining

Brains of mice were isolated and fixed with 4% formaldehyde and sectioned coronally with a cryotome at a thickness of 20-μm. Sectioned brains were stained with filtered cresyl violet acetate (0.5%) (Sigma–Aldrich, St. Louis, MO, United States), which was dissolved in 300 mL distilled water with 10% glacial acetic acid. Slides were incubated with cresyl violet solution for 3 min at room temperature and coverslipped with permanent mounting medium (Vector Laboratories), and then, samples were observed under a microscope (Olympus).

Enzyme-Linked Immunosorbent Assay (ELISA)

To evaluated cytokine levels from tissue, BV2 microglia cell line, BV2 microglial supernatants, RAW 264.7 macrophage cell line and RAW264.7 macrophage supernatants, ELISA assays were performed according to commercial protocols. Levels of pro-inflammatory cytokines, such as IL-1β, IL-6, and TNF-α, and anti-inflammatory cytokines including IL-10, were measured. Samples were analyzed by High Sensitivity mouse IL-1 beta/IL-1F2, IL-6, TNF-alpha, and IL-10 Quantikine ELISA kits (R&D systems, Minneapolis, MN, United States). Following the manufacturer's instructions, reagents and standards in the ELISA kits were prepared, and prepared sample was added to each well with assay diluents and incubated. After washing with wash buffer for three times, samples were incubated with mouse IL-1β, IL-6, TNF-α, or IL-10 conjugates for 2 h at room temperature. After reactions completed, samples were read at a 450-nm wavelength by an ELISA reader.

Real-Time-PCR

To evaluate M1 and M2 phenotypes, BV2 microglia and RAW 264.7 macrophage cell lines were collected from which total RNA was extracted by using RNeasy® Mini Kit (QIAGEN, Austin, TX, United States). RNA concentration was assessed

using NanoDrop® ND-1000 (Thermo Scientific, NanoDrop Technologies, Wilmington, DE, United States). Real-time PCR was performed using the one-step SYBR PrimeScript RT-PCR Kit II (Perfect Real Time) (Takara Bio Inc., JAPAN) on an ABI StepOne Plus. PCR was performed in a total reaction mixture volume of 20 μl, composed of One step SYBR RT-PCR Buffer, PrimeScript 1 step Enzyme Mix 2, ROX Reference Dye, each forward primer (100 nM), each reverse primer (100 nM), and sample RNA diluted in RNase Free dH_2O. The RNA samples were used by 10-fold serial dilution. The primers were as follows: TNF-α: Forward (F) 5′-ACGGCATGGATCTCAAAGAC-3′, Reverse (R) 5′-AGATAG CAAATCGGCTGACG-3′, IL-1β: (F) 5′-TGTCTTGGCCGAGG ACTAAGG-3′, (R) 5′-TGGGCTGGACTGTTTCTAATGC-3′, IL-6: (F) 5′-TCCAGTTGCCTTCTTGGGAC-3′, (R) 5′-GTG TAATTAAGCCTCCGACTTG-3′, iNOS: (F) 5′- CAGCTGG GCTGTACAAACCTT-3′, (R) 5′-CATTGGAAGTGAAGCGTT TCG-3′, Cxcl10: (F) 5′-GGATGGCTGTCCTAGCTCTG-3′, (R) 5′-TGAGCTAGGGAGGACAAGGA-3′, IL-10: (F) 5′-GCTCT TACTGACTGGCATGAG-3′, (R) 5′-CGCAGCTCTAGGAGCA TGTG-3′, Ym-1: (F) 5′-GGGCATACCTTTATCCTGAG-3′, (R) 5′-CCACTGAAGTCATCCATGTC-3′, ASK1: (F) 5′-AGGACGG AGACTGTGAGGGT-3′, (R) 5′-GTCCTGCATAGACGATCC CAT-3′, GAPDH: (F) 5′-CCATTTGCAGTGGCAAAG-3′, (R) 5′-CACCCCATTTGATGTTAGTG-3′. The standard curve and melt curve analysis were used and cycling threshold (*C*t) values were normalized to *C*t values of housekeeping gene. The values were presented by relative quantity (RQ). The results were analyzed by StepOnesoftware v2.3.

Gap Closure Assay

Microglia or macrophages were seeded in 60-mm dishes 1 day prior to experimentation. A gap was made with a sterile, 1000-μl, blue pipette tip, and dishes were washed with DPBS to remove cell culture media and cell debris. Cultured cells underwent oxygen and glucose deprivation for 4 h and were transferred to normal culture media in a 37°C anaerobic chamber. Cells were incubated for 24 h in a 37°C anaerobic chamber, and images were obtained using inverted microscope with a digital camera (Leica, MC179, Wetzlar, Germany).

Flow Cytometry Analysis of BV2 Microglia and RAW 264.7 Macrophage Cell Lines

BV2 microglia and RAW264.7 macrophage cell line were collected and washed with DPBS. FACS buffer [Dulbecco's Phosphate-Buffered Saline (PBS) with 2% Fetal Bovine Serum, 0.09% Sodium Azide] (BD Pharmingen^{TM}, BD Biosciences, San Hose, CA, United States) were added to cells and incubated for 10 min. Next, cells were centrifuged at 250 *g* for 3 min, and the pellet was resuspended with 500 μl of FACS buffer. Cells were blocked with mouse Fc blocking solution (1:50, BD Biosciences) for 10 min on ice and centrifuged at 250 *g* for 3 min at 4°C. Cells were then stained with the following antibodies: mouse anti-CD40-FITC (1:50 MACS Miltenyi Biotec, Bergisch Gladbach, Germany) and mouse anti-CD206-PE (1:50, BD Pharmingen^{TM}, BD biosciences) for 30 min on ice. Cell suspensions were then filtered through a cell strainer with a 40-μm nylon mesh. Cell fluorescence was acquired using flow cytometry with a LSR II analyzer (BD Pharmingen^{TM}, BD biosciences). Data were analyzed using FlowJo software, version10 (FLOWJO, LLC, Ashland, OR, United States).

TUNEL Assay

Terminal deoxynucleotidyl transferase dUTP nick end labeling (TUNEL) assay was performed to evaluate DNA fragmentation. We used TUNEL assay kit, purchased from Roche Diagnostics (Indianapolis, IN, United States), and performed according to the manufacturer's manual. Counterstaining was performed with propidium iodide (PI) (Sigma–Aldrich) and the number of TUNEL-positive cells was counted in three 100 μm × 100 μm squares of each specimen and expressed as the number of TUNEL-positive cells square millimeter.

Statistical Analysis

Data are presented as the mean ± standard deviation (SD). Statistical comparisons between the groups were assessed with non-parametric Mann–Whitney test (Prism version 5.0 software, GraphPad Software, San Diego, CA, United States). Statistical significance among groups was assigned to *p*-values less than 0.05.

RESULTS

Increase in Microglia/Infiltrated Macrophages Reduced in the Ischemic Cortex and Striatum after ASK1 Silencing

The previous study showed that siRNA for ASK1 significantly reduces ASK1 level (Kim et al., 2011; Cheon et al., 2016b). In this study, we followed this method and confirmed immunohistochemistry for ASK1 with/without administration of siRNA for ASK1 at 7 days after I/R. We observed that ischemia-induced ASK1 expression was efficiently reduced after ASK1 silencing (Supplementary Figure 1A). In addition, at 3 days after I/R, we performed real-time PCR for ASK1. Upregulated ASK1 transcripts after I/R significantly diminished after ASK1 silencing (Supplementary Figure 1B). Ischemic injury induces a functional change in the brain and leads to cell death, the morphological changes of which were observed. To observe cell morphology after cerebral ischemia, we performed cresyl violet staining 7 days after (I/R) (**Figure 1A**). As shown in **Figure 1A**, cell bodies observed in the cortex and striatum in the I/R group were smaller and thinner than those in the control group. After silencing ASK1, we observed comparatively rounder and healthier cell bodies, compared with those of the I/R group, at 7 days after I/R. To examine microglia and infiltrated macrophages, we used microglia and macrophage markers, such as Iba-1 and CD11b, respectively (**Figure 1B**). In the control group, Iba-1-positive and CD11b-positive cells were rarely observed in the cortex and striatum. However, Iba-1-positive and CD11b-positive cells were

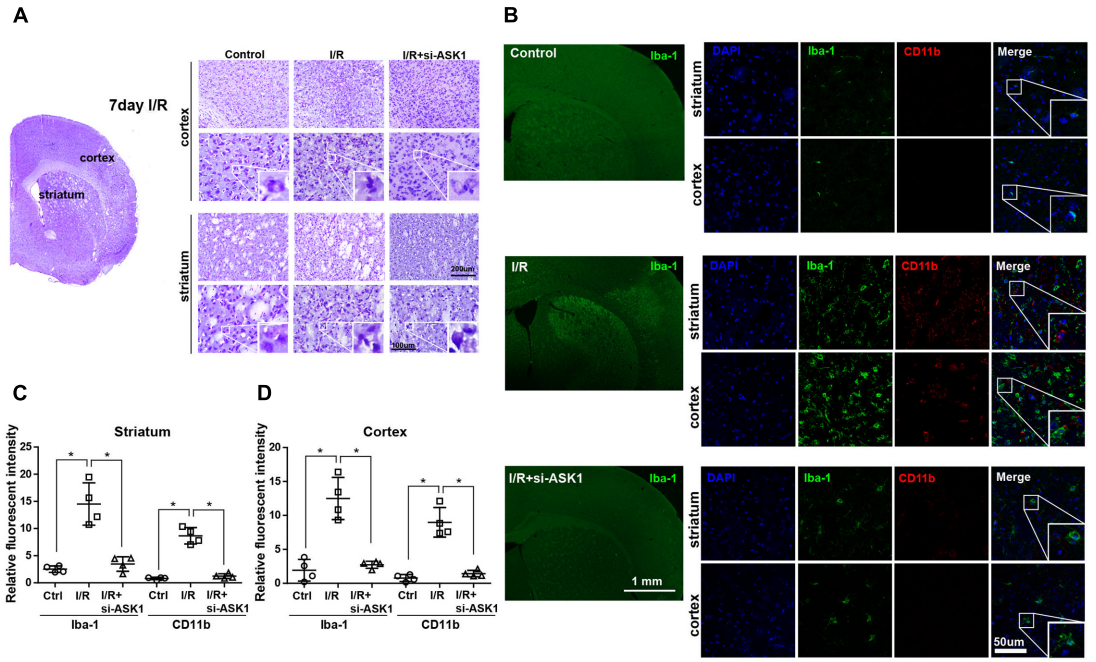

FIGURE 1 | Decreased microglia and macrophage markers in the striatum and cortex, respectively, upon ASK1 silencing at 7 days after cerebral ischemia. **(A)** Cresyl violet staining for cell histology in the cortex and striatum shows that I/R-induced cell loss was not detected at 7 days in the I/R+si-ASK1 group. **(B)** Immunofluorescent staining for Iba-1 (green) and CD11b (red) in the cortex and striatum reveals that I/R-induced increase in Iba-1 or CD11b-positive cells were reduced in the I/R+si-ASK1 group at 7 days. **(C)** The graph shows the relative fluorescent intensities for Iba-1 and CD11b in the striatum ($n = 4$). **(D)** The graph indicates the relative fluorescent intensities for Iba-1 and CD11b in the cortex ($n = 4$). Values are means ± SD. Statistical comparisons between the groups were assessed with non-parametric Mann–Whitney test (*$p < 0.05$, **$p < 0.01$, ***$p < 0.001$ vs. I/R group). Statistical parameter (Supplementary Table 1). I/R, ischemia/reperfusion.

densely expressed in the I/R group. After silencing ASK1, Iba-1-positive and CD11b-positive cells decreased in the cortex and striatum, respectively, despite ischemic injury. The graphs for relative fluorescent intensity showed increased intensities for Iba-1 and CD11b were efficiently decreased after silencing ASK1, compared with the I/R group (**Figures 1C,D**). Therefore, our data showed that ASK1 silencing results in reduced microglia and macrophages in the ischemic cortex and striatum, respectively. Statistical parameters were shown in Supplementary Table 1.

Enhanced Microglia/Infiltrated Macrophages Eliminated in Ischemic Hippocampus Tissue after ASK1 Silencing

In hippocampus specimens stained with cresyl violet, cells in CA1 and CA3 were easily observed as violet-stained intact cell bodies. However, I/R decreased violet-stained cells in the CA1 and CA3 regions after 7 days. In contrast, ASK1 silencing by genetic manipulation inhibited the reduction of violet-stained cells caused by I/R injury (**Figure 2A**). Also, we evaluated the expression of Iba-1 and CD11b in the hippocampus, via immunofluorescent staining at 7 days after I/R (**Figure 2B**). In the control group, CA1 and CA3 regions of the hippocampus displayed small amounts of Iba-1-positive and CD11b-positive cells. In the I/R group, Iba-1-positive cells and CD11b-positive cells were largely founded in the CA1 and CA3 regions of the hippocampus. On the contrary, ASK1-silenced brain tissue showed decreased levels of Iba-1 and CD11b expression in CA1 and CA3, respectively. The graphs for relative fluorescent intensity showed enhanced intensities for Iba-1 and CD11b were efficiently diminished after silencing ASK1, compared with the I/R group (**Figures 2C,D**). These results indicated that ASK1 silencing leads to suppressed activation of microglia and macrophages in the hippocampus. Statistical parameters were shown in Supplementary Table 1.

Silencing ASK1 Diminishes Pro-inflammatory and Increases Anti-inflammatory Mediators in Ischemic Brain Tissue

Several studies have demonstrated that microglia and macrophages can release pro-inflammatory mediators, such as IL-1β, IL-6, and TNF-α, under pathologic conditions. To investigate whether ASK1 silencing can reduce the release of pro-inflammatory cytokines, we assessed the expression there in the ischemic hemisphere at 7 days after I/R using ELISA (**Figure 3**). Our results showed that cerebral ischemia induced upregulation of IL-6, TNF-α, and IL-1β significantly, when compared with that of the control group. After silence of ASK1, increased levels of IL-6, TNF-α, and IL-1β were efficiently

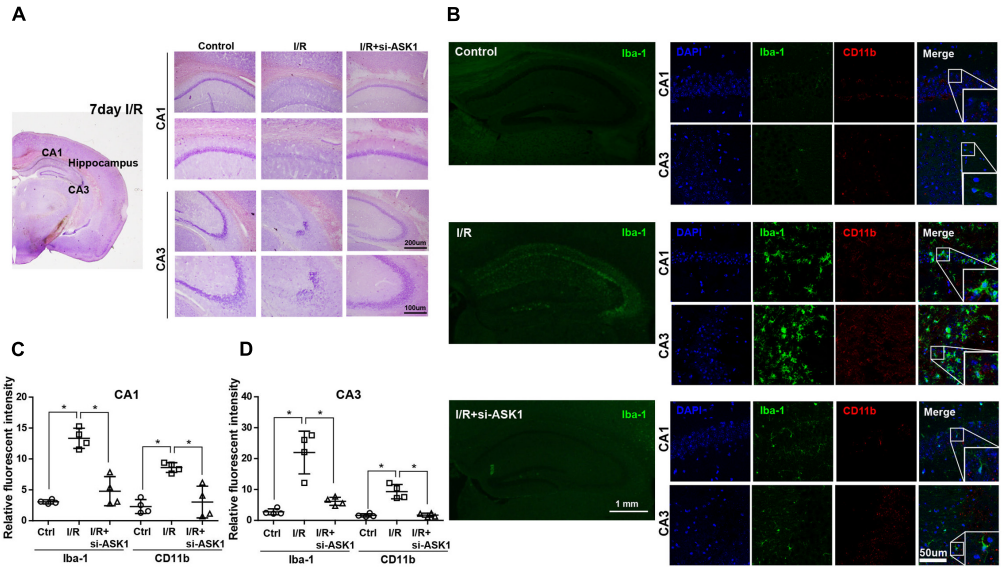

FIGURE 2 | Reduced microglia and macrophage markers in the hippocampus upon silence of ASK1 at 7 days after cerebral ischemia. **(A)** Cresyl violet staining for cell histology in the hippocampus shows that I/R-induced cell loss was not detected at 7 days in the I/R+si-ASK1 group. **(B)** Immunofluorescent staining for Iba-1 (green) and CD11b (red) in the hippocampus revealed that I/R-induced augmentation of Iba-1 or CD11b-positive cells was reduced in the I/R+si-ASK1 group at 7 days. **(C)** The graph shows the relative fluorescent intensities for Iba-1 and CD11b in the hippocampal CA1 region ($n = 4$). **(D)** The graph exhibits the relative fluorescent intensities for Iba-1 and CD11b in the hippocampal CA3 region ($n = 4$). Values are mean ± SD. Statistical comparisons between the groups were assessed with non-parametric Mann–Whitney test (*$p < 0.05$, **$p < 0.01$, ***$p < 0.001$ vs. I/R group). Statistical parameter (Supplementary Table 1). I/R, ischemia/reperfusion.

decreased in the ischemic hemisphere. Our ELISA data showed that ASK1 silencing reduces the expression of pro-inflammatory cytokines in the ischemic hemisphere (**Figures 3A–C**).

In addition, to examine whether ASK1 silencing can increase anti-inflammatory mediators, we performed immunofluorescent staining for CD206 (**Figure 3D**). Our results showed that CD206-positive cells in the control group were not significantly different between those in the I/R group; however, ASK1 silencing increased CD206-positive cells in the striatum and cortex (**Figures 3D–G**). To determine the effect of ASK1 on the cell fate, we performed TUNEL assay to detect DNA fragmentation at 7 days after I/R (Supplementary Figure 1C). The images and graphs showed that increased the number of TUNEL-positive cells in the striatum and cortex after I/R was efficiently reduced after ASK1 silencing. Therefore, our data showed that ASK1 silencing suppresses M1 phenotype and increases M2 phenotype in ischemic brain and reduces apoptotic cell death. Statistical parameters were shown in Supplementary Table 1.

Inhibition of ASK1 Downregulates Pro-inflammatory Mediators, but Upregulates Anti-Inflammatory Mediators in Cultured BV2 Microglia Cell Line and Supernatants

To investigate the effects of ASK1 on function of microglia, we performed single cell line cultures with BV2 cells and ELISA assay of cells (**Figures 4A–D**) and supernatants (**Figures 4E–H**). We used NQDI-1 drug *in vitro* to exclude effects of genetic manipulation unlike *in vivo* experiments. To identify the release of inflammatory mediators from BV2 microglia cell line, we also assayed cytokine levels in BV2 microglial supernatants. Our quantitative analysis showed that hypoxia/reperfusion (H/R) upregulated M1 phenotypes, reflected as release of IL-6, TNF-α, and IL-1β, both in BV2 microglia cell line (**Figures 4A–C**) and in BV2 microglial supernatants (**Figures 4E–G**). After treatment with NQDI-1 drug, an ASK1 inhibitor, the upregulated M1 mediators were efficiently reduced despite H/R injury. Although H/R could not alter IL-10 levels in BV2 microglia cell line (**Figure 4D**), compared with the control, NQDI-1 drug treatment upregulated secretion of IL-10 after H/R injury both in BV2 microglia cell line (**Figure 4D**) and in BV2 microglial supernatants (**Figure 4H**). Therefore, the results indicated that inhibition of ASK1 suppresses M1 phenotype and activates the alternative M2 phenotype in BV2 microglia cell line after H/R injury. Statistical parameters were shown in Supplementary Table 2.

Suppression of ASK1 Decreases Pro-inflammatory Mediators, but Increases Anti-Inflammatory Mediators in Cultured RAW 264.7 Macrophage Cell Line and Supernatants

To examine the effects of ASK1 on macrophage function, we performed single cell line cultures with RAW 264.7 cells and ELISA of cells and supernatants (**Figure 5**). Our results suggested that H/R injury triggered expression of M1-related

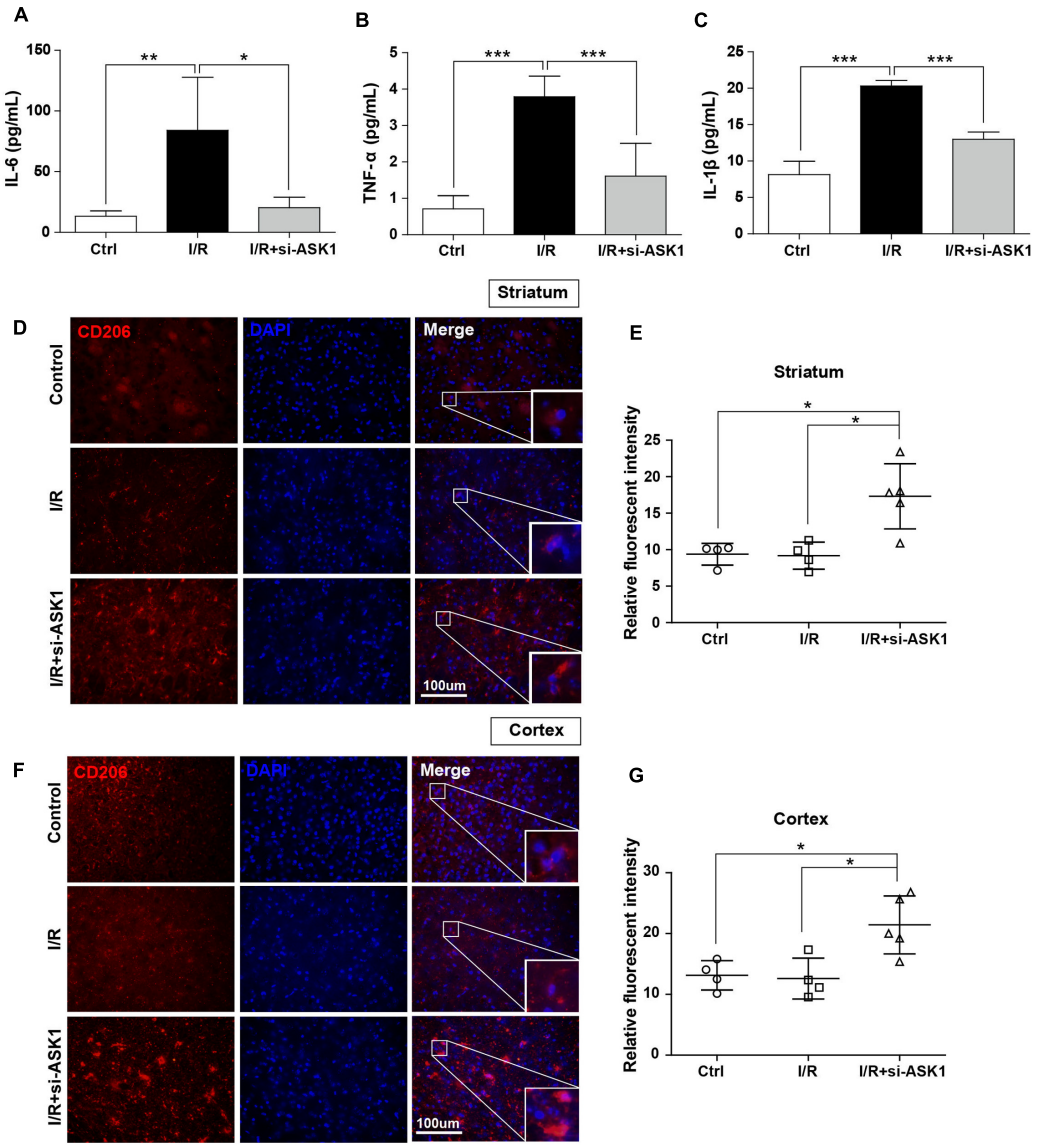

FIGURE 3 | Decreased pro-inflammatory and increased anti-inflammatory mediators in the ischemic brain by silencing of ASK1 at 7 days after cerebral ischemia. The levels of **(A)** IL-6, **(B)** TNF-α, and **(C)** IL-1β in the hemisphere were assessed by ELISA at 7 days after I/R. I/R-induced upregulation of **(A)** IL-6, **(B)** TNF-α, and **(C)** IL-1β was decreased in the I/R+si-ASK1 group at 7 days ($n = 8$). Immunofluorescent staining for CD206 was performed at 7 days after I/R **(D,F)**. **(D)** The relative intensity graph indicates CD206-positive cells were increased in the striatum **(E)** and cortex **(G)**, compared with other groups ($n = 4$–5). Values are mean ± SD. Statistical comparisons between the groups were assessed with non-parametric Mann–Whitney test (*$p < 0.05$, **$p < 0.01$, ***$p < 0.001$ vs. I/R group). Statistical parameter (Supplementary Table 1). I/R, ischemia/reperfusion.

mediators, such as IL-6, TNF-α, and IL-1β. However, suppression of ASK1 significantly decreased M1 phenotypes in RAW 264.7 cell line (**Figures 5A–C**) and in supernatants (**Figures 5E–G**). In addition, IL-10 levels were also increased after inhibition of ASK1 in spite of H/R injury, as compared with control and H/R injured macrophages, both in RAW 264.7 cell line (**Figure 5D**) and in supernatants (**Figure 5H**). Therefore, our data showed that inhibition of ASK1 reduces M1 phenotype and increases M2 phenotype in RAW 264.7 macrophage cell line. Statistical parameters were shown in Supplementary Table 2.

Inhibition of ASK1 Induces Transcription of M2 Polarization in BV2 Microglia and RAW 264.7 Macrophage Cell Lines

Genetic expression of M1 and M2 markers was quantified by real-time PCR in BV2 microglia (**Figure 6**) and in RAW 264.7 macrophage cell lines (**Figure 7**). Similar to cytokine levels evaluated by ELISA, the mRNA levels of M1 polarization-related factors such as IL-1β, TNF-α, inducible nitric oxide (iNOS), and CXCL10 were all significantly increased in BV2 microglia cell line after H/R injury (**Figures 6A–D**), and those of M2

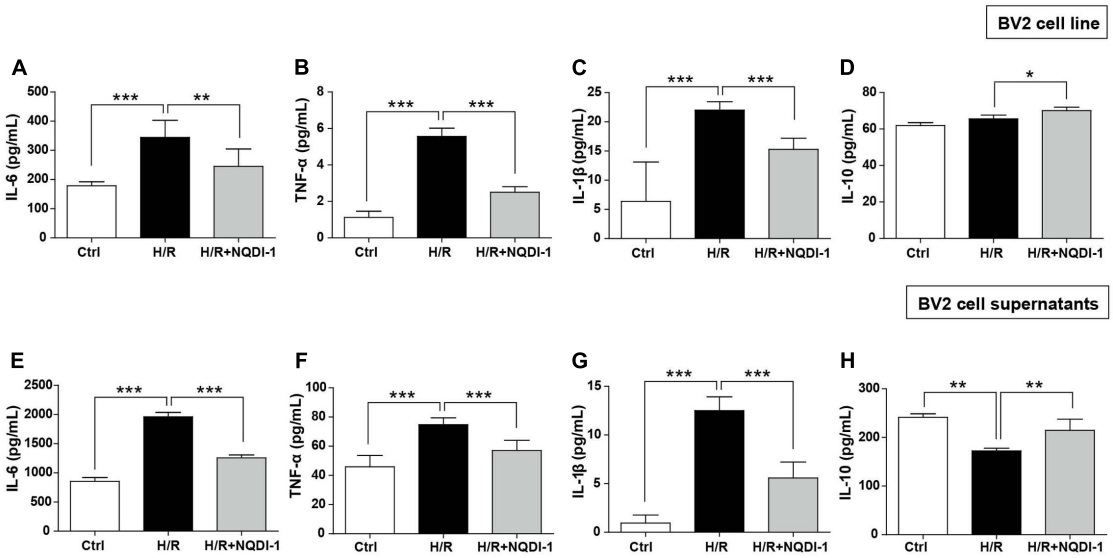

FIGURE 4 | Downregulated pro-inflammatory cytokines and upregulated anti-inflammatory cytokines after inhibition of ASK1 in cultured BV2 microglia cell line and supernatants. The levels of pro-inflammatory mediators, such as **(A)** IL-6, **(B)** TNF-α, and **(C)** IL-1β and the anti-inflammatory mediator **(D)** IL-10 were determined by ELISA in BV2 cell line after H/R (4 h/24 h). Increased **(A)** IL-6 (7 repeats), **(B)** TNF-α (8 repeats), and **(C)** IL-1β (8 repeats) levels after H/R were reduced and **(D)** IL-10 (4 repeats) levels were increased by inhibition of ASK1 in BV2 cell line. The levels of **(E)** IL-6, **(F)** TNF-α, and **(G)** IL-1β and the anti-inflammatory mediator **(H)** IL-10 were determined by ELISA in BV2 microglial supernatants after H/R (4 h/24 h). Upregulated levels of **(E)** IL-6 (9 repeats), **(F)** TNF-α (8 repeats), and **(G)** IL-1β (8 repeats) after H/R were decreased and downregulated levels of **(H)** IL-10 (5 repeats) were upregulated by inhibition of ASK1 in BV2 microglial supernatants. Values are mean ± SD. Statistical comparisons between the groups were assessed with non-parametric Mann–Whitney test (*$p < 0.05$, **$p < 0.01$, ***$p < 0.001$ vs. H/R). Statistical parameter (Supplementary Table 2). H/R, hypoxia/reperfusion.

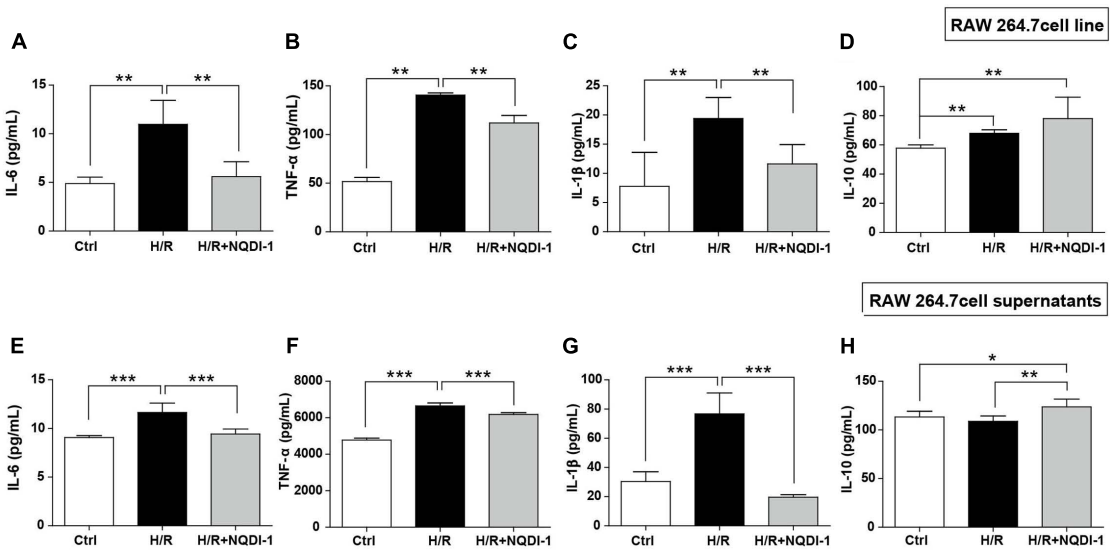

FIGURE 5 | Downregulated pro-inflammatory cytokines and upregulated anti-inflammatory cytokines after inhibition of ASK1 in cultured RAW264.7 macrophage cell line and supernatants. The levels of pro-inflammatory mediators such as **(A)** IL-6, **(B)** TNF-α, and **(C)** IL-1β and the anti-inflammatory mediator **(D)** IL-10 were determined by ELISA in RAW 264.7 cell line after H/R (4 h/24 h). Increased **(A)** IL-6 (6 repeats), **(B)** TNF-α (5 repeats), and **(C)** IL-1β (6 repeats) levels after H/R were decreased and **(D)** IL-10 (5 repeats) levels were increased by inhibition of ASK1 in RAW264.7 cell line. The levels of **(E)** IL-6, **(F)** TNF-α, and **(G)** IL-1β, and the anti-inflammatory mediator **(H)** IL-10 were determined by ELISA in RAW264.7 supernatants after H/R (4 h/24 h). Augmented **(A)** IL-6 (6 repeats), **(B)** TNF-α (6 repeats), and **(C)** IL-1β (6 repeats) levels after H/R were diminished and **(D)** IL-10 (6 repeats) levels were increased by inhibition of ASK1 in RAW264.7 supernatants. Values are mean ± SD. Statistical comparisons between the groups were assessed with non-parametric Mann–Whitney test (*$p < 0.05$, **$p < 0.01$, ***$p < 0.001$ vs. H/R). Statistical parameter (Supplementary Table 2). H/R, hypoxia/reperfusion.

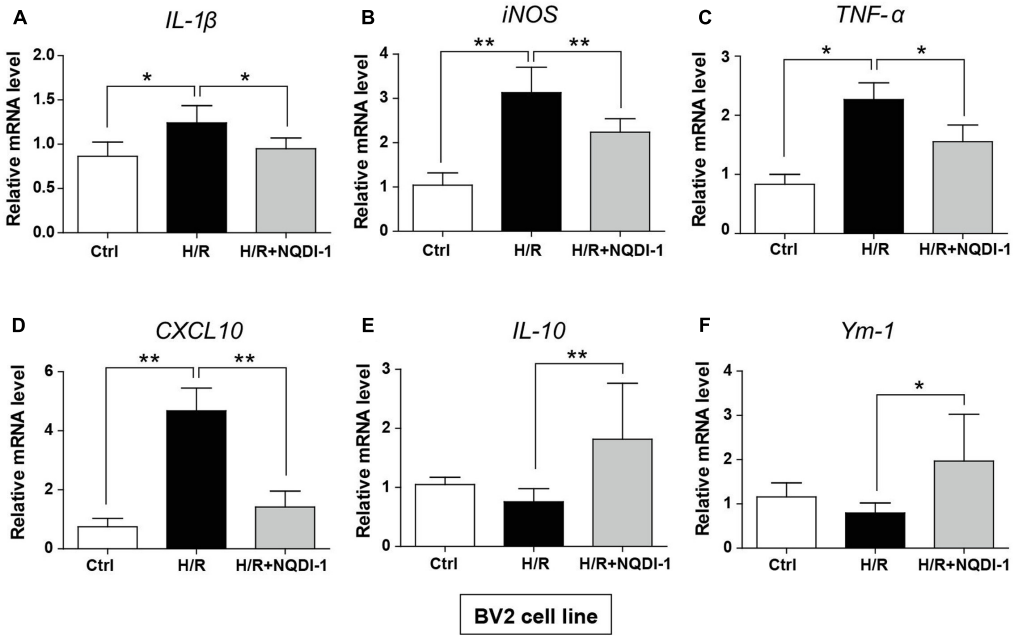

FIGURE 6 | Changes in M1 and M2 specific genes after inhibition of ASK1 in BV2 microglia cell line. The mRNA levels of M1 specific markers, such as **(A)** IL-1β (5 repeats), **(B)** iNOS (6 repeats), **(C)** TNF-α (5 repeats), and **(D)** CXCL10 (6 repeats), and M2 specific markers, such as **(E)** IL-10 (5 repeats), and **(F)** Ym-1 (4-5 repeats), were measured by real-time PCR in BV2 cell line after H/R (4 h/24 h). Increased mRNA levels of **(A)** IL-1β, **(B)** iNOS, **(C)** TNF-α, and **(D)** CXCL10 were downregulated, while **(E)** IL-10 and **(F)** Ym-1 levels were increased by inhibition of ASK1 in BV2 cell line. Values are mean ± SD. Statistical comparisons between the groups were assessed with non-parametric Mann–Whitney test (*$p < 0.05$, **$p < 0.01$, ***$p < 0.001$ vs. H/R group). Statistical parameter (Supplementary Table 3). H/R, hypoxia/reperfusion.

polarization-related factors such as IL-10 and Ym-1 showed no significant difference (**Figures 6E,F**). After treatment with NQDI-1 drug, mRNA levels of IL-1β, iNOS, TNF-α, and CXCL10 were all efficiently downregulated despite H/R injury (**Figures 6A–D**). The expression of M2-related factors including IL-10 and Ym-1 were remarkably higher in ASK1-inhibited BV2 microglia cell line (**Figures 6E,F**). Selected expression of M1 and M2 phenotypes was quantified by real-time PCR in RAW 264.7 macrophage cell line (**Figure 7**). As in the case of cytokine expression using ELISA, H/R induced mRNA levels of IL-1β, TNF-α, iNOS, and CXCL10 in macrophage cell line (**Figures 7A–D**). Treatment with NQDI-1 drug efficiently decreased mRNA levels of iNOS. Further, ASK1 inhibition induced anti-inflammatory IL-10 and Ym-1 mRNA levels, whereas H/R injury triggered M1-polarization (**Figures 7E,F**). Therefore, our data suggested that inhibition of ASK1 promotes BV2 microglia and RAW 264.7 macrophage cell lines toward M2 polarization after H/R injury. Statistical parameters were shown in Supplementary Table 3.

Inhibition of ASK1 Increases M2 Phenotype of Microglia and Macrophages

To confirm the expression of cell surface markers, we performed flow cytometry using BV2 microglia and RAW 264.7 macrophage cell lines. In this study, CD40 and CD206 were used as M1 and M2 markers, respectively (**Figure 8**). In BV2 cells, histograms showed that the expression of the M1 marker CD40 was highly present after H/R injury. However, NQDI-1 drug treatment reduced the expression of CD40-positive cells after H/R (**Figure 8A**). In the analysis of M2 phenotype, M2 marker (CD206-positive cells) was significantly increased on NQDI-1 drug treatment (**Figure 8B**). Moreover, in RAW 264.7 cells, histograms revealed higher counts of CD40-positive cells after H/R challenge, whereas inhibition of ASK1 decreased CD40-positive cell counts despite H/R injury (**Figure 8C**). In contrast, after suppression of ASK1 with NQDI-1 drug, the expression of CD206-positive cells was higher in the H/R stimulated RAW 264.7 cell line (**Figure 8D**). Statistical parameters were shown in Supplementary Table 3.

Microglia and Macrophage Hyper-Activation Is Reduced after Inhibition of ASK1

To analyze cell migration, we performed gap closure assay in cultured BV2 microglia and RAW 264.7 macrophage cell lines (**Figure 9**). Before H/R injury, we made a gap with a pipette tip, and cell debris was washed away with DPBS. We observed BV2 microglia cell line under a microscope immediately after H/R injury and at 24 h after H/R injury (**Figure 9A**). H/R injury increased migration rates of BV2 microglia cell line. However, inhibition of ASK1 reduced migration rates (**Figure 9B**). The same methods were used in RAW 264.7 macrophage cell culture. We observed RAW 264.7 cell line

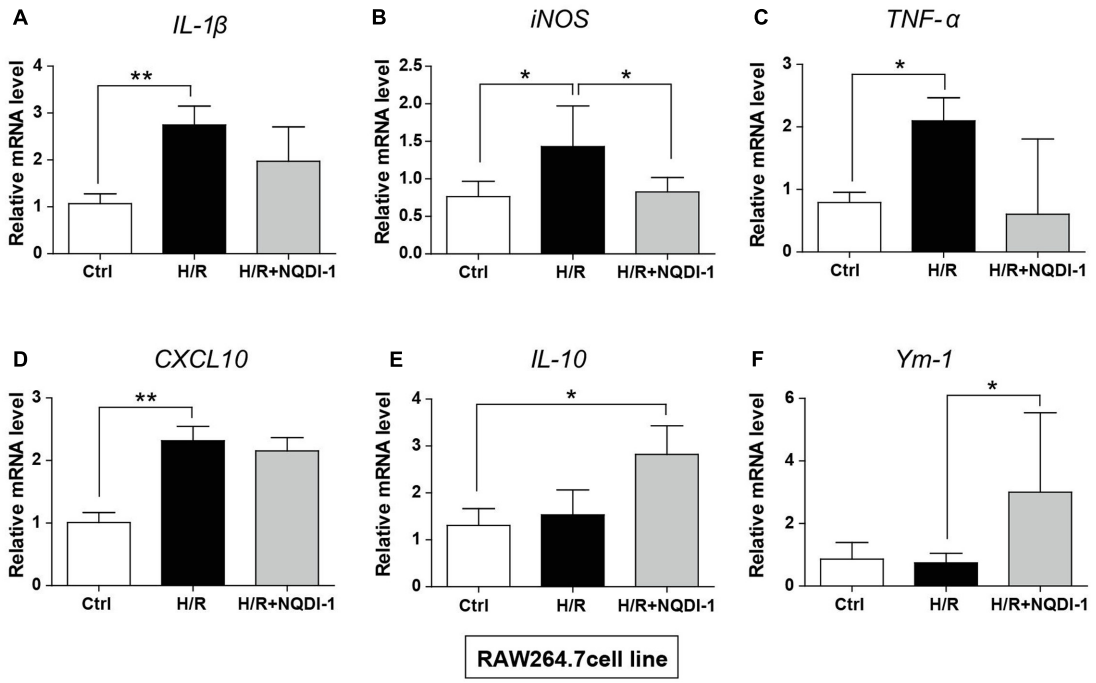

FIGURE 7 | Changes in M1 and M2 specific genes after inhibition of ASK1 in RAW264.7 macrophage cell line. The mRNA levels of M1 specific markers, such as **(A)** IL-1β (6 repeats), **(B)** iNOS (4–5 repeats), **(C)** TNF-α (4 repeats), and **(D)** CXCL10 (6 repeats), and M2 specific markers, such as **(E)** IL-10 (4 repeats) and **(F)** Ym-1 (5–6 repeats), were measured by real-time PCR in RAW264.7 cell line after H/R (4 h/24 h). The mRNA levels of **(A)** IL-1β, **(B)** iNOS, **(C)** TNF-α, and **(D)** CXCL10 were upregulated after H/R. The levels of iNOS were reduced, while **(E)** IL-10 and **(F)** Ym-1 levels were upregulated by inhibition of ASK1 in RAW264.7 cell line. Values are mean ± SD. Statistical comparisons between the groups were assessed with non-parametric Mann–Whitney test (*$p < 0.05$, **$p < 0.01$, ***$p < 0.001$ vs. H/R). Statistical parameter (Supplementary Table 3). H/R, hypoxia/reperfusion.

under a microscope right after H/R injury and at 24 h after H/R injury (**Figure 9C**). A high rate of migration was exhibited in H/R-injured macrophages; however, NQDI-1 drug treatment retarded the migration rate. Therefore, ASK1 is associated with microglia and macrophage migration capacity and ASK1 inhibition delayed migration rate. Statistical parameters were shown in Supplementary Table 3.

DISCUSSION

In this study, we performed *in vivo* and *in vitro* ischemic stroke model to examine whether ASK1 modulates microglia/macrophage polarization and function. We proved that ASK1 controls polarization and function of microglia/macrophage after ischemic/hypoxic injury. In previous reports, ASK1 is one of the early responders to different types of stress in the intracellular system, including oxidative stress, calcium overload, and immune response (Hayakawa et al., 2006; Takeda et al., 2008). ASK1 governs activation of mitogen-activated protein kinase (MAP kinase), which is essential for cellular function (Shiizaki et al., 2013), and several studies support that ASK1 is closely related to cerebral ischemia (Kim et al., 2011; Cheon et al., 2016b). Under inflammatory conditions, ASK1 signaling is necessary for TLRs, which recognize LPS (Soga et al., 2012). ASK1 deficiency represents LPS resistance, and genetic deletion of ASK1 involves inhibition of pro-inflammatory mediator production (Matsukawa et al., 2004; Sumbayev, 2008; Takeda et al., 2008; Mnich et al., 2010). The ASK1/p38 signaling pathway via TLRs is critical for chemokine production and promotes inflammation and neurotoxicity after multiple sclerosis (Guo et al., 2010). In line with studies that have demonstrated that ASK1 inhibition attenuates pro-inflammatory cytokines in microglia, ASK1 was found to be associated with TNF-α and iNOS production in primary microglial cell culture, and M1 macrophage suppression by a Class A scavenger receptor resulted in reductions of IL-6, IL-1β, and TNF-α, decreasing ASK1/p38/NF-κB pathway signaling, under pathologic conditions (Hu et al., 2011; Katome et al., 2013; Song and Lee, 2015). Previous reports have shown that inhibition of ASK1 reduces M1 phenotype after injury and ASK1 also played a role in our results. The main findings of this study are (1) in the ipsilateral hemisphere, ASK1 silencing resulted in a reduction of ischemic-induced activation of microglia/infiltrated macrophages and increased M2 phenotype in the late phase of cerebral ischemia and (2) ASK1 inhibition polarized BV2 microglia and RAW 264.7 macrophage cell lines toward M2 phenotype after hypoxia/reperfusion injury. Our *in vivo* study revealed that cerebral ischemia promotes activation of microglia and infiltration of macrophages in brain regions. In the ipsilateral hemisphere, upregulation of pro-inflammatory cytokines, such as IL-6, TNF-α, and IL-1β, was observed.

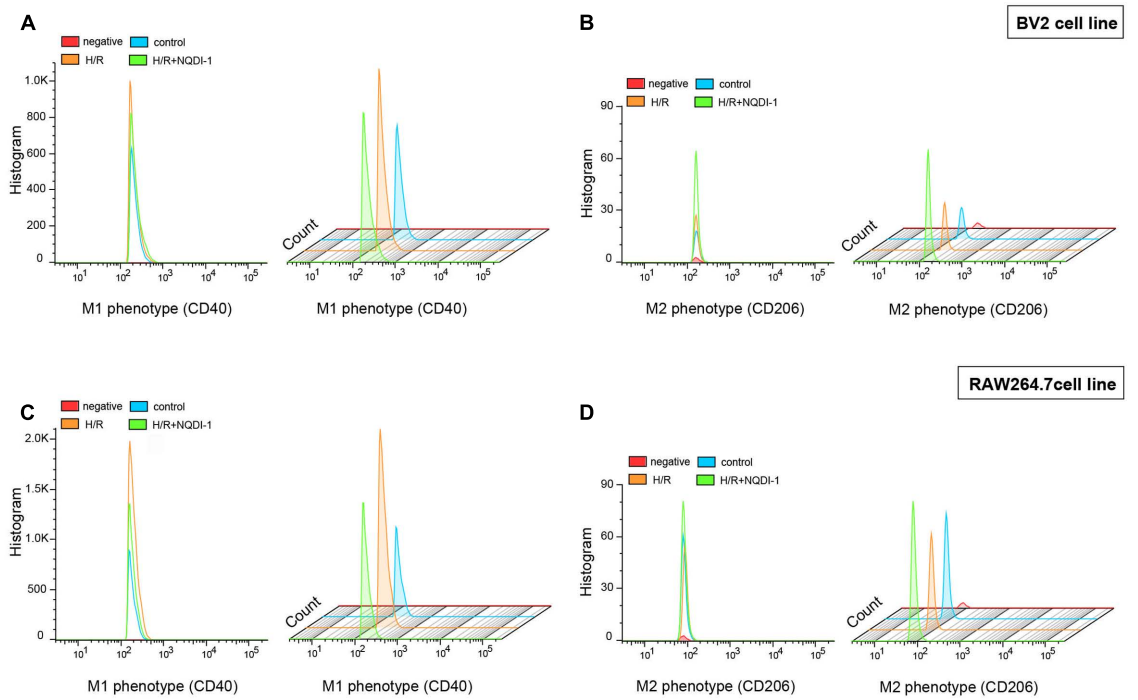

FIGURE 8 | Alteration of M1 and M2 surface markers after inhibition of ASK1 in BV2 microglia and RAW264.7 macrophages. Flow cytometry was performed for discrimination of **(A)** M1 (CD40) or **(B)** M2 (CD206) positive cell populations of BV2 cell line after H/R (4 h/24 h). The histogram of flow cytometry shows **(C)** M1 (CD40) and **(D)** M2 (CD206) positive cells in RAW 264.7 cell line after H/R (4 h/24 h). H/R, hypoxia/reperfusion.

However, ASK1 silenced by siRNA downregulated activation of microglia/macrophage and pro-inflammatory cytokine levels and upregulated the anti-inflammatory mediators. Our *in vitro* study for M1/M2 polarization of microglia/macrophages revealed that hypoxic injury stimulates M1-related factors, while ASK1 inhibition by NQDI-1 drug suppressed M1-related factors and promoted M2-related factors in microglia and macrophage cell lines. In addition, inhibition of ASK1 retarded the migration rate of both microglia and macrophages in gap closure assay.

Inflammation has emerged as the key factor in progression of ischemic stroke, and the inflammatory mediators play an important role in enlargement of brain damage and neurological dysfunction (Matsukawa et al., 2004; Quan and Banks, 2007; Quan, 2008; Banks and Erickson, 2010; Fu et al., 2015; Anrather and Iadecola, 2016). At the onset of ischemic stroke, stagnant blood flow initiates an aberrant immune response that promotes infiltration of immune cells such as leukocytes and macrophages, via a disrupted BBB (Matsukawa et al., 2004; Quan and Banks, 2007; Quan, 2008; Banks and Erickson, 2010; Fu et al., 2015; Anrather and Iadecola, 2016). Under the altered environment, microglia are activated. Meanwhile, the morphology and activation of peripherally infiltrated macrophages in the brain changes depending on the extracellular stimuli (Durafourt et al., 2012; Hu et al., 2015; Orihuela et al., 2016), after which activated microglia migrate quickly toward lesion sites, and lead to cell accumulation by releasing inflammation-associated mediators (Danton and Dietrich, 2003). Based on the microenvironment, microglia/macrophage can switch between phenotypes M1 (classically activated) and M2 (alternative activated). Under M1 conditions stimulated by LPS or IFN-γ, M1 microglia/macrophage express pro-inflammatory mediators of IL-1β, IL-6, TNF-α, iNOS, and CXCL10 and the cell surface markers CD40, CD80, and CD86. Also, cytotoxic effects of the M1 phenotype can exacerbate tissue damage (Durafourt et al., 2012; Hu et al., 2015; Kapellos and Iqbal, 2016; Orihuela et al., 2016; Plastira et al., 2016). On the contrary, M2 microglia/macrophages exert anti-inflammatory responses by upregulating IL-10, arginase-1, Ym-1 (heparin-binding lectin), and mannose receptor CD206, which modulate tissue repair, regeneration, and remodeling (Durafourt et al., 2012; Barakat and Redzic, 2016; Orihuela et al., 2016). During the early stage after ischemic insult, expression of the pro-inflammatory cytokine TNF-α is increased in neurons. However, during the late phase of ischemic insult, it is augmented in microglia/macrophage and other immune cells, with microglia/macrophage being major sources of pro-inflammatory cytokine in ischemic lesions after ischemic stroke (Gregersen et al., 2000; Clausen et al., 2008). Late inflammation in the brain after ischemic stroke is represented by persistent immune cell infiltration and cerebral infarctions (Mena et al., 2004; Brea et al., 2009; Vogelgesang et al., 2014; Walter et al., 2015; Anrather and Iadecola, 2016). Several studies have reported that microglia/macrophage shift their phenotype from M2

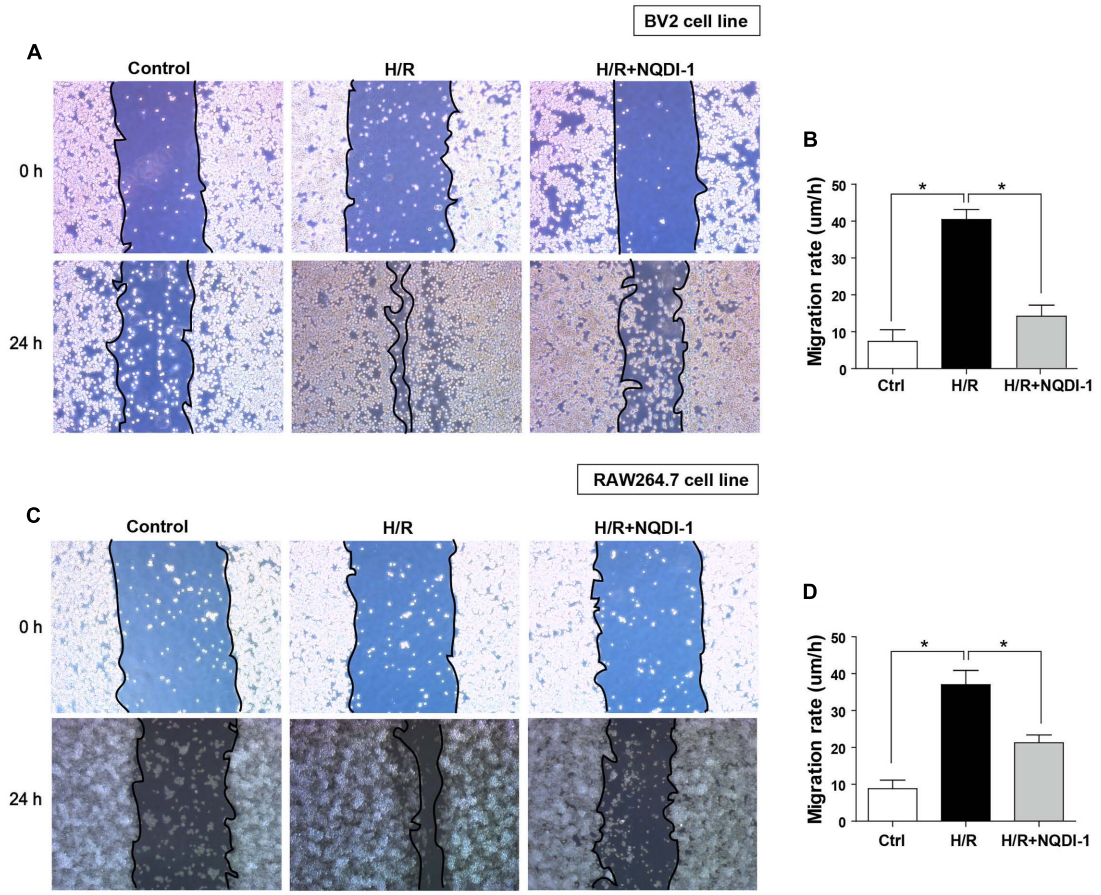

FIGURE 9 | Function of BV2 microglia and RAW264.7 macrophages after inhibition of ASK1. **(A,B)** Gap closure assay was performed for BV2 and RAW264.7 cells **(A)** Images at 0 h after hypoxia and 24 h after hypoxia/reperfusion in BV2 cell line. **(B)** The graph represents that H/R-induced increases in migration rate were decreased by inhibition of ASK1 in BV2 cell line (4 repeats). **(C)** Images at 0 h after hypoxia and 24 h after hypoxia/reperfusion in RAW264.7 cell line. **(D)** The graph represents that H/R-induced increases in migration rate were reduced by inhibition of ASK1 in RAW264.7 cell line (4 repeats). Values are mean ± SD. Statistical comparisons between the groups were assessed with non-parametric Mann–Whitney test (*$p < 0.05$, **$p < 0.01$, ***$p < 0.001$ vs. H/R). Statistical parameter (Supplementary Table 3). H/R, hypoxia/reperfusion.

to M1 after cerebral ischemia and M1 microglia/macrophage dominate the ischemic lesion in the brain, which exacerbate brain injury (Frieler et al., 2011; Hu et al., 2012). M1 polarized microglia/macrophage during chronic inflammation augment neuronal damage and block reestablishment of neuronal network, thereby retarding brain recovery (Hu et al., 2012). However, M2 polarized microglia/macrophage show improved phagocytic activity for clearance of necrotic debris and ameliorate production of inflammatory mediators (Hu et al., 2012). M2 phenotype modifies the extracellular matrix and promotes axonal regeneration and angiogenesis (Kigerl et al., 2009). In addition, after ischemic/hypoxic insult, M2 microglia/macrophage mediates clearance of ischemic tissue and blockade of brain injury, leading to neuronal survival (Hu et al., 2012). Therefore, anti-inflammatory M2 may have beneficial effects on ameliorating the development of brain damage. In the current study, cerebral ischemia augmented the recruitment of macrophage and microglia activation and migration, and led the brain toward M1 environment. However, ASK1 silencing by si-RNA/ASK1 inhibition by NQDI-1 drug diminished M1 phenotype-specific markers (secretion of pro-inflammatory mediators and downregulation of pro-inflammatory mediator genes) of macrophage/microglia and upregulated M2 specific markers (expression of anti-inflammatory mannose receptor and upregulation of anti-inflammatory mediator genes) in the later stages of the recovery period after ischemic/hypoxic injuries. To our knowledge, this is the first investigations of ASK1 in regards to M1/M2 polarization of microglia and macrophages in the late stage of ischemic stroke.

However, our limitations are as follows: first, it is not clarified which ASK1-downstream or -related signaling pathway affects M1/M2 phenotype. Although several molecules (JNK, p38, and Akt) are known to be involved in polarization (Zhang and Zhang, 2015; Vergadi et al., 2017; Zhong et al., 2017), we only proceeded to examine changes of M1/M2 phenotype by silencing/inhibiting ASK1 levels. Second, we focused on "classical" M1/M2 polarization in this

study. However, Martinez et al. (2008) and Mantovani et al. (2004) review the subpopulation of polarization, such as M1, M2a, M2b, and M2c. Ransohoff (2016) raises some concerns on existence of M1/M2 polarization (Mantovani et al., 2004; Martinez et al., 2008). Third, the previous studies proved that ASK1 inhibitor NQDI-1 shows a possible therapeutic application as a protective drug in ischemic stroke (Song et al., 2015; Cheon et al., 2016a). However, it is not fully demonstrated its safety and application. If this limitation is resolved, it will be one of the candidates for use in ischemic stroke patients.

CONCLUSION

We showed that ASK1 mediates M1/M2 polarization and the functions of microglia and macrophages. Modulation of the late inflammatory environment by M1/M2 regulation of microglia and macrophage via ASK1 silencing after cerebral ischemia may be an attractive strategy for recovery from stroke.

AUTHOR CONTRIBUTIONS

B-NK designed this study, supervised the project, interpreted all data, and wrote the manuscript. SC participated in the collection of data, interpretation of data, and writing of the first draft of the manuscript. EJK, JK, EHK, and BK participated in the data collection and interpretation.

FUNDING

This study was supported by a National Research Foundation of Korea (NRF) grant funded by the Korea government (MSIP) (No. 2017R1A2B4009) awarded to B-NK.

SUPPLEMENTARY MATERIAL

The Supplementary Material for this article can be found online at: http://journal.frontiersin.org/article/10.3389/fnmol.2017.00261/full#supplementary-material

REFERENCES

Amantea, D., Nappi, G., Bernardi, G., Bagetta, G., and Corasaniti, M. T. (2009). Post-ischemic brain damage: pathophysiology and role of inflammatory mediators. *FEBS J.* 276, 13–26. doi: 10.1111/j.1742-4658.2008.06766.x

Anrather, J., and Iadecola, C. (2016). Inflammation and stroke: an overview. *Neurotherapeutics* 13, 661–670. doi: 10.1007/s13311-016-0483-x

Banks, W. A., and Erickson, M. A. (2010). The blood-brain barrier and immune function and dysfunction. *Neurobiol. Dis.* 37, 26–32. doi: 10.1016/j.nbd.2009.07.031

Barakat, R., and Redzic, Z. (2016). The role of activated microglia and resident macrophages in the neurovascular unit during cerebral ischemia: Is the jury still out? *Med. Princ. Pract.* 25(Suppl. 1), 3–14. doi: 10.1159/000435858

Brea, D., Sobrino, T., Ramos-Cabrer, P., and Castillo, J. (2009). Inflammatory and neuroimmunomodulatory changes in acute cerebral ischemia. *Cerebrovasc. Dis.* 27(Suppl. 1), 48–64. doi: 10.1159/000200441

Cheon, S. Y., Cho, K. J., Kim, S. Y., Kam, E. H., Lee, J. E., and Koo, B. N. (2016a). Blockade of apoptosis signal-regulating kinase 1 attenuates matrix metalloproteinase 9 activity in brain endothelial cells and the subsequent apoptosis in neurons after ischemic injury. *Front. Cell Neurosci.* 10:213. doi: 10.3389/fncel.2016.00213

Cheon, S. Y., Cho, K. J., Lee, J. E., Kim, H. W., Lee, S. K., Kim, H. J., et al. (2013). Cerebroprotective effects of red ginseng extract pretreatment against ischemia-induced oxidative stress and apoptosis. *Int. J. Neurosci.* 123, 269–277. doi: 10.3109/00207454.2012.758120

Cheon, S. Y., Cho, K. J., Song, J., and Kim, G. W. (2016b). Knockdown of apoptosis signal-regulating kinase 1 affects ischaemia-induced astrocyte activation and glial scar formation. *Eur. J. Neurosci.* 43, 912–922. doi: 10.1111/ejn.13175

Cho, K. J., Cheon, S. Y., and Kim, G. W. (2016). Apoptosis signal-regulating kinase 1 mediates striatal degeneration via the regulation of C1q. *Sci. Rep.* 6:18840. doi: 10.1038/srep18840

Clausen, B. H., Lambertsen, K. L., Babcock, A. A., Holm, T. H., Dagnaes-Hansen, F., and Finsen, B. (2008). Interleukin-1beta and tumor necrosis factor-alpha are expressed by different subsets of microglia and macrophages after ischemic stroke in mice. *J. Neuroinflammation* 5:46. doi: 10.1186/1742-2094-5-46

Danton, G. H., and Dietrich, W. D. (2003). Inflammatory mechanisms after ischemia and stroke. *J. Neuropathol. Exp. Neurol.* 62, 127–136.

Denes, A., Thornton, P., Rothwell, N. J., and Allan, S. M. (2010). Inflammation and brain injury: acute cerebral ischaemia, peripheral and central inflammation. *Brain Behav. Immun.* 24, 708–723. doi: 10.1016/j.bbi.2009.09.010

Durafourt, B. A., Moore, C. S., Zammit, D. A., Johnson, T. A., Zaguia, F., Guiot, M. C., et al. (2012). Comparison of polarization properties of human adult microglia and blood-derived macrophages. *Glia* 60, 717–727. doi: 10.1002/glia.22298

Frieler, R. A., Meng, H., Duan, S. Z., Berger, S., Schutz, G., He, Y., et al. (2011). Myeloid-specific deletion of the mineralocorticoid receptor reduces infarct volume and alters inflammation during cerebral ischemia. *Stroke* 42, 179–185. doi: 10.1161/STROKEAHA.110.598441

Fu, Y., Liu, Q., Anrather, J., and Shi, F. D. (2015). Immune interventions in stroke. *Nat. Rev. Neurol.* 11, 524–535. doi: 10.1038/nrneurol.2015.144

Gregersen, R., Lambertsen, K., and Finsen, B. (2000). Microglia and macrophages are the major source of tumor necrosis factor in permanent middle cerebral artery occlusion in mice. *J. Cereb. Blood Flow Metab.* 20, 53–65. doi: 10.1097/00004647-200001000-00009

Guo, X., Harada, C., Namekata, K., Matsuzawa, A., Camps, M., Ji, H., et al. (2010). Regulation of the severity of neuroinflammation and demyelination by TLR-ASK1-p38 pathway. *EMBO Mol. Med.* 2, 504–515. doi: 10.1002/emmm.201000103

Hayakawa, T., Matsuzawa, A., Noguchi, T., Takeda, K., and Ichijo, H. (2006). The ASK1-MAP kinase pathways in immune and stress responses. *Microbes Infect.* 8, 1098–1107. doi: 10.1016/j.micinf.2005.12.001

Hu, X., Leak, R. K., Shi, Y., Suenaga, J., Gao, Y., Zheng, P., et al. (2015). Microglial and macrophage polarization-new prospects for brain repair. *Nat. Rev. Neurol.* 11, 56–64. doi: 10.1038/nrneurol.2014.207

Hu, X., Li, P., Guo, Y., Wang, H., Leak, R. K., Chen, S., et al. (2012). Microglia/macrophage polarization dynamics reveal novel mechanism of injury expansion after focal cerebral ischemia. *Stroke* 43, 3063–3070. doi: 10.1161/STROKEAHA.112.659656

Hu, Y., Zhang, H., Lu, Y., Bai, H., Xu, Y., Zhu, X., et al. (2011). Class A scavenger receptor attenuates myocardial infarction-induced cardiomyocyte necrosis through suppressing M1 macrophage subset polarization. *Basic Res. Cardiol.* 106, 1311–1328. doi: 10.1007/s00395-011-0204-x

Iadecola, C., and Anrather, J. (2011). The immunology of stroke: from mechanisms to translation. *Nat. Med.* 17, 796–808. doi: 10.1038/nm.2399

Kapellos, T. S., and Iqbal, A. J. (2016). Epigenetic control of macrophage polarisation and soluble mediator gene expression during inflammation. *Mediators Inflamm.* 2016:6591703. doi: 10.1155/2016/6591703

Katome, T., Namekata, K., Guo, X., Semba, K., Kittaka, D., Kawamura, K., et al. (2013). Inhibition of ASK1-p38 pathway prevents neural cell death

following optic nerve injury. *Cell Death Differ.* 20, 270–280. doi: 10.1038/cdd.2012.122

Kigerl, K. A., Gensel, J. C., Ankeny, D. P., Alexander, J. K., Donnelly, D. J., and Popovich, P. G. (2009). Identification of two distinct macrophage subsets with divergent effects causing either neurotoxicity or regeneration in the injured mouse spinal cord. *J. Neurosci.* 29, 13435–13444. doi: 10.1523/JNEUROSCI.3257-09.2009

Kim, H. W., Cho, K. J., Lee, S. K., and Kim, G. W. (2011). Apoptosis signal-regulating kinase 1 (Ask1) targeted small interfering RNA on ischemic neuronal cell death. *Brain Res.* 1412, 73–78. doi: 10.1016/j.brainres.2011.07.018

Mantovani, A., Sica, A., Sozzani, S., Allavena, P., Vecchi, A., and Locati, M. (2004). The chemokine system in diverse forms of macrophage activation and polarization. *Trends Immunol.* 25, 677–686. doi: 10.1016/j.it.2004.09.015

Martinez, F. O., Sica, A., Mantovani, A., and Locati, M. (2008). Macrophage activation and polarization. *Front. Biosci.* 13:453–461.

Matsukawa, J., Matsuzawa, A., Takeda, K., and Ichijo, H. (2004). The ASK1-MAP kinase cascades in mammalian stress response. *J. Biochem.* 136, 261–265. doi: 10.1093/jb/mvh134

Mena, H., Cadavid, D., and Rushing, E. J. (2004). Human cerebral infarct: a proposed histopathologic classification based on 137 cases. *Acta Neuropathol.* 108, 524–530. doi: 10.1007/s00401-004-0918-z

Mnich, S. J., Blanner, P. M., Hu, L. G., Shaffer, A. F., Happa, F. A., O'Neil, S., et al. (2010). Critical role for apoptosis signal-regulating kinase 1 in the development of inflammatory K/BxN serum-induced arthritis. *Int. Immunopharmacol.* 10, 1170–1176. doi: 10.1016/j.intimp.2010.06.023

Orihuela, R., McPherson, C. A., and Harry, G. J. (2016). Microglial M1/M2 polarization and metabolic states. *Br. J. Pharmacol.* 173, 649–665. doi: 10.1111/bph.13139

Plastira, I., Bernhart, E., Goeritzer, M., Reicher, H., Kumble, V. B., Kogelnik, N., et al. (2016). 1-Oleyl-lysophosphatidic acid (LPA) promotes polarization of BV-2 and primary murine microglia towards an M1-like phenotype. *J. Neuroinflammation* 13:205. doi: 10.1186/s12974-016-0701-9

Qin, Y., Sun, X., Shao, X., Hu, M. X., Feng, J., Chen, Z., et al. (2016). Lipopolysaccharide preconditioning induces an anti-inflammatory phenotype in BV2 microglia. *Cell Mol. Neurobiol.* 36, 1269–1277. doi: 10.1007/s10571-015-0324-1

Quan, N. (2008). Immune-to-brain signaling: How important are the blood-brain barrier-independent pathways? *Mol. Neurobiol.* 37, 142–152. doi: 10.1007/s12035-008-8026-z

Quan, N., and Banks, W. A. (2007). Brain-immune communication pathways. *Brain Behav. Immun.* 21, 727–735. doi: 10.1016/j.bbi.2007.05.005

Ransohoff, R. M. (2016). A polarizing question: Do M1 and M2 microglia exist? *Nat. Neurosci.* 19, 987–991. doi: 10.1038/nn.4338

Shiizaki, S., Naguro, I., and Ichijo, H. (2013). Activation mechanisms of ASK1 in response to various stresses and its significance in intracellular signaling. *Adv. Biol. Regul.* 53, 135–144. doi: 10.1016/j.jbior.2012.09.006

Sica, A., Erreni, M., Allavena, P., and Porta, C. (2015). Macrophage polarization in pathology. *Cell Mol. Life Sci.* 72, 4111–4126. doi: 10.1007/s00018-015-1995-y

Soga, M., Matsuzawa, A., and Ichijo, H. (2012). Oxidative stress-induced diseases via the ASK1 signaling pathway. *Int. J. Cell Biol.* 2012:439587. doi: 10.1155/2012/439587

Song, J., Cheon, S. Y., Lee, W. T., Park, K. A., and Lee, J. E. (2015). The effect of ASK1 on vascular permeability and edema formation in cerebral ischemia. *Brain Res.* 1595, 143–155. doi: 10.1016/j.brainres.2014.11.024

Song, J., and Lee, J. E. (2015). ASK1 modulates the expression of microRNA Let7A in microglia under high glucose in vitro condition. *Front. Cell Neurosci.* 9:198. doi: 10.3389/fncel.2015.00198

Sumbayev, V. V. (2008). LPS-induced Toll-like receptor 4 signalling triggers cross-talk of apoptosis signal-regulating kinase 1 (ASK1) and HIF-1alpha protein. *FEBS Lett.* 582, 319–326. doi: 10.1016/j.febslet.2007.12.024

Takeda, K., Noguchi, T., Naguro, I., and Ichijo, H. (2008). Apoptosis signal-regulating kinase 1 in stress and immune response. *Annu. Rev. Pharmacol. Toxicol.* 48, 199–225. doi: 10.1146/annurev.pharmtox.48.113006.094606

Tugal, D., Liao, X., and Jain, M. K. (2013). Transcriptional control of macrophage polarization. *Arterioscler. Thromb. Vasc. Biol.* 33, 1135–1144. doi: 10.1161/ATVBAHA.113.301453

Vergadi, E., Ieronymaki, E., Lyroni, K., Vaporidi, K., and Tsatsanis, C. (2017). Akt signaling pathway in macrophage activation and M1/M2 Polarization. *J. Immunol.* 198, 1006–1014. doi: 10.4049/jimmunol.1601515

Vogelgesang, A., Becker, K. J., and Dressel, A. (2014). Immunological consequences of ischemic stroke. *Acta Neurol. Scand.* 129, 1–12. doi: 10.1111/ane.12165

Walter, H. L., Walberer, M., Rueger, M. A., Backes, H., Wiedermann, D., Hoehn, M., et al. (2015). In vivo analysis of neuroinflammation in the late chronic phase after experimental stroke. *Neuroscience* 292, 71–80. doi: 10.1016/j.neuroscience.2015.02.024

Zhang, O., and Zhang, J. (2015). Atorvastatin promotes human monocyte differentiation toward alternative M2 macrophages through p38 mitogen-activated protein kinase-dependent peroxisome proliferator-activated receptor gamma activation. *Int. Immunopharmacol.* 26, 58–64. doi: 10.1016/j.intimp.2015.03.005

Zhong, J., Wang, H., Chen, W., Sun, Z., Chen, J., Xu, Y., et al. (2017). Ubiquitylation of MFHAS1 by the ubiquitin ligase praja2 promotes M1 macrophage polarization by activating JNK and p38 pathways. *Cell Death Dis.* 8:e2763. doi: 10.1038/cddis.2017.102

Conflict of Interest Statement: The authors declare that the research was conducted in the absence of any commercial or financial relationships that could be construed as a potential conflict of interest.

frontiers in Molecular Neuroscience

ORIGINAL RESEARCH
published: 11 July 2017
doi: 10.3389/fnmol.2017.00211

Neuronal Cholesterol Accumulation Induced by Cyp46a1 Down-Regulation in Mouse Hippocampus Disrupts Brain Lipid Homeostasis

Sophie Ayciriex[1†], Fathia Djelti[2,3†], Sandro Alves[2,3], Anne Regazzetti[1], Mathieu Gaudin[1,4], Jennifer Varin[5], Dominique Langui[6], Ivan Bièche[5], Eloise Hudry[7], Delphine Dargère[1], Patrick Aubourg[2,3], Nicolas Auzeil[1*], Olivier Laprévote[1,8†] and Nathalie Cartier[2,3†]*

[1] UMR Centre National de la Recherche Scientifique 8638 COMETE, Sorbonne Paris Cité, Faculté des Sciences Pharmaceutiques et Biologiques, Université Paris Descartes, Paris, France, [2] Institut National de la Santé et de la Recherche Médicale U1169, CHU Bicêtre Paris Sud, Le Kremlin-Bicêtre, France, [3] CEA Fontenay aux Roses, Fontenay aux Roses, France, [4] Division Métabolisme, Technologie Servier, Orléans, France, [5] Génétique, Physiopathologie et Approches Thérapeutiques des Maladies Héréditaires du Système Nerveux, EA7331, Faculté des Sciences Pharmaceutiques et Biologiques, Université Paris Descartes, Sorbonne Paris Cité, Paris, France, [6] Plate-forme d'Imagerie Cellulaire Pitié Salpêtrière, Hôpital Pitié-Salpêtrière, Paris, France, [7] Alzheimer's Disease Research Laboratory, Department of Neurology, Massachusetts General Hospital, Charlestown, MA, United States, [8] Service de Toxicologie Biologique, Hôpital Lariboisière, Paris, France

OPEN ACCESS

Edited by:
Clevio Nobrega, University of the Algarve, Portugal

Reviewed by:
Yuchio Yanagawa, Gunma University, Japan
Zheng Wu, Pennsylvania State University, United States

***Correspondence:**
Sophie Ayciriex
sophie.ayciriex@isa-lyon.fr
Nicolas Auzeil
nicolas.auzeil@parisdescartes.fr

†These authors have contributed equally to this work.

Received: *28 April 2017*
Accepted: *14 June 2017*
Published: *11 July 2017*

Citation:
Ayciriex S, Djelti F, Alves S, Regazzetti A, Gaudin M, Varin J, Langui D, Bièche I, Hudry E, Dargère D, Aubourg P, Auzeil N, Laprévote O and Cartier N (2017) Neuronal Cholesterol Accumulation Induced by Cyp46a1 Down-Regulation in Mouse Hippocampus Disrupts Brain Lipid Homeostasis. Front. Mol. Neurosci. 10:211. doi: 10.3389/fnmol.2017.00211

Impairment in cholesterol metabolism is associated with many neurodegenerative disorders including Alzheimer's disease (AD). However, the lipid alterations underlying neurodegeneration and the connection between altered cholesterol levels and AD remains not fully understood. We recently showed that cholesterol accumulation in hippocampal neurons, induced by silencing *Cyp46a1* gene expression, leads to neurodegeneration with a progressive neuronal loss associated with AD-like phenotype in wild-type mice. We used a targeted and non-targeted lipidomics approach by liquid chromatography coupled to high-resolution mass spectrometry to further characterize lipid modifications associated to neurodegeneration and cholesterol accumulation induced by CYP46A1 inhibition. Hippocampus lipidome of normal mice was profiled 4 weeks after cholesterol accumulation due to *Cyp46a1* gene expression down-regulation at the onset of neurodegeneration. We showed that major membrane lipids, sphingolipids and specific enzymes involved in phosphatidylcholine and sphingolipid metabolism, were rapidly increased in the hippocampus of AAV-shCYP46A1 injected mice. This lipid accumulation was associated with alterations in the lysosomal cargoe, accumulation of phagolysosomes and impairment of endosome-lysosome trafficking. Altogether, we demonstrated that inhibition of cholesterol 24-hydroxylase, key enzyme of cholesterol metabolism leads to a complex dysregulation of lipid homeostasis. Our results contribute to dissect the potential role of lipids in severe neurodegenerative diseases like AD.

Keywords: neurodegeneration, gene silencing, Cyp46a1, cholesterol, lipidomics, lipid dysregulation, ER stress

INTRODUCTION

Mammalian brain, most cholesterol-rich organ contains 10-fold more cholesterol than any other organ (Dietschy and Turley, 2004; Bjorkhem, 2006; Bjorkhem et al., 2010). The capacity of the brain to store such a large amount of cholesterol indicates that this sterol plays a central role in the development and function of the brain. About 70% of cholesterol is found in myelin. The remaining 30% of brain cholesterol is distributed between glial cells (20%) and neurons (10%) (Pfrieger, 2003; Bjorkhem and Meaney, 2004; Dietschy and Turley, 2004; Vance et al., 2005; Bjorkhem et al., 2010). Cholesterol is involved in the formation of axons and dendrites during development, neuronal repair and remodeling, formation of new synapses, learning, and memory (de Chaves et al., 1997; Xu et al., 1998; Mahley and Rall, 2000; Mauch et al., 2001). Brain cholesterol metabolism is tightly regulated. The cholesterol abundance in the central nervous system depends primarily on local synthesis and efflux. Cholesterol does not freely cross the intact blood-brain barrier (BBB) and nearly all cholesterol in the adult brain is formed by *in situ* synthesis (Turley et al., 1996; Vance et al., 2005; Bjorkhem et al., 2010). One of the mechanisms for cholesterol clearance from the brain is its conversion into an hydroxylated metabolite, the 24(*S*)-hydroxycholesterol (24-OHC), which is able to cross the BBB and enter the circulation to the liver to be further metabolized to bile acids (Lund et al., 2003; Bjorkhem, 2006; Russell et al., 2009). This conversion is catalyzed by an enzyme cytochrome P450, the cholesterol 24-hydroxylase, also called CYP46A1, mainly expressed by neuronal cells (Lutjohann et al., 1996; Lund et al., 1999). This conversion represents one of the most important mechanisms for cholesterol clearance from the brain (Bjorkhem, 2006; Russell et al., 2009).

Several clinical and biochemical studies have suggested that cholesterol imbalance in the brain may be associated to neurodegenerative disorders, such as Alzheimer's disease (AD), Niemann–Pick disease type C, Huntington's disease and Parkinson's disease (Puglielli et al., 2003; Wolozin, 2004; Valenza et al., 2005, 2010; Liu et al., 2010; Cheng et al., 2011; Meljon et al., 2013). In AD, cholesterol affects amyloid processing pathway (Aβ generation and aggregation). Aβ is produced by sequential cleavage of the amyloid precursor protein (APP) by β-secretase (BACE1) and γ-secretase. Cholesterol promotes the co-clustering of APP and BACE1 in lipid raft domains leading to Aβ production and accumulation (Marquer et al., 2011; Ayciriex et al., 2016). Cholesterol seems to play a pivotal role in the neurodegenerative process of AD.

We recently developed an *in vivo* model to study the consequences of neuronal cholesterol accumulation in normal mice (Djelti et al., 2015). We delivered a *Cyp46a1* specific short-hairpin RNA (shCYP46A1) in C57Bl/6 mice hippocampus using stereotactic injection of an adeno-associated viral vector serotype 5 (AAV5). Efficient inhibition of *Cyp46a1* gene expression in hippocampus of injected mice led to an accumulation of cholesterol in neurons 3 and 4 weeks after injection (Chali et al., 2015; Djelti et al., 2015). This cholesterol accumulation was accompanied by marked changes in endosomes, Aβ peptides production, tau phosphorylation and endoplasmic reticulum (ER) stress. This cascade of events finally triggered apoptotic cell death, 4 weeks after injection. These processes induced cognitive impairment and hippocampal atrophy, 12 weeks after injection. All these observations closely mimic the pathological hallmarks of AD. Down-regulation of *Cyp46a1* gene expression in APP23 mice strongly aggravated the increase of Aβ peptides production, and induced phosphorylation of tau protein and neuronal death (Djelti et al., 2015). These results strongly suggest that accumulation of cholesterol plays a pivotal role in neurodegenerative process and AD.

Altered lipid homeostasis alteration in the brain could be a risk factor for the many types of neurodegenerative disorders, including Alzheimer's disease, Huntington's disease, and Parkinson's disease. These neurodegenerative disorders are marked by extensive neuronal apoptosis, gliosis (Han, 2005; Fan et al., 2013; Yadav and Tiwari, 2014). Several lipidomics studies have shown lipid homeostasis modifications in AD brain tissue (Han, 2005; Di Paolo and Kim, 2011; Chan et al., 2012; Panchal et al., 2014). Changes in cholesterol, sulfatide, ceramide, galactosylceramide, and plasmalogens are highlighted in brain of AD patients (Han et al., 2001, 2002; Cutler et al., 2004; Han, 2005). However, the connection between lipids alterations, cholesterol accumulation and neurodegenerative process in AD remains not fully understood.

In the present work, we investigated the consequences of *Cyp46a1* gene expression inhibition and neuronal cholesterol accumulation on hippocampal lipidome, 4 weeks after AAV-shCYP46A1 injection a time corresponding to the onset of neuronal loss. First, the sterol and oxysterol contents were analyzed by a targeted approach combining ultra-performance liquid chromatography (UPLC) and high-resolution mass spectrometry (Ayciriex et al., 2012). Second, an untargeted lipidomics approach without *a priori* knowledge was performed using the same analytical platform to monitor lipid perturbations. Our data showed that *Cyp46a1* gene silencing lead to a decrease of 24(*S*)-hydroxycholesterol, 25-hydroxycholesterol and to an increase of cholesterol content. The major membrane lipids, such as phosphatidylethanolamine (PE) and phosphatidylcholine (PC) were increased together with sphingolipids including sulfatides, ceramides (Cer), and glucosylceramides (GlcCer), and gangliosides GM1. Diacylglycerols (DAG) with long and unsaturated fatty acid moieties were also increased. Expression of genes encoding

Abbreviations: AD, Alzheimer's disease; AAV5, Adenovirus associated vector serotype 5; 24-OHC, 24(S)-hydroxycholesterol; Cyp46a1, cholesterol-24(S)-hydroxylase gene; Aβ, amyloid peptide; APP, Amyloid precursor protein; BACE1, β-secretase; sh-CYP46A1, short hairpin RNAi CYP46A1; UPR, Unfolded Protein Response; UPLC, Ultra-performance liquid chromatography; PE, Phosphatidylethanolamine; PC, Phosphatidylcholine; Cer, Ceramide; GlcCer, Glucosylceramide; DG, Diacylglycerol; TBP, TATA-box binding protein gene; PCA, Principal Components Analysis; PLS-DA, Partial least square-Discriminant Analysis; OPLS-DA, Orthogonal Partial least square-Discriminant Analysis; QC, quality control; PCYT1α, choline cytilyltransferase α; PCYT1β, choline cytilyltransferase β; SMPD1, Sphingomyelin phosphodiesterase 1; SMPD3, Sphingomyelin phosphodiesterase 3; LASS2, ceramide synthase 2; ST3GAL1, ST3 β -galactoside α -2,3-sialyltransferase 1; UGCG, UDP-glucose ceramide glucosyltransferase; DAPI, 4′,6-diamidino-2-phenylindole; eGFP, enhanced green fluorescent protein; LAMP-1, lysosomal-associated membrane protein 1.

specific enzymes involved in phosphatidylcholine and sphingolipid metabolism was also increased in response to cholesterol overload induced by *Cyp46a1* gene silencing. In parallel, we highlighted lysosomal dysfunction characterized by an increase of lysosomes number and the presence of phagolysosomes in the hippocampus of AAV-shCYP46A1 injected mice. Our results further contribute to understand the mechanisms of neurodegeneration mediated by cholesterol accumulation in neurons following impairment of *Cyp46a1* gene expression.

MATERIALS AND METHODS

Chemicals and Reagents

Triethylamine, 4-(dimethylamino)phenyl isocyanate, formic acid and butylated hydroxytoluene (BHT) were obtained from Sigma-Aldrich (Saint-Quentin Fallavier, France). Hexane and dichloromethane were obtained from CarloErbaReactifs SDS (Val-de-Reuil, France). Acetonitrile, methanol, isopropanol were of LC-MS grade (J.T. Baker, Phillipsburg, NJ, USA). 24(*R/S*)-hydroxycholesterol d6 [26,26,26,27,27,27-hexadeuterocholest-5-ene-3ß,24-diol], cholesterol d7 [cholest-5-en-3ß-ol(d7)], 1,2-diheptadecanoyl-*sn*-glycero-3-phosphate, PA(17:0/17:0), 1,2-diheptadecanoyl-*sn*-glycero-3-phospho-L-serine, PS (17:0/17:0), 1,2-diheptadecanoyl-*sn*-glycero-3-phosphoethanolamine, PE(17:0/17:0), 1,2-diheptadecanoyl-*sn*-glycero-3-phosphocholine, PC(17:0/17:0), 1,2-diheptadecanoyl-*sn*-glycero-3-phospho-(1′-rac-glycerol), PG(17:0/17:0), 1,2-diheptadecanoyl-*sn*-glycerol, DG (17:0/17:0/0:0) and *N*-heptadecanoyl-D-*erythro*-sphingosine, Cer(d18:1(4E)/17:0) were obtained from Avanti Polar Lipids, Inc. (Alabaster, AL, USA).

AAV Plasmid Design and Vectors Production

The short-hairpin (sh) RNA, against the sequence specific of *Cyp46a1* gene with the promoter U6, was amplified and cloned into AAV5 vector (Djelti et al., 2015). In parallel a scramble sequence that contained no similarity to the endogenous mRNA, was used as a negative control. AAV5 vector also contained eGFP reporter sequence under the control of the PGK promoter. AAV5 viral stocks were produced by transient transfection of 293T cells with the respective viral vector and the subsequent purification of the cell culture supernatant by a caesium-chloride ultracentrifugation gradient to yield titers of 4 to 9×101^2 Vg/mL (Sevin et al., 2006). The vectors, used in this study, were named AAV-scramble (control) or AAV-shCYP46A1 (Supplementary Table S1).

Animals and Intracerebral Injections of AAVs

Twelve weeks-old female wild-type C57Bl/6 mice (Janvier, France) were housed in pathogen-free conditions with a 12 h light/dark cycle (average weight 20–25 g). These experiments were carried out in strict accordance with the recommendations in the Guide for the Care and Use of Laboratory Animals of the National Institutes of Health (NIH publication no.85-24) and the European Committee Council Directive (86/89/EEC). The protocol for animal experiments was approved by the Committee on the Ethics of Animal Experiments of the Ministere de l'Enseignement Superieur et de la Recherche (Permit Number: B92-032-02).

Mice were anesthetized by intraperitoneal injection of ketamine (80 mg/kg) and xylazine (50 mg/kg) and placed on a stereotaxic frame (David Kopf Instruments, Tujunga, CA). All efforts were made to minimize suffering. The AAV5-vector was injected in one hippocampus (*stratum lacunosum moleculare*) with 2 µl of viral preparation (2×10^9 vg) using a 30-gauge needle attached to a 10-µL Hamilton syringe (Hamilton Medical, Reno, NV) at a rate of 0.2 µL/min. Stereotactic coordinates of injection sites from bregma were anterior-posterior: -2 mm; medial-lateral: −1.2 mm; dorsal-ventral: −2 mm. C57Bl/6 mice were sacrificed at 3 and 4 weeks after injection for gene expression, immunofluorescence, electron microscopy studies ($n = 5$ mice per vector, per time, per analysis). The lipid analyses were undertaken only at 4 weeks after injection, at the onset of neuronal loss. Anesthetized animals were transcardially perfused with PBS1X (Life technologies). Dissected hippocampi were frozen in liquid nitrogen and conserved at −80°C.

Gene Expression Analysis by qPCR

Dissected hippocampi were snap frozen in liquid nitrogen and ground into powder for total mRNA extration using the RNAble kit (Eurobio laboratories, Les Ulis France). Quantitative real-time PCR (qPCR) analysis was carried out using the ABI Prism® 7900HT sequence detection system (Applied Biosystems, Foster City, CA, USA) as described previously (Bieche et al., 2004). As an endogenous RNA control, transcripts of the TATA-box binding protein gene (TBP) were measured. Primers for TBP and the other gene were chosen with the assistance of the Oligo 5.0 computer program (National Biosciences, Plymouth, MN) (Supplementary Table S2). Target transcript levels (N_{target}) were normalized according to TBP content and then to a basal mRNA level following the equation $N_{target} = 2.\delta^{Ct}$, where δ^{Ct} is the Ct value of the target gene after subtraction of Ct for the TBP gene.

Lipid Sample Preparation

Hippocampus tissues were homogenized in cold water containing 0.1% BHT with a Precellys®24-Dual (Precellys) during 15 s at 5,000 rpm. The brain tissue homogenization was performed in 2 mL tube prefilled with 1.4 mm ceramic beads. 5 µL of homogenate were used for protein estimation using the BCA Protein Assay Kit-Reducing Agent Compatible (Pierce). The rest of the homogenate were spiked with an internal standard mix composed of PA(17:0/17:0), PS(17:0/17:0), PE(17:0/17:0), PC(17:0/17:0), PG(17:0/17:0), DG(17:0/17:0/0:0), and Cer(d18:1(4E)/17:0)] at a concentration of 6.25 µM prior to lipid extraction. Lipids were extracted with hexane/methanol mixture (3:1, *v/v*) by mechanical shaking for 1 h, at room temperature in 13 × 100 mm glass tubes with PTFE-lined caps. The extracts were centrifuged at 2,500 rpm for 10 min to achieve phase separation. The organic phase (upper layer) was collected and washed with 600 µL water for 10 min on a mechanical shaker. The upper phases were pooled and divided

into two fractions: one fraction for cholesterol and oxysterol analysis (fraction F1) and the other for global lipidomics analysis (fraction F2). All fractions were dried under nitrogen gas.

Cholesterol and Oxysterols Analysis

F1 was resuspended in 200 μL of methanol and spiked with 24(*R/S*)-hydroxycholesterol (*d6*) (20 ng) and cholesterol (*d7*) (20 ng) used as an internal standard for oxysterols and cholesterol quantification, respectively. Oxysterols and cholesterol were derivatized with 4-(dimethylamino)phenyl isocyanate and analyzed by UPLC-ESI-HRMS according to the procedure previously described in Ayciriex et al. (2012). Oxysterols and cholesterol contained in hippocampi was in the range of ng/mg and μg/mg of proteins, respectively.

Lipidomics Analysis of Mice Hippocampus by UPLC-ESI-QTOF-MS^E

F2 was resuspended in 200 μL of acetonitrile/isopropanol mixture (1:1, *v/v*). Quality control (QC) samples were prepared by combining 20 μL of each lipid extracts. After evaporation, QC samples were reconstituted in a small volume of acetonitrile/isopropanol mixture and further diluted to one-third and one-sixth diluted QC samples. A 3 μL aliquot of QC and samples were injected into ACQUITY UPLC® system coupled to an ESI-QTOF-MS (SYNAPT® G2 High Definition MS™ mass spectrometer, Waters, UK). Lipids were separated on an ACQUITY UPLC® HSS T3 1.8 μm column (2.1 × 100 mm) thermostated at 50°C at a flow rate of 0.40 mL.min^{-1} with acetonitrile and water with 10 mM ammonium acetate (40:60, *v/v*) as eluent A and acetonitrile/isopropanol (10:90, *v/v* containing 10 mM ammonium acetate as eluent B (Castro-Perez et al., 2010). Data were collected separately both in positive (ESI$^+$) and negative (ESI$^-$) ion mode. ESI source parameters were as follows: source temperature 120°C, desolvation temperature 450°C, cone gas flow 20 L/h, desolvation gas flow 800 L/h, capillary voltage 2,400 V (ESI$^-$), 3,000 V (ESI$^+$), cone voltage 45 V (ESI$^-$), and 30 V for (ESI$^+$). The mass spectrometer was operated in the MS^E mode of acquisition for both polarities. Two independent acquisitions functions are automatically created in MS^E mode. The first function set at 5 eV collects data on unfragmented ions while the second function collects fragmentation data by using a collision energy ramp from 20 to 50 eV. In addition MS^2 experiments were performed to confirm structural identification of ions of interest.

Centroided accurate mass spectra were acquired over the *m/z* range 50–1,000 with a scan time of 0.1 s and an interscan delay of 0.01 s using a target mass resolution of 21,500 (Full width at half maximum, FWHM as defined at *m/z* 500). Mass was corrected during acquisition using a 2 ng/μL solution of leucine enkephalin in acetonitrile/water (1:1, *v/v*) as an external reference (LockSprayTM), with an analyte-to-reference scan ratio of 20:1. Ten QC samples were injected at the beginning of the run in order to condition the column and also injected regularly throughout the analytical batch to ensure system stability and robustness of the method (Want et al., 2013). No major drift in signal response during the analytical run was observed. Each sample was injected in triplicate. In addition, to avoid any bias related to the order of injection, sample run order was set orthogonal to experimental design (Want et al., 2010).

Data Processing

Raw data files (.raw format) acquired on the UPLC-MS^E platform were converted to NetCDF format (Waters Databridge software). Deconvolution of data was performed on XCMS online software with parameters settings suitable for high resolution UPLC-MS data acquired in centroid mode (Smith et al., 2006; Tautenhahn et al., 2012b). Subsequent to data pre-processing, a table listing peak intensity associated to a unique retention time and *m/z* as identifiers (tR_*m/z* data pairs) vs. samples, blank and QC, was generated in both ionization modes. After normalization of the variables to the total intensity and protein concentration, the final dataset was analyzed by multivariate data analysis. The discriminating lipid species identified after supervised analyses were quantified by normalizing the intensities of their peaks to the intensity of the peaks of the corresponding internal standards spiked into the sample prior to lipid extraction and expressed as pmol/mg proteins.

Multivariate Statistical Analysis

Data was pareto-scaled and subjected to principal component analysis (PCA) and orthogonal partial least square discriminant analysis (OPLS-DA) using SIMCA software (v. 13, MKS Umetrics AB, Sweden) (Wiklund et al., 2008).

Lipid Nomenclature

The abbreviations used were according to LipidMaps recommendations (Fahy et al., 2005, 2009). Glycerophospholipids and diacylglycerol were annotated as <lipid subclass>(<total fatty acyl chain length>: <total number of unsaturated bonds>). Sphingolipids were annotated as <lipid subclass>(<sphingoid base residue>/<fatty acyl residue>). Sulfoglycosphingolipids or sulfatides were annotated according to their common name described in Lipid Maps structure database. Lipid identification Lipid species annotation was performed through the online database LIPID MAPS (http://www.lipidmaps.org/) and METLIN Metabolite Database (metlin.scripps.edu) using 5 ppm of mass accuracy as a tolerance window (Sud et al., 2007; Tautenhahn et al., 2012a). Lipid species structure was confirmed by MS^E fragmentation spectra analysis and selected MS^2 experiments. MS^2 data analysis highlights product ions, which are characteristic of lipid class and can serve to discriminate between database hits. The analytical reliability of each ion signal of interest was checked by calculating its relative standard deviation (% r.s.d.) in QC samples (Chan et al., 2011). Electron Microscopy 4 weeks after injection, C57Bl/6 mice were lethally anesthetized and perfused with 4% paraformaldehyde and 2.5% glutaraldehyde in phosphate buffer (PB) 0.12 M pH 7.4. Brains were post-fixed in 2.5% glutaraldehyde in PB. The eGFP fluorescent region from the hippocampus of C57Bl/6 mice injected with AAV−scramble or AAV-shCYP46A1 was excised under a fluorescence dissecting binocular microscope (Leica Z16 APO). Sections of 50 μm were cut with a vibratome and post-fixed in 1% osmium tetroxide for 30 min, rinsed in PB, dehydrated in a graded series of ethanol solutions (75, 80,

90, and 100%), infiltrated with EponTM812, placed in molds and the resin was cured at 60°C in a dry oven during 48 h. Hippocampal semi-thin sections, 0.5 μm thick, obtained with a Leica UC7 ultramicrotome, were stained with a 1% toluidine solution. Ultra-thin sections (90 nm) were cut, counterstained with uranyl acetate (2%) and Reynolds lead citrate (Reynolds, 1963) and observed with a Hitachi HT7700 electron microscope, operating at 80 kV. Pictures (2,048 × 2,048 pixels) were taken with an AMT41B (size of the pixel 7.4 × 7.4 μm).

Immunohistochemical Analysis

Brain tissue obtained at 4 weeks after AAV5-vector injection (scramble or shCYP46A1) was used for anatomical experiments ($n = 5$ mice from by vector). Animals were lethally anesthetized and perfused transcardially with PBS1X (Life technologies™, France). After a post-fixation in PBS1X, 4% paraformaldehyde in for 24 h, the brain was embedded in paraffin. Sections of 6 μm thickness were sequentially (i) deparaffined in xylene, (ii) rehydrated in ethanol, (iii) permeabilized in PBS1X, 0.1% triton X100, (iv) blocked in PBS1X, 0.1% triton X100, 5% normal goat serum and incubated at 4°C for 30 min, in PBS1X, 0.1% triton X100, 5% normal goat serum with an antibody against anti-LAMP1 coupled to biotin for 1 h (1/200, Abcys). Appropriate secondary antibodies were applied 1 h at room temperature. The slides were then mounted in Vectashield® mounting medium containing DAPI (Vectorlabs) and examined by fluorescence or confocal microscopy.

For fluorescence microscopy, images were taken with a Nikon microscope (Eclipse 800) and a digital QIMAGING camera (CCD QICAM cooled plus RGB filter pixel 4.65 × 4.65 μm). Control and test slices were processed the same day and under the same condition. Images were acquired by confocal microscopy using Zeiss LSM 510 Meta confocal laser microscope with a Plan apochromat 63x/1.4 numeric aperture oil immersion objective using the LSM 10v4.osp2. The number of LAMP-1 positive lysosomes in pyramidal neurons of CA3a region was measured in 60 cells per mouse ($n = 5$ mice per vector, six sections) using Image J software.

Electron Microscopy

Four weeks after injection, C57Bl/6 mice were lethally anesthetized and perfused with 4% paraformaldehyde and 2.5% glutaraldehyde in phosphate buffer (PB) 0.12 M pH 7.4. Brains were post-fixed in 2.5% glutaraldehyde in PB. The eGFP fluorescent region from the hippocampus of C57Bl/6 mice injected with AAV5-scramble or AAV5-shCYP46A1 was excised under a fluorescence dissecting binocular microscope (Leica Z16 APO). Sections of 50 μm were cut with a vibratome and post-fixed in 1% osmium tetroxide for 30 min, rinsed in PB, dehydrated in a graded series of ethanol solutions (75, 80, 90, and 100%), infiltrated with EponTM812, placed in molds and the resin was cured at 60°C in a dry oven during 48 h. Hippocampal semi-thin sections, 0.5 μm thick, obtained with a Leica UC7 ultramicrotome, were stained with a 1% toluidine solution. Ultra-thin sections (90 nm) were cut, counterstained with uranyl acetate (2%) and Reynolds lead citrate (Reynolds, 1963), and observed with a Hitachi HT7700 electron microscope, operating at 80 kV. Pictures (2,048 × 2,048 pixels) were taken with an AMT41B (size of the pixel 7.4 × 7.4 μm).

Statistical Analysis

Experimental values are presented as mean ± SEM. Statistical analysis was performed using GraphPad Prism software version 5.0 (San Diego, CA). The significance of cholesterol and oxysterols concentration was determined using Mann-Whitney test with Bonferroni correction. Unpaired *t*-test was performed for gene expression analysis. In all cases, $^{*}p < 0.05$, $^{**}p < 0.01$, and $^{***}p < 0.001$.

RESULTS

Effects of *Cyp46a1* Silencing on the Hippocampus Steroidome

AAV-shCYP46A1 and AAV-scramble (control) vectors were injected in the *stratum lacunosum moleculare* region of the hippocampus of 12 weeks old C57Bl/6 mice ($n = 5$ mice per time per vector). The viral vectors were engineered to express the green fluorescent reporter protein (eGFP) to allow the detection of transduced cells. Three weeks after vector injection, eGFP expression was mainly detected in the neurons of CA3a region of the injected hippocampus (Djelti et al., 2015). Real-time qPCR experiments confirmed that the injection of AAV-shCYP46A1 induced 70% inhibition of *Cyp46a1* gene expression, 3 and 4 weeks after injection (Djelti et al., 2015). Cholesterol-24(*S*)-hydroxylase encoded by *Cyp46a1* gene converts the cholesterol into 24(*S*)-hydroxycholesterol and to a lesser extend into 25-hydroxycholesterol (Lund et al., 1999). The inhibition of *Cyp46a1* gene expression leads to a decrease of 24(*S*)-hydroxycholesterol content by 57% and of 25-hydroxycholesterol content by 52%, 4 weeks after injection (**Figure 1**). As expected, 27-hydroxycholesterol content, which is not produced by cholesterol-24(*S*)-hydroxylase, was not modified. A 3-fold increase of cholesterol content was observed in the hippocampus of mice injected with AAV-shCYP46A1 after 4 weeks. No change in other sterols or oxidative product of cholesterol, such as desmosterol or 5α,6α-epoxycholesterol was observed (Supplementary Figure 1). These results indicate that the injection of AAV-shCYP46A1 induced a strong reduction of cholesterol-24(*S*)-hydroxylase activity leading to a decreased production of 24-(*S*) hydroxycholesterol and to an accumulation of cholesterol.

Cholesterol Accumulation Was Associated with an Increase in Phospholipids and Sphingolipid Species

Multivariate Data Analyses

To investigate the consequences of neuronal cholesterol accumulation on hippocampus lipidome, we performed an untargeted lipidomic analysis 4 weeks after AAV5-vector injection. The lipid contents of hippocampus tissue from control or AAV-shCYP46A1 mice, 4 weeks after injection, were analyzed by UPLC-ESI-MS^{E} in negative and positive ion mode (Supplementary Figure 2). First, UPLC-MS

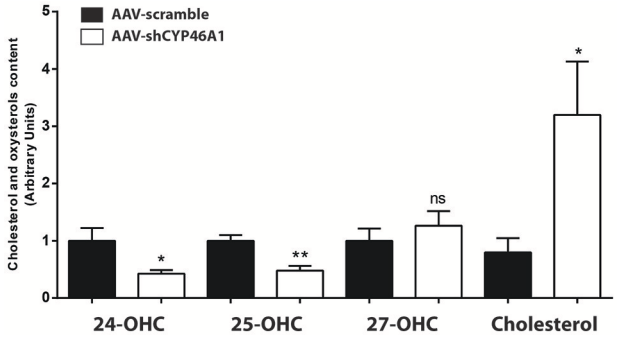

FIGURE 1 | Measurement of cholesterol and oxysterols content 4 weeks after hippocampal injection of AAV-shCYP46A1 vector. AAV-scramble (control) or AAV-shCYP46A1 vector was injected in the *stratum lacunosum moleculare* of hippocampus in C57BL/6 mice. Sterols were extracted, derivatized and analyzed by UPLC-ESI-Q-TOF in MS scan mode. Cholesterol, 24-, 25-, and 27-hydroxycholesterol contents were quantified and normalized to AAV-scramble content ($n = 5$ mice). Unpaired *t*-test was performed. * $P < 0.05$, ** $P < 0.01$; ns, non-significant.

data set obtained from ESI^+ and ESI^- were processed by XCMS software. This processing step generates a list of variables annotated with *t*R_*m/z* ions pairs. After data set normalization, the data analysis is followed by multivariate analysis to identify the most discriminating lipids between the two groups. To easily visualize any clustering between the different sample groups between AAV-scramble (control) and AAV-shCYP46A1 samples, an unsupervised analysis was performed. Indeed, the dimensionality of the listed variables was reduced by unsupervised PCA and a pareto scaling was applied to the data-sets obtained in positive and negative ionization modes. The two sample groups, AAV-scramble and AAV-shCYP46A1 exhibited a separation suggesting that cholesterol accumulation induced by *Cyp46a1* gene silencing led to differences in hippocampus lipidome (**Figures 2A,B**). To identify the variables contributing to the separation between the two sample groups, a supervised OPLS-DA was performed. The score plot of OPLS method shows an excellent group separation between the two sample groups (**Figures 2A,B**). The corresponding S-plot allowed the selection of discriminating variables. Only variables that exhibit a correlation p (corr) higher than 0.7 or lower than −0.7, were explored.

Lipid Annotation and Identification

The variables selected, characterized by *t*R_*m/z* ions pairs, were annotated using LipidMaps and Metlin online databases, according to the exact mass. Among 709 and 234 variables detected, respectively in ESI^- and ESI^+, 22 lipid species in total were annotated (**Tables 1, 2**). These 22 lipids species in AAV-shCYP46A1 hippocampus were increased compared to AAV-scramble. No decrease of any lipid species was observed. The untargeted analysis revealed an increase in glycerophospholipids (PE, PE-P, PC) and glycerolipids (DG) and sphingolipids (Cer, GlcCer, sulfatide) in AAV-shCYP46A1 injected hippocampus (**Tables 1**, **2**). Confirmation of lipid identity was achieved by the analysis of the spectra acquired in MS^E and MS^2 modes.

The identities of the glycerophospholipids PC, PE, and PE-plasmalogens (PE-P) were confirmed by monitoring their respective characteristic polar head group ions: m/z 184.07 in ESI^+ (phosphocholine), m/z 196.03 in ESI-(glycerol phosphoethanolamine with a water loss) (**Tables 1**, **2**).

The fatty acyl chains detected in negative ion mode enable to determine the molecular species, e.g., m/z 253.2 (FA 16:1), 255.2 (FA 16:0), 281.2 (FA 18:1), 283.2 (FA 18:0), 303.23 (FA 20:4), 327.2 (FA 22:6) (**Table 2**). PE(P-18:0/18:1) upon collision-induced dissociation (CID) exhibits fragment-ions at m/z 392.2 and 339.2, corresponding to the fatty alcohol species C18:0 at sn-1 position and the fatty acyl moiety (FA 18:1) at sn-2 position of the glycerol backbone (Zemski Berry and Murphy, 2004).

Sphingolipids species were also subjected to the analysis of characteristic fragments upon MS/MS experiments (**Table 2**). In negative ion mode, the quasi-molecular ion Cer(d18:1/24:1) appears at [M-H]-m/z 646.61. Upon CID, Cer(d18:1/24:1) yield an ion at m/z 628.4, corresponding to loss of water, followed by loss of formaldehyde (HCHO) to give m/z 616.6, which dissociates to m/z 406.4 and 390.4 by loss of the fatty acyl moiety as ketene (loss of C22H43CH=C=O) (Supplementary Figure 3). The m/z 628.4 ion also gives m/z 237.2 and 263.2 (long-chain base moiety, LCB) by elimination of the fatty acyl moiety as an amide (loss of $C_{17}H_{33}CONH_2$, 281 Da). GlcCer(d18:1/24:0) and GlcCer(d18:1/24:1) were observed at m/z 810.68 and 806.66, respectively, were identified similarly (Supplementary Figure 4; Hsu and Turk, 2002).

In ESI-, (3′-sulfo)Galβ-Cer(d18:1/18:0) or C18 sulfatide and (3′-sulfo)Galβ-Cer[d18:1/18:0(2OH)] or C18-OH sulfatide were observed as quasi-molecular ion $[M\text{-}H]^-$ whereas C24:1-OH sulfatide was detected as $[M\text{-}H_2O\text{-}H]^-$ ion. Upon CID (MS^E acquisition mode), m/z 97 and m/z 241 ions were observed corresponding to sulfate ion ($HOSO_3^-$) and to 3-sulfogalactosyl moiety, respectively. The direct loss of the fatty acyl (FA 18:0) as a ketene from m/z 822.54 (C18-OH sulfatide) via the NH-CO bond cleavage results in m/z 540 (LCB moiety), which undergoes a water loss to yield m/z 522 ion. The FA moiety for C18 sulfatide, C18-OH sulfatide and C24:1-OH sulfatide were recorded at m/z 308.2, 324.2, and 388, respectively (Hsu and Turk, 2004).

Semi-quantitative ESI-HRMS analysis of the lipid molecular species in AAV-scramble and AAV-shCYP46A1 hippocampus tissues is presented in **Figures 3A,B**. Upon cholesterol accumulation, an increase of long-chain polyunsaturated fatty acids was observed. Phospholipids (PE, PE-P, PC) consisted mostly of long-chain fatty acid residues with 16 or 18 carbons and few very long-chain fatty acid residues (20 or 22 carbons) mainly with one unsaturation and in a less extend with 4 up to 6 double bonds (**Figures 3A,B**). AAV-shCYP46A1 injection induced an increase of DG species with medium chain length (36–38 carbons) and 4–5 double bonds (**Figure 3A**). An increase of GlcCer(d18:1/24:1), GlcCer(d18:1/24:0) and Cer(d18:1/24:1) were observed. For sulfatide species, an increase in C18 sulfatide, followed by C18-OH and C24:1-OH sulfatide were noticed (**Figure 3B**).

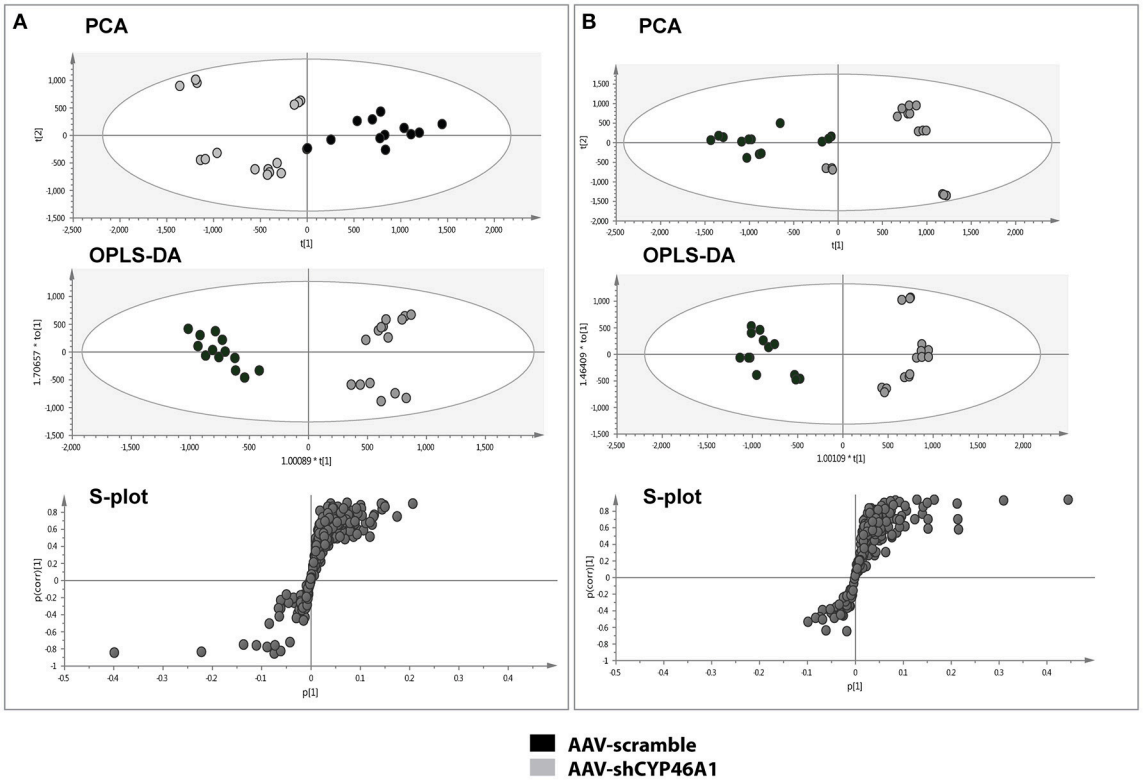

FIGURE 2 | Multivariate data analysis of AAV-scramble and AAV-shCYP46A1 hippocampus lipid data. After extraction, the lipid content of AAV-scramble (control) and AAV-shCYP46A1 hippocampus 4 weeks after injection were analyzed by UPLC-ESI-MS^E. **(A)** PCA, OPLS-DA scores plots and OPLS-DA loadings S-plot for ESI$^+$ mode. For the PCA score plot, the principal component 1 (87%) and principal component 2 (5%) account for 92% of the variance. For the OPLS-DA score plot: one orthogonal and two predictive components, R2X(cum) = 0.837, R2Y(cum) = 0.947, Q2(cum) = 0.927 with a *p*-value, $p = 7.27e\text{-}11$. S-plot from OPLS-DA analysis emphasizes variables that strongly contributed to the class separation between the two groups. **(B)** PCA, OPLS-DA scores plots and OPLS-DA loadings S-plot for ESI- mode. For the PCA score plot, the principal component 1 (87%) and principal component 2 (4%) account for 91% of the variance. For the OPLS-DA score plot: one orthogonal and two predictive components, R2X(cum)=0.757, R2Y(cum) = 0.953, Q2(cum) = 0.905 927 with a *p*-value, $p = 1.14e\text{-}9$. S-plot from OPLS-DA analysis emphasizes variables that strongly contributed to the class separation between the two groups. AAV-scramble and AAV-shCYP46A1 are represented by black and gray dots, respectively. Details of variables are shown in **Tables 1, 2**.

Cholesterol Accumulation Resulting to *Cyp46a1* Gene Inhibition Leads to Increased PC Biosynthesis

We observed by an untargeted approach an increase of PC species in AAV-shCYP46A1 injected hippocampus. We were wondering if this increase of PC species was due to an activation of the biosynthetic pathway. PC is primarily synthetized by the citydine diphosphocholine (CDP) pathway (Kennedy pathway). After phosphorylation of choline into phosphocholine, choline cytidylyltransferase converts phosphocholine to CDP-choline in the presence of Cytidine Triphosphate (CTP) (**Figure 4A**). Phosphocholine moiety is then transferred to CDP-choline to diacylglycerol, producing PC (Fagone and Jackowski, 2013).

In vitro data show a relation between the expression of spliced XBP1 form and the choline phosphate cytidylyltransferase (Sriburi et al., 2004, 2007). Spliced XBP1 form is involved in ER stress previously described in our model (Djelti et al., 2015). Thus, we monitored the expression of gene encoding spliced XBP1 form and the two isoforms, α (*Pcyt1a*) and β (*Pcyt1b*) of the choline phosphate cytidylyltransferase by RT-qPCR (**Figures 4B–D**). We focus our attention on the mRNA expression of choline cytidyltransferase because it's the rate-limiting enzyme required for the synthesis of PC through the CDP-choline pathway (Pelech and Vance, 1984; Pelech et al., 1984). The expression of spliced *XBP1* gene, was increased by 1.5-fold, at 3 and 4 weeks after injection of AAV-shCYP46A1 vector (**Figure 4B**). In parallel, a 1.5-fold increase of *Pcyt1a gene expression* was evidenced 4 weeks after injection (**Figure 4C**). No increase of *Pcyt1b* was observed 3 and 4 weeks after injection (**Figure 4D**). The increase of *Pcyt1a* gene expression suggests that the accumulation of cholesterol resulting of CYP46A1 inhibition induced the expression of spliced XBP1 form and the increase of PC biosynthesis, 4 weeks after injection.

Neuronal Cholesterol Accumulation Induced Imbalance in Sphingolipid Metabolism

Lipidomics analysis revealed an increase of ceramides and glucosylceramides species with long-chain fatty acids, namely

TABLE 1 | Discriminative lipid species whose detected levels in AAV-shCYP46A1 4 weeks after injection are higher than in the control (AAV-scramble) predicted by OPLS-DA obtained from positive ion mode data set.

m/z $[M+H]^+$	t_R (min)	Annotation	Fold change in level content (sh/scramble)	p (corr)	p (1)	CV% in QC	MS/MS (*m/z*)[#]
706.53	5.72	PC 14:0/16:0	1.56	0.82	0.05	6	184.07–450.29–468.30–478.32–496.33
732.55	5.82	PC 16:0/16:1	1.49	0.89	0.09	3	184.07–313.27–476.31–478.32–496.33
760.58	6.33	PC 16:0/18:1	1.35	0.90	0.44	1	184.07–478.32–496.33–504.34–577.52
762.60	6.75	PC 16:0/18:0	1.24	0.73	0.14	2	184.07–478.32–496.33–506.36–524.37
786.60	6.41	PC 18:1/18:1	1.41	0.92	0.13	4	184.07-478.32-504.34-522.35-603.53
788.61	6.83	PC 18:0/18:1	1.37	0.69	0.22	2	184.07–339.29–504.34-506.36-522.35
806.56	5.81	PC 16:0/22:6	1.48	0.83	0.14	3	184.07-385.27-478.33–496.33–623.50
832.58	5.88	PC 18:1/22:6	1.61	0.81	0.06	10	184.07–385.27–504.34–550.32–649.52
634.54	7.08	DAG 36:4	1.64	0.78	0.04	4	ND
660.55	7.13	DAG 38:5	1.75	0.72	0.03	15	ND
662.57	7.51	DAG 38:4	1.69	0.78	0.11	8	ND

[#]*Indicates characteristic fragment ions.*

TABLE 2 | Discriminative lipid species whose detected levels in AAV-shCYP46A1 4 weeks after injection are higher than in the control (AAV-scramble) predicted by OPLS-DA obtained from negative ion mode data set.

m/z	t_R (min)	Annotation	Fold change in level content (sh/scramble)	p (corr)	p (1)	CV% in QC	MS/MS (*m/z*)[#]
646.61[a]	7.76	Cer d18:1/24:1	1.65	−0.81	−0.06	6	237.22–263.24–390.37–406.37–598.60–616.60
810.68[a]	7.67	GlcCer d18:1/24:0	1.62	−0.68	−0.09	5	237.22–263.24–392.38–408.37–600.60–648.63
808.66[a]	7.28	GlcCer d18:1/24:1	1.64	−0.69	−0.16	5	237.22–263.24–390.37–406.37–598.60–646.61
764.52[a]	6.06	PE 18:1/20:4	1.37	−0.65	−0.07	6	196.04–281.24–303.23–478.29
788.52[a]	5.95	PE 18:1/22:6	1.32	−0.75	−0.05	5	196.04–281.24–327.23–478.29
744.55[a]	6.88	PE 18:0/18:1	1.53	−0.65	−0.09	4	196.03–281.24–283.26
716.52[a]	5.77	PE 16:0/18:1	1.53	−0.74	−0.03	14	196.03–253.21–255.23–281.24–283.26
728.55[a]	7.14	PE P-18:0/18:1	1.86	−0.66	−0.12	4	196.03–281.24–339.29–392.29
806.54[a]	5.33	sulfatide C18:0	2.03	−0.82	−0.07	6	96.95–241–308.29–522.27–564.53–566.30
822.54[a]	5.21	sulfatide C18:0(OH)	2.08	−0.71	−0.04	10	96.96–241–324.29–522.27–540.28
886.60[b]	5.93	sulfatide C24:1(OH)	2.12	−0.72	−0.04	11	96.96–241–327.23–581.30–599.32

[#]*Indicates characteristic fragment ions.*

Cer(d18:1/24:1), GlcCer(d18:1/24:0) and GlcCer(d18:1/24:1). No increase in sphingomyelin species was observed. To get further insight into the mechanism of ceramide increase, we investigated the expression of enzymes involved in ceramide metabolism. Ceramides are mostly generated by *de novo* synthesis from serine and palmitoyl-CoA. Ceramides are also produced by hydrolysis of sphingomyelin or by sphingosine from the salvage pathway (**Figure 5A**). The salvage pathway re-utilizes long chain sphingoid bases to form ceramide, through the action of ceramide synthase (Lass2) (Hannun and Obeid, 2008). LASS2 synthesizes ceramide species containing mainly long-chain fatty acyl moieties (22 up to 24 carbons), while synthesis of medium-chain ceramides (16 and 18 carbons) is relatively marginal (Laviad et al., 2008). We observed a tendency of the expression of Lass2 mRNA to be increased (1.6-fold) from 4 weeks after injection of AAV-shCYP46A1 (**Figure 5B**). Expression of *Smpd1* and *Smpd3* genes, coding, respectively for the acid sphingomyelinase and the neutral sphingomyelinase enzymes catalyzing the conversion of sphingomyelin into ceramide was then investigated. A 1.6-fold increase of *Smpd1* gene expression was observed 4 weeks after injection (**Figure 5C**) while no change was observed in *Smpd3* gene expression (**Figure 5D**). The increase of ceramides seems to result from the acid hydrolysis of sphingomyelin by the acid sphingomyelinase, SMPD1.

An increase in GlcCer species was also observed in AAV-CYP46A1 injected mice. We thus investigated the expression level of the enzymes involved in their synthesis. GlcCer is synthetized from ceramides (**Figure 5A**). A glucose residue is transferred to Cer by the UDP-glucose ceramide glucosyltransferase (UGCG) enzyme to form GlcCer. Addition of galactose to GlcCer results in the formation of lactosyl ceramide (LacCer), which is the precursor of the glycolipids also called gangliosides. Gangliosides are found on the surface of essentially all mammalian cells but are particularly abundant on neuronal cell surfaces like for instance GM1. Further addition of different sugars moieties (galactose, N-acetylgalactosamine, N-acetylglucosamine, sialic acid) in different configurations generates large numbers of gangliosides (Kolter et al.,

2002; Yu et al., 2004). The biosynthetic pathway of the gangliosides is controlled by a few key glycosyltransferases and sialyltransferases. One of these reactions, is mediated by the transfer of sialic acid from CMP-sialic acid to galactose-containing substrates, to form GM1. As shown in **Figure 6A**, the expression of Ugcgc gene revealed no significant changes 3 or 4 weeks after injection of the AAV-shCYP46A1 vector. However, the expression of St3gal1 gene involved in conversion of lactosylceramide in gangliosides was increased 4 weeks after injection only (**Figure 6B**).

Increased Level of the Lysosomal Protein LAMP-1 and Accumulation of Phagolysosomes after Inhibition of *Cyp46a1* Gene Expression

Late endosomal cholesterol accumulation leads to impaired intra-endosomal trafficking (Sobo et al., 2007). In our previous study, we found that endosomal trafficking was disturbed in CA3a pyramidal cells of mice injected with AAV-shCYP46A1 vector leading to enlarged endosomes (Djelti et al., 2015). To confirm that neuronal cholesterol accumulation in AAV-shCYP46A1 injected animals leads to impaired endosomal trafficking, we investigated lysosome number and morphology. First, we observed that the immunoreactivity of the lysosomal-associated membrane protein 1 (LAMP-1) was increased together with a 2.9 ± 0.42-fold increase in lysosome numbers in neurons of AAV-shCYP46A1 injected mice compared to the control (AAV-scramble) (**Figures 7A,B**). Ultrastructural analysis revealed abnormal lysosomes in CA3a neurons of mice injected with AAV-shCYP46A1, 4 weeks after injection (**Figure 7C**). In neurons of AAV-scramble injected mice, the arrows represent mitochondria (M), primary lysosomes (L1) and secondary lysosomes (L2) with normal morphology and homogenous with finely granular content (**Figure 7C**-left panel). In contrast, in neurons of AAV-shCYP46A1 injected mice, electron micrograph exhibits autophagolysosomes containing dark content with numerous electron-dense vesicles and mitochondria in the lumen (**Figure 7C**-right panel). Altogether, these observations suggest that cholesterol accumulation in neurons leads to an impairment of the endosomal-lysosomal membrane trafficking.

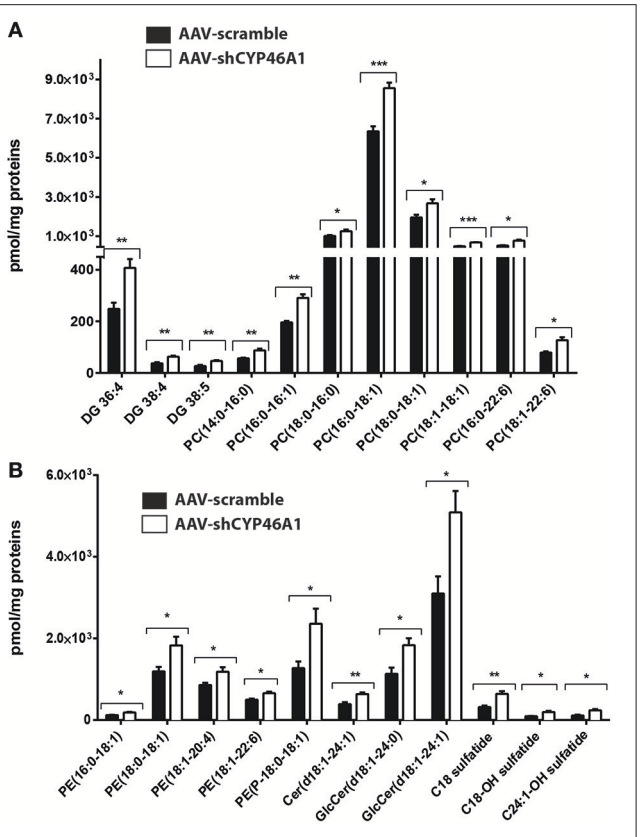

FIGURE 3 | Relative quantification of lipids in hippocampus of C57Bl/6 mice after injection of AA V5-scramble (control) and AA V5-shCYP46A1. **(A,B)** Rise of phosphatidylcholine (PC), diacylglycerol (DAG), ceramides (Cer), sulfatide, phosphatidylethanolamine plasmalogen (PE-P) and phosphatidylethanolamine (PE) in AAV-shCYP46A1 hippocampus compared to the control. The results are expressed as nmol per mg of proteins and as the mean ± SD ($n = 5$ mice per group). Measurements were performed in triplicate. Unpaired *t*-test was performed. *$P < 0.05$, **$P < 0.01$, and ***$P < 0.001$.

DISCUSSION

Impairment in cholesterol metabolism is involved in many neurodegenerative diseases including AD (Anstey et al., 2008). However, the molecular mechanism that stands behind altered cholesterol levels and neurodegeneration remains incompletely understood. We established an *in vivo* mouse model to bring out the consequences of lipid perturbation associated with a specific cholesterol accumulation in neurons by down-regulating *in vivo* the cholesterol-24 hydroxylase coding gene (*cyp46a1*) expression using an AAV5-based RNA interference strategy (Djelti et al., 2015; **Figure 8**). The neuronal cholesterol-24 hydroxylase enzyme is involved in the cerebral clearance of cholesterol by catalyzing the conversion of cholesterol into 24(*S*)-hydroxycholesterol and, to a lesser extent, 25-hydroxycholesterol (Lund et al., 1999, 2003). The synthesis of 24(*S*)-hydroxycholesterol and its secretion from the brain represent the main mechanism of cholesterol turnover in this organ (Lund et al., 2003).

Our previous study showed that inhibition of *cyp46a1* gene expression in wild-type mice lead to abnormal processing of APP with Aβ peptides accumulation and tau hyperphosphorylation, two hallmarks of AD, associated with ER stress and enlargement of the endosomal/lysosomal compartments. This cascade of events finally caused apoptotic neuronal death leading to cognitive impairment and hippocampal atrophy. These toxic consequences of cholesterol increase were strongly aggravated in APP23 mice (Djelti et al., 2015).

The aim of the present study was to characterize the detailed lipid perturbations associated with cholesterol accumulation induced by CYP46A1 inhibition in hippocampal neurons. Lipid modifications were analyzed 4 weeks after injection of an AAV5 vector expressing a short-hairpin (sh) RNA against *cyp46a1* gene, a time where neuronal loss was shown to appear in this model (Djelti et al., 2015).

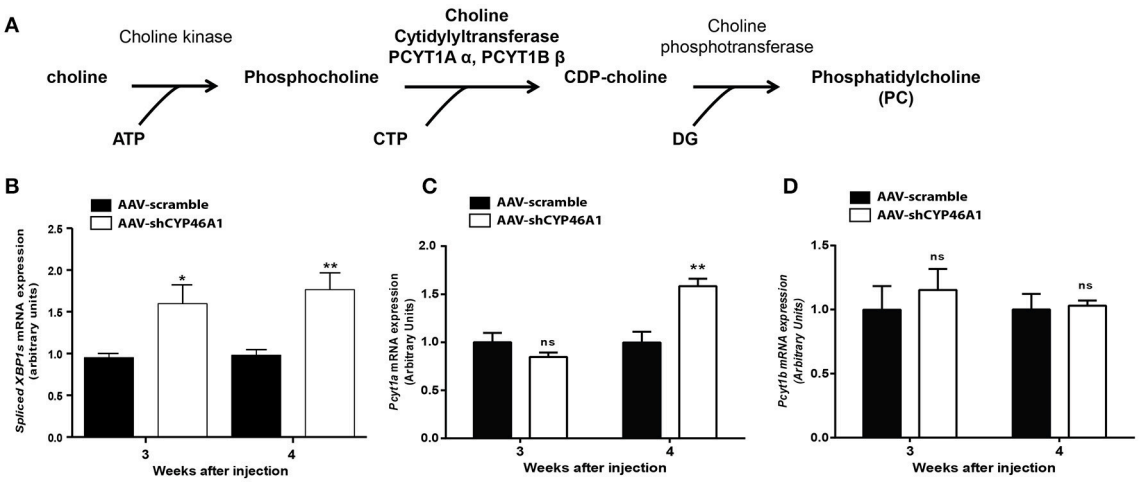

FIGURE 4 | *De novo* synthesis of phosphatidylcholine *via* the Kennedy pathway **(A)**. Quantitative expression of spliced XBP1 form **(B)** and choline-phosphate cytidylyltransferase α (PCYT1A) **(C)** and choline-phosphate cytidylyltransferase β (PCYT1B) **(D)** genes after injection of AAV5-scramble and AAV-shCYP46A1 vectors in the hippocampus of C57BL/6 mice. Quantitative expression of murine spliced XBP1 **(B)**, Pcyt1a **(C)** and Pcyt1b **(D)** genes were performed after 3 and 4 weeks post-injection ($n = 5$ mice per vector, per time). Expression data are normalized to the expression of AAV-scramble. Unpaired *t*-test was performed. $^*P < 0.05$; $^{**}P < 0.01$; ns, non-significant.

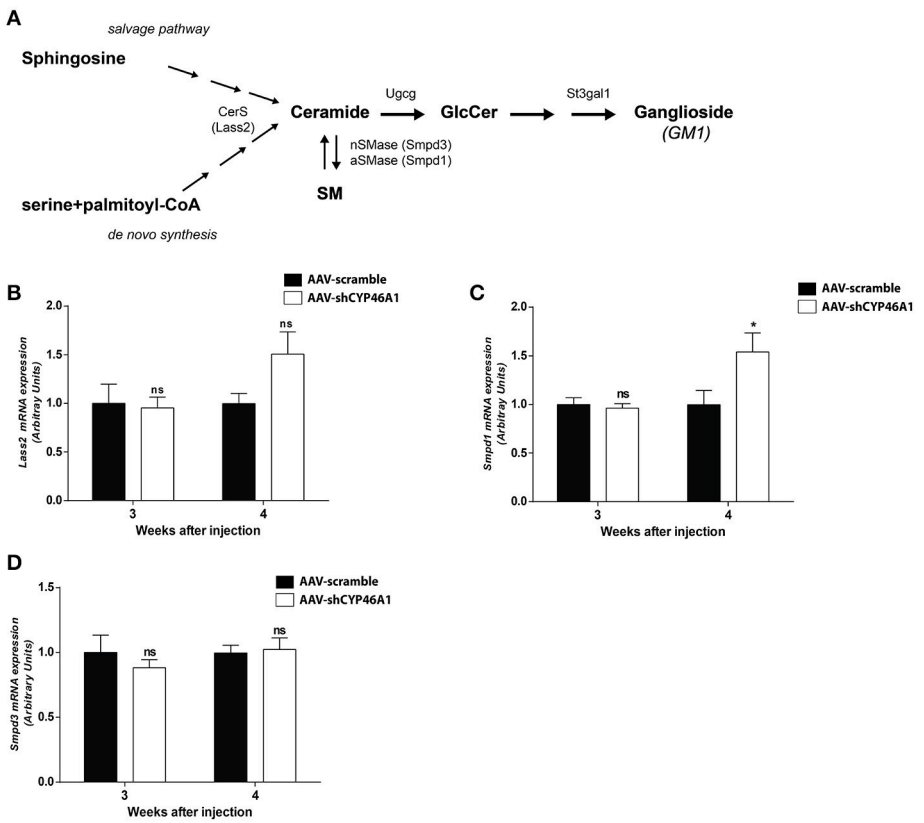

FIGURE 5 | Sphingolipid metabolism **(A)**. Quantitative expression of ceramide synthase 2 (LASS2) **(B)**, acid sphingomyelinase (SMPD1) **(C)** and neutral sphingomyelinase (SMPD3) **(D)** genes in C57BL/6 mice after cerebral injections of AAV-scramble and AAV-shCYP46A1 vectors. Quantitative expression of murine *Lass2* (B), *Smpd1* (C) and *Smpd3* (D) genes were performed 3 and 4 weeks post-injection ($n = 5$ mice). Expression data are normalized to the expression of AAV5-scramble (control). Unpaired *t*-test was performed. $^*P < 0.05$; ns, non-significant.

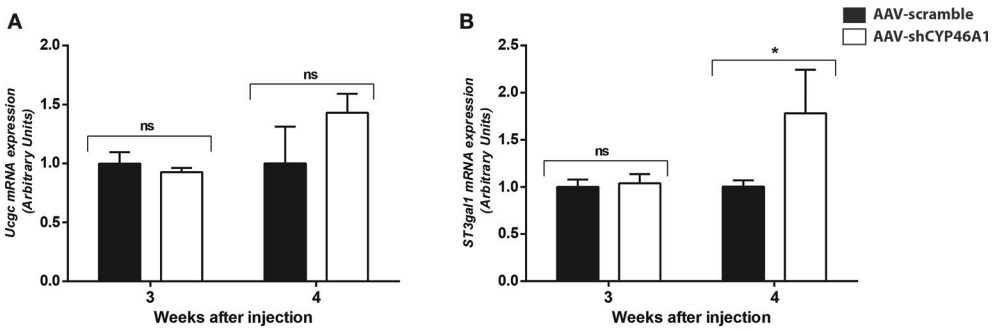

FIGURE 6 | Quantitative expression of UDP-glucose ceramide glucosyltransferase (UCGC) **(A)** and ST3 beta-galactoside alpha-2,3-sialyltransferase (ST3GAL1) **(B)** after hippocampal injections of AAV-scramble and AAV-shCYP46A1 vectors. Quantitative expression of murine *Ucgc* **(A)**, *St3gal1* **(B)** genes were performed 3 and 4 weeks post-injection ($n = 5$ mice). Expression data are normalized to the expression of AAV-scramble (control). Unpaired *t*-test was performed. $^*P < 0.05$; ns, non-significant.

The delivery of *Cyp46a1* sh-RNA in the *stratum lacunosum moleculare* region of C57Bl/6 mice hippocampus using AAV5 vector stereotactic injection leads to an efficient neuronal inhibition of *Cyp46a1* gene expression in CA3a region in AAV-shCYP46A1 injected mice (Chali et al., 2015). This inhibition leads to a decrease of 24(*S*)-hydroxycholesterol and 25-hydroxycholesterol content, accompanied by an accumulation of cholesterol.

Previous studies have shown that the cholesterol 24-hydroxylase knock-out mice (*Cyp46a1*$^{(-/-)}$ exhibit 50% decrease in *de novo* cholesterol synthesis and a corresponding 50% decrease in cholesterol excretion from the brain without modification of the cholesterol content (Lund et al., 2003; Xie et al., 2003; Meljon et al., 2014). This shows that alterations of *Cyp46a1* gene expression at an early developmental stage are compensated by homeostatic adaptation of cholesterol metabolism, and in particular cholesterol synthesis. In our *in vivo* model, the cholesterol synthesis was not modified. Indeed, we did not monitor any changes in cholesterol precursors content, such as cholestanol, desmosterol or 5α,6α-epoxycholesterol. Moreover, expression of genes coding the enzymes involved in the synthesis of cholesterol or its regulation (HMG-CoA reductase and Srebp-1) remained unchanged in the hippocampus of injected mice (Djelti et al., 2015). The 70% inhibition of *Cyp46a1* gene expression by AAV-shCYP46A1 blocks the clearance of cholesterol leading to an accumulation of cholesterol with no effect on cholesterol biosynthesis (Djelti et al., 2015).

The lipid analysis carried out in the present study revealed an increase of brain structural glycerophospholipids (PC, PE, PE-P) and sphingolipids. PE, PE-P and PC species with medium-chain length fatty acyls were augmented in hippocampi with an accumulation of cholesterol as well as an increase of *Pcyt1α* expression, an enzyme involved in the rate-limiting step of PC biosynthesis. An *in vitro* study showed that free cholesterol accumulation in macrophages up-regulated PC synthesis (Sriburi et al., 2004, 2007). The increase of PC bulk is an adaptive response to prevent toxic effect of cholesterol excess by maintaining the ratio free cholesterol: PC in the membrane to a physiological level. Increase of PC was shown to be induced by ER stress. In our previous study, we showed in our model a rapid and major increase of ER stress (already present 3 weeks after injection) with phosphorylation of PERK and an increase of CHOP protein in response of neuronal accumulation of cholesterol.

Sphingolipids e.g., sphingomyelin, ceramides, sulfatides, gangliosides are enriched in the central nervous system. In addition to important structural role like membrane integrity, sphingolipids (ceramides or sphingosine-1-phosphate) in association with cholesterol function as second messengers to modulate a variety of signaling event. Perturbations in sphingolipid homeostasis and trafficking have been extensively documented in neurodegeneration disorders like Niemann-Pick type C or AD (He et al., 2010; Fan et al., 2013). The lipid profiling carried out in the present study also revealed that elevated species across multiple sphingolipid classes were increasing with cholesterol accumulation. Ceramides, glucosylceramides and sulfatides with medium or long-chain fatty acyls (C18; C24) were increased. Though, sphingomyelin content was not modified. Early reports show that ceramide levels are elevated at the earliest clinically recognizable stage of AD mediating oxidative stress-induced neuronal death (Cutler et al., 2004; He et al., 2010). Alterations of long-chain ceramides together with an increase of cholesterol were observed in brains of AD patients (Soreghan et al., 2003; Cutler et al., 2004; Han, 2005; Mattson et al., 2005).

Ceramide is generated either by the degradation of sphingomyelin *via* the action of sphingomyelinases or *via de novo* synthesis through the enzyme ceramide synthase, Lass2. Sphingomyelin degradation is achieved either by the acid sphingomyelinase, Smpd1 (lysosomal) or the neutral sphingomyelinase Smpd3 (membrane) to form ceramide. We observed that the expression of *Smpd1* gene encoding acid sphingomyelinase was increased while the expression of *Smpd3* gene encoding neutral sphingomyelinase and *Lass2* gene encoding ceramide synthase were not modified. This observation is in a perfect agreement with a previous study showing that the expression of several genes involved in sphingomyelin metabolism, are increased in AD brain including acid sphingomyelinase (Katsel et al., 2007).

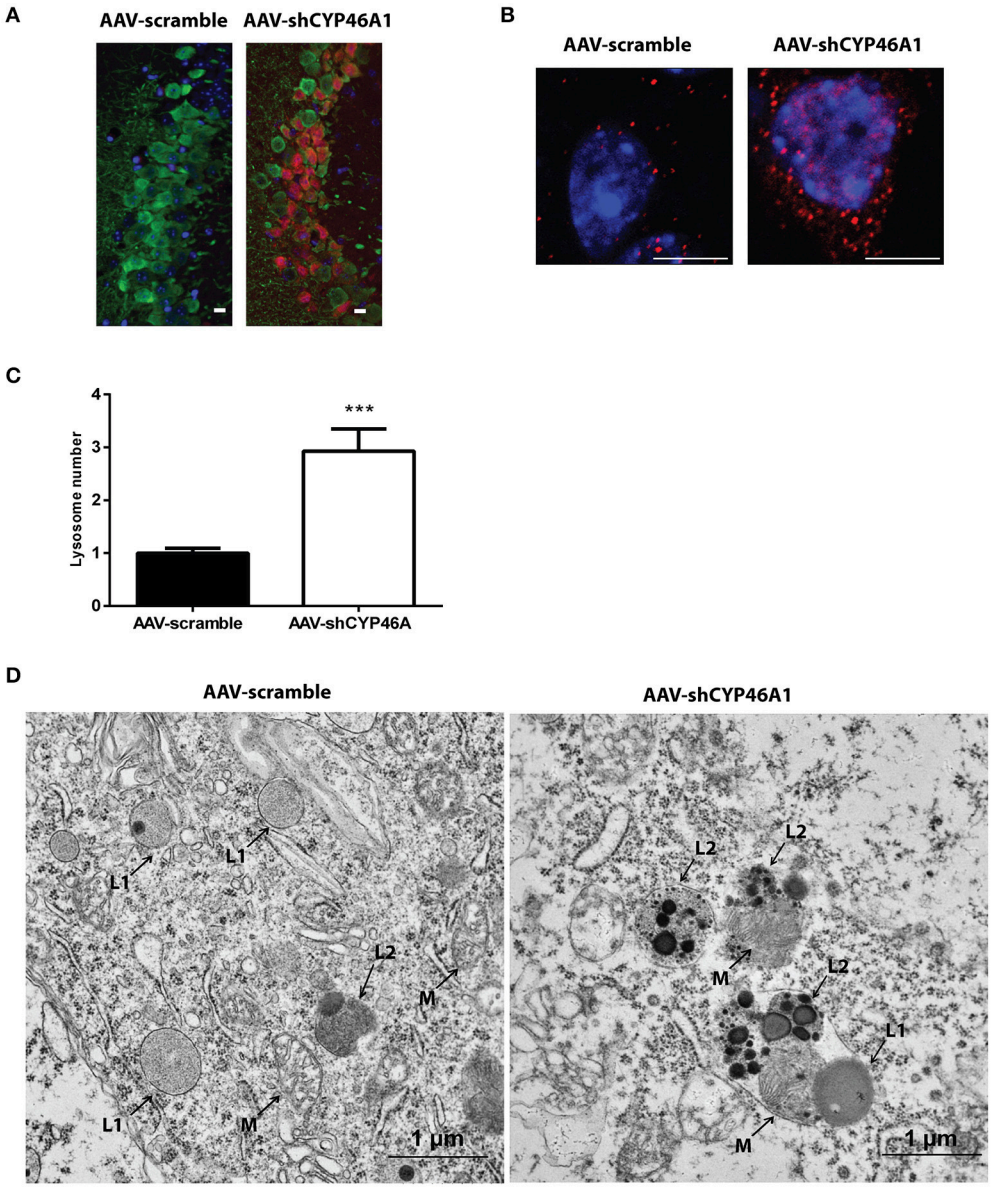

FIGURE 7 | Accumulation and ultrastructural modifications of lysosomes in CA3a neurons of AAV-shCYP46A1 injected mice. **(A)** Representative eGFP immunostaining (green) and LAMP-1 immunoreactivity (lysosomal cell, red) (scale bar: 50 μm) **(B)** Representative image by laser confocal microscopy showing increased puncta-like immunoreactivity of LAMP-1 (red) in CA3a neurons of the hippocampus of C57BL/6 mice 4 weeks after injection of AAV-shCYP46A1 vector compared to AAV-scramble. Nuclei are counterstained with DAPI (blue) (scale bar: 6 μm). **(C)** Quantification of the number of LAMP-1-positive lysosomes in CA3a pyramidal cells at 4 weeks after AAV5-shCYP injection normalized to values from AAV5-scramble injected mice (30 cells of 5 mice per vector per time; 2-tailed unpaired *t*-test was performed. ***$P < 0.0001$. **(D)** Electron micrographs showing abnormal lysosomes in CA3a neurons of C57BL/6 mice 4 weeks after injection of AAV-shCYP46A1 vector (scale bar: 1 μm). (M): mitochondria, (L1): primary lysosomes, (L2): secondary lysosomes.

The excess of neuronal cholesterol after injection of AAV5-shCYP46A1 conduced to an increase in gangliosides GM1. A significant increase expression of gene encoding ST3 β-galactoside α-2,3-sialyltransferase 1, ST3GAL1 was observed. Interestingly, several strong indications point toward an important role of gangliosides in AD pathogenesis. Indeed, β-amyloid peptides interact with GM1, which is abundantly expressed in neural cell membranes and pile in lipid rafts to form amyloid fibrils (Yamamoto et al., 2008; Ariga et al., 2011; Matsuzaki, 2011; Yanagisawa, 2011). Some studies reported that the concentration and composition of gangliosides are altered in the brains of AD patients and in transgenic mouse models of AD (Chan et al., 2012). In our previous study, we showed that neuronal cholesterol accumulation was associated with the enlargement of the endosomal/lysosomal compartments disturbing the processing of APP and leading to the accumulation of Aβ peptides (Djelti et al., 2015). Various studies have documented abnormal endosomal morphology in the brain of

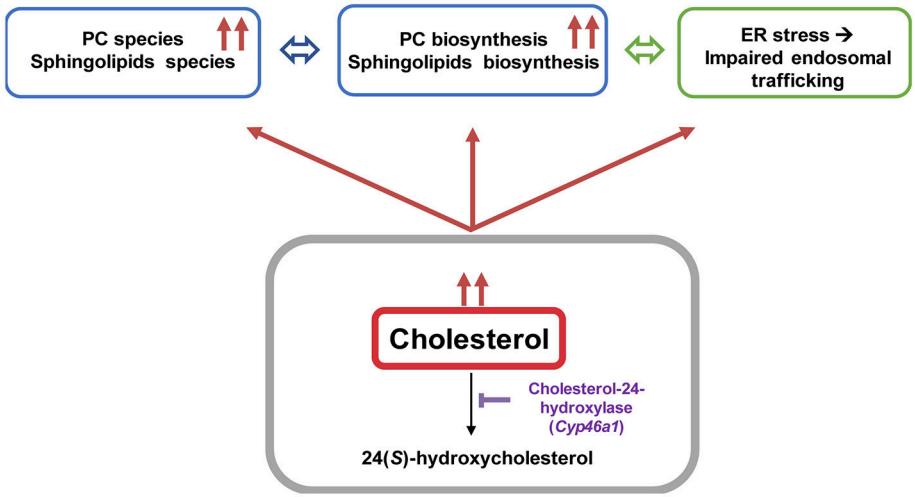

FIGURE 8 | Cholesterol overload in neurons induced by Cyp46a1 down-regulation in mice hippocampus disrupts lipid metabolism and lysosomal trafficking.

individuals with AD. Enlarged early endosomes were formed in most pyramidal neurons in the brains of patients with sporadic AD (Cataldo et al., 2000). *In vitro*, after cholesterol loading treatment, primary culture neurons exhibited enlarged endosomes (Cossec et al., 2010). Increase in number of secondary lysosomes and changes in levels of lysosomal enzymes have previously been also associated with brain aging and age-related neurodegeneration (Lynch and Bi, 2003). It has been also shown that the lysosomal membrane protein LAMP-1 was upregulated at both the mRNA and protein level in the AD brain (Barrachina et al., 2006). Our experiment revealed that the lysosomes were abnormal, swelling and their numbers increased. These observations confirmed previous results showing modification of lysosome morphology induced by cholesterol excess (Barrachina et al., 2006). To summarize, we showed that *in vivo* cholesterol accumulation in hippocampal neurons following inhibition of CYP46A1 enzyme leads to major dysregulation of lipid homeostasis with combined accumulation of different lipid species from PC, PE, ceramides, sulfatides and gangliosides classes (**Figure 8**). Such modifications of the lipidome were also identified in cerebral tissues of AD patients (Han et al., 2001, 2002; Cutler et al., 2004; Han, 2005; Chan et al., 2012). Moreover, *in vivo* cholesterol accumulation in neurons induced a cascade of events with amyloid pathology, tau hyperphosphorylation and ER stress leading to neuronal dysfunction and cell death. In conclusion, lipidomics analysis combined with RNA interference-based strategy thus provides a powerful tool to further elucidate the specific roles of lipid intermediates in cell signaling and pathology of neurodegenerative diseases.

AUTHOR CONTRIBUTIONS

SAy, FD, SAl, MG, NA, PA, and NC conceived the experiments. FD performed AAV injections. SAy, AR, DD, MG, and NA performed MS experiments. FD, JV, and IB performed RT-PCR experiments. FD, SAl, and DL performed microscopy experiments. SAy, FD, SAl, NA, AR, and NC analyzed the data. SAy, FD, SAl, EH, NA, NC, and OL interpreted the experiments and wrote the paper.

ACKNOWLEDGMENTS

The post-doctoral position of SAy was funded by Agence Nationale de la Recherche (French-Canadian Cooperation-Project Cholesterol Alzheimer disease, 2010-MALZ-10303). The PhD position of FD was funded by the Ministère de l'Enseignement Supérieur et de la Recherche and the University Paris Descartes. The PhD position of MG was funded by Technologie Servier (Orléans, France). OL is indebted to Fondation pour la Recherche Médicale, Région-Île-de-France and Centre National de la Recherche Scientifique for their financial support.

SUPPLEMENTARY MATERIAL

The Supplementary Material for this article can be found online at: http://journal.frontiersin.org/article/10.3389/fnmol.2017.00211/full#supplementary-material

REFERENCES

Anstey, K. J., Lipnicki, D. M., and Low, L. F. (2008). Cholesterol as a risk factor for dementia and cognitive decline: a systematic review of prospective studies with meta-analysis. *Am. J. Geriatr. Psychiatry* 16, 343–354. doi: 10.1097/01.JGP.0000310778.20870.ae

Ariga, T., Wakade, C., and Yu, R. K. (2011). The pathological roles of ganglioside metabolism in Alzheimer's disease: effects of gangliosides on neurogenesis. *Int. J. Alzheimers. Dis.* 2011:193618. doi: 10.4061/2011/193618

Ayciriex, S., Gerber, H., Osuna, G. M., Chami, M., Stahlberg, H., Shevchenko, A., et al. (2016). The lipidome associated with the gamma-secretase

complex is required for its integrity and activity. *Biochem. J.* 473, 321–334. doi: 10.1042/BJ20150448

Ayciriex, S., Regazzetti, A., Gaudin, M., Prost, E., Dargere, D., Massicot, F., et al. (2012). Development of a novel method for quantification of sterols and oxysterols by UPLC-ESI-HRMS: application to a neuroinflammation rat model. *Anal. Bioanal. Chem.* 404, 3049–3059. doi: 10.1007/s00216-012-6396-6

Barrachina, M., Maes, T., Buesa, C., and Ferrer, I. (2006). Lysosome-associated membrane protein 1 (LAMP-1) in Alzheimer's disease. *Neuropathol. Appl. Neurobiol.* 32, 505–516. doi: 10.1111/j.1365-2990.2006.00756.x

Bieche, I., Lerebours, F., Tozlu, S., Espie, M., Marty, M., and Lidereau, R. (2004). Molecular profiling of inflammatory breast cancer: identification of a poor-prognosis gene expression signature. *Clin. Cancer Res.* 10, 6789–6795. doi: 10.1158/1078-0432.CCR-04-0306

Bjorkhem, I. (2006). Crossing the barrier: oxysterols as cholesterol transporters and metabolic modulators in the brain. *J. Intern. Med.* 260, 493–508. doi: 10.1111/j.1365-2796.2006.01725.x

Bjorkhem, I., Leoni, V., and Meaney, S. (2010). Genetic connections between neurological disorders and cholesterol metabolism. *J. Lipid Res.* 51, 2489–2503. doi: 10.1194/jlr.R006338

Bjorkhem, I., and Meaney, S. (2004). Brain cholesterol: long secret life behind a barrier. *Arterioscler. Thromb. Vasc. Biol.* 24, 806–815. doi: 10.1161/01.ATV.0000120374.59826.1b

Castro-Perez, J. M., Kamphorst, J., DeGroot, J., Lafeber, F., Goshawk, J., Yu, K., et al. (2010). Comprehensive LC-MS E lipidomic analysis using a shotgun approach and its application to biomarker detection and identification in osteoarthritis patients. *J. Proteome Res.* 9, 2377–2389. doi: 10.1021/pr901094j

Cataldo, A. M., Peterhoff, C. M., Troncoso, J. C., Gomez-Isla, T., Hyman, B. T., and Nixon, R. A. (2000). Endocytic pathway abnormalities precede amyloid beta deposition in sporadic Alzheimer's disease and Down syndrome: differential effects of APOE genotype and presenilin mutations. *Am. J. Pathol.* 157, 277–286. doi: 10.1016/S0002-9440(10)64538-5

Chali, F., Djelti, F., Eugene, E., Valderrama, M., Marquer, C., Aubourg, P., et al. (2015). Inhibiting cholesterol degradation induces neuronal sclerosis and epileptic activity in mouse hippocampus. *Eur. J. Neurosci.* 41, 1345–1355. doi: 10.1111/ejn.12911

Chan, E. C., Pasikanti, K. K., and Nicholson, J. K. (2011). Global urinary metabolic profiling procedures using gas chromatography-mass spectrometry. *Nat. Protoc.* 6, 1483–1499. doi: 10.1038/nprot.2011.375

Chan, R. B., Oliveira, T. G., Cortes, E. P., Honig, L. S., Duff, K. E., Small, S. A., et al. (2012). Comparative lipidomic analysis of mouse and human brain with Alzheimer disease. *J. Biol. Chem.* 287, 2678–2688. doi: 10.1074/jbc.M111.274142

Cheng, D., Jenner, A. M., Shui, G., Cheong, W. F., Mitchell, T. W., Nealon, J. R., et al. (2011). Lipid pathway alterations in Parkinson's disease primary visual cortex. *PLoS ONE* 6:e17299. doi: 10.1371/journal.pone.0017299

Cossec, J. C., Marquer, C., Panchal, M., Lazar, A. N., Duyckaerts, C., and Potier, M. C. (2010). Cholesterol changes in Alzheimer's disease: methods of analysis and impact on the formation of enlarged endosomes. *Biochim. Biophys. Acta* 1801, 839–845. doi: 10.1016/j.bbalip.2010.03.010

Cutler, R. G., Kelly, J., Storie, K., Pedersen, W. A., Tammara, A., Hatanpaa, K., et al. (2004). Involvement of oxidative stress-induced abnormalities in ceramide and cholesterol metabolism in brain aging and Alzheimer's disease. *Proc. Natl. Acad. Sci. U.S.A.* 101, 2070–2075. doi: 10.1073/pnas.0305799101

de Chaves, E. I., Rusinol, A. E., Vance, D. E., Campenot, R. B., and Vance, J. E. (1997). Role of lipoproteins in the delivery of lipids to axons during axonal regeneration. *J. Biol. Chem.* 272, 30766–30773. doi: 10.1074/jbc.272.49.30766

Dietschy, J. M., and Turley, S. D. (2004). Thematic review series: brain Lipids. Cholesterol metabolism in the central nervous system during early development and in the mature animal. *J. Lipid Res.* 45, 1375–1397. doi: 10.1194/jlr.R400004-JLR200

Di Paolo, G., and Kim, T. W. (2011). Linking lipids to Alzheimer's disease: cholesterol and beyond. *Nat. Rev. Neurosci.* 12, 284–296. doi: 10.1038/nrn3012

Djelti, F., Braudeau, J., Hudry, E., Dhenain, M., Varin, J., Bieche, I., et al. (2015). CYP46A1 inhibition, brain cholesterol accumulation and neurodegeneration pave the way for Alzheimer's disease. *Brain* 138, 2383–2398. doi: 10.1093/brain/awv166

Fagone, P., and Jackowski, S. (2013). Phosphatidylcholine and the CDP-choline cycle. *Biochim. Biophys. Acta* 1831, 523–532. doi: 10.1016/j.bbalip.2012.09.009

Fahy, E., Subramaniam, S., Brown, H. A., Glass, C. K., Merrill, A. H. Jr., Murphy, R. C., et al. (2005). A comprehensive classification system for lipids. *J. Lipid Res.* 46, 839–861. doi: 10.1194/jlr.E400004-JLR200

Fahy, E., Subramaniam, S., Murphy, R. C., Nishijima, M., Raetz, C. R., Shimizu, T., et al. (2009). Update of the LIPID MAPS comprehensive classification system for lipids. *J. Lipid Res.* 50(Suppl.) S9–S14. doi: 10.1194/jlr.R800095-JLR200

Fan, M., Sidhu, R., Fujiwara, H., Tortelli, B., Zhang, J., Davidson, C., et al. (2013). Identification of Niemann-Pick C1 disease biomarkers through sphingolipid profiling. *J. Lipid Res.* 54, 2800–2814. doi: 10.1194/jlr.M040618

Han, X. (2005). Lipid alterations in the earliest clinically recognizable stage of Alzheimer's disease: implication of the role of lipids in the pathogenesis of Alzheimer's disease. *Curr. Alzheimer Res.* 2, 65–77. doi: 10.2174/1567205052772786

Han, X., Holtzman, D. M., and McKeel, D. W. Jr. (2001). Plasmalogen deficiency in early Alzheimer's disease subjects and in animal models: molecular characterization using electrospray ionization mass spectrometry. *J. Neurochem.* 77, 1168–1180. doi: 10.1046/j.1471-4159.2001.00332.x

Han, X., Holtzman, D. M., McKeel, D. W. Jr., Kelley, J., and Morris, J. C. (2002). Substantial sulfatide deficiency and ceramide elevation in very early Alzheimer's disease: potential role in disease pathogenesis. *J. Neurochem.* 82, 809–818. doi: 10.1046/j.1471-4159.2002.00997.x

Hannun, Y. A., and Obeid, L. M. (2008). Principles of bioactive lipid signalling: lessons from sphingolipids. *Nat. Rev. Mol. Cell Biol.* 9, 139–150. doi: 10.1038/nrm2329

He, X., Huang, Y., Li, B., Gong, C. X., and Schuchman, E. H. (2010). Deregulation of sphingolipid metabolism in Alzheimer's disease. *Neurobiol. Aging* 31, 398–408. doi: 10.1016/j.neurobiolaging.2008.05.010

Hsu, F. F., and Turk, J. (2002). Characterization of ceramides by low energy collisional-activated dissociation tandem mass spectrometry with negative-ion electrospray ionization. *J. Am. Soc. Mass Spectrom.* 13, 558–570. doi: 10.1016/S1044-0305(02)00358-6

Hsu, F. F., and Turk, J. (2004). Studies on sulfatides by quadrupole ion-trap mass spectrometry with electrospray ionization: structural characterization and the fragmentation processes that include an unusual internal galactose residue loss and the classical charge-remote fragmentation. *J. Am. Soc. Mass Spectrom.* 15, 536–546. doi: 10.1016/j.jasms.2003.12.007

Katsel, P., Li, C., and Haroutunian, V. (2007). Gene expression alterations in the sphingolipid metabolism pathways during progression of dementia and Alzheimer's disease: a shift toward ceramide accumulation at the earliest recognizable stages of Alzheimer's disease? *Neurochem. Res.* 32, 845–856. doi: 10.1007/s11064-007-9297-x

Kolter, T., Proia, R. L., and Sandhoff, K. (2002). Combinatorial ganglioside biosynthesis. *J. Biol. Chem.* 277, 25859–25862. doi: 10.1074/jbc.R200001200

Laviad, E. L., Albee, L., Pankova-Kholmyansky, I., Epstein, S., Park, H., Merrill, A. H. Jr., et al. (2008). Characterization of ceramide synthase 2: tissue distribution, substrate specificity, and inhibition by sphingosine 1-phosphate. *J. Biol. Chem.* 283, 5677–5684. doi: 10.1074/jbc.M707386200

Liu, J. P., Tang, Y., Zhou, S., Toh, B. H., McLean, C., and Li, H. (2010). Cholesterol involvement in the pathogenesis of neurodegenerative diseases. *Mol. Cell. Neurosci.* 43, 33–42. doi: 10.1016/j.mcn.2009.07.013

Lund, E. G., Guileyardo, J. M., and Russell, D. W. (1999). cDNA cloning of cholesterol 24-hydroxylase, a mediator of cholesterol homeostasis in the brain. *Proc. Natl. Acad. Sci. U.S.A.* 96, 7238–7243. doi: 10.1073/pnas.96.13.7238

Lund, E. G., Xie, C., Kotti, T., Turley, S. D., Dietschy, J. M., and Russell, D. W. (2003). Knockout of the cholesterol 24-hydroxylase gene in mice reveals a brain-specific mechanism of cholesterol turnover. *J. Biol. Chem.* 278, 22980–22988. doi: 10.1074/jbc.M303415200

Lutjohann, D., Breuer, O., Ahlborg, G., Nennesmo, I., Siden, A., Diczfalusy, U., et al. (1996). Cholesterol homeostasis in human brain: evidence for an age-dependent flux of 24S-hydroxycholesterol from the brain into the circulation. *Proc. Natl. Acad. Sci. U.S.A.* 93, 9799–9804. doi: 10.1073/pnas.93.18.9799

Lynch, G., and Bi, X. (2003). Lysosomes and brain aging in mammals. *Neurochem. Res.* 28, 1725–1734. doi: 10.1023/A:1026069223763

Mahley, R. W., and Rall, S. C. Jr. (2000). Apolipoprotein E: far more than a lipid transport protein. *Annu. Rev. Genomics Hum. Genet.* 1, 507–537. doi: 10.1146/annurev.genom.1.1.507

Marquer, C., Devauges, V., Cossec, J. C., Liot, G., Lecart, S., Saudou, F., et al. (2011). Local cholesterol increase triggers amyloid precursor protein-Bace1

clustering in lipid rafts and rapid endocytosis. *FASEB J.* 25, 1295–1305. doi: 10.1096/fj.10-168633

Matsuzaki, K. (2011). Formation of toxic amyloid fibrils by amyloid beta-protein on ganglioside clusters. *Int. J. Alzheimers. Dis.* 2011:956104. doi: 10.4061/2011/956104

Mattson, M. P., Cutler, R. G., and Jo, D. G. (2005). Alzheimer peptides perturb lipid-regulating enzymes. *Nat. Cell Biol.* 7, 1045–1047. doi: 10.1038/ncb1105-1045

Mauch, D. H., Nagler, K., Schumacher, S., Goritz, C., Muller, E. C., Otto, A., et al. (2001). CNS synaptogenesis promoted by glia-derived cholesterol. *Science* 294, 1354–1357. doi: 10.1126/science.294.5545.1354

Meljon, A., Wang, Y., and Griffiths, W. J. (2014). Oxysterols in the brain of the cholesterol 24-hydroxylase knockout mouse. *Biochem. Biophys. Res. Commun.* 446, 768–774. doi: 10.1016/j.bbrc.2014.01.153

Meljon, A., Watson, G. L., Wang, Y., Shackleton, C. H., and Griffiths, W. J. (2013). Analysis by liquid chromatography-mass spectrometry of sterols and oxysterols in brain of the newborn *Dhcr7*$^{\Delta 3-5/T93M}$ mouse: A model of Smith-Lemli-Opitz syndrome. *Biochem. Pharmacol.* 86, 43–55. doi: 10.1016/j.bcp.2013.03.003

Panchal, M., Gaudin, M., Lazar, A. N., Salvati, E., Rivals, I., Ayciriex, S., et al. (2014). Ceramides and sphingomyelinases in senile plaques. *Neurobiol. Dis.* 65, 193–201. doi: 10.1016/j.nbd.2014.01.010

Pelech, S. L., Cook, H. W., Paddon, H. B., and Vance, D. E. (1984). Membrane-bound CTP: phosphocholine cytidylyltransferase regulates the rate of phosphatidylcholine synthesis in HeLa cells treated with unsaturated fatty acids. *Biochim. Biophys. Acta* 795, 433–440. doi: 10.1016/0005-2760(84)90169-3

Pelech, S. L., and Vance, D. E. (1984). Regulation of phosphatidylcholine biosynthesis. *Biochim. Biophys. Acta* 779, 217–251. doi: 10.1016/0304-4157(84)90010-8

Pfrieger, F. W. (2003). Cholesterol homeostasis and function in neurons of the central nervous system. *Cell. Mol. Life Sci.* 60, 1158–1171. doi: 10.1007/s00018-003-3018-7

Puglielli, L., Tanzi, R. E., and Kovacs, D. M. (2003). Alzheimer's disease: the cholesterol connection. *Nat. Neurosci.* 6, 345–351. doi: 10.1038/nn0403-345

Reynolds, E. S. (1963). The use of lead citrate at high pH as an electron-opaque stain in electron microscopy. *J. Cell Biol.* 17, 208–212. doi: 10.1083/jcb.17.1.208

Russell, D. W., Halford, R. W., Ramirez, D. M., Shah, R., and Kotti, T. (2009). Cholesterol 24-hydroxylase: an enzyme of cholesterol turnover in the brain. *Annu. Rev. Biochem.* 78, 1017–1040. doi: 10.1146/annurev.biochem.78.072407.103859

Sevin, C., Benraiss, A., Van Dam, D., Bonnin, D., Nagels, G., Verot, L., et al. (2006). Intracerebral adeno-associated virus-mediated gene transfer in rapidly progressive forms of metachromatic leukodystrophy. *Hum. Mol. Genet.* 15, 53–64. doi: 10.1093/hmg/ddi425

Smith, C. A., Want, E. J., O'Maille, G., Abagyan, R., and Siuzdak, G. (2006). XCMS: processing mass spectrometry data for metabolite profiling using nonlinear peak alignment, matching, and identification. *Anal. Chem.* 78, 779–787. doi: 10.1021/ac051437y

Sobo, K., Le Blanc, I., Luyet, P. P., Fivaz, M., Ferguson, C., Parton, R. G., et al. (2007). Late endosomal cholesterol accumulation leads to impaired intra-endosomal trafficking. *PLoS ONE* 2:e851. doi: 10.1371/journal.pone.0000851

Soreghan, B., Thomas, S. N., and Yang, A. J. (2003). Aberrant sphingomyelin/ceramide metabolic-induced neuronal endosomal/lysosomal dysfunction: potential pathological consequences in age-related neurodegeneration. *Adv. Drug Deliv. Rev.* 55, 1515–1524. doi: 10.1016/j.addr.2003.07.007

Sriburi, R., Bommiasamy, H., Buldak, G. L., Robbins, G. R., Frank, M., Jackowski, S., et al. (2007). Coordinate regulation of phospholipid biosynthesis and secretory pathway gene expression in XBP-1(S)-induced endoplasmic reticulum biogenesis. *J. Biol. Chem.* 282, 7024–7034. doi: 10.1074/jbc.M609490200

Sriburi, R., Jackowski, S., Mori, K., and Brewer, J. W. (2004). XBP1: a link between the unfolded protein response, lipid biosynthesis, and biogenesis of the endoplasmic reticulum. *J. Cell Biol.* 167, 35–41. doi: 10.1083/jcb.200406136

Sud, M., Fahy, E., Cotter, D., Brown, A., Dennis, E. A., Glass, C. K., et al. (2007). LMSD: LIPID MAPS structure database. *Nucleic Acids Res.* 35, D527–D532. doi: 10.1093/nar/gkl838

Tautenhahn, R., Cho, K., Uritboonthai, W., Zhu, Z., Patti, G. J., and Siuzdak, G. (2012a). An accelerated workflow for untargeted metabolomics using the METLIN database. *Nat. Biotechnol.* 30, 826–828. doi: 10.1038/nbt.2348

Tautenhahn, R., Patti, G. J., Rinehart, D., and Siuzdak, G. (2012b). XCMS Online: a web-based platform to process untargeted metabolomic data. *Anal. Chem.* 84, 5035–5039. doi: 10.1021/ac300698c

Turley, S. D., Burns, D. K., Rosenfeld, C. R., and Dietschy, J. M. (1996). Brain does not utilize low density lipoprotein-cholesterol during fetal and neonatal development in the sheep. *J. Lipid Res.* 37, 1953–1961.

Valenza, M., Leoni, V., Karasinska, J. M., Petricca, L., Fan, J., Carroll, J., et al. (2010). Cholesterol defect is marked across multiple rodent models of Huntington's disease and is manifest in astrocytes. *J. Neurosci.* 30, 10844–10850. doi: 10.1523/JNEUROSCI.0917-10.2010

Valenza, M., Rigamonti, D., Goffredo, D., Zuccato, C., Fenu, S., Jamot, L., et al. (2005). Dysfunction of the cholesterol biosynthetic pathway in Huntington's disease. *J. Neurosci.* 25, 9932–9939. doi: 10.1523/JNEUROSCI.3355-05.2005

Vance, J. E., Hayashi, H., and Karten, B. (2005). Cholesterol homeostasis in neurons and glial cells. *Semin. Cell Dev. Biol.* 16, 193–212. doi: 10.1016/j.semcdb.2005.01.005

Want, E. J., Masson, P., Michopoulos, F., Wilson, I. D., Theodoridis, G., Plumb, R. S., et al. (2013). Global metabolic profiling of animal and human tissues via UPLC-MS. *Nat. Protoc.* 8, 17–32. doi: 10.1038/nprot.2012.135

Want, E. J., Wilson, I. D., Gika, H., Theodoridis, G., Plumb, R. S., Shockcor, J., et al. (2010). Global metabolic profiling procedures for urine using UPLC-MS. *Nat. Protoc.* 5, 1005–1018. doi: 10.1038/nprot.2010.50

Wiklund, S., Johansson, E., Sjostrom, L., Mellerowicz, E. J., Edlund, U., Shockcor, J. P., et al. (2008). Visualization of GC/TOF-MS-based metabolomics data for identification of biochemically interesting compounds using OPLS class models. *Anal. Chem.* 80, 115–122. doi: 10.1021/ac0713510

Wolozin, B. (2004). Cholesterol and the biology of Alzheimer's disease. *Neuron* 41, 7–10. doi: 10.1016/S0896-6273(03)00840-7

Xie, C., Lund, E. G., Turley, S. D., Russell, D. W., and Dietschy, J. M. (2003). Quantitation of two pathways for cholesterol excretion from the brain in normal mice and mice with neurodegeneration. *J. Lipid Res.* 44, 1780–1789. doi: 10.1194/jlr.M300164-JLR200

Xu, G., Servatius, R. J., Shefer, S., Tint, G. S., O'Brien, W. T., Batta, A. K., et al. (1998). Relationship between abnormal cholesterol synthesis and retarded learning in rats. *Metab. Clin. Exp.* 47, 878–882. doi: 10.1016/S0026-0495(98)90130-5

Yadav, R. S., and Tiwari, N. K. (2014). Lipid integration in neurodegeneration: an overview of Alzheimer's disease. *Mol. Neurobiol.* 50, 168–176. doi: 10.1007/s12035-014-8661-5

Yamamoto, N., Matsubara, T., Sato, T., and Yanagisawa, K. (2008). Age-dependent high-density clustering of GM1 ganglioside at presynaptic neuritic terminals promotes amyloid beta-protein fibrillogenesis. *Biochim. Biophys. Acta* 1778, 2717–2726. doi: 10.1016/j.bbamem.2008.07.028

Yanagisawa, K. (2011). Pathological significance of ganglioside clusters in Alzheimer's disease. *J. Neurochem.* 116, 806–812. doi: 10.1111/j.1471-4159.2010.07006.x

Yu, R. K., Bieberich, E., Xia, T., and Zeng, G. (2004). Regulation of ganglioside biosynthesis in the nervous system. *J. Lipid Res.* 45, 783–793. doi: 10.1194/jlr.R300020-JLR200

Zemski Berry, K. A., and Murphy, R. C. (2004). Electrospray ionization tandem mass spectrometry of glycerophosphoethanolamine plasmalogen phospholipids. *J. Am. Soc. Mass Spectrom.* 15, 1499–1508. doi: 10.1016/j.jasms.2004.07.009

Conflict of Interest Statement: The authors declare that the research was conducted in the absence of any commercial or financial relationships that could be construed as a potential conflict of interest.

frontiers in Molecular Neuroscience

ORIGINAL RESEARCH
published: 29 May 2017
doi: 10.3389/fnmol.2017.00164

Mitochondrial Effects of PGC-1alpha Silencing in MPP+ Treated Human SH-SY5Y Neuroblastoma Cells

Qinyong Ye[1,2], Chun Chen[1], Erwang Si[1], Yousheng Cai[1], Juhua Wang[1], Wanling Huang[1], Dongzhu Li[1], Yingqing Wang[1] and Xiaochun Chen[1,2]*

[1]*Department of Neurology, Fujian Institute of Geriatrics, Fujian Medical University Union Hospital, Fuzhou, China,* [2]*Key Laboratory of Brain Aging and Neurodegenerative Diseases, Fujian Key Laboratory of Molecular Neurology, Fujian Medical University, Fuzhou, China*

The dopaminergic neuron degeneration and loss that occurs in Parkinson's disease (PD) has been tightly linked to mitochondrial dysfunction. Although the aged-related cause of the mitochondrial defect observed in PD patients remains unclear, nuclear genes are of potential importance to mitochondrial function. Human peroxisome proliferator-activated receptor γ coactivator-1alpha (PGC-1α) is a multi-functional transcription factor that tightly regulates mitochondrial biogenesis and oxidative capacity. The goal of the present study was to explore the potential pathogenic effects of interference by the PGC-1α gene on N-methyl-4-phenylpyridinium ion (MPP^+)-induced SH-SY5Y cells. We utilized RNA interference (RNAi) technology to probe the pathogenic consequences of inhibiting PGC-1α in the SH-SY5Y cell line. Remarkably, a reduction in PGC-1α resulted in the reduction of mitochondrial membrane potential, intracellular ATP content and intracellular H_2O_2 generation, leading to the translocation of cytochrome c (cyt c) to the cytoplasm in the MPP^+-induced PD cell model. The expression of related proteins in the signaling pathway (e.g., estrogen-related receptor α (ERRα), nuclear respiratory factor 1 (NRF-1), NRF-2 and Peroxisome proliferator-activated receptor γ (PPARγ)) also decreased. Our finding indicates that small interfering RNA (siRNA) interference targeting the PGC-1α gene could inhibit the function of mitochondria in several capacities and that the PGC-1α gene may modulate mitochondrial function by regulating the expression of ERRα, NRF-1, NRF-2 and PPARγ. Thus, PGC-1α can be considered a potential therapeutic target for PD.

Keywords: Parkinson's disease, SH-SY5Y cells, PGC-1α, RNA interference, ERRα

OPEN ACCESS

Edited by:
Clevio Nobrega, University of the Algarve, Portugal

Reviewed by:
Maciej Maurycy Lalowski, University of Helsinki, Finland
Liliana Simões Mendonça, University of Coimbra, Portugal

****Correspondence:***
Qinyong Ye
unionqyye@163.com

Received: *06 February 2017*
Accepted: *11 May 2017*
Published: *29 May 2017*

Citation:
Ye Q, Chen C, Si E, Cai Y, Wang J, Huang W, Li D, Wang Y and Chen X (2017) Mitochondrial Effects of PGC-1alpha Silencing in MPP+ Treated Human SH-SY5Y Neuroblastoma Cells. Front. Mol. Neurosci. 10:164. doi: 10.3389/fnmol.2017.00164

INTRODUCTION

Parkinson's disease (PD) is a neurodegenerative disorder that is characterized by the progressive loss of dopaminergic neurons and affects more than 1% of the population older than 60 years of age (Abou-Sleiman et al., 2006). Both clinical and experimental data have indicated that mitochondrial dysfunction is a common feature of PD that results in a decrease in complex I activity and the overproduction of oxygen radicals (Schapira et al., 1990; Greenamyre et al., 2001). Mitochondria may, therefore, be critical to understanding the etiology of both familial and sporadic PD (Moore et al., 2005; McInnes, 2013). Furthermore, the substantia nigra (SN) of PD patients exhibits a higher mutation rate in mitochondrial DNA than other regions of the brain.

Peroxisome proliferator-activated receptor γ (PPARγ) coactivator 1α (PGC-1α), together with PGC-1β and PGC-related co-activator (PRC), comprise a family of transcriptional co-activators (Scarpulla, 2008a). PGC-1α initiates a diverse set of metabolic programs through its interaction with a variety of transcription factors, including PPARγ (De Nuccio et al., 2011), nuclear respiratory factors 1 and 2 (NRF-1, NRF-2) and estrogen-related receptor α (ERRα; Lin et al., 2005). Additionally, NRF-1, NRF-2, ERRα and PPARγ are primarily responsible for regulating the expression of nuclear-encoded mitochondrial genes, including the components of complexes I-V, cytochrome c (cyt c) and mitochondrial transcription factor A (TFAM; Kelly and Scarpulla, 2004). Furthermore, those nuclear-encoded mitochondrial genes are regulating the energy metabolism of the brain. PGC-1α is, thus, believed to be a major regulator of mammalian mitochondrial biogenesis during physiological or pathological stress.

Recent studies have implicated impaired PGC-1α function in mitochondrial dysfunction in PD. The activation or overexpression of PGC-1α can protect neurons from the loss of mitochondria induced by mutant α-synuclein or mutant huntingtin (Htt; Wareski et al., 2009). Increased PGC-1α expression could improve dopaminergic neuronal viability and mitochondrial activity in *in vivo* and *in vitro* PD models (Mudò et al., 2012; Ferretta et al., 2014; Mäkelä et al., 2016). Our previous work has also suggested that the up-regulation of PGC-1α may have a significant impact on mitochondrial signal transduction by up-regulating the expression of ERRα, NRF-1, NRF-2 and PPARγ (Ye et al., 2016). Meanwhile, PD patients exhibit declining levels of cellular bioenergetic-related gene expression that closely corresponded to the level of PGC-1α (Zheng et al., 2010). However, in the absence of PGC-1α condition, the potential regulation of PGC-1α on mitochondria in *in vitro* PD models is still unclear. Therefore, the down-regulation effect of PGC-1α on related transcription cofactors and mitochondrial function was investigated in PD-liked pathological damage induced by N-methyl-4-phenylpyridinium ion (MPP^+) in this study.

MATERIALS AND METHODS

Cell Culture

Human SH-SY5Y neuroblastoma cells were obtained from the Chinese Academy of Sciences Committee Type Culture Collection cell bank and were cultured in Dulbecco's Modified Eagle's Medium (DMEM/F12, Hyclone, Logan, UT, USA) supplemented with 10% fetal bovine serum (Gibco, Grand Island, NY, USA), 100 U/ml penicillin (Hyclone, Logan, UT, USA) and 100 U/ml streptomycin (Hyclone, Logan, UT, USA; complete media, CM). The cell line was cultured in 100 mm tissue culture plates at 37°C in a humidified incubator (Model No. 3130, Forma Scientific, OH, USA) containing 5% CO_2. When the cell density reached 80%–90%, the cells were harvested and dispersed. We replaced the culture medium every 2 days. The cells in CM were treated with 1 mM MPP^+ (D048, Sigma-Aldrich, St. Louis, MO, USA) for 24 h (The antibodies and abbreviations lists see Supplement Materials 1, 2).

Viral Infection

Human SH-SY5Y neuroblastoma cells were infected through incubation in high titer Adenovirus-Green Fluorescent Protein (Ad-GFP) diluted in a small volume of DMEM/F12 at 37°C for 2 h with gentle swaying every 20 min. The infected cells were maintained for 24 h in fresh CM and were treated with 1 mM MPP^+ for 24 h. Briefly, 5.0×10^3 cells/well in 100 ul of culture medium were seeded into a 96-well plate and incubated at 37°C in 5% CO_2 for 24 h to allow cells to grow to 50%–60% confluency. The culture medium was replaced by 100 ul of serum-free medium. The different amount of viruses, 1.25×10^5 pfu/well, 2.5×10^5 pfu/well and 5×10^5 pfu/well, according to multiplicity of infection (MOI; 25, 50, 100) values were applied for infection. The plate was shaken one time every 20 min to increase infection efficiency. After 2 h incubation, the medium was replaced by 100 ul of 5% FBS DMEM/F12 medium. The expression of GFP was observed by fluorescence microscopy (Leica, Germany) 24 h after infection. The transfer efficiency of adenovirus to the SH-SY5Y cells was relatively high, and a MOI of 50 was found to be the most suitable. This MOI was predicted to infect 90%–100% of the SH-SY5Y cells. Then SH-SY5Y cells were also infected with adenovirus in 6-well plates. The number of cells per well was 1.0×10^5 cells/well in 2 ml of culture medium, and the corresponding amount of viruses was 5×10^6 pfu/well (MOI = 50). Adenoviral vector delivery of small interfering RNA (siRNA) targeting PGC-1α (GeneBank accession number: NM_013261) and nonsense control (Ad) were purchased from SBO Medical Biotechnology Co., Ltd (Shanghai, China). The sequences of siRNAs were as follows:

3-[4,5-dimethylthiazol-2-yl]-2,5-diphenyl-tetrazolium bromide (MTT) Assay to Evaluate Cell Survival

3-[4,5-dimethylthiazol-2-yl]-2,5-diphenyl-tetrazolium bromide (MTT; Solarbio, Beijing, China) is absorbed into cells and then converted to formazan by mitochondrial succinate dehydrogenase. The accumulation of formazan directly reflects the activity of mitochondria and indirectly reflects cell viability. Cells were plated at a density of 1×10^4 cells/well in 96-well plates and were cultured, differentiated and treated according to the above described methods. Twenty microliter of 0.5 mg/ml MTT was added to each well. After 4 h of incubation at 37°C, the initial 220 μl of solution was removed from each well, and then 100 μl of dimethyl sulfoxide (DMSO) was added to each well. Optical density (OD) was evaluated at 570 nm on an ELISA plate reader (Bio-Rad, Hercules, CA, USA) after the precipitate in the well was dissolved on a microplate mixer for 10 min. All results were normalized against the OD

Marker	Target Sequence	Unit	GC%
siRNA PGC-1	GCAATAAAGCGAAGAGTAT	4.4×10^{11} pfu/ml	36.9
siRNA PGC-2	CCACCACTCCTCCTCATAA	4.3×10^{11} pfu/ml	52.6
siRNA PGC-3	CCGAAATTCTCCCTTGTAT	1.3×10^{11} pfu/ml	42.1
siRNA PGC-4	GCTATGGTTTCATTACCTA	2.1×10^{11} pfu/ml	36.9
Ad	TTCTCCGAACGTGTCACGT	1.4×10^{11} pfu/ml	52.6

measured in a well under the same conditions without cell culture.

Detection of Tyrosine Hydroxylase (TH) in SH-SY5Y Cells by Immunocytochemistry

Human SH-SY5Y neuroblastoma cells were permeabilized and fixed with 0.5% Triton X-100 and 4% paraformaldehyde. Slides were blocked with 1% normal donkey serum (Merck, Darmstadt, Germany) in phosphate buffered saline (PBS) for 60 min at room temperature. Cells were washed with 0.1% bovine serum albumin (BSA, Beyotime Institute of Biotechnology, Shanghai, China) in PBS three times with gentle shaking, then incubated with the primary antibody Tyrosine Hydroxylase (TH; 1:100, Santa Cruz, CA, USA) diluted in 0.1% BSA/PBS at 4°C overnight. Labeled donkey anti-rabbit IgG (1:1000 Invitrogen, Paisley, UK) was used as the secondary antibody and was incubated in the dark for 2 h at room temperature. The samples were subjected to chromogenic diaminobenzidine (DAB) staining. In general, one drop of A, B, C reagents was respectively added into 1 ml of distilled water. The mixture was used for cell staining. The color development was monitored under the microscope at room temperature. The reaction stopped by adding distilled water when the ideal color was developed. Hematoxylin was used as a counterstain. The samples mounted by mounting medium were visualized by an inverted microscope under 200 times and 400 times magnification.

Western Blot Analysis

Human SH-SY5Y neuroblastoma cells, plated at a density of 1×10^5 cells per 6-well dish, were treated according to the aforementioned methods. The cells were washed with ice-cold PBS three times, then the PBS was removed, and the cells were harvested in RIPA Lysis Buffer [50 mM Tris pH 7.4, 150 mM NaCl, 1% Triton X-100, 1% sodium deoxycholate, 0.1% SDS, 1 mM sodium orthovanadate, 50 mM sodium fluoride, 1 mM Ethylenediaminetetraacetic acid (EDTA)], and 0.5 mM phenylmethanesulfonylfluoride (PMSF; Beyotime Institute of Biotechnology, Shanghai, China). The lysates were incubated for 10 min on ice and centrifuged at 12,000× *g* for 10 min at 4°C. The supernatant containing the cell lysates was collected. The protein concentration was measured using BCA Protein Assay Kit (Beyotime Institute of Biotechnology, Shanghai, China). Thirty micrograms of proteins from total cell lysates were denatured by boiling in 1× SDS sample buffer (P0015, Beyotime Institute of Biotechnology, Shanghai, China). Thirty micrograms of denatured protein by boiling were loaded per lane and resolved by 10% sodium dodecyl sulfate-polyacrylamide gel electrophoresis (SDS-PAGE) for 90 min at 80 V. The separated proteins were transferred onto polyvinylidene fluoride (PVDF) membranes (Millipore, Carrigtwohill, Ireland) for 2 h at 200 mA with Bradford reagent (Bio-Rad, Hercules, CA, USA). The membranes were blocked with 5% skim milk in 1× PBS containing 0.05% Tween 20 (PBST) for 4 h at room temperature. The following primary antibodies were incubated with: anti-PGC-1α (1:1500 EMD Millipore Billerica, MA, USA); anti-ERRα (1:2500 EMD Millipore Billerica, MA, USA); anti-NRF1 (1:800 Abcam Cambridge, MA, USA); anti-NRF2 (1:1000 Abcam Cambridge, MA, USA), anti-PPARγ (1:1000 Abcam Cambridge, MA, USA), anti-Actin (1:2000 Beyotime Company of Biotechnology Shanghai, China), anti-GAPDH (1:1000 Beyotime Company of Biotechnology Shanghai, China) in PBST at 4°C overnight, the membranes were washed three times in PBST for 10 min. Subsequently, the membranes were incubated for 1.5 h in PBST containing secondary antibody conjugated to horseradish peroxidase (HRP; anti-mouse IgG 1:2000 and anti-rabbit IgG 1:2000, Beyotime Institute of Biotechnology, Shanghai, China). The immunoreactive bands were visualized and quantified using the enhanced chemiluminescence (ECL) detection kit (Millipore, USA). Protein levels were normalized to the housekeeping protein β-actin or GAPDH to adjust for variability of protein loading and expressed as a percentage of the vehicle control (deemed to be 100%).

Quantitative Real-Time PCR Analysis

Total RNA from human SH-SY5Y neuroblastoma cells was isolated according to the manufacturer's protocol using TRizol reagent (Invitrogen, Carlsbad, CA, USA). Total RNA purity and integrity was confirmed using an ND-1000 NanoDrop (NanoDrop Technologies, Wilmington, NC, USA) and 2100 Bioanalyzer (Agilent, Santa Clara, CA, USA). RNA (1 μg) was reverse-transcribed into cDNA in a total volume of 20 μl using the RevertAid^{TM} First Strand cDNA Synthesis Kit (k1621, Fermentas, St. Leon-Rot, Germany). The cDNA (2 μl) was amplified using a sequence detection system (ABI Prism 7500) in a total volume of 20 μl containing 10 μl of Fast Start Universal SYBR Green Master Mix (ROX; Roche, Penzberg, Germany) and each primer at 0.3 μM. Quantitative real-time PCR was performed using the ABI prism 7500 HT sequence detection system (Applied Biosystems, Forster City, CA, USA) based on the 59-nuclease assay for the indicated genes and the housekeeping gene GAPDH. Relative quantification of mRNAs was calculated with the $^{\Delta\Delta}$Ct method**.** Relative expression was calculated using the $^{\Delta\Delta}$Ct method. The absolute value of the slope of ΔCT vs. a log input <0.1 was considered as a criterion for passing the validation experiment. PCR amplification was carried out on cDNA equivalent to 10 ng of starting mRNA with the following specific oligonucleotide primers:

PGC-1α (Forward, 5-acacagtcgcagtcacaacac-3
Reverse, 5-gcagttccagagagttccaca-3,)
GAPDH (Forward, 5-agaaggctggggctcatttg -3
Reverse, 5-aggggccatccacagtcttc-3).

The conditions for PCR were as follows: initial denaturation for 3 min followed by 40 cycles of two steps: 1st: 95°C for 1 min, 2nd: 72°C (annealing) for 1 min 30 s. Followed by a final incubation of 72°C for 10 min. The results are expressed as the average of triplicate samples from at least three independent experiments for both control and treated cells.

Mitochondrial Membrane Potential

Loss of mitochondrial membrane potential was assessed using Rhodamine 123 (Sigma, USA). Human SH-SY5Y neuroblastoma cells were seeded in 6-well plates at a concentration of 10^5 cells per well. After the cells were treated with viral infection and

MPP^+, the medium was removed, and the cells were washed three times with DMEM/F12. The cells were incubated with Rhodamine 123 (Rh123) at a final concentration of 10 μg/ml in FBS-free DMEM/F12 for 30 min at 37°C. The fluorescence signal was measured using a flow cytometer (FACScalibur, San Jose, CA, USA) with excitation and emission wavelengths set at 530 and 590 nm, respectively. For each analysis, 10,000 events were recorded. The value for each treatment group was converted to a percentage of the control value.

Intracellular ATP Measurement

ATP levels were assessed using a luciferin/luciferase-based ATP assay kit (no. 11699709001, Roche). Briefly, SH-SY5Y cells were treated with 1 mM MPP^+ for 24 h. Cells were harvested, centrifuged and diluted to a concentration of 1×10^6 cells/ml. The cells were plated at 25 μl/well in black 96-well plates. An ATP standard was serially diluted in dilution buffer to the range of 10^{-6} to 10^{-12} M ATP. The same volume of cell lysis reagent was added to the samples, which were then incubated for 5 min at 25°C. Appropriate volumes of luciferase reagents were added to the samples and readings were recorded between 1 s and 10 s at an interval of 1 s using a multifunctional microplate reader (SpectraMax M3, Sunnyvale, CA, USA).

Intracellular H_2O_2 Measurement

Intracellular production of H_2O_2 was fluorometrically assayed according to the manufacturer's instructions (Amplex® Red, Molecular Probes, A22188, Invitrogen, Eugene, OR, USA). The Amplex® Red reagent reacts with H_2O_2 in a 1:1 stoichiometry to produce the red-fluorescent oxidation product, resorufin. The resorufin was measured with excitation and emission wavelengths at 530 and 590 nm. SH-SY5Y cells in which the PGC-1α gene was silenced were treated with 1 mM MPP^+ for 24 h. Cells were harvested, centrifuged, and diluted to a concentration of 1×10^6 cells/ml. An H_2O_2 standard curve was prepared, and the cells were plated on black 96-well plates to be tested. Cultures were exposed to a working solution containing 50 μM Amplex Red reagent and 0.1 U/ml HRP for 30 min and were assayed using a multifunctional microplate reader (SpectraMax M3, Sunnyvale, CA, USA) equipped for excitation at 540 nm and fluorescence emission at 590 nm.

Intracellular cyt c Measurement by ELISA

Mitochondria were extracted according to the Mitochondria Fractionation Kit (Active Motif, Cat.40015, Carlsbad, CA 92008, USA) instructions. A cyt c standard was serially diluted with dilution buffer to 5.0, 2.5, 1.25, 0.625, 0.31, 0.155, 0.078 and 0 ng/ml according to the instructions accompanying the cyt c Human ELISA Kit (Abcam, Cambridge, MA, USA). The sample and standard specimens were added to 96-well plates filled with equal volumes (100 μl/well), specimen diluent was added to the blank wells, and biotinylated antibody solution (50 μl/well) was incubated for 2 h in the dark at room temperature. Then, the enzyme conjugate working solution was added (100 μl/well) after washing the plates three times for 1 h in the dark at room temperature. Next, the reaction was terminated after the addition of chromogenic substrate for 25 min, and the results were read using a multifunctional microplate reader (SpectraMax M3, Sunnyvale, CA, USA) at OD 450.

Data Analysis

All quantitative data were collected from at least three independent experiments. The final data are expressed as the mean ± SEM, and analyzed using SPSS 17.0 statistical software (SPSS, Inc., Chicago, IL, USA) by means of one-way analysis of variance (ANOVA), followed by Tukey's multiple comparison *post hoc* test. Real Time PCR data (Ct) were translated into the $2^{-\Delta\Delta Ct}$ format for statistical analysis; differences between mean values were analyzed by one-way ANOVA, $P < 0.05$ and $P < 0.01$ were considered as significant.

RESULTS

Cell Viability after MPP^+-Induced Toxicity in SH-SY5Y Cells

To establish an MPP^+-induced cell model of PD for investigating the potential pathogenic effects of PGC-1α on PD, we first examined whether SH-SY5Y cell could be eligible for a dopaminergic neuronal-like cell model of PD by expressing TH. As shown in **Figure 1A**, the brown particles staining in cytoplasm of SH-SY5Y cells but not in nuclei suggested that SH-SY5Y cells could be used as a dopaminergic neuronal-like PD cell model due to their expression of TH. Next, to evaluate the viability of SH-SY5Y cells after exposure to oxidative injury, cells were treated with several concentrations of MPP^+ (0 μM–2 mM) for 24 h. Cell viability was measured using the MTT assay. MPP^+ significantly decreased MTT levels, indicating that cell loss is concentration-dependent. In addition, 1 mM MPP^+ was selected as an optimal concentration when cell viability was decreased by 35.24% ($P < 0.01$; **Figure 1B**).

Selection of the Most Efficient siRNA Specific to PGC-1α

Real-time PCR and Western blot were used to detect the expression of PGC-1α mRNA and PGC-1α protein, respectively, in each group. In order to clarify the infection level of adenovirus to SH-SY5Y cells, SH-SY5Y cells were infected by adenovirus expressing GFP with MOI 25, 50 and 100. The expression level of GFP was observed under fluorescence microscope and the cells were counted (**Figure 2A**). The results showed that SH-SY5Y cells could be infected by adenovirus efficiently with MOI 50 and 100. However, SH-SY5Y cells infected with MOI 100 showed severe toxicity when comparing to those infected with MOI 50. Therefore, for follow-up experiments we chose MOI 50. The PGC-1α mRNA and protein levels of groups transfected with siRNA PGC-1, siRNA PGC-2, siRNA PGC-3 and siRNA PGC-4 were lower than those of the control group ($P < 0.01$), among which the PGC-1 group was the most marked: gene and protein expression levels were 30.74% (**Figure 2B**)

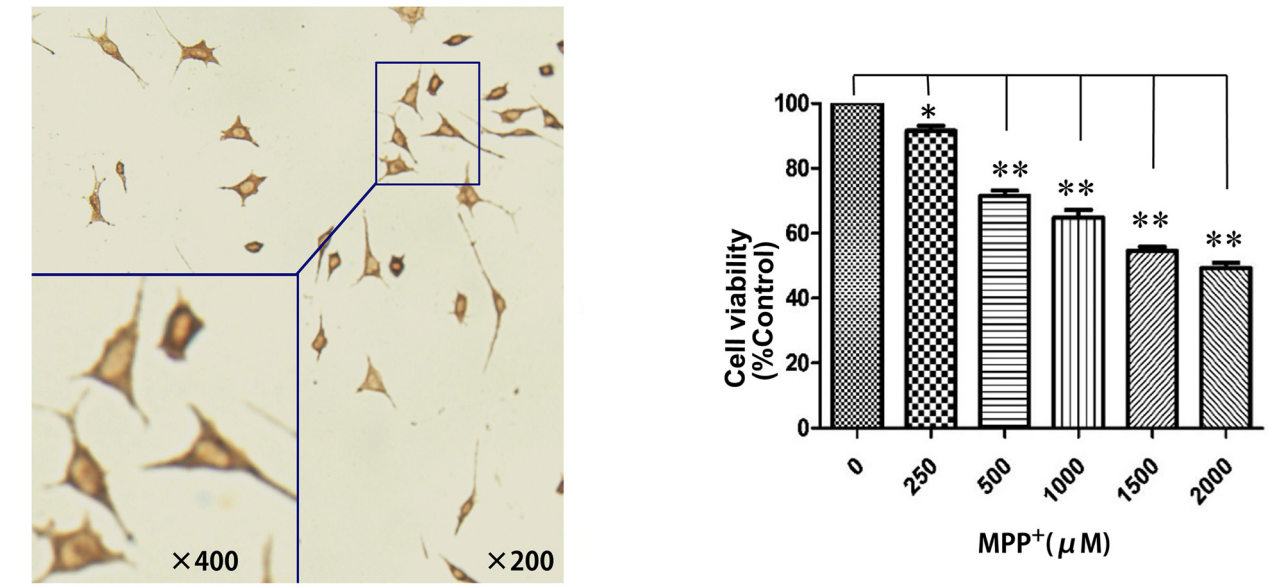

FIGURE 1 | Establishment of a dopaminergic neuronal-like Parkinson's disease (PD) cell model. **(A)** SH-SY5Y cells showed distinct positive TH staining in the cytoplasm; **(B)** N-methyl-4-phenylpyridinium ion (MPP^+; 0 μM–2 mM) treatment for 24 h. (*$P < 0.05$, **$P < 0.01$, vs. controls. $n = 4$ for cell viability; $n = 5$ for immunocytochemistry staining. Data were analyzed by analysis of variance (ANOVA), followed by Tukey's LSD *post hoc* tests).

and 15.56% (**Figures 2C,D**) of the wild type, respectively. There was no difference between the control group and the nonsense control group. This indicated that PGC-1 was the most efficient siRNA specific to PGC-1α in SH-SY5Y cells.

The PGC-1α mRNA Expression Levels Upon siRNA Silencing

The real-time PCR showed that (**Figure 3**) the PGC-1α mRNA level was increased in MPP^+ treated cells compared with the control group. Compared with the control viral (Ad) group, the expression of PGC-1α mRNA was decreased by 49.67% ($P < 0.05$) in the PGC-1α silencing group. In PD model groups, which further silenced the PGC-1α gene, PGC-1α mRNA expression decreased by 41.34% ($P < 0.05$) compared with the Ad+MPP^+ groups.

The Protein Expression Levels of PGC-1α, PPARγ, NRF-1, ERRα and NRF-2 Upon PGC-1α Silencing

The immunoreactive bands specific to PGC-1α, NRF-1, PPARγ, ERRα, NRF-2, β-actin and GAPDH were present by Western blot (**Figure 4A**). Compared with the control group, PGC-1α protein expression in the MPP^+ group was decreased by 23.41% ($P < 0.05$), while PGC-1α protein expression decreased by 57.31% ($P < 0.01$) when the PGC-1α gene was silenced. Compared with the nonsense control group, PGC-1α protein expression in the PGC-1α gene silencing groups decreased by 31.84% ($P < 0.05$). Further treated with MPP^+ produced a more significant decrease in PGC-1α protein expression of 66.81% ($P < 0.01$), compared with Ad+MPP^+ group (**Figure 4B**). As shown in **Figure 4C**, NRF-1 protein expression decreased by 38.25% ($P < 0.05$) following treatment with MPP^+ when compared with the nonsense control group, while NRF-1 protein expression decreased by 65.81% ($P < 0.05$) in the PGC-1α gene silencing groups. Compared with the control viral (Ad) groups, NRF-1 protein expression decreased 32.35% ($P < 0.05$) when the PGC-1α gene was silenced. In the PD model groups, upon silencing the PGC-1α gene, NRF-1 protein expression decreased by 69.39% ($P < 0.05$), and compared with the Ad+MPP^+ groups, NRF-1 protein expression decreased by 36.12% ($P < 0.05$) in the PGC-1α+MPP^+ groups. At the same time (in **Figure 4D**), PPARγ protein expression in the MPP^+ groups decreased by 21.69% ($P < 0.05$) compared with the control group, while PPARγ protein expression decreased more significantly, reaching 78.87% ($P < 0.05$) when the PGC-1α gene was silenced. In PD model groups, in which the PGC-1α gene was further silenced, PPARγ protein expression decreased by 75.32% ($P < 0.05$); compared with the control viral group, PPARγ protein expression in the PGC-1α gene silencing groups decreased by 50.87% ($P < 0.05$). As for ERRα protein (in **Figure 4E**), compared with the control group, ERRα protein expression decreased by 46.17% ($P < 0.05$) when treated with MPP^+ only, while ERRα protein expression decreased by 40.74% ($P < 0.01$) in the PGC-1α gene silencing groups. Compared with the nonsense control group, ERRα protein expression decreased 15.10% ($P < 0.05$) when silencing the PGC-1α gene. In PD model groups, which further silenced the PGC-1α gene, ERRα protein expression decreased by 78.66% ($P < 0.01$); compared with the Ad+MPP^+ groups, ERRα protein expression decreased

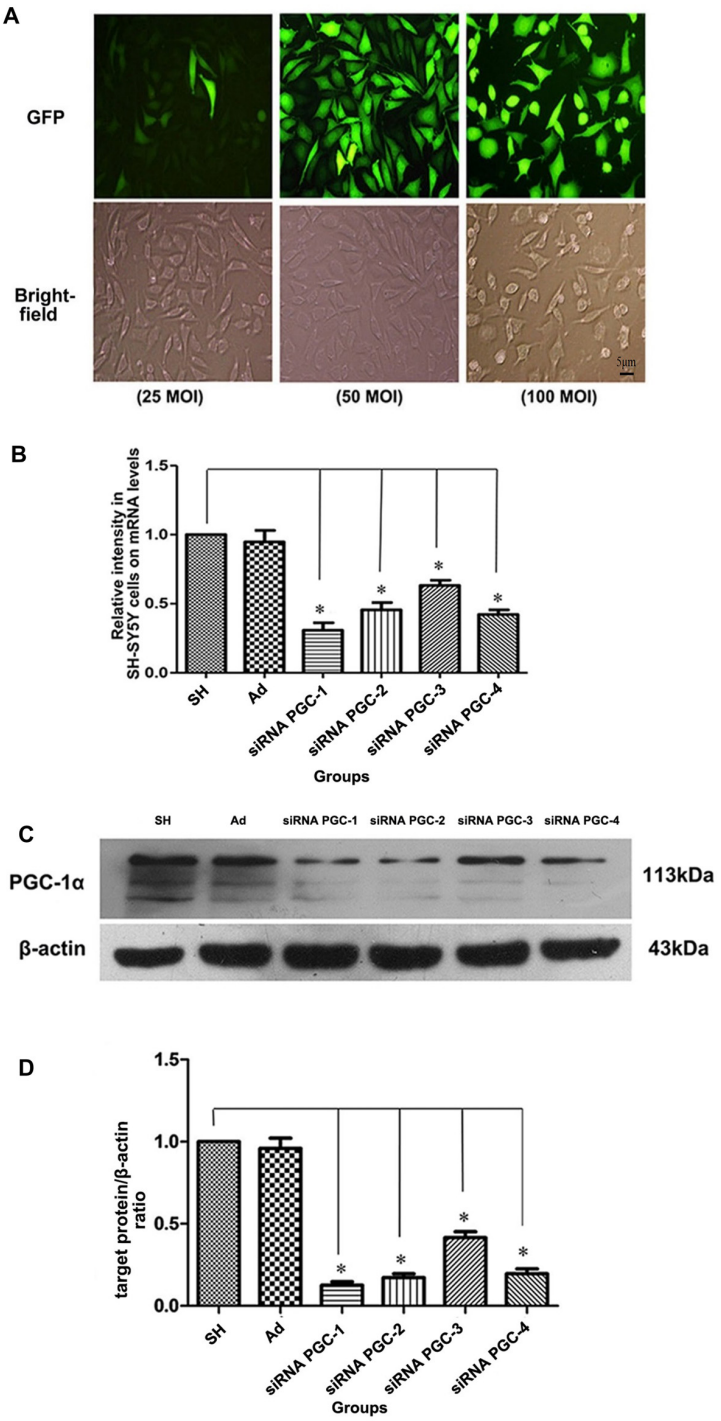

FIGURE 2 | Testing for most efficient infection multiple and silencing conditions of peroxisome proliferator-activated receptor γ coactivator-1alpha (PGC-1**α**) gene in SH-SY5Y cells. **(A)** On upper panel, fluorescent images from green fluorescent protein (GFP) of SH-SY5Y cells infected with adenovirus vectors (25 multiplicity of infection (MOI), 50 MOI, 100 MOI) for 24 h. On the lower panel, the bright-field images from the same fields as fluorescent ones. **(B)** The relative expression level of PGC-1α mRNA in different groups was assessed by real-time PCR after SH-SY5Y cells not transfected with any viral vector, SH-SY5Y infected with adenoviruses carrying nonsense control, small interfering RNA (siRNA) PGC-1, siRNA PGC-2, siRNA PGC-3 and siRNA PGC-4, respectively. **(C)** Representative image of PGC-1α in the different groups by western blot analysis. The groups: SH (control group, SH-SY5Y cells not transfected with any viral vector group), Ad (nonsense control group), siRNA PGC-1, siRNA PGC-2, siRNA PGC-3 and siRNA PGC-4. **(D)** Quantification of PGC-1α protein in the different groups by Image J. (*$P < 0.01$ vs. controls. $n = 4$ for fluorescent image; $n = 5$ for real-time PCR; $n = 8$ for western blots. Data were analyzed by ANOVA, followed by Tukey's LSD *post hoc* tests).

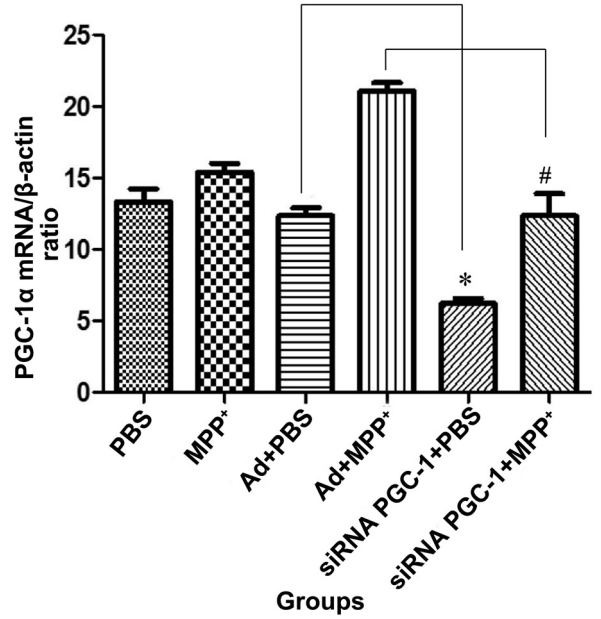

FIGURE 3 | The effect of MPP^+ and/or siRNA PGC-1 interference on PGC-1α mRNA expression. SH-SY5Y cells treated with MPP^+ and/or siRNA PGC-1 interference were evaluated for PGC-1α mRNA. The assessed groups were: phosphate buffered saline (PBS; control group), MPP^+ (1 mM MPP^+ group), Ad+PBS (negative control group), Ad+MPP^+ (negative control group with 1 mM MPP^+), siRNA PGC-1+PBS (PGC-1α gene silencing), siRNA PGC-1+MPP^+ (PGC-1α gene silencing with 1 mM MPP^+). (*$P < 0.05$, siRNA PGC-1+PBS vs. Ad+PBS group; $^{\#}P < 0.05$, siRNA PGC-1+MPP^+ vs. Ad+MPP^+ group. $n = 5$ for real-time PCR analysis. Data were analyzed by ANOVA, followed by Tukey's LSD *post hoc* tests).

by 36.12% ($P < 0.05$) in the siRNA PGC-1+MPP^+ groups. As shown in **Figure 4F**, NRF-2 protein expression in the MPP^+ groups decreased by 30.02% ($P < 0.05$) compared with the control group, while NRF-2 protein expression decreased by 73.31% ($P < 0.01$) when silencing the PGC-1α gene. Compared with the control viral (Ad) groups, NRF-2 protein expression decreased by 45.47% ($P < 0.05$) when silencing the PGC-1α gene. Compared with the only MPP^+ group, which further silenced the PGC-1α gene, NRF-2 protein expression decreased by 55.20% ($P < 0.05$); compared with the control viral group, NRF-2 protein expression in the PGC-1α gene silencing groups decreased by 31.87% ($P < 0.05$).

Effect of Silencing the PGC-1α Gene on Mitochondrial Function

PGC-1α expression is associated with mitochondrial respiration in regulation of energy metabolism and oxidative stress. To analyze the effects of silencing PGC-1α genes on the mitochondrial function of SH-SY5Y cells, we first evaluated whether silencing PGC-1α would affect the mitochondrial membrane potential (ΔΨM) using Rh123 as an indicator, as well as cell viability (**Figures 5**, **6A**). Upon MPP^+ exposure, SH-SY5Y cells showed a statistically significant decrease in ΔΨM and cell viability when compared to the control. However, pre-treatment with PGC-1α silencing further decreased 41.19% ($P < 0.01$) of ΔΨM and 47.15% ($P < 0.05$) of cell viability when compared to SH-SY5Y cells treated with MPP^+ alone, indicating that expression of PGC-1α rendered dysfuction of mitochondrial respiration induced by MPP^+ through inhibiting mitochondrial complex I. We then asked whether knockdown of PGC-1α would result in further depletion of ATP upon MPP^+ treatment. To this end, we measured ATP levels. As shown in **Figure 6B**, ATP generation in SH-SY5Y cells treated with MPP^+ was decreased when compared to the control group. However, silencing the PGC-1α gene resulted in a further decrease (63.94%, $P < 0.05$) in ATP level when compared to SH-SY5Y cells treated with MPP^+ alone. In agreement with the data from mitochondrial potential assay, decreases in ATP levels were correlated with the change in ΔΨM. In fact, decrease of ATP and change of mitochondrial ΔΨM can lead to an increase of reactive oxygen species (ROS). Given that mitochondria generate and accumulate the majority of ROS and H_2O_2 and that mitochondrial dysfunction causes an increase in radical production, we next assessed the effect of MPP^+ on H_2O_2 production. As shown in **Figure 6C**, H_2O_2 was significantly increased (43.38%, $P < 0.01$) in SH-SY5Y cells exposed to MPP^+. However, pre-treatment to silence the PGC-1α gene resulted in a more marked increase H_2O_2 level (93.44%, $P < 0.01$) compared to SH-SY5Y cells treated with MPP^+ alone. In general, overloading of ROS causes cells undergoing apoptosis. We, therefore, detected changes in mitochondrial cyt c using ELISA (**Figures 6D,E**). Cyt c is an important component of the mitochondrial electron transport chain and is located in the mitochondria, but it can be released into the cytoplasm upon apoptosis. We found that the mitochondrial cyt c level was significantly decreased after SH-SY5Y cells were treated with MPP^+, and it was reduced further (11.35%, $P < 0.01$) following PGC-1α gene silencing (**Figure 6D**). Correspondingly, the cyt c in the cytoplasm tended to increase (**Figure 6E**). In comparison with the control group, cyt c in the mitochondria decreased by 16.02% ($P < 0.05$) after cells were treated with MPP^+ only. In PD model groups, compared with the control viral groups, the mitochondrial cyt c decreased by 16.22% ($P < 0.05$) in PGC-1α gene silencing groups, and the difference was statistically significant. Meanwhile, cyt c in the cytoplasm increased by 32.66% ($P < 0.05$). Thus, we can conclude that silencing the PGC-1α gene caused mitochondrial damage in the PD cell model and led to mitochondrial cyt c release into the cytoplasm.

DISCUSSION

PD is a common neurodegenerative disease with clinical features including resting tremor, bradykinesia, rigidity and abnormal posture and gait. In recent decades, the incidence of PD among the aging population in China has increased. This progressive and highly disabling movement disorder has devastating long-term effects for patients, their families and society. For years, many resources have been devoted to exploring the pathogenetic mechanism of PD. More recently, mitochondrial dysfunction and oxidative stress have been widely believed to contribute to the occurrence and development of PD. In this *in vitro* study, we utilized

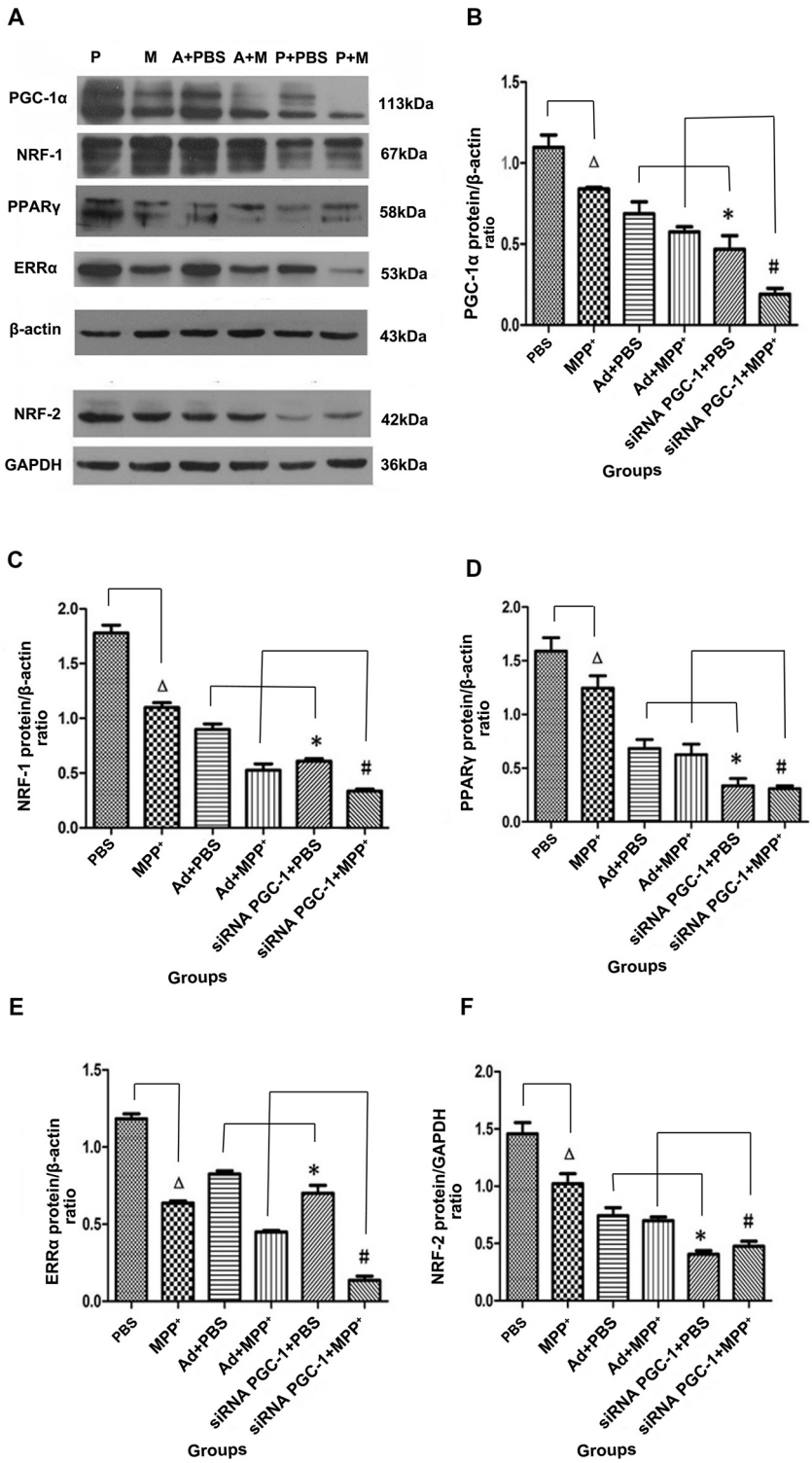

FIGURE 4 | The effects of silencing PGC-1**α** on the protein levels of its downstream molecules nuclear respiratory factor 1 (NRF-1), peroxisome proliferator-activated receptor **γ** (PPAR**γ**), estrogen-related receptor **α** (ERR**α**), NRF-2 in SH-SY5Y cells treated with MPP^+ and/or siRNA PGC-1 interference were evaluated for western blot. **(A)** Representative image of western blot analysis of NRF-1, PPARγ, ERRα and NRF-2. **(B–F)** Quantification of PGC-1α, NRF-1, PPARγ, ERRα, NRF-2 protein in different groups by normalizing to β-actin or GAPDH. The groups: PBS (control group), M (MPP^+ 1 mM group), A (negative control group), P (PGC-1α gene silencing). ($^{\Delta}P < 0.05$, MPP^+ vs. PBS group; $^{*}P < 0.05$, siRNA PGC-1+PBS vs. Ad+PBS group; $^{\#}P < 0.05$, siRNA PGC-1+MPP^+ vs. Ad+MPP^+ group; $n = 10$ for western blots. Data were analyzed by ANOVA, followed by Tukey's LSD *post hoc* tests).

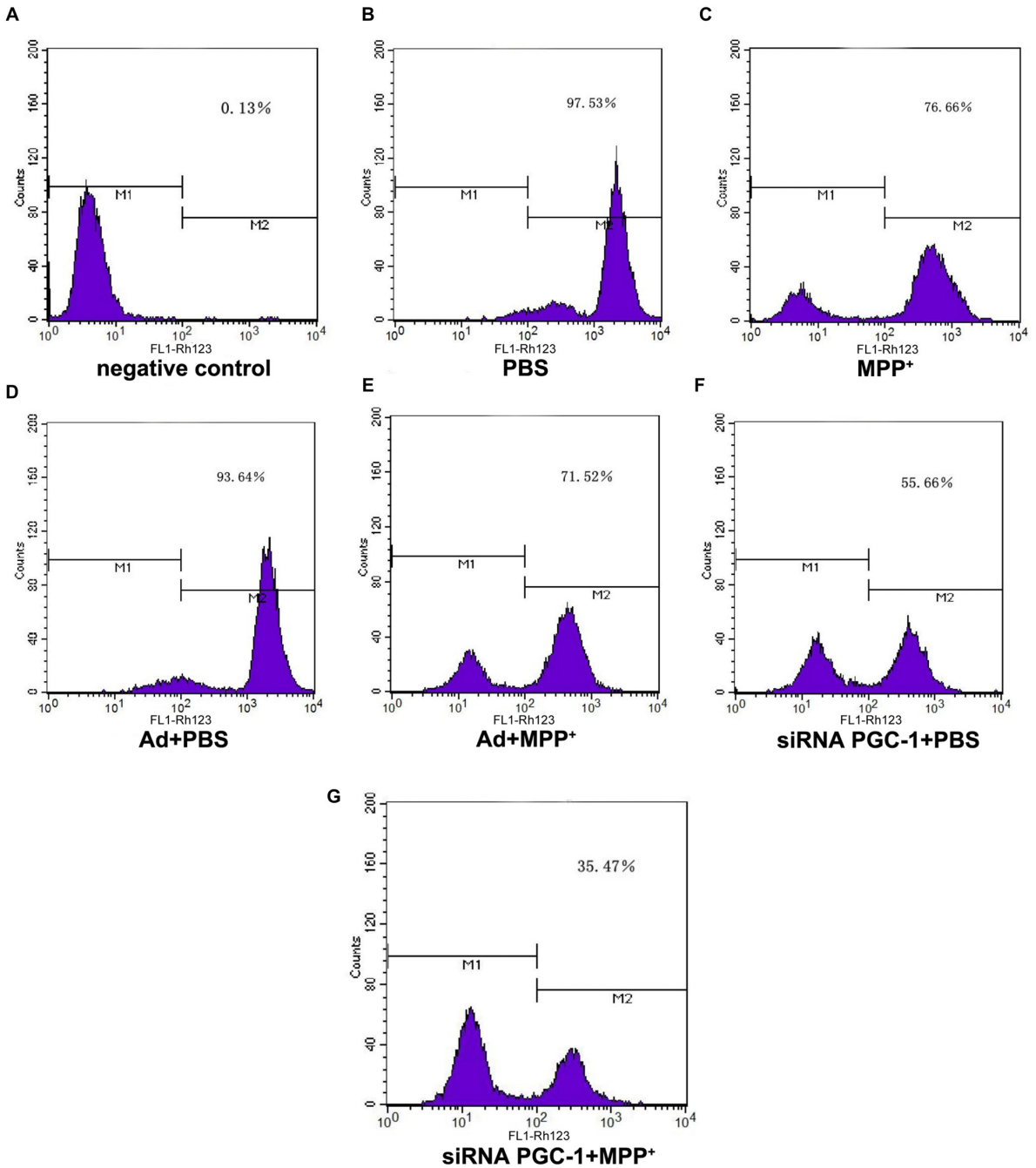

FIGURE 5 | The effect of PGC1-α silencing on mitochondrial membrane potential upon MPP^+ insult. SH-SY5Y cells treated with MPP^+ and/or siRNA PGC-1 interference were evaluated for mitochondrial membrane potential. The assessed groups were: **(A)** negative control without Rh123; **(B)** PBS; **(C)** MPP^+ 1 mM; **(D)** Ad+PBS; **(E)** Ad+MPP^+ 1 mM; **(F)** siRNA PGC-1+PBS; and **(G)** siRNA PGC-1+MPP^+ 1 mM. M1: negative control peak; M2: DCFH positive peak; mitochondrial membrane potential was determined by Rh123 fluorescence; $n = 6$ for fluorescence signal measurement.

the active ion form (MPP^+) of the neurotoxin 1-methyl-4-phenyl-1,2,3,6-tetrahydropyridine (MPTP) to establish a cell model of classic PD (Swerdlow et al., 1996). SH-SY5Y cells were fully exposed to a range of MPP^+ concentrations, and their survival rate decreased in a dose-dependent manner. We found that at 1 mM, MPP^+ reduced the cell population by nearly one third, and we chose this concentration for our model.

PGC-1α was recently identified as a multifunctional transcriptional coactivator that could regulate mitochondrial biogenesis, oxidative stress, cell metabolism and glucose metabolism through its interaction with relative nuclear

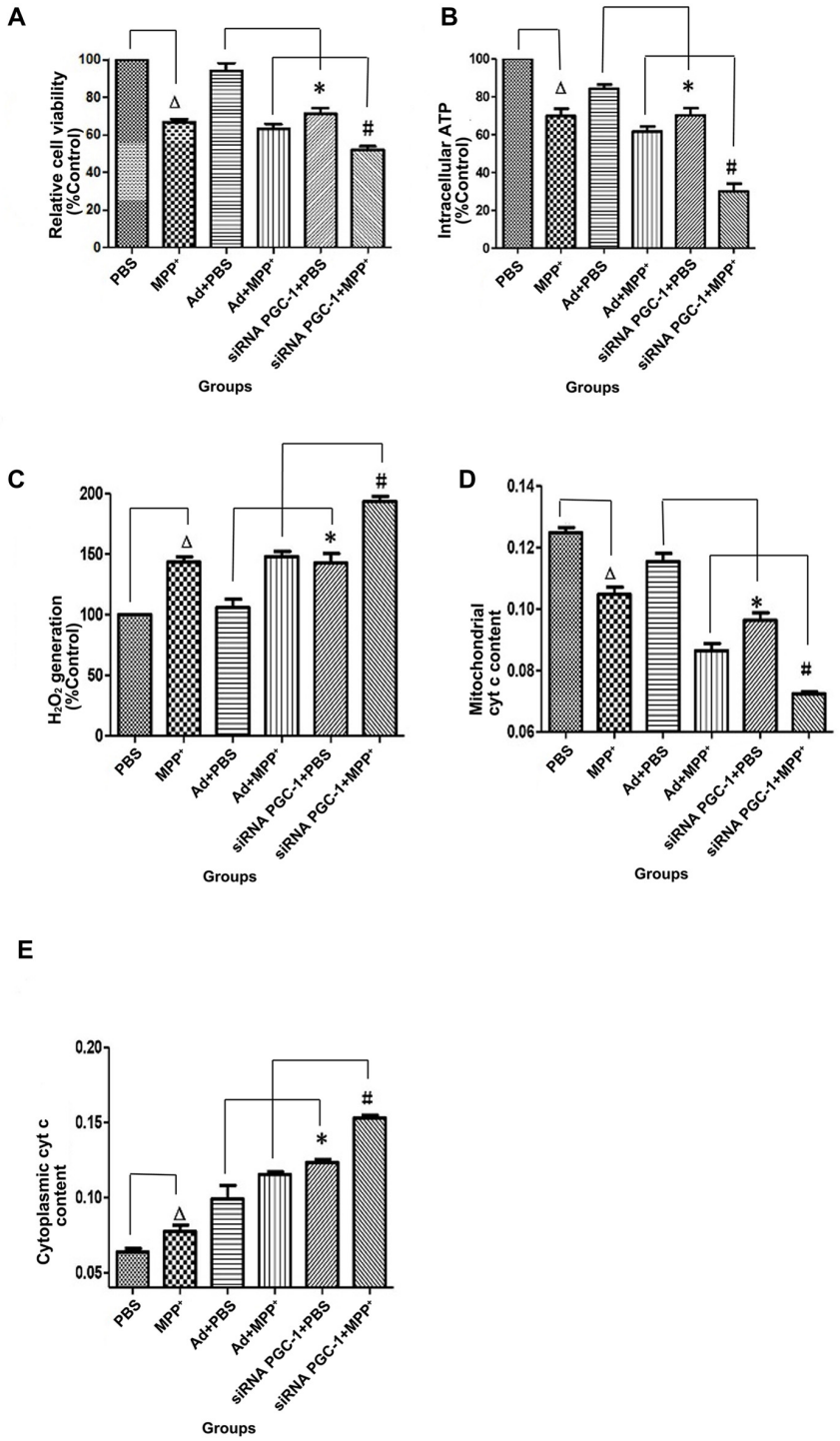

FIGURE 6 | The effects of PGC-1α silencing in SH-SY5Y cells on cell viability, ATP level, H_2O_2 level and cytochrome c (cyt c) content upon MPP^+ insult. SH-SY5Y cells treated with MPP^+ and/or siRNA PGC-1 interference were evaluated for cell viability, ATP level, H_2O_2 level and cyt c content. The assessed groups were: PBS, control group; MPP^+, MPP^+ (1 mM); Ad+PBS, nonsense control+PBS; Ad+MPP^+, nonsense control+1 mM MPP^+; siRNA PGC-1+PBS, PGC-1α gene silencing, siRNA PGC-1+1 mM MPP^+, PGC-1α gene silencing+1 mM MPP^+. **(A)** 3-[4,5-dimethylthiazol-2-yl]-2,5-diphenyl-tetrazolium bromide (MTT) for cell viability. **(B)** Intracellular ATP content was assayed using the luciferase-luciferin reaction. **(C)** Intracellular H_2O_2 level was assayed using Amplex® Red reagent. **(D)** Changes in mitochondrial cyt c content. **(E)** Changes of cytoplasmic cyt c content. ($^{\Delta}P < 0.05$, MPP^+ vs. PBS group; $^{*}P < 0.05$, siRNA PGC-1+PBS vs. Ad+PBS group; $^{\#}P < 0.05$, siRNA PGC-1+MPP^+ vs. Ad+MPP^+ group. $n = 6$ for MTT Assay; $n = 5$ for intracellular ATP measurement; $n = 6$ for fluorescence signal measurement by Amplex® Red reagent; $n = 9$ for mitochondrial cyt c measurement by ELISA; $n = 5$ for cytoplasmic cyt c measurement by ELISA. Data were analyzed by ANOVA, followed by Tukey's LSD *post hoc* tests).

receptors (NR). Studies have revealed possible connections between PGC-1α and several neurodegenerative diseases (Rona-Voros and Weydt, 2010; Tsunemi and La Spada, 2012), including Huntington's disease (HD; Cui et al., 2006), amyotrophic lateral sclerosis (ALS; Zhao et al., 2011), Alzheimer's disease (AD; Sheng et al., 2012) and PD (Shin et al., 2011). Because no effective inhibitor for PGC-1α exists, we designed an adenovirus vector-based siRNA to target the PGC-1α gene. Our study found that upon suppressing the PGC-1α gene, changes in cellular morphology changed were significantly observed when compared with the controlled groups with respect to PGC-1α knockout mice that have been shown to develop remarkable neuron degeneration in several brain regions, especially the striatum, which is accompanied by abnormal exercise behavior (Lin et al., 2005). Furthermore, with continued MPP^+ treatment, more cells were lost, which strongly supports the conclusion that PGC-1α knockout mice are highly susceptible to oxidative stress and the neurotoxin MPTP (St-Pierre et al., 2006).

Cyt c is a water-soluble electron carrier located in the intermembrane space (IMS) of mitochondria. It transports electrons from cyt c oxidoreductase (complex III, or cytochrome bc1) to cyt c oxidase (COX, complex IV, or cytochrome a/a3; San Francisco et al., 2013) and can significantly suppress the generation of H_2O_2. Mature cyt c is localized to the lateral region of the inner mitochondrial membrane through strong electrostatic and hydrophobic interactions with cardiolipin (Hong et al., 2012). When it is released from the mitochondria into the cytoplasm, cyt c-mediated cell death pathways are activated (Bergstrom et al., 2013). In the cytoplasm, cyt c binds Apaf-1 to form the apoptosome and activate the caspase9 (Li et al., 1997), which functions as an upstream initiator of apoptosis. The caspase pathway may play an important role in the occurrence of PD (Jiang and Wang, 2004). Lin et al. (2005) found that the expression of cyt c in the hearts and brains of PGC-1α knockout mice was decreased compared to wild-type (WT) mice. In our study, mitochondrial cyt c in PGC-1α-silenced cells was also reduced compared to the control group. After MPP^+ treatment, the level of mitochondrial cyt c decreased further. The level of cytoplasmic cyt c was correspondingly increased. This suggests that the downregulation of PGC-1α could lead to the partial release of cyt c from the mitochondria into the cytoplasm.

PGC-1α is another key transcription cofactor in the oxidative defense system. PGC-1α is co-induced with several ROS-detoxifying enzymes, including copper/zinc superoxide dismutase (SOD1), manganese SOD (SOD 2), catalase, and glutathione peroxidase1 (GPx1). In PGC-1α knockout mice, these enzymes were markedly decreased compared with WT mice (Lin et al., 2005). Thus, the decrease in ROS-detoxifying enzymes could be due to the down-regulation of PGC-1α, which would result in an increased ROS level and the release of cyt c by changing the permeability of the mitochondrial membrane and would eventually induce apoptosis. We also found that when the PGC-1α mRNA was down-regulated/silenced, the stability of mitochondria in both normal and disease model cells was compromised, as was their membrane potential. Because the major functions of mitochondria are mainly related to oxidative phosphorylation and ATP biogenesis, we examined changes in H_2O_2 and ATP production and found that the suppression of the PGC-1α gene in normal cells lead to an increase of H_2O_2 and a decrease of ATP. These trends were most obvious in the PD model, where apoptosis was observed. We, therefore, concluded that the down-regulation of PGC-1α might not only induce the decrease in mitochondrial membrane potential and ATP production as well as the accumulation of H_2O_2, but could also lead to excessive oxidative stress and the loss of dopamine neurons, eventually aggravating PD pathology.

To explore which co-factors are involved in mitochondrial signal transduction, we examined the protein levels of PGC-1α, ERRα, NRF-1, NRF-2, and PPARγ. We found that PGC-1α mRNA in SH-SY5Y cells was increased after MPP^+ treatment, which could be a short-term stress reaction in response to MPP^+. The protein levels of PGC-1α, ERRα, NRF-1, NRF-2, and PPARγ consistently decreased after MPP^+ intervention, indicating that they were sensitive to MPP^+ toxicity. In the PGC-1α down-regulation group, the levels of ERRα, NRF-1, NRF-2 and PPARγ protein decreased correspondingly.

Similar to PGC-1α, ERRα is mainly expressed in hypermetabolic tissues, including heart, kidney, intestine, skeletal muscle, brown adipose tissue and brain-especially in the hypothalamus (Giguère, 2008). It also regulates mitochondrial biogenesis and oxidative phosphorylation by activating transcription-related genes (Duellman et al., 2010). Cold, physical exercise and hunger stimulate the expression of the PGC-1α and ERRα genes (Cartoni et al., 2005). Both genes are able to regulate the expression of genes related to myocardial metabolism, further promoting the expression of transcription factors and genes that could trans-activate the oxidation of fatty acid. Study found that one surface of the PGC-1α protein reacts specifically with ERRα, and ERRα could in turn regulate the expression of PGC-1α by binding conserved elements in the PGC-1α promoter in cardiomyocytes, suggesting that the interaction between PGC-1α and ERRα is crucial and unique (Schreiber et al., 2003). ERRα exhibited the more obvious response to the suppression of the PGC-1α gene. Thus, we believe that PGC-1α/ERR may play a prominent role in the mitochondrial function of dopaminergic neurons in PD pathogenesis due to their physiological and structural features, although the exact mechanism must be elucidated in future studies.

Nuclear related factors, specifically NRF-1 and NRF-2, are the downstream targets of PGC-1α and key transcription factors involved in mitochondrial biogenesis. Thus far, PGC-1 is thought to be the primary regulator of NRFs (Virbasius and Scarpulla, 1994; Scarpulla, 2008a). Studies have found that both the gene activation and transcription of NRF-1 are induced by the phosphorylation and overexpression of PGC-1α, which in turn modulates the mitochondrial respiratory chain (Yan, 2009; Schilling and Kelly, 2011). The levels of NRF-1 and TFAM in the SN and the striatum decreased in the MPTP-induced PD mice model, whereas the overexpression of NRF-1 or TFAM reversed MPP^+-induced mitochondrial dysfunction, including the activity of mitochondrial complex I, the mitochondrial membrane potential, and the levels of ATP and ROS (Piao et al., 2012). One study also showed

that the mRNA levels of PGC-1α and NRF-1 in the SN and striatum were decreased in a PD mouse model, and there exists a positive correlation between the expression of PGC-1α and NRF-1 (Shin et al., 2011). The expression of NRF-1 and NRF-2 can be increased by PGC-1α in response to the oxidative stress induced by lipopolysaccharide (LPS; Suliman et al., 2004). Our results showed that NRF-1 protein expression was decreased in the PGC-1α silencing group and was accompanied by a decline in the PGC-1α level. Both proteins are significantly depressed by MPP^+, demonstrating that PGC-1α could also positively regulate NRF-1. The pattern of NRF-2 distribution in the primate visual cortex is virtually identical to that of COX, and both proteins are extremely abundant in cells exhibiting high COX activity (Wong-Riley et al., 2005). Under physiological conditions, NRF-2 is retained in the cytoplasm by the inhibitory protein kelch-like ECH-associated protein 1 (Keap1). Oxidative stress activates NRF-2 and dissociates it from Keap1. NRF-2 translocates into the nucleus and binds to electrophile response element (EpRE) sites to trigger the expression of cytoprotective genes (Bryan et al., 2013). Studies have implicated the transactivational activity of NRF-2 in the expression of respiratory chain enzymes, especially that of some nuclear-encoded COX subunits and human COX VIaL (Ongwijitwat and Wong-Riley, 2004). Moreover, NRF-2 could regulate genes that encode the mitochondrial transcription factors A and B (TFAM, TFB1M and TFB2M). Thus, NRF-2 has the potential to connect the regulation of the nucleus and mitochondria through COX-related gene expression by these two genomes (Scarpulla, 2008b). In our study, NRF-2 protein expression was significantly decreased in the PGC-1α gene silencing group, further suggesting the involvement of NRF-2 in the regulation of PGC-1α by downstream members.

Of note, we previously found that expression of PGC-1α protects mitochondrial dysfunction via increasing mitochondrial membrane potential, reducing the release of mitochondrial cyt c, inhibiting H_2O_2 production, and promoting ATP level in SH-SY5Y cells after MPP^+ insult, which is correlated with increase of protein levels of ERRα, PPARγ, NRF-1, and NRF-2 (Ye et al., 2016). Taken together, in agreement with our new data from silencing PGC-1α, our data indicate that ERRα, PPARγ, and NRF-1 along with PGC-1α may be involved in the mitochondria protection in MPP^+-induced cell model of PD.

CONCLUSION

In summary, we found that after silencing the PGC-1α gene, SH-SY5Y cells showed increased susceptibility to MPP^+ and alternation of mitochondrial function, including higher level of H_2O_2 and the release of cyt c into cytoplasm. Also, the expression of ERRα, NRF-1, NRF-2 and PPARγ were correspondingly decreased along with PGC-1α silencing. Especially, ERRα showed more correlation among those factors, providing new experimental evidence for understanding the pathogenesis of PD. In addition, studies have found that PGC-1α can be induced by calcium and cAMP signals in common pathways found in most tissues, indicating the possibility of developing a new drug to elevate PGC-1α levels in brain tissue.

AUTHOR CONTRIBUTIONS

QY conceived and supervised the study. ES, JW, CC and YW participated in the flow cytometry assay, ELISA assay, immunohistochemistry, western blot analysis, realtime-PCR. CC, YC, DL and WH helped to draft the manuscript; XC also conceived the study. All authors read and approved the final manuscript.

FUNDING

This work was supported by the National Natural Science Foundation of China (General Program) *PGC-1α Signal transduction mechanism for the regulation of mitochondrial function Parkinson's disease model* (No. 81271414).

ACKNOWLEDGMENTS

We thank Dr. Dianbo Qu for his proofreading and helpful discussion.

SUPPLEMENTARY MATERIAL

The Supplementary Material for this article can be found online at: http://journal.frontiersin.org/article/10.3389/fnmol.2017.00164/full#supplementary-material

REFERENCES

Abou-Sleiman, P. M., Muqit, M. M., and Wood, N. W. (2006). Expanding insights of mitochondrial dysfunction in Parkinson's disease. *Nat. Rev. Neurosci.* 7, 207–219. doi: 10.1038/nrn1868

Bergstrom, C. L., Beales, P. A., Lv, Y., Vanderlick, T. K., and Groves, J. T. (2013). Cytochrome c causes pore formation in cardiolipin-containing membranes. *Proc. Natl. Acad. Sci. U S A* 110, 6269–6274. doi: 10.1073/pnas.1303819110

Bryan, H. K., Olayanju, A., Goldring, C. E., and Park, B. K. (2013). The Nrf2 cell defence pathway: keap1-dependent and -independent mechanisms of regulation. *Biochem. Pharmacol.* 85, 705–717. doi: 10.1016/j.bcp.2012.11.016

Cartoni, R., Léger, B., Hock, M. B., Praz, M., Crettenand, A., Pich, S., et al. (2005). Mitofusins 1/2 and ERRα expression are increased in human skeletal muscle after physical exercise. *J. Physiol.* 567, 349–358. doi: 10.1113/jphysiol.2005.092031

Cui, L., Jeong, H., Borovecki, F., Parkhurst, C. N., Tanese, N., and Krainc, D. (2006). Transcriptional repression of PGC-1α by mutant huntingtin leads to mitochondrial dysfunction and neurodegeneration. *Cell* 127, 59–69. doi: 10.1016/j.cell.2006.09.015

De Nuccio, C., Bernardo, A., De Simone, R., Mancuso, E., Magnaghi, V., Visentin, S., et al. (2011). Peroxisome proliferator-activated receptor γ agonists accelerate oligodendrocyte maturation and influence mitochondrial functions and oscillatory Ca^{2+} waves. *J. Neuropathol. Exp. Neurol.* 70, 900–912. doi: 10.1097/NEN.0b013e3182309ab1

Duellman, S. J., Calaoagan, J. M., Sato, B. G., Fine, R., Klebansky, B., Chao, W. R., et al. (2010). A novel steroidal inhibitor of estrogen-related receptor α (ERRα). *Biochem. Pharmacol.* 80, 819–826. doi: 10.1016/j.bcp.2010.05.024

Ferretta, A., Gaballo, A., Tanzarella, P., Piccoli, C., Capitanio, N., Nico, B., et al. (2014). Effect of resveratrol on mitochondrial function: implications in parkin-associated familiar Parkinson's disease. *Biochim. Biophys. Acta* 1842, 902–915. doi: 10.1016/j.bbadis.2014.02.010

Giguère, V. (2008). Transcriptional control of energy homeostasis by the estrogen-related receptors. *Endocr. Rev.* 29, 677–696. doi: 10.1210/er.2008-0017

Greenamyre, J. T., Sherer, T. B., Betarbet, R., and Panov, A. V. (2001). Complex I and Parkinson's disease. *IUBMB Life* 52, 135–141. doi: 10.1080/15216540152845939

Hong, Y., Muenzner, J., Grimm, S. K., and Pletneva, E. V. (2012). Origin of the conformational heterogeneity of cardiolipin-bound cytochrome *C. J. Am. Chem. Soc.* 134, 18713–18723. doi: 10.1021/ja307426k

Jiang, X., and Wang, X. (2004). Cytochrome *C*-mediated apoptosis. *Annu. Rev. Biochem.* 73, 87–106. doi: 10.1146/annurev.biochem.73.011303.073706

Kelly, D. P., and Scarpulla, R. C. (2004). Transcriptional regulatory circuits controlling mitochondrial biogenesis and function. *Genes Dev.* 18, 357–368. doi: 10.1101/gad.1177604

Li, P., Nijhawan, D., Budihardjo, I., Srinivasula, S. M., Ahmad, M., Alnemri, E. S., et al. (1997). Cytochrome c and dATP-dependent formation of Apaf-1/caspase-9 complex initiates an apoptotic protease cascade. *Cell* 91, 479–489. doi: 10.1016/s0092-8674(00)80434-1

Lin, J., Handschin, C., and Spiegelman, B. M. (2005). Metabolic control through the PGC-1 family of transcription coactivators. *Cell Metab.* 1, 361–370. doi: 10.1016/j.cmet.2005.05.004

Mäkelä, J., Tselykh, T. V., Kukkonen, J. P., Eriksson, O., Korhonen, L. T., and Lindholm, D. (2016). Peroxisome proliferator-activated receptor-γ (PPARγ) agonist is neuroprotective and stimulates PGC-1α expression and CREB phosphorylation in human dopaminergic neurons. *Neuropharmacology* 102, 266–275. doi: 10.1016/j.neuropharm.2015.11.020

McInnes, J. (2013). Insights on altered mitochondrial function and dynamics in the pathogenesis of neurodegeneration. *Transl. Neurodegener.* 2:12. doi: 10.1186/2047-9158-2-12

Moore, D. J., West, A. B., Dawson, V. L., and Dawson, T. M. (2005). Molecular pathophysiology of Parkinson's disease. *Annu. Rev. Neurosci.* 28, 57–87. doi: 10.1146/annurev.neuro.28.061604.135718

Mudò, G., Mäkelä, J., Di Liberto, V., Tselykh, T. V., Olivieri, M., Piepponen, P., et al. (2012). Transgenic expression and activation of PGC-1α protect dopaminergic neurons in the MPTP mouse model of Parkinson's disease. *Cell. Mol. Life Sci.* 69, 1153–1165. doi: 10.1007/s00018-011-0850-z

Ongwijitwat, S., and Wong-Riley, M. T. T. (2004). Functional analysis of the rat cytochrome c oxidase subunit 6A1 promoter in primary neurons. *Gene* 337, 163–171. doi: 10.1016/j.gene.2004.04.024

Piao, Y., Kim, H. G., Oh, M. S., and Pak, Y. K. (2012). Overexpression of TFAM, NRF-1 and myr-AKT protects the MPP^+-induced mitochondrial dysfunctions in neuronal cells. *Biochim. Biophys. Acta* 1820, 577–585. doi: 10.1016/j.bbagen.2011.08.007

Rona-Voros, K., and Weydt, P. (2010). The role of PGC-1α in the pathogenesis of neurodegenerative disorders. *Curr. Drug Targets* 11, 1262–1269. doi: 10.2174/1389450111007011262

San Francisco, B., Bretsnyder, E. C., and Kranz, R. G. (2013). Human mitochondrial holocytochrome *c* synthase's heme binding, maturation determinants, and complex formation with cytochrome *c*. *Proc. Natl. Acad. Sci. U S A* 110, E788–E797. doi: 10.1073/pnas.1213897109

Scarpulla, R. C. (2008a). Nuclear control of respiratory chain expression by nuclear respiratory factors and PGC-1-related coactivator. *Ann. N Y Acad. Sci.* 1147, 321–334. doi: 10.1196/annals.1427.006

Scarpulla, R. C. (2008b). Transcriptional paradigms in mammalian mitochondrial biogenesis and function. *Physiol. Rev.* 88, 611–638. doi: 10.1152/physrev.00025.2007

Schapira, A. H. V., Cooper, J. M., Dexter, D., Clark, J. B., Jenner, P., and Marsden, C. D. (1990). Mitochondrial complex I deficiency in Parkinson's disease. *J. Neurochem.* 54, 823–827. doi: 10.1111/j.1471-4159.1990.tb02325.x

Schilling, J., and Kelly, D. P. (2011). The PGC-1 cascade as a therapeutic target for heart failure. *J. Mol. Cell. Cardiol.* 51, 578–583. doi: 10.1016/j.yjmcc.2010.09.021

Schreiber, S. N., Knutti, D., Brogli, K., Uhlmann, T., and Kralli, A. (2003). The transcriptional coactivator PGC-1 regulates the expression and activity of the orphan nuclear receptor estrogen-related receptor α (ERRα). *J. Biol. Chem.* 278, 9013–9018. doi: 10.1074/jbc.M212923200

Sheng, B., Wang, X., Su, B., Lee, H. G., Casadesus, G., Perry, G., et al. (2012). Impaired mitochondrial biogenesis contributes to mitochondrial dysfunction in Alzheimer's disease. *J. Neurochem.* 120, 419–429. doi: 10.1111/j.1471-4159.2011.07581.x

Shin, J. H., Ko, H. S., Kang, H., Lee, Y., Lee, Y. I., Pletinkova, O., et al. (2011). PARIS (ZNF746) repression of PGC-1α contributes to neurodegeneration in Parkinson's disease. *Cell* 144, 689–702. doi: 10.1016/j.cell.2011.02.010

St-Pierre, J., Drori, S., Uldry, M., Silvaggi, J. M., Rhee, J., Jäger, S., et al. (2006). Suppression of reactive oxygen species and neurodegeneration by the PGC-1 transcriptional coactivators. *Cell* 127, 397–408. doi: 10.1016/j.cell.2006.09.024

Suliman, H. B., Welty-Wolf, K. E., Carraway, M., Tatro, L., and Piantadosi, C. A. (2004). Lipopolysaccharide induces oxidative cardiac mitochondrial damage and biogenesis. *Cardiovasc Res.* 64, 279–288. doi: 10.1016/j.cardiores.2004.07.005

Swerdlow, R. H., Parks, J. K., Miller, S. W., Tuttle, J. B., Trimmer, P. A., Sheehan, J. P., et al. (1996). Origin and functional consequences of the complex I defect in Parkinson's disease. *Ann. Neurol.* 40, 663–671. doi: 10.1002/ana.410400417

Tsunemi, T., and La Spada, A. R. (2012). PGC-1α at the intersection of bioenergetics regulation and neuron function: from Huntington's disease to Parkinson's disease and beyond. *Prog. Neurobiol.* 97, 142–151. doi: 10.1016/j.pneurobio.2011.10.004

Virbasius, J. V., and Scarpulla, R. C. (1994). Activation of the human mitochondrial transcription factor A gene by nuclear respiratory factors: a potential regulatory link between nuclear and mitochondrial gene expression in organelle biogenesis. *Proc. Natl. Acad. Sci. U S A* 91, 1309–1313. doi: 10.1073/pnas.91.4.1309

Wareski, P., Vaarmann, A., Choubey, V., Safiulina, D., Liiv, J., Kuum, M., et al. (2009). PGC-1α and PGC-1β regulate mitochondrial density in neurons. *J. Biol. Chem.* 284, 21379–21385. doi: 10.1074/jbc.m109.018911

Wong-Riley, M. T., Yang, S. J., Liang, H. L., Ning, G., and Jacobs, P. (2005). Quantitative immuno-electron microscopic analysis of nuclear respiratory factor 2 alpha and beta subunits: normal distribution and activity-dependent regulation in mammalian visual cortex. *Vis. Neurosci.* 22, 1–18. doi: 10.1017/s0952523805221016

Yan, Z. (2009). Exercise, PGC-1α, and metabolic adaptation in skeletal muscle. *Appl. Physiol. Nutr. Metab.* 34, 424–427. doi: 10.1139/H09-030

Ye, Q., Huang, W., Li, D., Si, E., Wang, J., Wang, Y., et al. (2016). Overexpression of PGC-1α influences mitochondrial signal transduction of dopaminergic neurons. *Mol. Neurobiol.* 53, 3756–3770. doi: 10.1007/s12035-015-9299-7

Zhao, W., Varghese, M., Yemul, S., Pan, Y., Cheng, A., Marano, P., et al. (2011). Peroxisome proliferator activator receptor gamma coactivator-1alpha (PGC-1α) improves motor performance and survival in a mouse model of amyotrophic lateral sclerosis. *Mol. Neurodegener.* 6:51. doi: 10.1186/1750-1326-6-51

Zheng, B., Liao, Z., Locascio, J. J., Lesniak, K. A., Roderick, S. S., Watt, M. L., et al. (2010). PGC-1α, a potential therapeutic target for early intervention in Parkinson's disease. *Sci. Transl. Med.* 2:52ra73. doi: 10.1126/scitranslmed.3001059

Conflict of Interest Statement: The authors declare that the research was conducted in the absence of any commercial or financial relationships that could be construed as a potential conflict of interest.

frontiers in Molecular Neuroscience

ORIGINAL RESEARCH
published: 08 August 2017
doi: 10.3389/fnmol.2017.00253

The Generation of Mouse and Human Huntington Disease iPS Cells Suitable for *In vitro* Studies on Huntingtin Function

*Wojciech J. Szlachcic[1], Kalina Wiatr[1], Marta Trzeciak[1], Marek Figlerowicz[2] and Maciej Figiel[1]**

[1] Department of Molecular Neurobiology, Institute of Bioorganic Chemistry, Polish Academy of Sciences, Poznań, Poland, [2] Department of Molecular and Systems Biology, Institute of Bioorganic Chemistry, Polish Academy of Sciences, Poznań, Poland

Huntington disease (HD) is an incurable neurodegenerative disorder caused by expansion of CAG repeats in huntingtin (HTT) gene, resulting in expanded polyglutamine tract in HTT protein. Although, HD has its common onset in adulthood, subtle symptoms in patients may occur decades before diagnosis, and molecular and cellular changes begin much earlier, even in cells that are not yet lineage committed such as stem cells. Studies in induced pluripotent stem cell (iPSC) HD models have demonstrated that multiple molecular processes are altered by the mutant HTT protein and suggested its silencing as a promising therapeutic strategy. Therefore, we aimed to generate HD iPS cells with stable silencing of HTT and further to investigate the effects of HTT knock-down on deregulations of signaling pathways e.g., p53 downregulation, present in cells already in pluripotent state. We designed a gene silencing strategy based on RNAi cassette in piggyBAC vector for constant shRNA expression. Using such system we delivered and tested several shRNA targeting huntingtin in mouse HD YAC128 iPSC and human HD109, HD71, and Control iPSC. The most effective shRNA (shHTT2) reagent stably silenced HTT in all HD iPS cells and remained active upon differentiation to neural stem cells (NSC). When investigating the effects of HTT silencing on signaling pathways, we found that in mouse HD iPSC lines expressing shRNA the level of mutant HTT inversely correlated with p53 levels, resulting in p53 level normalization upon silencing of mutant HTT. We also found that p53 deregulation continues into the NSC developmental stage and it was reversed upon HTT silencing. In addition, we observed subtle effects of silencing on proteins of Wnt/β-catenin and ERK1/2 signaling pathways. In summary, we successfully created the first mouse and human shRNA-expressing HD iPS cells with stable and continuous HTT silencing. Moreover, we demonstrated reversal of HD p53 phenotype in mouse HD iPSC, therefore, the stable knockdown of HTT is well-suited for investigation on HD cellular pathways, and is potentially useful as a stand-alone therapy or component of cell therapy. In addition, the total HTT knock-down in our human cells has further implications for mutant allele selective approach in iPSC.

Keywords: Huntington disease, iPS cells, NS cells, YAC128, shRNA, huntingtin, p53, juvenile HD

OPEN ACCESS

Edited by:
Clevio Nobrega,
University of the Algarve, Portugal

Reviewed by:
Carlos Adriano Albuquerque Andrade Matos,
Centro de Neurociências e Biologia Celular (CNC), Portugal
Maciej Maurycy Lalowski,
University of Helsinki, Finland
Jessica Elaine Young,
University of Washington, United States

***Correspondence:**
Maciej Figiel
mfigiel@ibch.poznan.pl

Received: *14 May 2017*
Accepted: *26 July 2017*
Published: *08 August 2017*

Citation:
Szlachcic WJ, Wiatr K, Trzeciak M, Figlerowicz M and Figiel M (2017) The Generation of Mouse and Human Huntington Disease iPS Cells Suitable for In vitro Studies on Huntingtin Function.
Front. Mol. Neurosci. 10:253.
doi: 10.3389/fnmol.2017.00253

1. INTRODUCTION

Huntington disease (HD) is an incurable autosomal dominant neurodegenerative disorder caused by CAG repeat expansion in exon 1 of the huntingtin (HTT) gene (The-Huntington's-Disease-Collaborative-Research-Group, 1993). A prominent feature of HD is neuronal loss, with medium spiny neurons predominantly affected (Bates et al., 2015). Disease pathogenesis is primarily caused by the presence of mutant HTT that contains a polyQ stretch of over 40 glutamines, encoded by the CAG repeats; however, RNA toxicity might also be involved (Marti, 2016; Urbanek et al., 2016) The polyglutamine tract in the protein interferes with the physiological activity of the HTT protein, causing both loss of function and acquisition of new toxic functions (Bates et al., 2015). HTT is a multifunctional protein that is both essential in development and important for adult brain homeostasis (Wiatr et al., 2017). Mutant HTT alters multiple physiological pathways, including transcriptional regulation, signal transduction, apoptosis, intracellular vesicle trafficking, cytoskeleton assembly, and centrosome formation, making the disease pathology highly complex (Bates et al., 2015).

Despite such profound and widespread effects of mutant HTT on cellular function, disease onset usually occurs at age 30–50, and its average duration is 15–20 years (Bates et al., 2015). In rare cases of longer CAG tracts (70 or more CAG repeats), HD can develop early in life, with onset before age 20 or in childhood; such cases are called juvenile HD (Squitieri et al., 2006; Quigley, 2017). Interestingly, the process of neurodegeneration in distinct brain regions can be observed many years before the onset of motor symptoms (Tabrizi et al., 2013), even in typical HD. Although, traditionally considered a late-onset neurodegenerative disorder, a growing amount of compelling evidence has suggested that HD may be considered a neurodevelopmental disease (Wiatr et al., 2017). HTT is essential in development; lack of HTT expression results in embryonic lethality in mice at E6.5 (Duyao et al., 1995; Nasir et al., 1995; Zeitlin et al., 1995). Embryos of HdhQ111 mice, a model with mild HD features, exhibit an altered cell cycle and impaired differentiation of striatal neural progenitor cells, resulting in abnormal striatal development at E13.5–E18.5 (Molero et al., 2009). Moreover, cortical and striatal synaptic development is similarly disturbed in HD and conditional HTT knockout models (McKinstry et al., 2014). Another study has shown that the expression of mutant HTT only during mouse development is sufficient to induce HD-like phenotypes (Molero et al., 2016).

Recently, this new idea about a developmental role for mutant HTT has been strongly supported by a growing amount of research using new cellular models, including patient-derived induced pluripotent and neuronal stem cells (iPSCs and NSCs, respectively) (Mattis and Svendsen, 2015; Zhang et al., 2015; Wiatr et al., 2017). We previously demonstrated that similar molecular changes can be observed in the iPSC stage in both YAC128 mouse- and juvenile HD patient-derived cells (Szlachcic et al., 2015). The common alterations included decreased MAPK (mitogen-activated protein kinase) signaling activity and increased expression of the antioxidative protein SOD1 (superoxide dismutase 1). Finally, expression of p53 protein, which interacts with HTT and is involved in the above pathways, was decreased in both YAC128 mouse- and juvenile HD iPSCs. In addition, results from HD patient tissues and animal models demonstrate involvement of multiple signaling pathways, including the MAPK and p53 pathways, in HD pathogenesis (Bowles and Jones, 2014; Wiatr et al., 2017).

Gene silencing is one of the therapeutic strategies (Kordasiewicz et al., 2012; Miniarikova et al., 2016; Rué et al., 2016) which can potentially be used for neurodegenerative disease treatment such as cell therapy to correct patient cells or to determine how the level of mutant protein (e.g., HTT) interferes with the deregulated disease pathways. Therefore, our aim was to establish stable silencing of HTT in mouse and human HD iPS cells and subsequently to investigate the effects of HTT knock-down on deregulations of signaling pathways characteristic for HD. We designed a gene silencing strategy based on RNAi cassette in piggyBAC vector for constant shRNA expression. The HD lines with stable expression of anti HTT shRNA possess the same genetic background as the parental lines (i.e., they are isogenic) therefore another aim of isogenic line generation in the present work was the improved quality of comparison of HD phenotypes between genetically similar lines with and without stable HTT knockdown. For this we have selected the most effective HTT silencing reagents and investigated MAPK, Wnt, and p53 deregulations, which are important molecules affected in HD.

2. MATERIALS AND METHODS

This study was carried out in accordance with the recommendations of Local Ethical Commission for Animal Experiments in Poznan. The protocol was approved by the Local Ethical Commission for Animal Experiments in Poznan.

2.1. Mouse iPS Cells Culture

The HD YAC128 and WT iPSC lines were described previously (Szlachcic et al., 2015). These lines were reprogrammed using the piggyBac transposon system (Yusa et al., 2009, 2011) and were shown to be free of the reprogramming cassette after its seamless excision. Cells were cultured on gelatin-coated mitomycin C-inactivated mouse embryonic fibroblast (MEF) feeders in a medium consisting of Knockout Dulbeccos modified Eagle medium (DMEM), 15% KnockOut Serum Replacement (both Thermo Fisher Scientific, Waltham, MA), 2 mM L-Gln, 1x antibiotic antimycotic mixture, 1x MEM non-essential amino acids, 0.1 mM β-mercaptoethanol (all SigmaAldrich, St. Louis, MO), and 1,000 U/mL leukemia inhibitory factor (LIF, ORF Genetics, Kopavogur, Iceland). iPSCs were passaged with TrypLE Select (Thermo Fisher Scientific).

NSCs medium consisted of a 7:3 mixture of DMEM with Hams F12 Nutrient mix, 2% B27 supplement, 1x CTS GlutaMAX-I supplement, 1x penicillin-streptomycin (all Thermo Fisher Scientific), 5 μg/mL heparin (Sigma-Aldrich), 20 ng/mL basic fibroblast growth factor (bFGF), and 20 ng/mL

Abbreviations: HD, Huntington disease; iPSCs, induced pluripotent stem cells; NSC, neural stem cells; HTT, huntingtin.

epidermal growth factor (EGF; both ORF Genetics). Floating NSCs were derived from iPSCs by gentle dissociation of colonies with collagenase type IV (Thermo Fisher Scientific). The enzyme was aspirated while colonies were still attached to a plate followed by detachment with a cell scraper in DMEM/F12 plus 0.075% bovine serum albumin (BSA) Fraction V (both Thermo Fisher Scientific), and collection with a 5-mL pipette. Cell clumps were then centrifuged for 3 min at 1,300 rpm. Clumps were gently resuspended in NSC culture medium with the bFGF and EGF concentrations increased to 100 ng/mL, and the cells were seeded onto wells that had been precoated with polyHema (Santa Cruz Biotechnology, Dallas, TX, USA) to prevent adhesion. One near-confluent well of iPSCs was used for the induction of NSCs in two wells of a 6-well plate. The medium was changed every other day by allowing the spheres to settle to the bottom of a tube, after which the old medium was aspirated, and the spheres were gently resuspended in fresh medium and returned to the plates. NSCs were passaged every 4–6 days using a chopping method (Svendsen et al., 1998; Ebert et al., 2013). After 2–3 passages, bFGF and EGF concentrations were reduced to 20 ng/mL.

2.2. Human iPS Cells Culture

Human episomal HD and control iPSCs lines were previously acquired (Szlachcic et al., 2015) from public repository (NINDS Human Genetics Resource Center DNA and Cell Line Repository; https://catalog.coriell.org/1/ninds). For establishing the lines containing the stable expression of the reagents, we used HD lines with 71 CAG repeats (HD71; ND42228; derived from a 20-year-old patient), juvenile HD line with 109 CAG repeats (HD109; ND42224; derived from a 9-year-old patient), and a control line with 21 CAG repeats (ND42245). Human iPSCs were cultured in Essential 8 medium (Life Technologies) on human vitronectin-coated surfaces (VTN-N, Life Technologies) and were passaged using 0.5 mM EDTA in PBS.

2.3. Construct and Isogenic Line Derivation

Constructs (**Figure 1A**) composed of a U6 promoter, a miR-30 5′ flank (151 bp), an shRNA sequence, a miR-30 3′ flank (128 bp), a U6 terminator (TTTTTT), an EF1alpha promoter, an mOrange2 reporter gene, and an SV40 pA site were were synthesized by Genscript (Piscataway, NJ) and cloned into a pPB-HKS-neoL vector obtained, by removing the EGFP reporter gene, from a pPB-UbC.eGFP-neo plasmid (Yusa et al., 2009). The shRNA sequences (**Figure 1B**, Table S1) targeting human huntingtin (shHTT) and EGFP (control reagent, shCTRL) were designed using the RNAi Codex database (Olson et al., 2006) with a mir-30 loop between the passenger and guide strands. The allele-specific shCAG reagent targeting the CAG tract in mutant HTT was adapted from ref. (Fiszer et al., 2013), along with the miR-25 loop. To generate cell lines stably expressing the shRNA construct, 0.56 x 10^6 cells from two iPS lines derived from YAC128 animals were electroporated with 10 μg of the piggyBac transposase-encoding plasmid (hyPBase) (Yusa et al., 2011) and 2 μg of each shRNA plasmid in HEPES-buffered DMEM. Cells were seeded in K15 medium and selected on G418 (300 μg/mL) (Thermo Fisher Scientific) for 8 days. For derivation of clonal lines, after another 7 days without selection, colonies expressing the mOrange2 reporter gene were picked and expanded. In the case of human iPSCs, the cells were gently detached in clumps containing several cells. For each electroporation, 1/3 well of a confluent 6-well plate was used. The same plasmid concentration, electroporation, and selection protocols were used as for mouse cells. After the antibiotic selection all cells were mOrange2 positive and were passaged after reaching confluence. Material for protein expression analysis was collected after at least three passages.

2.4. PCR Genotyping

For genotyping, DNA was isolated using a Spin Column Genomic DNA Kit (Bio Basic Inc., Markham, Canada), and GoTaq G2 polymerase (Promega GmbH, Mannheim, Germany) was used for PCR. Genotyping to confirm insertion of the shHTT and shGFP constructs was performed using multiplex PCR with a set of primers specific for the YAC128 transgene [intron 26–27 of human HTT; forward (F): 5′-CCTCTTATA TATGGATGCTAATCTCATTC-3′ and reverse (R): 5′-AAT ACACAACACATGAGAGCATATAGAAC-3′] as the internal control, and primers specific for the construct. The forward, universal primer (U6: 5′-CGGCAGCACATATACTAGTCGA-3′) was designed to be in the U6 promotor-miR30 boundary, while the reverse primers were specific for each construct (shHTT: 5′-GCCTCTATATATTCTGGGCGCT-3′, shCTRL: 5′-GAAGTTCACCTTGATGCCGG-3′). The genotyping analyses were performed using Touchdown PCR with the following cycling conditions: 3 min at 94°C; 12 x (35 s at 94°C, [45 s at 64°C - 0.5°C/cycle], and 45 s at 72°C); 25 x (35 s at 94°C, 30 s at 58°C, and 45 s at 72°C); and finally, 2 min at 72°C. Genotyping for the CAG-composed shCAG construct was conducted using two pairs of primers in separate reactions: pair 1 with the universal U6 forward primer and the shCAG-specific reverse primer (A2_R: 5′-TGTGACAGGAAGCAGCTGC-3′); and pair 2 with the shCAG-specific forward primer (A2_F: 5′-CTGCTGCTGCTTTGCCTACT-3′) and the universal EF1a-promoter specific primer (EF1a: 5′-GGGGCGAGTCCTTTTGTATGA-3′). Standard PCR cycling was used for these reactions. Reaction products were separated on 1.3% agarose gels in TBE buffer and were visualized using ethidium bromide.

2.5. ERK Activation Assay

The ERK assay in iPSCs was performed as described previously (Szlachcic et al., 2015). Briefly, the day before the start of experiments, the medium was exchanged for serum-free medium without LIF, and the cells were starved for 24 h. Then, without changing the medium, 20 ng/mL bFGF was added, and the cells were incubated for 5, 10, or 30 min. After each incubation period, the medium was quickly discarded, and the cells were immediately lysed using a protein-lysis buffer. As NSC culture media containing bFGF and NSCs depend on the MAPK signaling pathway, the basal levels of pERK1/2 were measured in cell lysates taken directly from cultures.

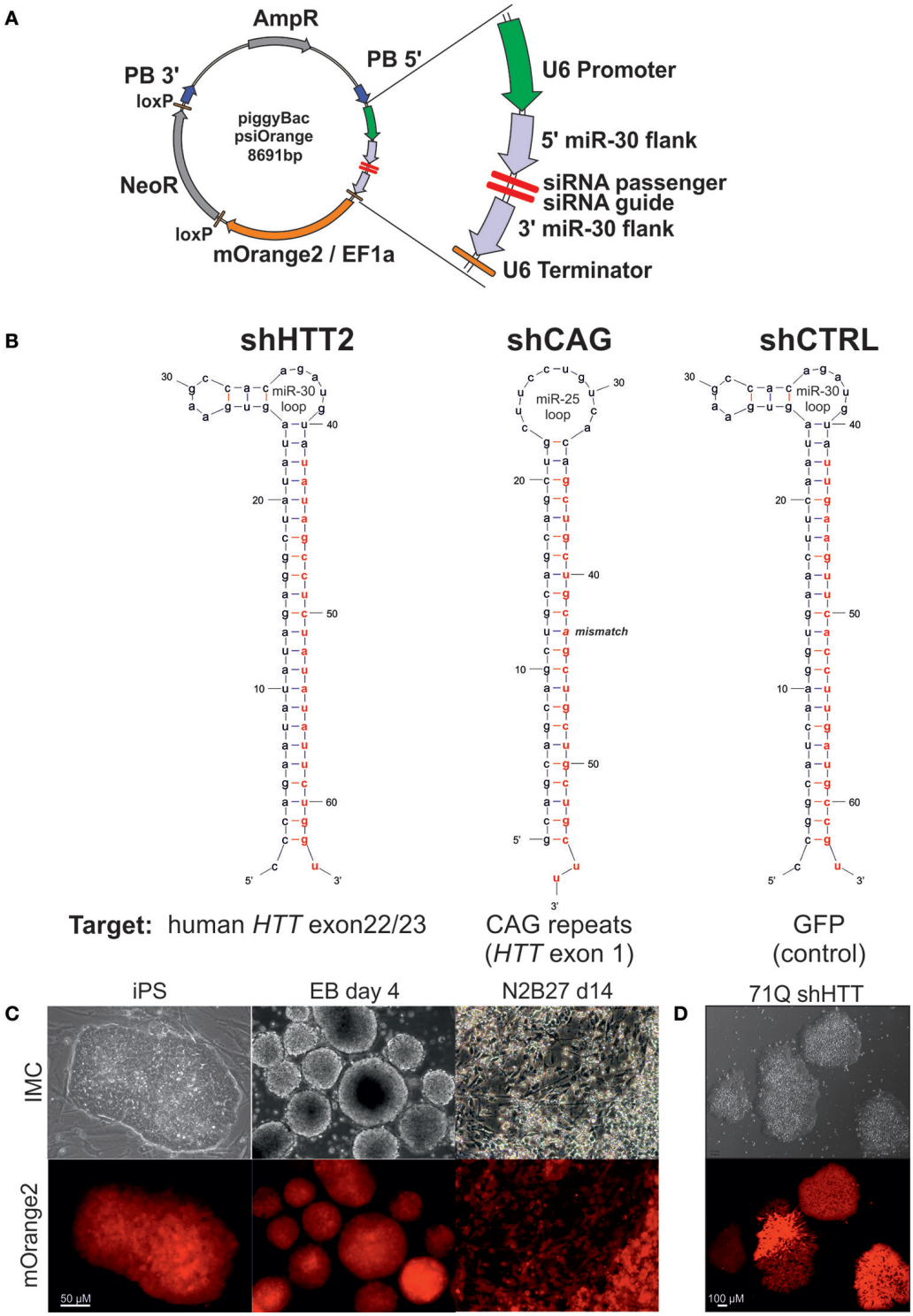

FIGURE 1 | The silencing cassette design and derivation of the iPSC lines. **(A)** Schematic of the psiOrange vector. The silencing cassette is inserted into the iPSC genome as a piggyBac (PB) transposon bordered by 5′ and 3′ PB arms. An shRNA is expressed under regulation of a U6 promoter and is flanked by pri-miR-30 5′ and 3′ sequences, which are 151 and 128 bp long, respectively. Additionally, the mOrange2 fluorescent reporter and NeoR resistance genes are included within the transposon. **(B)** Schematic of shRNA sequences. Effector guide strands are marked in red. **(C)** mOrange reporter expression is sustained in the mouse iPSC state and upon differentiation as embryonic bodies (EB) or neuroectoderm (N2B27 conditions). **(D)** mOrange reporter is expressed in human iPSCs with shRNA cassettes.

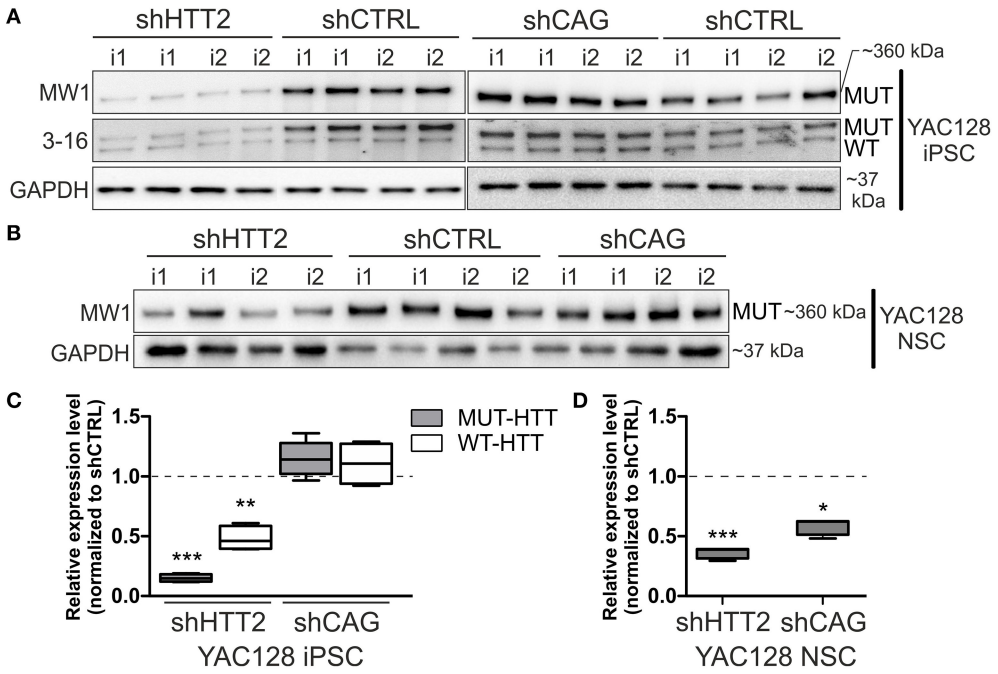

FIGURE 2 | Isogenic YAC128 iPSC and NSC lines with efficient shRNA-mediated silencing of mutant HTT. **(A,B)** Western blot analysis reveals efficient mutant HTT silencing in iPSC lines with shHTT2 but not shCAG reagent, compared to shCTRL lines. **(C,D)** Mutant HTT is continuously silenced by the shHTT2 reagent after iPSCs differentiating into the NSC state, as assessed by western blots. However, the shCAG reagent changes its mode of action, decreasing mutant HTT expression in NSCs. *$p<0.05$, **$p < 0.01$, ***$p<0.001$; $N = 4$ lines for each reagent for both iPSC and NSC analysis (the same lines were used); i1, i2 isogenic lines derived from separate parental lines 1 and 2. In (**A**, iPSCs) blots were cropped; full-length blots are presented in Figure S8.

2.6. Western Blotting

For protein isolation, the cells were washed using PBS, lysed in a protein-lysis buffer containing 60 mM Tris base, 2% SDS, 10% sucrose, 2 mM PMSF, and 1x Halt Phosphatase Inhibitor Cocktail (Thermo Scientific), and then homogenized. An aliquot of 20–30 μg of total protein per lane was dissolved in loading buffer containing 2-mercaptoethanol and was then boiled for 5 min. The proteins were separated using SDS-PAGE (5/10% stacking/resolving gels) and Laemmli buffer. For comparison of NS WT vs HD cell lines, we used 10% TGX Stain-free FastCast Acrylamide gels (Bio-Rad, Hercules, CA, USA). HTT was separated in 4% stacking/5% resolving gels using commercial XT Tricine running buffer (Bio-Rad). The proteins were semi-dry-transferred (Transblot Turbo, Bio-Rad) to nitrocellulose or PVDF (huntingtin) membranes and the blots were blocked using 5% nonfat milk in TBS-Tween. Blots were subsequently incubated overnight at 4°C with primary antibody diluted in TBS-Tween containing 5% milk or BSA. The antibodies used were purchased from Cell Signaling (Danvers, MA) unless otherwise stated and were as follows: rabbit anti-β-catenin (1:1,000, cat. 8480); rabbit anti-phospho-β-catenin (Ser33/37) (1:1,000, cat. 2009); rabbit anti-p44/42 MAPK (ERK1/2) (1:2,000, cat. 4695); rabbit anti-phospho-p44/42 MAPK (ERK1/2) (Thr202/Tyr204) (1:1,000, cat. 4370); mouse anti-p53 (1:1,000, cat. 2524); rabbit anti-p53 (DO-1, 1:600, Santa Cruz, sc-126); mouse anti-phospho-p53 (S15) (1:1,000, cat. 9284); mouse anti-OCT3/4 (1:1,000, Santa Cruz, sc-5279); mouse anti-nestin [Rat-401 (Hockfield and McKay, 1985), 1:100; DSHB, Iowa City, IA]; rabbit anti-PAX6 (1:1,000; Millipore, Billerica, MA; AB2237); rabbit anti-SOX1 (1:1,000, cat. 4194); mouse anti-TUBB3 [6G7 (Halfter et al., 2002), 1:100, DSHB]; anti-huntingtin antibodies: mouse MW1 (Ko et al., 2001) (1:1,000, DSHB), 4–19 (Macdonald et al., 2014) (1:1,000; CH00146, CHDI Foundation, Corriel Cell Repositories), 3–16 (1:1,000; Sigma-Aldrich; H7540), and MAB2166 (1:2,000, Millipore); and mouse anti-GAPDH (1:10,000, Millipore, MAB374). The blots were then incubated for 2 h at RT with HRP-conjugated secondary antibodies raised against rabbit or mouse antibodies (1:2,000–1:20,000 dilution, Jackson ImmunoResearch, West Grove, PA), and the labeled bands were detected using the ECL-based WesternBright Quantum (Advansta Inc., Menlo Park, CA) or homemade ECL reagent. Data was collected using ChemiDoc XRS+ System with Image Lab v5.2 Software (Bio-Rad). To avoid overexposure of any band, image acquisition times were set based on image histograms. Images were not processed before quantitation. All analyses were performed as three independent technical replicates. Data within a gel were normalized to GAPDH or total protein (WT vs, HD NSC analyses), and data between gels were normalized to the average of WT or isogenic shGFP samples.

2.7. Immunostaining

For immunostaining, the cells were cultured in 24-well dishes on gelatin- and feeder cell-coated coverslips. The cells were washed

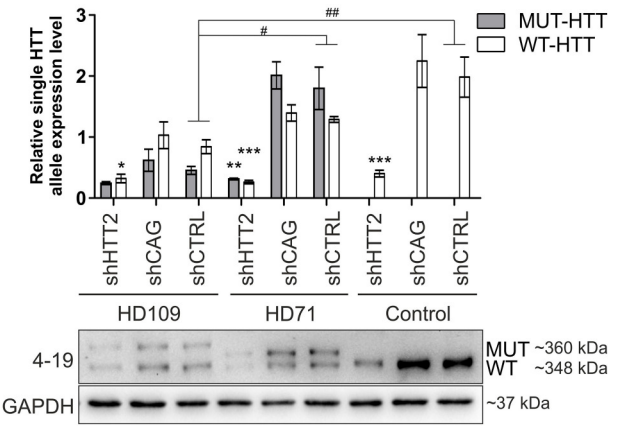

FIGURE 3 | Huntingtin can be effectively and stably silenced with shRNAs in human HD and control lines Western blot analysis of mutant (MUT) and wild-type (WT) huntingtin protein expression in iPSC lines from patients with 109 CAGs (HD109) and 71 CAGs (HD71) and healthy controls (Control, 21 CAGs) with shRNA reagents reveal efficient silencing with the shHTT2 reagent. Despite differences in initial alleles expression levels between cell lines the reagent lowered both alleles to similar levels. *Statistically significant difference vs. isogenic shCTRL line; #Statistically significant difference vs. Control shCTRL line; * and #p <0.05; ** and ##p<0.01; ***p<0.001. Note that the results for Control lines were normalized to reflect the level of one HTT allele (densitometry values of detected HTT level in control lines was divided by 2). For each patient, one cell line per each reagent was used (9 modified cell lines in total).

using PBS, fixed by incubation with 4% paraformaldehyde for 15 min at RT, washed, and permeabilized using 0.3% Triton in PBS for 10 min at RT. Blocking was performed in 3% BSA, 0.1% Tween-20 in PBS for 30 min at RT, and the primary-antibody incubation was conducted overnight at 4°C in an antibody dilution solution composed of 5% normal serum of secondary antibody species (Jackson Immunoresearch) and 0.1% Tween-20 in PBS. The primary antibodies used were as follows: anti-OCT3/4 (1:500, Santa Cruz, sc-5279), rabbit anti-nestin (1:400, Abcam, ab27952), mouse anti-nestin (1:50, DSHB, Rat-401), rabbit anti-PAX6 (1:50, Millipore, AB2237), rabbit anti-SOX1 (1:100, cat. 4194), and mouse anti-TUBB3 (Tuj1) (1:400, Millipore, MAB1637). After washing with PBS, the cells were incubated for 1 h at RT with a proper Cy3- or AlexaFluor488-conjugated secondary antibody (1:500, Jackson Immunoresearch) in the antibody dilution solution. A 5-min incubation in DAPI (1:10,000) dissolved in water was used for counterstaining. Additionally, the primary antibodies were omitted in the secondary antibody controls. The coverslips containing the cells were mounted on slides using anti-fade glycerol/propyl gallate mounting medium. The specimens were analyzed using a DMIL LED inverted fluorescence microscope (Leica Microsystems, Wetzlar, Germany) and Leica Application Suite Software. Confocal microscopy was performed using a Leica TCS SP5 microscope.

2.8. Statistics

Two-group comparisons of the gene expression data were conducted using the unpaired Students *t*-test. The data for ERK1/2 activation in iPSCs were subjected to a two-way ANOVA, followed by Bonferroni *post-hoc* tests. Pearsons simple correlation was used to determine relationships between mutant HTT and other analyzed protein expression levels. *P*-values of less than 0.05 were considered significant. Whiskers in box plots represent 5–95 percentile, while error bars on bar graphs are presented as SEM.

Full description of methods is provided in the Supplementary Materials online.

3. RESULTS

3.1. Generation of Mouse YAC128-HD-iPSCs and Human HD109, HD71, and Control iPS Isogenic Cell Lines with Stable Expression of shRNA Targeting Mutant HTT

Cell lines with continuous expression of RNAi constructs that effectively silence target genes can be used as tools in cell therapy and for the generation of shRNA isogenic lines to specifically assess the effect of mutant HTT on early HD phenotypes. We have assembled a silencing construct and stably integrated it into the iPSC genome; this construct is based on the piggyBac transposase system (Yusa et al., 2011) and contains anti-HTT or control shRNA in the mir-30 backbone (Paddison et al., 2004), and the gene encoding mOrange2 fluorescent protein (Shaner et al., 2008) as a reporter (**Figure 1A**). To establish mouse isogenic iPSC, we used our previously generated HD iPSC lines (Szlachcic et al., 2015) derived from YAC128 mice (Slow et al., 2003) and several shRNA silencing constructs. Using the constructs, we first evaluated the efficiency of 3 anti-HTT shRNAs (shHTT1-3) in iPSCs (see next section, Table S1). Then, we used the most effective reagent (shHTT2), as well as a reagent specifically targeting the CAG repeats (shCAG) (Fiszer et al., 2013) or targeting EGFP as a control (shCTRL), and we generated 12 isogenic iPSC lines expressing these shRNAs from two HD iPSC lines (two clones per line and reagent; **Figure 1B**, Table S1). The lines were genotyped for the presence of a proper shRNA construct (Figure S1). We also established human HD iPSCs expressing the sHTT2, shCAG, or shCTRL from HD109 (109 CAG repeats), HD71 (71 CAG repeats), and Control (21 CAG repeats) iPSC lines.

Floating neurospheres (non-adherent neural stem cells, NSCs) with and without the reagents were generated by iPSC differentiation and expressed characteristic cellular markers (Figures S2A–E). To investigate survival of cells containing reagents in the mouse brain, we injected the cells into the mouse striatum, and using the PACT method (Yang et al., 2014) we found that they survived for the 8-week test period (Figure S2F). The mOrange2 reporter exhibited a strong red fluorescent signal in pluripotent shRNA iPSCs, embryoid bodies and throughout adherent differentiation (**Figures 1C,D**). Summarizing, we have generated both mouse and human HD lines containing construct with several shRNA reagents targeting various parts of mRNA for human HTT able to differentiate to NSC and able to survive in mouse brain upon delivery by injection.

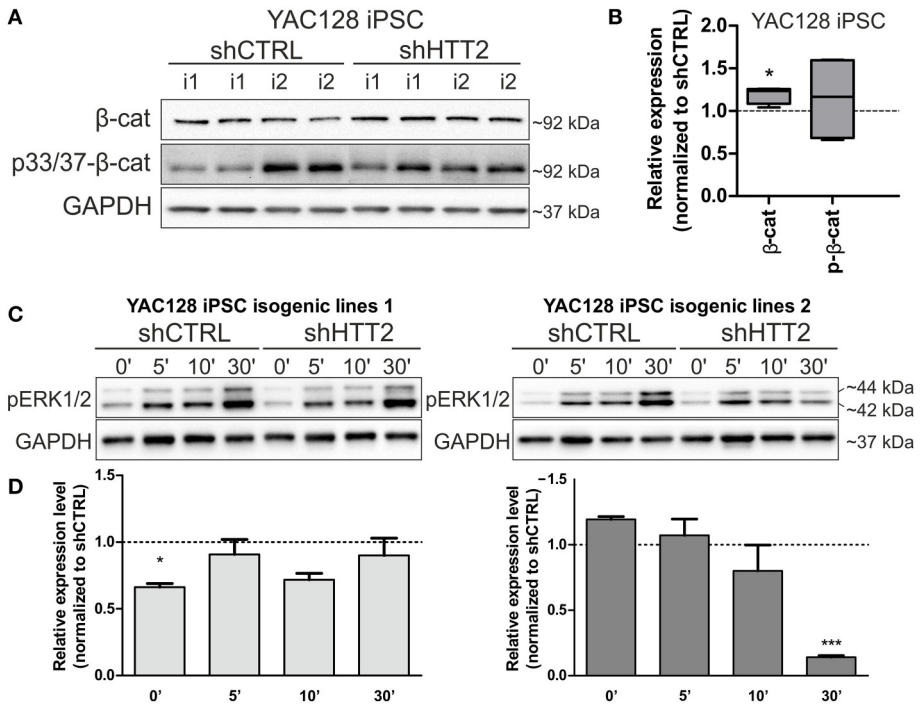

FIGURE 4 | Effects of mutant HTT knockdown on MAPK and Wnt pathways in mouse iPSCs. **(A,B)** Western blot analysis of shHTT2 effects on the Wnt pathway revealed a significant increase in total β-catenin levels but not phospho-β-catenin (S33/37) levels. $N = 4$ lines for each reagent; **(C,D)** Isogenic lines ($N = 2$ for each reagent) originating from separate parental lines (1 and 2) show different responses to bFGF-induced activation of ERK1/2 phosphorylation (Thr202/Tyr204) after 30 min of stimulation. $^{*}p<0.05$, $^{***}p<0.001$. In Panel **(A)** blots were cropped; full-length blots are presented in Figure S8.

3.2. Continuously Expressed shRNA Reagents Can Efficiently Silence Mutant HTT in Mouse iPSCs and NSCs

We first evaluated efficiency of three anti-huntingtin shRNA reagents (shHTT1, shHTT2, and shHTT3) in mouse HD iPSCs without clonal selection. shHTT1 and shHTT3 reagents lowered levels of mutant huntingtin by 54 ± 8% ($p = 0.0042$) and 35 ± 7% ($p = 0.004$), respectively (Figure S3), as assessed by western blotting. The most efficient reagent, shHTT2, which lowered HTT expression up to 85% was used in further studies and derivation of clonal mouse HD iPSC lines. The lines containing shHTT2, shCAG, or shCTRL reagents were tested for the expression of mutant and normal HTT. Western blotting with polyQ-specific antibody revealed that HTT was effectively silenced in iPSC lines containing the shHTT2 reagent (−85 ± 3%, $p = 0.0043$; shHTT2 vs. shCTRL; **Figures 2A,C**). HTT was not silenced, and in some cases was upregulated, in lines containing stable expression of the shCAG reagent; however, the upregulation was non-significant (19.5 ± 13%, $p = 0.2$; shCAG vs. shCTRL). We also analyzed the effects of shRNA reagents on expression of wild-type mouse HTT. Its expression was reduced in shHTT2-iPSC lines (−53 ± 13%; $p = 0.032$) but was unchanged in shCAG-iPSC lines.

Next, we assessed whether the effect of HTT silencing with shRNA reagents was preserved after differentiation from iPSCs into a neural lineage. Therefore, we differentiated iPSCs containing shHTT2 to the state of non-adherent NSCs in bFGF and EGF conditions (Figure S1). Similar to iPSCs, mutant HTT was also effectively silenced in shHTT-NSC lines but with a slightly lower efficiency (−62 ± 19%, $p = 0.0005$; shHTT vs. shCTRL; **Figures 2B,D**). Surprisingly, the shCAG reagent, which was previously ineffective in iPSCs, became effective in the NSC state and decreased mutant HTT protein levels by 40 ± 10% ($p = 0.01$; shCAG vs. shCTRL). Summarizing, we have selected a shHTT2 reagent which is suitable for continuous expression iPSC and evokes stable silencing of mutant HTT with high efficiency in mouse cells.

3.3. Stable Expression of shRNA Reagents Silenced Total HTT in Human HD Cells

Human HD109, HD71, and Control iPSC lines expressing the HTT targeting shHTT2 reagent revealed effective silencing of both mutant (HD109: −51 ± 22%, $p = 0.059$; HD71: −83 ± 21%, $p<0.01$) and normal HTT (HD109: −62 ± 18% $p<0.05$; HD71: −79 ± 4% $p<0.001$; Control: −80 ± 17% $p<0.001$; **Figure 3**). In addition we have also tested the total level of HTT mRNA and found its effective silencing (Figure S4). Similarly to mouse HD iPSCs, the shCAG reagent was ineffective in human iPSC lines. We have also noticed major differences in expression levels of mutant and normal HTT which seemed to be dependent on CAG length in human iPSC lines. The expression level of normal HTT and total HTT was most significantly decreased in HD109

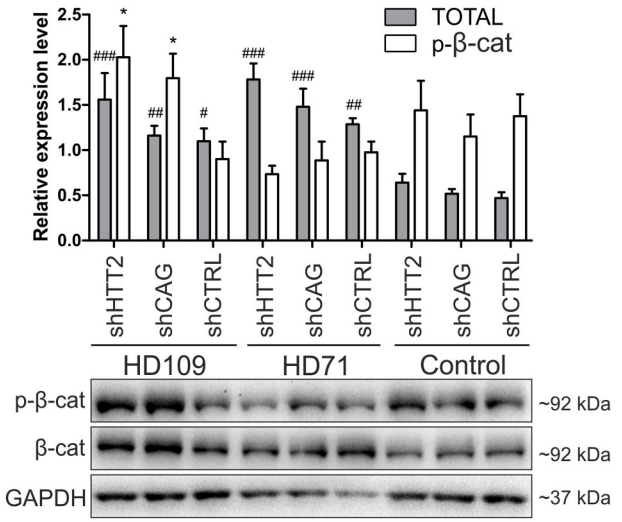

FIGURE 5 | Effects of mutant HTT knockdown on Wnt pathway in human iPSCs. Western blot analysis of shHTT2 effects on the Wnt pathway revealed a significant increase in total β-catenin levels in HD109 and HD71 lines as compared to healthy Control lines, but no effects of shRNA reagents. Phospho-β-catenin (S33/37) did not differ between lines with different CAG numbers, however its level was affected by both effective shHTT2 and ineffective shCAG reagents in HD109 iPSCs only. *Statistically significant difference vs. isogenic shCTRL line; #Statistically significant difference vs. Ctrl shCTRL line; * and #$p < 0.05$; ##$p<0.01$; ###$p<0.001$. For each patient, one cell line per each reagent was used (9 modified cell lines in total).

(normal allele: $-63 \pm 17.5\%$ $p<0.05$ as normalized to a single allele; total HTT level: $-72 \pm 16\%$, $p<0.01$; HD109 vs. Control) while the level of normal HTT have revealed the trend toward decreased HTT level in HD71 (normal allele: $-39 \pm 17\%$ $p = 0.0599$ as normalized to a single allele; total HTT level: $-25 \pm 17\%$ $p =$ ns; HD71 vs. Control). Moreover, HD109 had lower protein expression level of both HTT alleles as compared to HD71 lines (mutant allele: $-78 \pm 21\%$, $p< 0.01$; normal allele: $-40 \pm 10\%$ $p<0.05$; total HTT: $-62 \pm 15\%$ $p<0.05$). Regardless of the basal level of the HTT, the level of both mutant and normal allele dropped to comparable levels after silencing with shHTT2 in all lines. Therefore, some border level of HTT protein remains after silencing by a given shRNA and is independent of the initial level of the HTT. The low level of the normal HTT in HD109 iPSC is distinct to the much higher normal mouse HTT level in mHD-YAC128 iPSC (Figure S5). In summary, the silencing of HTT in human cells was efficient with shHTT2 reagent however the experiments additionally revealed a general decrease in expression of both mutant and normal HTT in HD109 iPSC vs. Control iPSC.

3.4. The Effects of HTT Silencing on Wnt and ERK Signaling in HD shRNA-iPS Cell Lines

We next asked whether downregulation of mutant HTT protein in shHTT2 iPSC lines would affect the pathways that were identified for HD and which were also affected in HD iPSC (Bowles and Jones, 2014; Szlachcic et al., 2015; Wiatr et al., 2017). Therefore, we examined β-catenin, phospho-β-catenin and phospho-ERK 1/2 by western blotting in HD YAC128 iPSC (**Figure 4**) and human HD109 and HD 71 iPSCs (**Figure 5**, Figure S5). In our previous study, we observed that more β-catenin protein is tagged for decay by Wnt-mediated phosphorylation at serines 33 and 37 in HD iPSCs (Szlachcic et al., 2015). The downregulation of mutant HTT did not affect this phenotype; however, the total β-catenin expression was increased ($19 \pm 6\%$, $p = 0.0126$) in mouse shHTT2-iPSC lines (**Figures 4A,B**). MAPK signaling is suppressed in HD YAC128 iPSCs, as indicated by the weaker ERK1/2 phosphorylation observed upon bFGF stimulation (Szlachcic et al., 2015). In the present study we observed an inconsistent response to HTT silencing (**Figures 4C,D**) showing no rescue (in isogenic lines derived from lines 1) or further decrease of ERK1/2 phosphorylation (in isogenic lines derived from line 2) after 30 min of bFGF stimulation ($-87 \pm 14\%$; shHTT2 vs. shCTRL Bonferroni *post-hoc* test $p<0.001$).

In the case of Wnt in human cells (**Figure 5**) we observed a general increase in phospho-β-catenin in HD109 cells with HTT knockdown ($+125 \pm 44\%$; $p<0.05$; shHTT2 vs shCTRL), while it was not changed in HD71 upon HTT knockdown. In HD109 and HD71 shCtrl lines total β-catenin level was increased as compared to Control shCtrl cells ($+134 \pm 40\%$, $p< 0.05$ and $174 \pm 21\%$, $p<0.01$, respectively). Silencing of HTT with shHTT2 in HD71 further increased the level of total β-catenin ($39 \pm 15\%$; $p<0.05$; shHTT2 vs. shCTRL) but no significant increase was present in HD109 ($42 \pm 30\%$, not significant, shHTT2 vs. shCTRL). ERK1/2 phosphorylation was not affected in human HD109 and HD71 cells with shHTT vs shControl (Figure S6). In general we observed moderate effects of the HTT silencing on Wnt and Erk1/2 pathways in both mouse and human HD iPSC.

3.5. HTT Silencing Is Able to Reverse p53 Deregulation in Mouse Isogenic iPSCs and NSCs

Along with our previous data showing decreased levels of p53 expression in YAC128 iPSCs and human juvenile HD iPSCs (Szlachcic et al., 2015), we found a similar decrease in p53 expression in NSCs originating from YAC128 iPSCs ($-52 \pm 7\%$, $p = 0.0006$) (**Figures 6A,B**). Subsequently, we investigated the YAC128 iPSCs and NSCs with shHTT and shCAG reagents vs isogenic shCTRL lines. In **Figures 6C,D**, we show that shHTT2 is able to rescue the decrease in p53 protein expression and to drive p53 expression well above the levels seen with the shCTRL reagent in both iPSCs and NSCs ($56 \pm 11\%$, $p = 0.0003$ and $44 \pm 19\%$, $p = 0.053$, respectively). Interestingly, the shCAG reagent did not rescue p53 expression in iPSCs or NSCs and led to further decreases in the p53 levels (**Figures 6C,D**). The pattern of p53 deregulation was followed by similar deregulation of phospho-p53 (S15) (Figure S7). The correlation study on isogenic lines expressing all anti-HTT reagents (shHTT1-3) or shCTRL reagents revealed that the levels of mutant HTT and p53 were

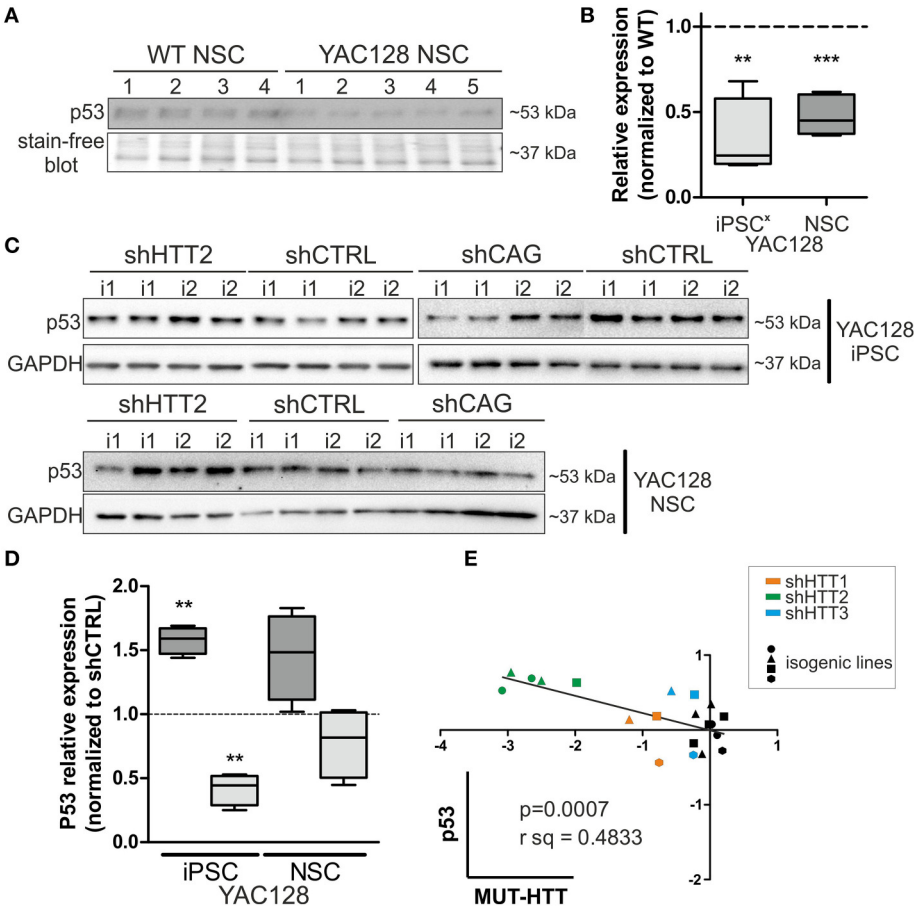

FIGURE 6 | p53 protein levels in iPSC and NSC states are dependent on mutant HTT levels. **(A,B)** The decreased p53 level is maintained in HD YAC128 NSCs after differentiation of iPSCs, as assessed by western blotting ($N = 4$ for WT and $N = 5$ for YAC128). The data was normalized to total protein visualized on blots using Bio-rads stain-free technology. Data from YAC128 iPS cells (X) was adapted from our previous work (Szlachcic et al., 2015) ($N = 6$ for WT, $N = 5$ for YAC128). shHTT iPSC **(C)** and NSC **(D)** lines show reversal of the p53 phenotype, whereas shCAG reagents further decrease the p53 expression level. $N = 4$ for each reagent in both iPSC and NSC. **(E)** Pearson correlation reveals an inverse correlation of mutant HTT and p53 expression levels ($N = 11$ for HTT reagents and $N = 9$ for control shCTRL reagent). In NSCs, the correlation is not significant $^{**}p < 0.01$, $^{***}p < 0.001$. In Panel **(A)** and (**C**, iPSCs) blots were cropped; full-length blots are presented in Figure S8.

inversely correlated in iPSCs (Pearson $r = -0.6952$; $p = 0.0007$; **Figure 6E**).

Although, p53 level was strongly decreased in human 109Q lines as compared to healthy control lines with shRNAs expression ($-85 \pm 15\%$, $p<0.001$ between shCTRL lines), we found no effects of HTT silencing with shHTT2 reagent on the p53 expression level (**Figure 7**). In summary, we found the that the low level of p53 in mouse YAC128 iPSC and derived NSC was reversible after shHTT2, while the decreased level of p53 in human cells did not react to silencing.

4. DISCUSSION

An experimental system in which the expression of a causative gene can be constantly depleted or eliminated should be considered for studying the pathogenesis of genetic neurodegenerative disorders and for therapeutic approaches. Therefore our aim was to generate HD iPSC lines with stable depletion of mutant HTT and to identify whether phenotypes characteristic for HD can be affected by HTT knockdown in HD iPSC. In addition, such approach allows for generation of cell lines with or without HTT silencing on the same, homogenous genetic background, i.e., isogenic lines. Use of isogenic lines reduces variability between compared cell lines that could mask discovery of relevant phenotypes.

One of the suitable strategies for genetic correction of HD cells is the constant expression of shRNA and gene silencing. We used a piggyBac transposase system (Yusa et al., 2011) and anti-HTT shRNA in the mir-30 backbone (Paddison et al., 2004) which provides additional possibility for future excision of the reagent if desired. Using the strategy (**Figure 8**), we derived isogenic mouse YAC128 HD and human HD iPSCs with continuous expression of shRNA targeting HTT. In the case of mouse iPSC, we tested 3 reagents targeting human HTT shHTT1-3 and a reagent targeting CAG repeats in mutant HTT (shCAG). The most potent anti-HTT reagent, shHTT2,

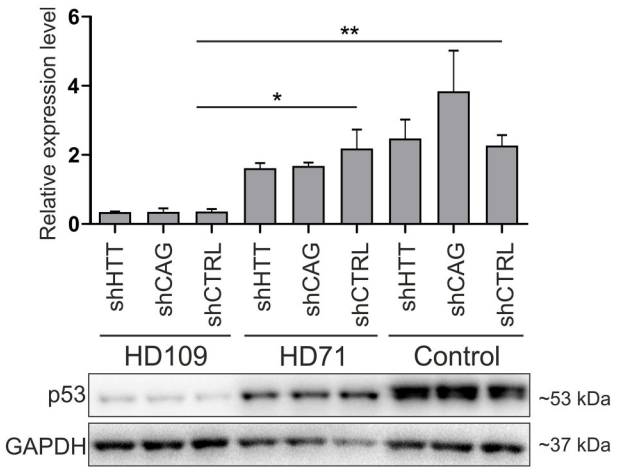

FIGURE 7 | Non-allele selective silencing of HTT does not affect p53 expression level in human juvenile HD and control iPSCs. Western blot analysis of p53 expression in human HD109, HD71 and Control iPSCs with shHTT2, shCAG and shCTRL reagents. Although, in HD109 shCTRL line expression of p53 was significantly lower than in shCTRL HD71 ($p = 0.0104$) or Control line ($p = 0.0045$), shHTT reagent did not affect the phenotype in any of lines. *$p<0.05$; **$p< 0.01$. For each patient, one cell line per each reagent was used (9 modified cell lines in total).

was continuously effective in both mouse iPSC and NSC lines with approximately 85 and 62% silencing of the mutant human protein, respectively; the silencing was similar between isogenic lines with different reagents. However, the shHTT2 reagent also reduced by approximately 53% expression of wild-type mouse huntingtin, which is expressed in YAC128 mice from 2 alleles. The shHTT2 reagent was also further used to generate shRNA expressing human HD109, HD71 and Control iPSCs. In human lines the reagent was silencing both mutant and normal allele with similarly high efficiency (over 80% silencing in HD71 and Control iPSCs). We also observed lower levels of both normal and mutant HTT in HD109 cells; however after knockdown with shHTT2 reagent the expression level of each allele reached similar levels in all lines, irrespectively of their expression levels in isogenic lines without silencing. The factor interfering with the HTT protein and transcript level may be a transcript retention in the nuclear foci demonstrated for HD cells which may result in prevention of the effective transport and translation of both mutant and normal transcripts (Urbanek et al., 2016). This may result in knock down of normal and mutant HTT in stem cells and insufficiency of HTT during development in juvenile patients. Low level of normal huntingtin may also indicate that its silencing via non-allele specific strategies might be detrimental in the case of juvenile HD.

The action of the shCAG reagent whose design was based on published allele-selective reagent revealed a dependency on cell type. In mouse iPSCs, the reagent increased mutant HTT expression, in mouse NSCs it induced a 40% silencing effect, while in human iPS cells it remained ineffective. In previous studies, the shCAG reagent was very effective at silencing HTT in fibroblasts (Fiszer et al., 2013); the observed differences in shCAG activity might result from differences in processing of the reagent in different cell types (Meijer et al., 2014; Tan et al., 2014). The described phenomena may depend on differences in the construct properties and the reagent delivery, e.g., our piggyBac construct vs. a lentiviral construct (Fiszer et al., 2013). Therefore, the shCAG reagent might be effective and should be examined in terminally differentiated neurons. Moreover, our results indicate the necessity of tailoring the therapeutic shRNA and delivery systems for disease-specific cell types, e.g., terminally differentiated neurons or astrocytes in the case of HD. In addition, the shCAG reagent demonstrates a new feature of our system namely as a reagent testing pipeline where the effects of reagents can be more precisely tested in consecutive cellular stages.

We have previously reported that YAC128 iPSCs exhibit phenotypes of early HD and share these phenotypes with human iPSCs from juvenile HD patients (Szlachcic et al., 2015). Among the changes, we identified decreased MAPK1 activation and p53 levels and increased β-catenin-p(33/37) levels. Using the established system for continuous silencing we have assessed whether the HD phenotypes demonstrated a dependency on the level of mutant HTT. In the case of the MAPK pathway and iPSCs, we observed minor changes in ERK1/2 activation depending on the iPSC line. In the case of mouse iPSC and Wnt pathway, the total β-catenin level had a slight dependency on the HTT level. Also in HD71 we have seen a greater total HTT level which may indicate recovery of Wnt signaling. In the case of HD109 we have demonstrated even higher phosphorylation of β-catenin, which may indicate an adverse effect on Wnt. We conclude that more human iPSC more HD iPS cell lines with mutant allele selective silencing originating from several patients are needed to investigate a fine relation of HTT expression and the pathways in iPSC. The differences in the phenotypes between HD109 and HD71 iPSC may be also attributed to number of CAG repeats in HTT but we can also not exclude the effect of the genetic background.

A large difference in p53 expression was found in the isogenic mouse iPSC and NSC. First, we demonstrated that p53 downregulation continued through to the NSC stage and the difference was similar to one previously seen by us for iPSC (Szlachcic et al., 2015). Moreover, shRNA isogenic cell lines at the iPSC and NSC stages demonstrated a clear dependency of p53 level on the mutant HTT level, although the effect was less prominent in NSCs. Interestingly, we observed recovery of decreased p53 expression with the shHTT2 reagent and a lack of recovery and a further decline in p53 expression with shCAG in both cell types. In the case of human HD109 iPS cells expressing the shHTT2 we did not observe the recovery of p53 level. Previously, p53 was shown to be involved in HD pathogenesis, with total levels in the brain increasing with HD severity and particularly being upregulated in late HD stages, in grade 3 and 4 patients (Bae et al., 2005). Although, p53 protein expression was upregulated in YAC128 mice, this upregulation was not observed in primary neuronal culture from E16.5 YAC128 mice unless cells were treated with the p53 activator camptothecin (Ehrnhoefer et al., 2013). Moreover, p53 phosphorylation and activation of the ATM DNA-damage-response pathway are downregulated

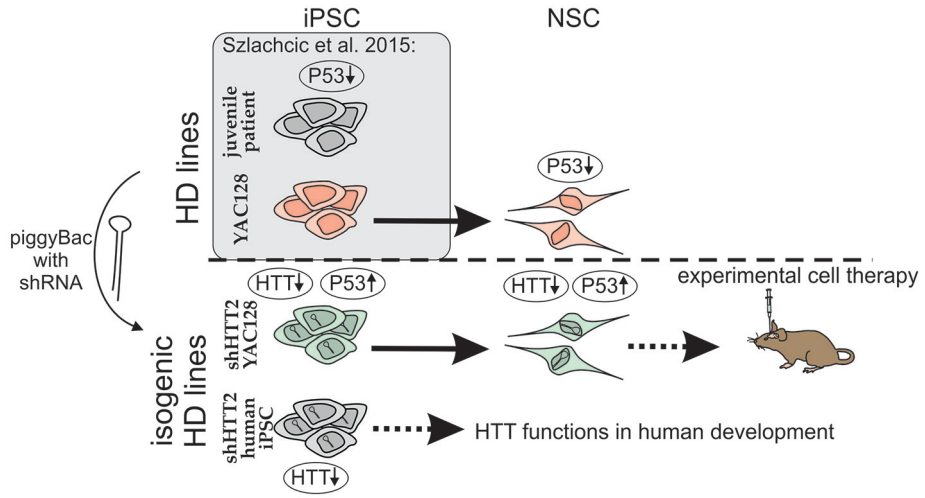

FIGURE 8 | Schematic illustration of the isogenic experimental system. Isogenic iPSC lines with HTT silencing by shHTT2 were derived from previously described HD-YAC128 iPSCs and human HD109, HD71, and Control iPSCs. Knockdown of HTT in both YAC128 iPSCs and NSCs resulted in rescue of p53 downregulation phenotype. iPSCs with HTT knockdown can be used for experimental cell therapy (mouse YAC128 iPSCs) or research on huntingtin developmental functions (human iPSCs). Gene expression changes are indicated by upward (upregulation) or downward arrows (downregulation).

in HD iPSCs (Tidball et al., 2015). Our results, together with the published data, may indicate that the gradient of p53 expression changes from downregulation in early HD stages (stem and NSCs) to upregulation in the adult brain during neurodegeneration. In general, it is well established that fine regulation of p53 expression in early developmental stages is essential to maintain the necessary balance between stem cell self-renewal and differentiation (Yang et al., 2014). In addition, high p53 expression levels may lead to terminal differentiation and growth arrest (Mendrysa et al., 2011). Decreased p53 levels in neurodegenerative diseases may lead to excessive NSC activation and insufficient differentiation potential, similar to what is observed in fragile X syndrome model (Li et al., 2016). NSCs from HD mouse models also show enhanced late-stage self-renewal, delayed cell cycle exit and impaired differentiation into striatal medium spiny neurons subtype (Molero et al., 2009; Molina-Calavita et al., 2014). Therefore, p53 may be a valid early therapeutic target in neurodegenerative diseases. Similar to p53 the Wnt is one of the major signaling pathways during development, it remains active in adult brain and is implicated in brain diseases (Noelanders and Vleminckx, 2017). In addition, the clear dependency of p53 on HTT expression in mouse cells and its downregulation in HD109 iPSCs implicates p53 in potential therapy in juvenile HD.

Sustained silencing of HTT via shRNA in iPSCs and NSCs, together with the observed p53 phenotype reversal, supports the idea of combining shRNA and autologous cell therapy. In therapeutic applications for HD, simple excision of the mutant allele via homologous recombination (An et al., 2012) or genome editing using, e.g., a CRISPR-Cas9 system, may be insufficient and could be accompanied by stable shRNA expression. An important reason for combining both approaches or even for selecting shRNA for cell therapy is evident from several demonstrations of neurodegeneration (including HTT aggregate formation) of healthy cells grafted into a brain undergoing neurodegeneration (Cicchetti et al., 2009, 2011, 2014; Jeon et al., 2016). One of the underlying mechanisms is the shuttling of HTT mRNA or HTT protein aggregates between cells, thus allowing them to spreading through the graft in a prion-like manner (Brundin et al., 2010; Herrera and Outeiro, 2012; Costanzo et al., 2013; Pecho-Vrieseling et al., 2014; Jeon et al., 2016; Zhang et al., 2016). Moreover, it is known that cells, including neurons and glia, can mediate exosomal and non-exosomal transfer of both proteins and RNAs (Vlassov et al., 2012; Frühbeis et al., 2013), including miRNAs (Wang et al., 2010; Hu et al., 2012) and synthetic mature shRNAs (Olson et al., 2012). Therefore, shRNA from grafted cells, if transferred via exosomes, may confer a therapeutic effect on host cells. Taken together, sustained expression of an HTT-silencing agent that also reverses the molecular phenotype has the capacity to protect grafts from non-cell-autonomous degeneration caused by surrounding HD-affected host cells.

To our knowledge, our human HD and Control iPSC lines with integrated shHTT2 are the first human iPSCs with stable huntingtin knock-down, and they can be helpful for *in vitro* research on huntingtin functions in human development.

AUTHOR CONTRIBUTIONS

WS and MacF conceived, designed, performed the experiments, and analyzed the data. KW performed ERK assay and consecutive western blotting analyses. KW and MT cultured and analyzed the phenotype of NSC. MacF planned and executed the live animal experiments (mouse brain injections). MarF critically revised the article. WS and MacF wrote the paper. MacF was responsible for concept and obtaining funding.

FUNDING

This work was supported by the European Regional Development Fund within the Innovative Economy Programme (grant number POIG.01.03.01-30-049/09), a grant from the National Science Centre (grant number 2013/10/E/NZ4/00621) and the Polish Ministry of Science and Higher Education, under the KNOW program (01/KNOW2/2014). WS received support for young investigators from the Polish Ministry of Science and Higher Education (statutory funds).

ACKNOWLEDGMENTS

We thank Professor Allan Bradley (Wellcome Trust Sanger Institute, Cambridge, UK) for kindly providing the piggyBac reprogramming system. We thank prof. Jerzy Ciesiołka for kindly providing DO-1 antibody. The MW1 (developed by P. H. Patterson), 6G7 (developed by W. M. Halfter) and Rat-401 (developed by S. Hockfield) antibodies were obtained from the Developmental Studies Hybridoma Bank, created by the NICHD of the NIH and maintained at The University of Iowa, Department of Biology, Iowa City, IA, USA. 4-19 antibody was obtained from CHDI Foundation Repository at Corriel Institute Cell Repositories, Camden, NJ, USA. Confocal images were obtained in the Laboratory of Subcellular Structures Analysis, IBCh, PAS, Poland. Cell cultures were conducted in Cell and Tissue Culture Laboratory, IBCh, PAS, Poland.

SUPPLEMENTARY MATERIAL

The Supplementary Material for this article can be found online at: http://journal.frontiersin.org/article/10.3389/fnmol.2017.00253/full#supplementary-material

REFERENCES

An, M. C., Zhang, N., Scott, G., Montoro, D., Wittkop, T., Mooney, S., et al. (2012). Genetic correction of Huntington's disease phenotypes in induced pluripotent stem cells. *Cell Stem Cell* 11, 253–263. doi: 10.1016/j.stem.2012.04.026

Bae, B.-I., Xu, H., Igarashi, S., Fujimuro, M., Agrawal, N., Taya, Y., et al. (2005). p53 mediates cellular dysfunction and behavioral abnormalities in Huntington's disease. *Neuron* 47, 29–41. doi: 10.1016/j.neuron.2005.06.005

Bates, G. P., Dorsey, R., Gusella, J. F., Hayden, M. R., Kay, C., Leavitt, B. R., et al. (2015). Huntington disease. *Nat. Rev. Dis. Primers* 1:15005. doi: 10.1038/nrdp.2015.5

Bowles, K. R., and Jones, L. (2014). Kinase signalling in Huntington's disease. *J. Huntingtons Dis.* 3, 89–123. doi: 10.3233/JHD-140106

Brundin, P., Melki, R., and Kopito, R. (2010). Prion-like transmission of protein aggregates in neurodegenerative diseases. *Nat. Rev. Mol. Cell Biol.* 11, 301–307. doi: 10.1038/nrm2873

Cicchetti, F., Lacroix, S., Cisbani, G., Vallières, N., Saint-Pierre, M., St-Amour, I., et al. (2014). Mutant huntingtin is present in neuronal grafts in Huntington disease patients. *Ann. Neurol.* 76, 31–42. doi: 10.1002/ana.24174

Cicchetti, F., Saporta, S., Hauser, R. A., Parent, M., Saint-Pierre, M., Sanberg, P. R., et al. (2009). Neural transplants in patients with Huntington's disease undergo disease-like neuronal degeneration. *Proc. Natl. Acad. Sci. U.S.A.* 106, 12483–12488. doi: 10.1073/pnas.0904239106

Cicchetti, F., Soulet, D., and Freeman, T. B. (2011). Neuronal degeneration in striatal transplants and Huntington's disease: potential mechanisms and clinical implications. *Brain* 134(Pt 3), 641–652. doi: 10.1093/brain/awq328

Costanzo, M., Abounit, S., Marzo, L., Danckaert, A., Chamoun, Z., Roux, P., et al. (2013). Transfer of polyglutamine aggregates in neuronal cells occurs in tunneling nanotubes. *J. Cell. Sci.* 126(Pt 16), 3678–3685. doi: 10.1242/jcs.126086

Duyao, M. P., Auerbach, A. B., Ryan, A., Persichetti, F., Barnes, G. T., McNeil, S. M., et al. (1995). Inactivation of the mouse Huntington's disease gene homolog Hdh. *Science* 269, 407–410.

Ebert, A. D., Shelley, B. C., Hurley, A. M., Onorati, M., Castiglioni, V., Patitucci, T. N., et al. (2013). EZ spheres: a stable and expandable culture system for the generation of pre-rosette multipotent stem cells from human ESCs and iPSCs. *Stem Cell Res.* 10, 417–427. doi: 10.1016/j.scr.2013.01.009

Ehrnhoefer, D. E., Skotte, N. H., Ladha, S., Nguyen, Y. T. N., Qiu, X., Deng, Y., et al. (2013). p53 increases caspase-6 expression and activation in muscle tissue expressing mutant huntingtin. *Hum. Mol. Genet.* 23, 717–729. doi: 10.1093/hmg/ddt458

Fiszer, A., Olejniczak, M., Galka-Marciniak, P., Mykowska, A., and Krzyzosiak, W. J. (2013). Self-duplexing CUG repeats selectively inhibit mutant huntingtin expression. *Nucleic Acids Res.* 41, 10426–10437. doi: 10.1093/nar/gkt825

Frühbeis, C., Fröhlich, D., Kuo, W. P., and Krämer-Albers, E.-M. (2013). Extracellular vesicles as mediators of neuron-glia communication. *Front. Cell. Neurosci.* 7:182. doi: 10.3389/fncel.2013.00182

Halfter, W., Dong, S., Yip, Y.-P., Willem, M., and Mayer, U. (2002). A critical function of the pial basement membrane in cortical histogenesis. *J. Neurosci.* 22, 6029–6040.

Herrera, F., and Outeiro, T. F. (2012). α-Synuclein modifies huntingtin aggregation in living cells. *FEBS Lett.* 586, 7–12. doi: 10.1016/j.febslet.2011.11.019

Hockfield, S., and McKay, R. D. (1985). Identification of major cell classes in the developing mammalian nervous system. *J. Neurosci.* 5, 3310–3328.

Hu, G., Drescher, K. M., and Chen, X.-M. (2012). Exosomal miRNAs: biological properties and therapeutic potential. *Front. Genet.* 3:56. doi: 10.3389/fgene.2012.00056

Jeon, I., Cicchetti, F., Cisbani, G., Lee, S., Li, E., Bae, J., et al. (2016). Human-to-mouse prion-like propagation of mutant huntingtin protein. *Acta Neuropathol.* 132, 577–592. doi: 10.1007/s00401-016-1582-9

Ko, J., Ou, S., and Patterson, P. H. (2001). New anti-huntingtin monoclonal antibodies: implications for huntingtin conformation and its binding proteins. *Brain Res. Bull.* 56, 319–329. doi: 10.1016/S0361-9230(01)00599-8

Kordasiewicz, H. B., Stanek, L. M., Wancewicz, E. V., Mazur, C., McAlonis, M. M., Pytel, K. A., et al. (2012). Sustained therapeutic reversal of Huntington's disease by transient repression of huntingtin synthesis. *Neuron* 74, 1031–1044. doi: 10.1016/j.neuron.2012.05.009

Li, Y., Stockton, M. E., Bhuiyan, I., Eisinger, B. E., Gao, Y., Miller, J. L., et al. (2016). MDM2 inhibition rescues neurogenic and cognitive deficits in a mouse model of fragile X syndrome. *Sci. Transl. Med.* 8:336ra61. doi: 10.1126/scitranslmed.aad9370

Macdonald, D., Tessari, M., Boogaard, I., Smith, M., Pulli, K., Szynol, A., et al. (2014). Quantification assays for total and polyglutamine-expanded huntingtin proteins. *PLoS ONE* 9:e96854. doi: 10.1371/journal.pone.0096854

Martí, E. (2016). RNA toxicity induced by expanded CAG repeats in Huntington's disease. *Brain Pathol.* 26, 779–786. doi: 10.1111/bpa.12427

Mattis, V. B., and Svendsen, C. N. (2015). Modeling Huntington's disease with patient-derived neurons. *Brain Res.* 1656, 76–87. doi: 10.1016/j.brainres.2015.10.001

McKinstry, S. U., Karadeniz, Y. B., Worthington, A. K., Hayrapetyan, V. Y., Ozlu, M. I., Serafin-Molina, K., et al. (2014). Huntingtin is required for normal excitatory synapse development in cortical and striatal circuits. *J. Neurosci.* 34, 9455–9472. doi: 10.1523/JNEUROSCI.4699-13.2014

Meijer, H. A., Smith, E. M., and Bushell, M. (2014). Regulation of miRNA strand selection: follow the leader? *Biochem. Soc. Trans.* 42, 1135–1140. doi: 10.1042/BST20140142

Mendrysa, S. M., Ghassemifar, S., and Malek, R. (2011). p53 in the CNS: perspectives on development, stem cells, and cancer. *Genes Cancer* 2, 431–442. doi: 10.1177/1947601911409736

Miniarikova, J., Zanella, I., Huseinovic, A., van der Zon, T., Hanemaaijer, E., Martier, R., et al. (2016). Design, Characterization, and lead selection of therapeutic miRNAs targeting huntingtin for development of gene therapy for Huntington's disease. *Mol. Ther. Nucleic Acids* 5:e297. doi: 10.1038/mtna.2016.7

Molero, A. E., Arteaga-Bracho, E. E., Chen, C. H., Gulinello, M., Winchester, M. L., Pichamoorthy, N., et al. (2016). Selective expression of mutant huntingtin during development recapitulates characteristic features of Huntington's disease. *Proc. Natl. Acad. Sci. U.S.A.* 113, 5736–5741. doi: 10.1073/pnas.1603871113

Molero, A. E., Gokhan, S., Gonzalez, S., Feig, J. L., Alexandre, L. C., and Mehler, M. F. (2009). Impairment of developmental stem cell-mediated striatal neurogenesis and pluripotency genes in a knock-in model of Huntington's disease. *Proc. Natl. Acad. Sci. U.S.A.* 106, 21900–21905. doi: 10.1073/pnas.0912171106

Molina-Calavita, M., Barnat, M., Elias, S., Aparicio, E., Piel, M., and Humbert, S. (2014). Mutant huntingtin affects cortical progenitor cell division and development of the mouse neocortex. *J. Neurosci.* 34, 10034–10040. doi: 10.1523/JNEUROSCI.0715-14.2014

Nasir, J., Floresco, S. B., O'Kusky, J. R., Diewert, V. M., Richman, J. M., Zeisler, J., et al. (1995). Targeted disruption of the Huntington's disease gene results in embryonic lethality and behavioral and morphological changes in heterozygotes. *Cell* 81, 811–823. doi: 10.1016/0092-8674(95)90542-1

Noelanders, R., and Vleminckx, K. (2017). How Wnt signaling builds the brain: bridging development and disease. *Neuroscientist* 23, 314–329. doi: 10.1177/1073858416667270

Olson, A., Sheth, N., Lee, J. S., Hannon, G., and Sachidanandam, R. (2006). RNAi Codex: a portal/database for short-hairpin RNA (shRNA) gene-silencing constructs. *Nucleic Acids Res.* 34(Database issue), D153–D157. doi: 10.1093/nar/gkj051

Olson, S. D., Kambal, A., Pollock, K., Mitchell, G.-M., Stewart, H., Kalomoiris, S., et al. (2012). Examination of mesenchymal stem cell-mediated RNAi transfer to Huntington's disease affected neuronal cells for reduction of huntingtin. *Mol. Cell. Neurosci.* 49, 271–281. doi: 10.1016/j.mcn.2011.12.001

Paddison, P. J., Cleary, M., Silva, J. M., Chang, K., Sheth, N., Sachidanandam, R., et al. (2004). Cloning of short hairpin RNAs for gene knockdown in mammalian cells. *Nat. Methods* 1, 163–167. doi: 10.1038/nmeth1104-163

Pecho-Vrieseling, E., Rieker, C., Fuchs, S., Bleckmann, D., Esposito, M. S., Botta, P., et al. (2014). Transneuronal propagation of mutant huntingtin contributes to non-cell autonomous pathology in neurons. *Nat. Neurosci.* 17, 1064–1072. doi: 10.1038/nn.3761

Quigley, J. (2017). Juvenile Huntington's disease: diagnostic and treatment considerations for the psychiatrist. *Curr. Psychiatry Rep.* 19:9. doi: 10.1007/s11920-017-0759-9

Rué, L., Banez-Coronel, M., Creus-Muncunill, J., Giralt, A., Alcalá-Vida, R., Mentxaka, G., et al. (2016). Targeting CAG repeat RNAs reduces Huntington's disease phenotype independently of huntingtin levels. *J. Clin. Invest.* 126, 4319–4330. doi: 10.1172/JCI83185

Shaner, N. C., Lin, M. Z., McKeown, M. R., Steinbach, P. A., Hazelwood, K. L., Davidson, M. W., et al. (2008). Improving the photostability of bright monomeric orange and red fluorescent proteins. *Nat. Methods* 5, 545–551. doi: 10.1038/nmeth.1209

Slow, E. J., van Raamsdonk, J., Rogers, D., Coleman, S. H., Graham, R. K., Deng, Y., et al. (2003). Selective striatal neuronal loss in a YAC128 mouse model of Huntington disease. *Hum. Mol. Genet.* 12, 1555–1567. doi: 10.1093/hmg/ddg169

Squitieri, F., Frati, L., Ciarmiello, A., Lastoria, S., and Quarrell, O. (2006). Juvenile Huntington's disease: does a dosage-effect pathogenic mechanism differ from the classical adult disease? *Mech. Ageing Dev.* 127, 208–212. doi: 10.1016/j.mad.2005.09.012

Svendsen, C. N., ter Borg, M. G., Armstrong, R. J., Rosser, A. E., Chandran, S., Ostenfeld, T., et al. (1998). A new method for the rapid and long term growth of human neural precursor cells. *J. Neurosci. Methods* 85, 141–152. doi: 10.1016/S0165-0270(98)00126-5

Szlachcic, W. J., Switonski, P. M., Krzyzosiak, W. J., Figlerowicz, M., and Figiel, M. (2015). Huntington disease iPSCs show early molecular changes in intracellular signaling, the expression of oxidative stress proteins and the p53 pathway. *Dis. Model Mech.* 8, 1047–1057. doi: 10.1242/dmm.019406

Tabrizi, S. J., Scahill, R. I., Owen, G., Durr, A., Leavitt, B. R., Roos, R. A., et al. (2013). Predictors of phenotypic progression and disease onset in premanifest and early-stage Huntington's disease in the TRACK-HD study: analysis of 36-month observational data. *Lancet Neurol.* 12, 637–649. doi: 10.1016/S1474-4422(13)70088-7

Tan, G. C., Chan, E., Molnar, A., Sarkar, R., Alexieva, D., Isa, I. M., et al. (2014). 5' isomiR variation is of functional and evolutionary importance. *Nucleic Acids Res.* 42, 9424–9435. doi: 10.1093/nar/gku656

The-Huntington's-Disease-Collaborative-Research-Group (1993). A novel gene containing a trinucleotide repeat that is expanded and unstable on Huntington's disease chromosomes. *Cell* 72, 971–983.

Tidball, A. M., Bryan, M. R., Uhouse, M. A., Kumar, K. K., Aboud, A. A., Feist, J. E., et al. (2015). A novel manganese-dependent ATM-p53 signaling pathway is selectively impaired in patient-based neuroprogenitor and murine striatal models of Huntington's disease. *Hum. Mol. Genet.* 24, 1929–1944. doi: 10.1093/hmg/ddu609

Urbanek, M. O., Jazurek, M., Switonski, P. M., Figura, G., and Krzyzosiak, W. J. (2016). Nuclear speckles are detention centers for transcripts containing expanded cag repeats. *Biochim. Biophys. Acta* 1862, 1513–1520. doi: 10.1016/j.bbadis.2016.05.015

Vlassov, A. V., Magdaleno, S., Setterquist, R., and Conrad, R. (2012). Exosomes: current knowledge of their composition, biological functions, and diagnostic and therapeutic potentials. *Biochim. Biophys. Acta* 1820, 940–948. doi: 10.1016/j.bbagen.2012.03.017

Wang, K., Zhang, S., Weber, J., Baxter, D., and Galas, D. J. (2010). Export of microRNAs and microRNA-protective protein by mammalian cells. *Nucleic Acids Res.* 38, 7248–7259. doi: 10.1093/nar/gkq601

Wiatr, K., Szlachcic, W. J., Trzeciak, M., Figlerowicz, M., and Figiel, M. (2017). Huntington disease as a neurodevelopmental disorder and early signs of the disease in stem cells. *Mol. Neurobiol.* doi: 10.1007/s12035-017-0477-7. [Epub ahead of print].

Yang, B., Treweek, J. B., Kulkarni, R. P., Deverman, B. E., Chen, C.-K., Lubeck, E., et al. (2014). Single-cell phenotyping within transparent intact tissue through whole-body clearing. *Cell* 158, 945–958. doi: 10.1016/j.cell.2014.07.017

Yusa, K., Rad, R., Takeda, J., and Bradley, A. (2009). Generation of transgene-free induced pluripotent mouse stem cells by the piggyBac transposon. *Nat. Methods* 6, 363–369. doi: 10.1038/nmeth.1323

Yusa, K., Zhou, L., Li, M. A., Bradley, A., and Craig, N. L. (2011). A hyperactive piggyBac transposase for mammalian applications. *Proc. Natl. Acad. Sci. U.S.A.* 108, 1531–1536. doi: 10.1073/pnas.1008322108

Zeitlin, S., Liu, J. P., Chapman, D. L., Papaioannou, V. E., and Efstratiadis, A. (1995). Increased apoptosis and early embryonic lethality in mice nullizygous for the Huntington's disease gene homologue. *Nat. Genet.* 11, 155–163. doi: 10.1038/ng1095-155

Zhang, N., Bailus, B. J., Ring, K. L., and Ellerby, L. M. (2015). iPSC-based drug screening for Huntington's disease. *Brain Res.* 1638(Pt A), 42–56. doi: 10.1016/j.brainres.2015.09.020

Zhang, X., Abels, E. R., Redzic, J. S., Margulis, J., Finkbeiner, S., and Breakefield, X. O. (2016). Potential transfer of polyglutamine and CAG-repeat RNA in extracellular vesicles in Huntington's disease: background and evaluation in cell culture. *Cell. Mol. Neurobiol.* 36, 459–470. doi: 10.1007/s10571-016-0350-7

Conflict of Interest Statement: The authors declare that the research was conducted in the absence of any commercial or financial relationships that could be construed as a potential conflict of interest.

frontiers in Molecular Neuroscience

CORRECTION
published: 28 September 2017
doi: 10.3389/fnmol.2017.00312

Corrigendum: The Generation of Mouse and Human Huntington Disease iPS Cells Suitable for *In vitro* Studies on Huntingtin Function

*Wojciech J. Szlachcic[1], Kalina Wiatr[1], Marta Trzeciak[1], Marek Figlerowicz[2] and Maciej Figiel[1]**

[1] Department of Molecular Neurobiology, Institute of Bioorganic Chemistry, Polish Academy of Sciences, Poznań, Poland, [2] Department of Molecular and Systems Biology, Institute of Bioorganic Chemistry, Polish Academy of Sciences, Poznań, Poland

Keywords: Huntington disease, iPS cells, NS cells, YAC128, shRNA, huntingtin, p53, juvenile HD

A corrigendum on

The Generation of Mouse and Human Huntington Disease iPS Cells Suitable for *In vitro* Studies on Huntingtin Function

by Szlachcic, W. J., Wiatr, K., Trzeciak, M., Figlerowicz, M., and Figiel, M. (2017). Front. Mol. Neurosci. 10:253. doi: 10.3389/fnmol.2017.00253

In the original article, in the Acknowledgments section there was a missing sentence with acknowledgments for Pawel M. Switonski. The authors apologize for this error and state that this does not change the scientific conclusions of the article in any way.

The following sentence was missing from the Acknowledgments section: "We kindly thank Pawel M. Switonski for his contribution to designing the psiOrange constructs." Therefore, the Acknowledgments section should have read as follows.

ACKNOWLEDGMENTS

We thank Professor Allan Bradley (Wellcome Trust Sanger Institute, Cambridge, UK) for kindly providing the piggyBac reprogramming system. We kindly thank Pawel M. Switonski for his contribution to designing the psiOrange constructs. We thank Professor Jerzy Ciesiołka for kindly providing DO-1 antibody. The MW1 (developed by P. H. Patterson), 6G7 (developed by W. M. Halfter) and Rat-401 (developed by S. Hockfield) antibodies were obtained from the Developmental Studies Hybridoma Bank, created by the NICHD of the NIH and maintained at The University of Iowa, Department of Biology, Iowa City, IA, USA. 4–19 antibody was obtained from CHDI Foundation Repository at Corriel Institute Cell Repositories, Camden, NJ, USA. Confocal images were obtained in the Laboratory of Subcellular Structures Analysis, IBCh, PAS, Poland. Cell cultures were conducted in Cell and Tissue Culture Laboratory, IBCh, PAS, Poland.

Conflict of Interest Statement: The authors declare that the research was conducted in the absence of any commercial or financial relationships that could be construed as a potential conflict of interest.

OPEN ACCESS

Edited and reviewed by:
Clevio Nobrega, University of Algarve, Portugal

***Correspondence:**
Maciej Figiel
mfigiel@ibch.poznan.pl

Received: *04 September 2017*
Accepted: *15 September 2017*
Published: *28 September 2017*

Citation:
Szlachcic WJ, Wiatr K, Trzeciak M, Figlerowicz M and Figiel M (2017) Corrigendum: The Generation of Mouse and Human Huntington Disease iPS Cells Suitable for In vitro Studies on Huntingtin Function. Front. Mol. Neurosci. 10:312. doi: 10.3389/fnmol.2017.00312

Advantages of publishing in Frontiers

OPEN ACCESS
Articles are free to read for greatest visibility and readership

FAST PUBLICATION
Around 90 days from submission to decision

HIGH QUALITY PEER-REVIEW
Rigorous, collaborative, and constructive peer-review

TRANSPARENT PEER-REVIEW
Editors and reviewers acknowledged by name on published articles

Frontiers
Avenue du Tribunal-Fédéral 34
1005 Lausanne | Switzerland

Visit us: www.frontiersin.org
Contact us: info@frontiersin.org | +41 21 510 17 00

REPRODUCIBILITY OF RESEARCH
Support open data and methods to enhance research reproducibility

DIGITAL PUBLISHING
Articles designed for optimal readership across devices

FOLLOW US
@frontiersin

IMPACT METRICS
Advanced article metrics track visibility across digital media

EXTENSIVE PROMOTION
Marketing and promotion of impactful research

LOOP RESEARCH NETWORK
Our network increases your article's readership